8-17-2011

# Mechanistic studies on xanthine oxidoreductase enzymes

Abebe Berhane

# Mechanistic Studies on Xanthine Oxidoreductase Enzymes

**BY**

**ABEBE BERHANE**

H.B.Sc.,Chemistry, Lakehead University, 1997
M.Sc., Chemistry, California State Polytechnic University-Pomona, 2002

DISSERTATION

Submitted in Partial Fulfillment of the
Requirements for the Degree of

**Doctor of Philosophy**

CHEMISTRY

The University of New Mexico
Albuquerque, New Mexico

**May, 2010**

## ACKNOWLEDGMENTS

I would like to thank Prof. Martin L. Kirk for his guidance, patience, support, understanding, ideas, and funding throughout my stay in his laboratory. I wholeheartedly acknowledge my gratitude for admitting me to his research group and his desire to support me in my future professional development. Thanks so much. I am so grateful.

I would like to thank Prof. Larry L. Barton (Department of Biology, The University of New Mexico, Albuquerque, NM) whose collaboration in the enzyme purification has been an invaluable aid. Thanks for all the ideas, explanations, conversations, instructions, materials, and aid in the cultivation of *Oligotropha carboxidovorans* bacteria and purification of the Cu/Mo-CODH enzyme. In addition, thanks for the encouragement and desire to support me in my future professional development.

I would like to thank Prof. Silke Leimkühler (Department of Plant Biology, Technical University Braunschweig, Braunschweig, Germany) for providing us with the wild type xanthine dehydrogenase (*Rc*XDH) and its variant (*Rc*XDH-$Glu_{232}$Ala mutant) enzymes.

I would like to thank Prof. Hua Guo (Department of Chemistry and Chemical Biology, The University of New Mexico, Albuquerque, NM) for his collaborative efforts with the computation modeling and desire to support me in my future professional development.

I would like to thank my committee members, Prof. Robert T. Paine, Prof. Larry L. Barton, and Prof. Wei Wang for agreeing to be part of my Dissertation Committee.

I would like to thank both past and present members of the Kirk lab, mainly, Diana Habel-Rodriguez, Joseph Sempombe, Regina Mtei, for the efforts they put towards the Cu/Mo-CODH project.

# Mechanistic Studies on Xanthine Oxidoreductase Enzymes

**BY**

**ABEBE BERHANE**

ABSTRACT OF DISSERTATION

Submitted in Partial Fulfillment of the
Requirements for the Degree of

**Doctor of Philosophy**

CHEMISTRY

The University of New Mexico
Albuquerque, New Mexico

**May, 2010**

**Mechanistic Studies on Xanthine Oxidoreductase Enzymes**

**by**

**Abebe Berhane**

H.B.Sc.,Chemistry, Lakehead University, 1997

M.Sc., Chemistry, California State Polytechnic University-Pomona, 2002

Ph.D., Chemistry,The University of New Mexico, 2010

## ABSTRACT

In humans, the xanthine oxidoreductase enzymes are known to catalyze the final two steps of purine metabolism by converting hypoxanthine successively to xanthine and uric acid. Xanthine oxidoreductase also metabolizes a wide variety of drugs in vivo, and activates a number of antiviral prodrugs of clinical importance. Therefore, understanding the reaction mechanism of this enzyme is of prime importance in furthering our understanding of enzyme-drug interactions. In order to provide a greater understanding on the reaction mechanism, theoretical and enzymatic spectroscopic experimental approaches have been utilized. The theoretical approaches were used to elucidate the electronic structure and geometry of the reductive-half reaction. During the initial stage of catalysis, the substrate bound tetrahedral complex was expected to be transformed to the product bound intermediate by passing through the tetrahedral transition state. The transition state structures were modeled and characterized by one imaginary negative frequency that were stabilized by energies ranging between 0.33 - 19.0 kcal/mol. The Mulliken atomic charge and Mayer bond order profiles were provided, respectively, for selected atoms and the bonds associated with them. Based on the electronic structure and bonding descriptions, the re-allocation of an electron on Mo-center was proposed to take

place through an inner-sphere mechanism, with concomitant transfer of a proton or "formal" hydride transfer from the substrate carbon to the active site sulfido terminal. The formation of stable intermediate, in the presence of lumazine and bovine milk xanthine oxidase, was described by spectral bands centered at 650 nm. Similar spectral bands were also detected, in the presence of an electron acceptor (2, 6 – dichlorophenolindophenol, $DCIP^-$), when the enzymes (*bm*XOR, wild type *Rc*XDH, or *Rc*XDH-$Glu_{232}$Ala mutant) were reacted with lumazine. Finally, the enzymes were shown to exhibit variable activities and steady-state kinetic parameters when the reactions between the same substrates and enzymes were probed using the Amplex/$H_2O_2$ and $DCIP^-/O_2^{\bullet-}$ assay methods. The variation in activities and steady-state kinetic parameters were then proposed to be due to the factors that affected the affinity and product release stages of the catalytic cycle.

## TABLE OF CONTENTS

# Chapter 1.0

# Introduction

## 1.1 Survey of molybdo-enzymes

In a natural environment, enzymes are distributed within living cells either in the cytoplasm or membrane, or they may be localized in both parts of the cell. They are proteins that may or may not require the presence of additional non-protein components, such as cofactors. The presence of cofactors (such as inorganic and/or organic) may have purely structural or functional, or the cofactor may possess both roles. One of the interesting metals that serve as an inorganic cofactor in the chemistry of life, although less commonly occurring, is the molybdenum (Mo) ion. The presence of Mo ion, in the active sites of some proteins, represents a group of proteins known as 'molybdo-proteins' or 'molybdo-enzymes' [1, 2, 3].

Molybdo-enzymes are an important class of enzymes, found in several organisms, which mediate the metabolism of essential elements. With the exception of nitrogen-fixing nitrogenase (which contains a Fe-Mo-S cluster), all molybdo-enzymes possess a pterin-type cofactor (Fig. 1.1.1, a) which distinguishes them from other enzymes. As shown in Figure (1.1.1, b), the pyranopterin dithiolene (Fig. 1.1.1, a) contains a pterin system fused to a pyran ring. The pyran ring is shown to bear a phosphorylated di-hydroxybutyl side-chain. The terminal phosphate, of the pyran ring, may be covalently attached to either hydrogen atom or nucleotides [5, 6, 7, 8, 9, 10, 11]. Most importantly, the pyran ring contains a dithiolene bond that is coordinated to the Mo ion [1, 12]. The coordination of the Mo ion to the dithiolene ligand(s) leads to the formation of an active site of the molybdo-enzymes, known as the molybdenum cofactor (Moco) (Fig. 1.1.1, b) [13, 14, 15, 16]. The Moco moiety (established through the efforts of K. V. Rajagopalan and J. L. Johnson [17] and other workers) is believed to play an important role in positioning the active site correctly and defining the redox behavior of the enzymes. Most importantly, the cofactor allows the enzymes to gain a biological activity since nature has developed ways of incorporating

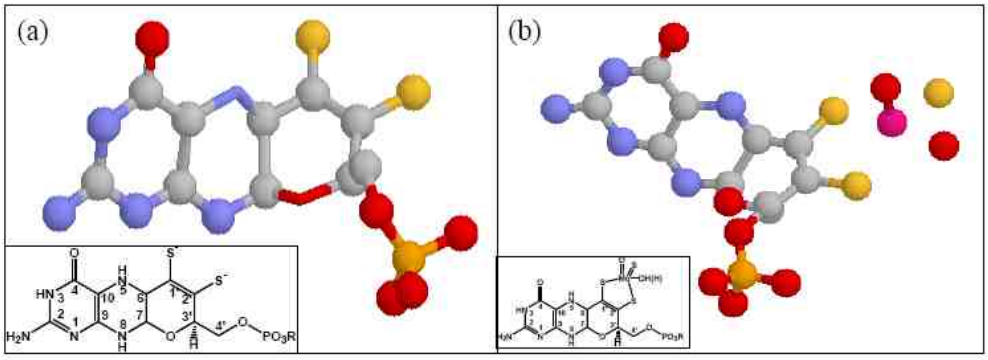


Figure 1.1.1. The structures of the pyranopterin dithiolene (a) and molybdenum cofactor (b) obtained from the X-ray crystal structure (PDB accession code of 1V97 [10]). The structures are reported for both the xanthine dehydrogenase and xanthine oxidase forms of the bovine milk xanthine oxidoreductase enzyme. The phosphorylated di-hydroxybutyl side-chain is attached to the pyran ring. The designation "R" may represent a hydrogen atom (in eukaryotic enzymes) or dinucleotides (in prokaryotic enzymes). The illustration is prepared with the application of protein explorer [21].

the Mo ion into more than fifty enzymes [1, 3, 18, 19, 20]. On the basis of the structure of Moco, as reviewed by G. Schwarz (2005) [4], molybdo-enzymes may be categorized into four different subgroups: The xanthine oxidase, XO (Fig. 1.1.2, a) [5, 10], carbon monoxide dehydrogenase, Cu/Mo-CODH (Fig. 1.1.2, b) [7, 8, 9], sulfite oxidase, SO (Fig. 1.1.2, c) [22], and dimethyl sulfoxide reductase, DMSO reductase (Fig. 1.1.2, d) [23] family of enzymes. However, R. Hille's (1996) [1] earlier classification recognized three major families of molybdo-enzymes [the XO (Fig. 1.1.2, a and b), SO (Fig. 1.1.2, c), and DMSO reductase (Fig. 1.1.2, d)], designated according to their most prominent members. As shown in Figure (1.1.2, a and b), the XO family of enzymes are defined by one pyranopterin dithiolene ligand. This designation is given for enzymes possessing $[MoSO](S_{dithiolene})_2 \cdot OH(H)$ unit such as xanthine oxidoreductase (XOR), aldehyde oxidoreductase (AOR), and carbon monoxide (CO) dehydrogenase (Cu/Mo-CODH) [4, 5, 8, 9, 10]. The SO family of enzymes are also defined by one pyranopterin dithiolene ligand, designated for enzymes possessing $[MoO_2](S_{dithiolene})_2S^{\gamma}_{Cys}$ unit (Fig. 1.1.2, c), such as sulfite oxidase and nitrate reductase (assimilatory) [1, 13, 24]. Finally, the DMSO reductase

family of enzymes has their Mo ion tethered by the two pyranopterin dithiolene ligands (Fig. 1.1.2, d). They are designated for the enzymes possessing [MoR] $(S^{1'}_{dithiolene})_2(S^{2'}_{dithiolene})_2X^{\gamma}$ (where R can be O or S and X can be $S_{Cys}$, $Se_{Cys}$, $O_{Ser}$, or $OH^-$) unit such as DMSO reductase and arsenite oxidase [1, 4, 13, 23].

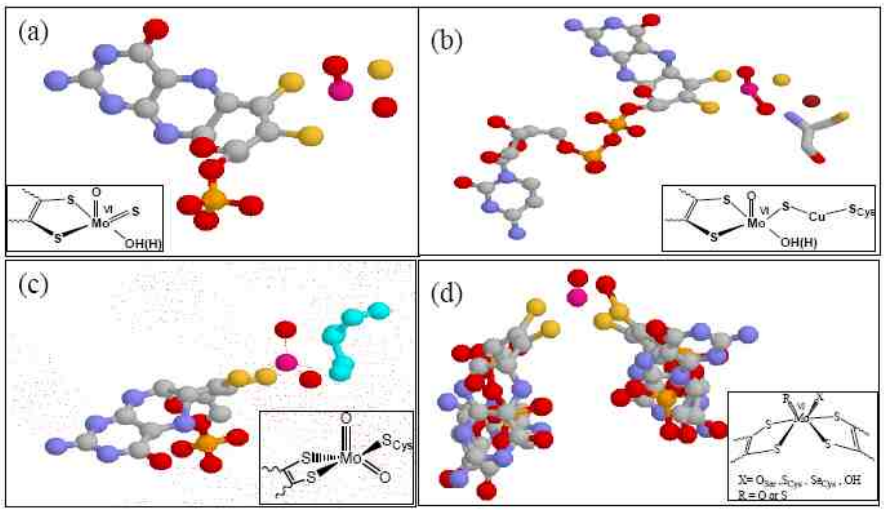


Figure 1.1.2. The reductive half-reaction active site structures obtained from X-ray crystal structures. The structures are reported for (a) xanthine oxidase (PDB accession code of 1V97) [10], (b) carbon monoxide dehydrogenase (PDB accession code of 1N5W) [8], (c) sulfite oxidase (PDB accession code of 1SOX) [22], and (d) DMSO reductase (PDB accession code of 1DMS) [23]. The illustration is prepared the same as Figure (1.1.1).

The molybdo-enzymes belong to the class of oxidoreductase enzymes, as classified by the International Enzyme Commission classification scheme [19]. As with many oxidoreductase enzymes, they are characterized for the suitability of their redox sites to undergo simultaneous interaction with both the reducing and oxidizing substrates. The reducing substrates react at the reductive and the oxidizing substrates at the oxidative half-reaction active sites. They also need additional components (such as pairs of $[Fe_2S_2](S^{\gamma}_{Cys})_4$ clusters) to facilitate the flow of electrons between the reductive and oxidative half-reaction active sites.

## 1.2 Physiology and biochemistry of xanthine oxidase family enzymes

The history of the XOR enzymes is believed to date back to the 19$^{th}$ century, when W. Spitzer (1899) recognized the XOR enzyme catalyzed oxidation of hypoxanthine to xanthine and xanthine to uric acid [25]. In 1902, F. Schardinger also described the reaction for the reduction of methylene blue in the presence of aldehyde and milk XOR enzyme (initially known as Schardinger enzyme [2, 5, 25]). After the enzyme is discovered by R. Burian (1905) [25] and Morgan *et al*. (1922) [25, 26] and isolated by Dixon *et al.* (1924) [27] from cow's milk, the XOR enzymes have been routinely isolated from various sources [28, 29, 30, 31, 32, 33, 34, 35, 36]. Although the mammalian XOR enzymes are synthesized in the form of dehydrogenase (XDH), the XDH form of the XOR enzyme is readily converted into the oxidase (XO) form by sulfhydryl oxidation or limited proteolysis [4, 5, 37, 38]. In humans, the function of the XOR enzymes is in purine metabolism. As shown in Scheme (1.1.1), the purine degredation pathway involves several steps that lead to the catabolism of AMP to hypoxanthine. In the presence of XOR enzymes and oxidizing substrates, hypoxanthine is successively converted to xanthine and uric acid. The catalytic conversion is also known to facilitate the reduction of oxidizing substrates to provide reactive oxygen species (ROS), such as superoxide radical ($O_2^{\cdot -}$) and hydrogen peroxide ($H_2O_2$) [2, 10, 31, 32, 41].

The XOR enzymes, as shown by several biochemical measurements [5, 14], are widely distributed throughout various mammalian organs [1, 4, 17, 35, 39, 40] and microorganism cells [14, 42]. In mammalian organs, the highest level of XOR activity is expressed in the liver [37]. The presence of XOR enzymes in the liver can be used as a marker for a hepatic damage, through the XOR enzymes circulating in the blood [2, 24, 37, 43]. However, the most noticeable disease in humans is the deposition of uric acid, known to be responsible for gouty conditions. This condition is more pronounced in the joints, through the deposition of sodium urate crystals [40]. In addition, as C. E. Berry and L. M. Hare (2004) [2] stated, these enzymes are also implicated in the production of pathogenic agents. As shown in the ischaemia–reperfusion injury hypothesis (Scheme 1.1.1), during the course of

reperfusion, XOR uses dissolved oxygen and hypoxanthine to generate $O_2^{\cdot-}$ and $H_2O_2$ [2, 37, 43]. On the other hand, during the course of ischaemia, the catabolism of cellular ATP

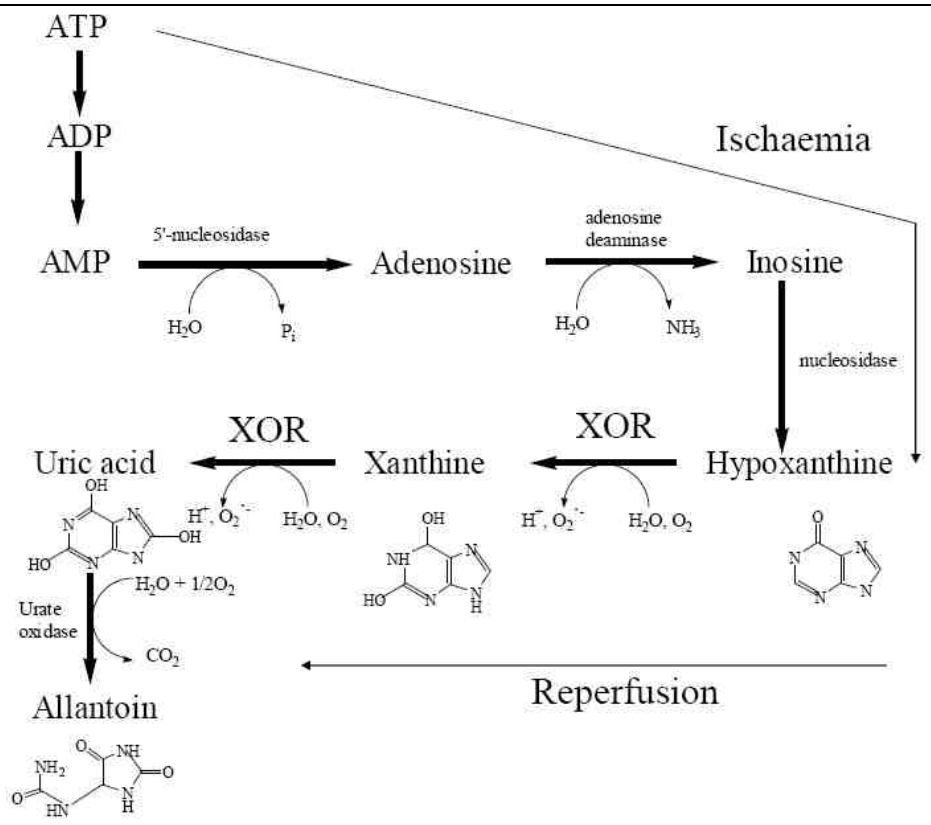


Scheme 1.1.1. A hypothetical schematic model for the purine degradation pathway and ischaemia–reperfusion injury hypothesis (adapted from reference 2).

to hypoxanthine is believed to create a potential gradient and pumps ions across the membrane. In turn, the dissipation of ions is believed to cause a buildup of calcium concentration that can initiate the proteolytic conversion of the dehydrogenase into the oxidase form of the enzyme [38, 43]. The proteolytic conversion of the enzyme and deposition of xanthine in various tissues may well lead to a multiple organ failure syndrome and an inherited XDH deficiency (or xanthinuria) [2, 39]. Xanthinuria, involving abnormalities of these enzymes, is believed to be caused by the deficiencies of XDH [32],

XOR, and AOR [2, 39], or Moco [2, 4, 17, 32, 39]. In nature, there are two major forms of XO family enzymes, the active and inactive forms. Although the active and inactive forms of the enzymes have similar overall structure [5, 43], the inactive forms of the enzymes lack one or more components of the active form of the enzymes. The inactive forms of XOR enzymes are the demolybdo [1, 43, 44], desulpho [11, 43, 45], and deflavo enzymes [43, 46, 47]. In addition to the inactive forms of XOR enzymes, the Cu/Mo-CODH enzymes also exist as Cu-deficient (Mo-CODH) [1, 4, 44]. The desulpho forms of the XOR enzymes are characterized by an activity loss. As a result, the enzymes are shown to lose their activities when the terminal sulfido is replaced by an oxo ligand. The desulpho forms of Cu/Mo-CODH enzymes are also known to assume structures similar to the desulpho forms of XOR enzymes [11, 24, 41, 45, 48, 49].

*The structures of the enzymes:* Insight, into the structural organization of the XO family enzymes, has been obtained from the X-ray crystallographic data reported for *Desulfovibrio gigas* aldehyde oxidoreductase (*Dg*AOR) [14, 42] (Fig. 1.1.3, a). The X-ray crystal structures for XOR and Cu/Mo-CODH enzymes are resolved from various sources such as bovine milk (as *bm*XOR) [5], *Rhodobacter capsulatus* (as *Rc*XDH) [6], *Oligotropha carboxidovorans* (as *Oc*Cu/Mo-CODH) [7, 8], and *Hydrogenophaga pseudoflava (*as *hp*Cu/Mo-CODH) [9]. The X-ray crystal structure for *bm*XOR bound to 4-[5-pyridin-4-yl-1H-[1, 2, 4]-triazol-3-yl]pyridine-2-carbonitrile (FYX-051) is also resolved [10]. According to the X-ray crystal structures, the XO family enzymes [*bm*XOR [5] (Fig. 1.1.3, b), *Rc*XDH [6] (Fig. 1.1.3, c), and *Oc*Cu/Mo-CODH [8] (Fig. 1.1.3, d] have similar overall structure and sequence homologies. The *bm*XOR enzyme is a $\alpha_2$ dimer that has a molecular mass of about ~300 kDa [5, 10]. The smallest (S) subunits (20-kDa each, consisting pairs of $[Fe_2S_2](S^{\gamma}_{Cys})_4$ clusters) are connected by a long segment to the medium (M) subunits (40-kDa each, consisting two FAD cofactors). Similarly, the medium subunits are connected to the large (L) subunits (85-kDa each, consisting two Moco cofactors) [5, 10]. Similar to the *bm*XOR enzymes, one of the well-characterized enzymes is the enzyme isolated from the phototrophic purple bacterium *Rhodobacter capsulatus*. The *Rc*XDH is a $\alpha_2\beta_2$ tetramer that has a molecular mass of about ~290 kDa

(Fig. 1.1.3, c) [6]. Similarly, the structure of the *Oc*Çu/Mo-CODH is an $\alpha_2\beta_2\gamma_2$ hexamer that has molecular mass of about ~273 kDa (Figs. 1.1.3, d) [7, 8, 9, 11, 16, 48, 49].

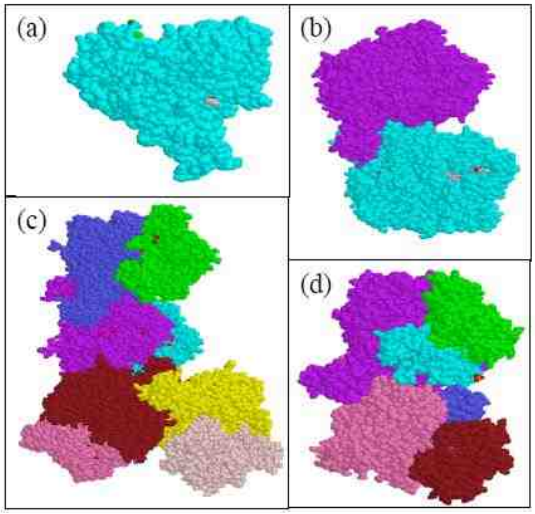


Figure 1.1.3. The space filled crystal structure and subunit compositions reported for (a) *Dg*AOR (PDB accession code of 1VLB) [42], (b) *bm*XOR (PDB accession code of 1FO4) [5], (c) *Rc*XDH (PDB accession code of 1JRO) [6], and (d) *Oc*Cu/Mo-CODH (PDB accession code of 1N5W) [8] enzymes. The illustration is prepared the same as Figure (1.1.1).

The *bm*XOR and *Oc*Cu/Mo-CODH enzymes are shown to exhibit similar physical and spectroscopic properties. As shown in Figure (1.1.4), the enzymes have common absorption maxima at 360 nm and 450 nm (corresponding to the maxima at 465 nm for *Rc*XDH, Figure (A. 1)). The absorption maximum at 450 nm ($\varepsilon$ = 37800 $M^{-1}$ $cm^{-1}$) is attributed to the FAD and $[Fe_2S_2](S^{\gamma}_{Cys})_4$ cofactors. The pair of $[Fe_2S_2](S^{\gamma}_{Cys})_4$ clusters are also characterized by the broad peak, centered at 550 nm. The spectra for *Oc*Cu/Mo-CODH are also shown to reveal shoulders at 330, 425, and 440 nm (corresponding to 364, 390, 428, and 550 nm for *Rc*XDH). Upon reduction with a strong reducing agent,

such as sodium dithionite, a complete bleaching is observed for the groups that give the enzymes very distinct features (Fig. 1.1.4).

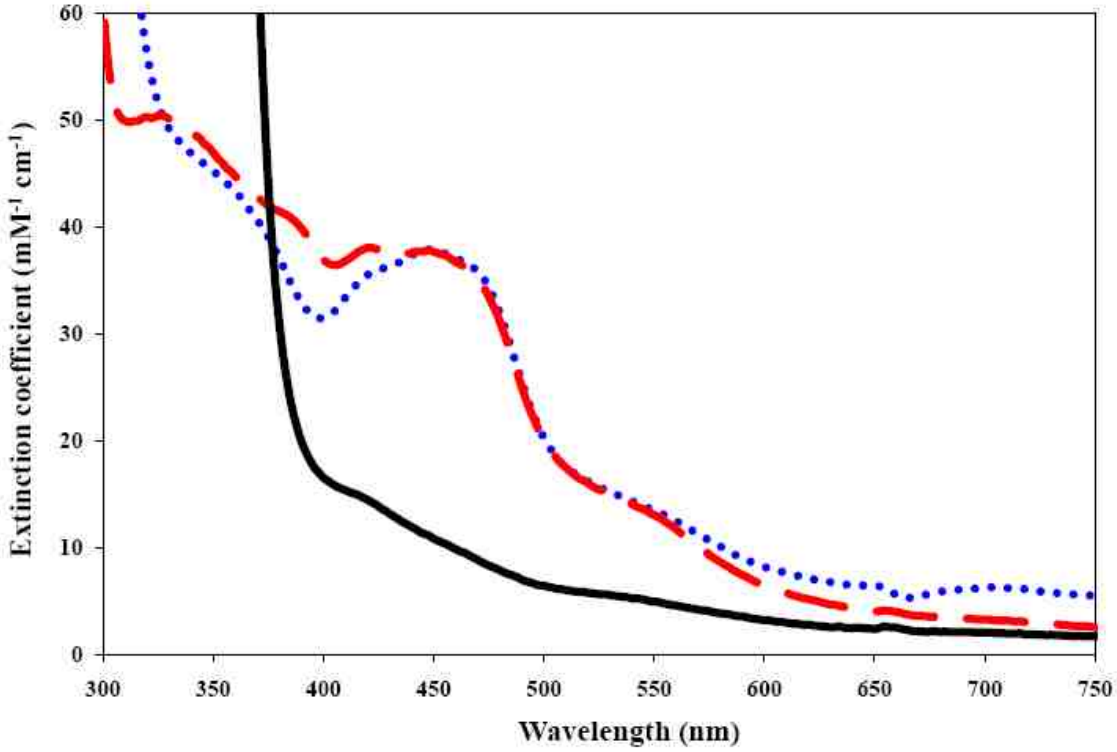


Figure 1.1.4. The electron absorption spectra observed for the native *bm*XOR (in 0.1 mM pyrophosphate buffer, pH 8.3) (*blue or dotted trace*) and *Oc*Cu/Mo-CODH (in 0.2 mM HEPES buffer, pH 8.2) (*red or broken line trace*). The trace for the reduced *bm*XOR enzyme (*black or solid line*) is obtained from an anaerobic titration of the oxidized *bm*XOR enzyme with an excess sodium dithionite.

*The redox active sites:* The XO family enzymes encompass a wide range of metalo-enzymes including the Mo hydroxylases and the Mo/Cu carbon monoxide dehydrogenase [1, 13, 24]. As shown in Figure (1.1.5), the cofactors of the XOR enzymes (such as XDH, EC: 1.1.1.204 and XO, EC: 1.1.3.22 or Cu/Mo-CODH, EC: 1.2.99.2) are organized in a linear fashion, ideal for electron transfer [5, 6, 7, 8, 9, 10]. However, the typical feature of the

XO family enzymes is the reductive half-reaction active site. The XO family enzymes, with the exception of Cu/Mo-CODH, are mono-nuclear since they contain a single Mo

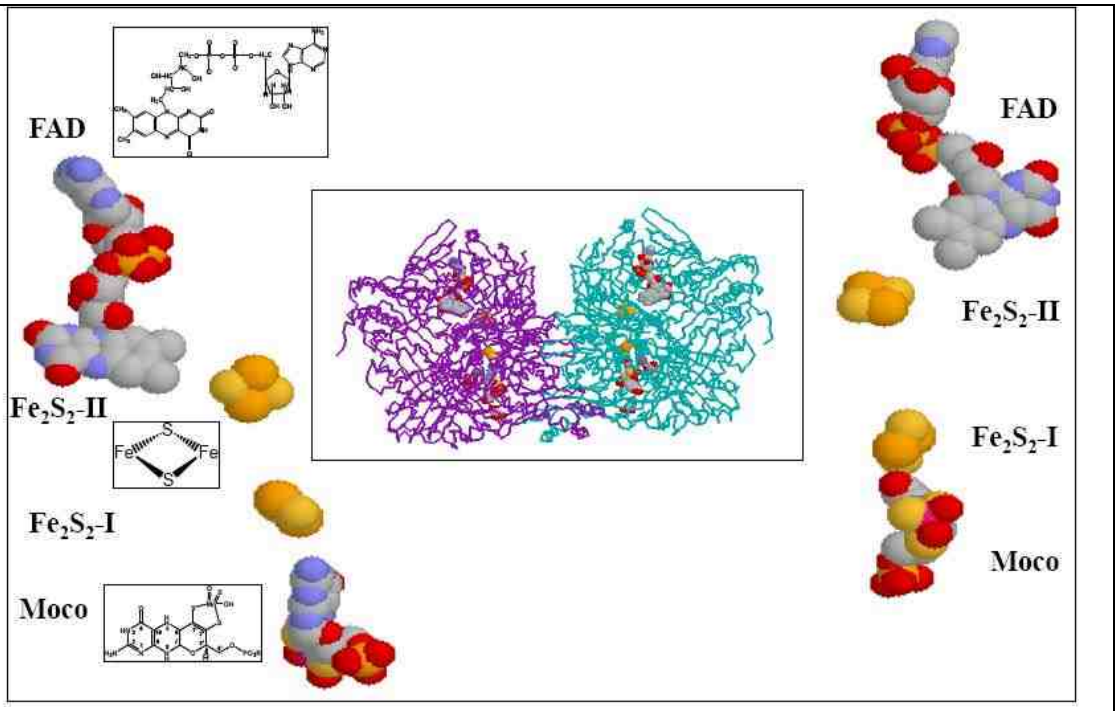


Figure 1.1.5. The overall structure (*center*) and cofactor compositions (*left and right*) of the *bm*XOR enzyme (PDB accession code of 10F4) [5]. *Left* and *right* display the linear arrangement of the cofactors: The FAD, pairs of [2Fe–2S], and Moco cofactors. The illustration is prepared the same as Figure (1.1.1).

ion at their reductive half-reaction active sites ([MoSO]($S_{dithiolene}$)$_2$·OH(H)) (Fig. 1.1.2, a). On the other hand, the Cu/Mo-CODH enzymes are di-nuclear metal clusters. At their reductive half-reaction active sites (($CuS^{\gamma}_{Cys}$)·[MoSO]($S_{dithiolene}$)$_2$·OH(H)), they contain both Mo and Cu ions (Fig. 1.1.2, b). The reductive half-reaction active site, as shown in Figure (1.1.6), is defined by three environments [1]. The active site environment, for XO family enzymes, is composed of the two coordination spheres (the primary and secondary) and the solvent access channel (that is directed towards the two coordination

spheres) [5, 6, 7, 8, 10]. The resting state geometry for the primary coordination sphere, as described by R. Hille (1996) [1], is a distorted penta-coordinate [12]. As shown in Figure (1.1.7), the $Mo^{VI}$ ion is tethered by axial and equatorial ligands located about 0.5 Å above the equatorial plane. In XOR enzymes, the equatorial plane of the primary coordination sphere is defined by ligands such as a single pyranopterin dithiolene, sulfido ($S_{Mo}$), and

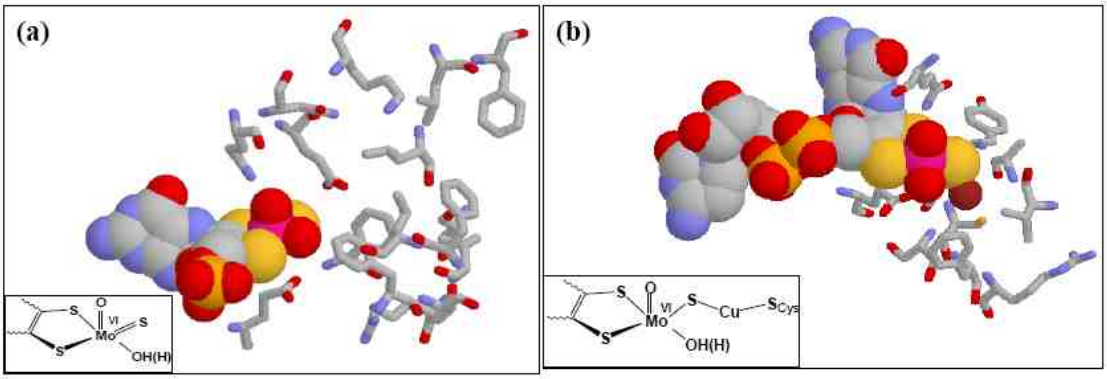


Figure 1.1.6. The reductive half-reaction active site environments for the (a) *bm*XOR (PDB accession code of 1V97) [10] and (b) *Oc*Cu/Mo-CODH (PDB accession code of 1N5W) [8] enzymes. The illustration is prepared the same as Figure (1.1.1).

hydroxide ($HO_{equatorial\ (eq)}$) [5, 8]. The pyranopterin dithiolene unit is ligated to Mo ion through the two-dithiolene sulphurs, as Mo-$(S_{dithiolene})_2$. The Cu/Mo-CODH also exhibit similar coordination with the Mo and Cu ions bridged by sulfur atom (Fig. 1.1.7, b) [8]. The $Cu^{I}$ ion is ligated, in a distorted linear geometry, to the inorganic bridging sulfur and $S^{\gamma}_{Cys}$ residue [11, 48, 49]. In both XOR and Cu/Mo-CODH enzymes, the fifth ligand is the apical oxo ($O_{apical}$). The obvious variation between XOR and Cu/Mo-CODH enzymes is not only the $S_{Mo}$ ligand, but the nature of the pyranopterin derivatives (Figs. 1.1.1 and 1.1.7). The pyranopterin moiety in *bm*XOR and *Rc*XDH, in contrast to most bacterial molybdo-enzymes, is dicarboxamidomethyl molybdo-pterin (MPT). In most bacterial enzymes the terminal phosphate of MPT is covalently attached to an additional nucleotide (Figs. 1.1.1 and 1.1.7, b) [5, 6, 7, 8, 9, 10, 11]. Unlike the reductive half-reaction

active site of Cu/Mo-CODH, which is non-covalently bound to the protein through the Moco moiety and Cu-$S^{\gamma}_{Cys}$ residue, the XOR enzymes are non-covalently bound to the large subunit of the protein through their Moco moiety [4, 17, 18, 42].

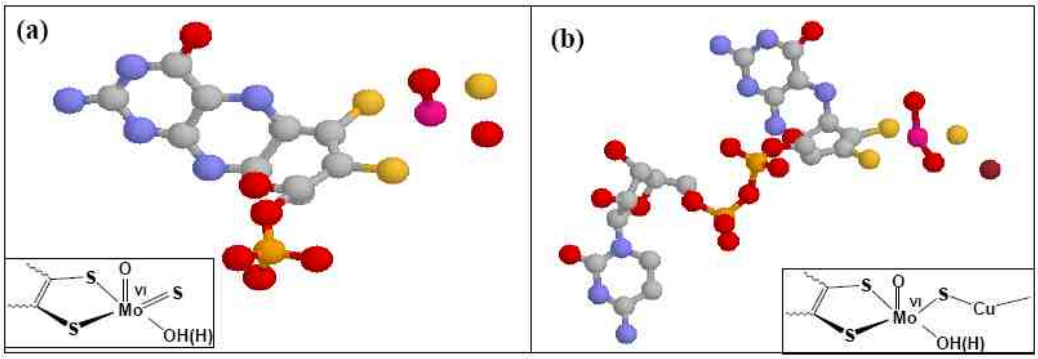


Figure 1.1.7. The primary coordination spheres of the reductive half-reaction active sites for the (a) *bm*XOR (PDB accession code of 1V97) [10] and (b) *Oc*Cu/Mo-CODH (PDB accession code of 1N5W) [8] enzymes. The illustration is prepared the same as Figure (1.1.1).

The secondary coordination sphere is defined by amino acid residues that are located in the binding pocket (Fig. 1.1.8). One of the most important active site residues, conserved in all XO family enzymes, is $Glu_{1261}$ (in *bm*XOR, that corresponds to $Glu_{730}$ in *Rc*XDH, $Glu_{869}$ in *Dg*AOR, and $Glu_{763}$ in *Oc*Cu/Mo-CODH) [5, 6, 7, 8, 10, 14, 42]. The amino acid residue is located trans to the $O_{apical}$ ligand and in a very close proximity to the Mo ion and the $HO_{eq}$ terminal. Due to its unique position, the [XOR]-$Glu_{1261/730/763/869}$ amino acid residue is proposed to play an important role in promoting the nucleophilicity of the $HO_{eq}$ ligand [1, 48]. As shown in Figure (1.1.8), the other amino acid residues that are important in substrate recognition are $Glu_{802}$ (in *bm*XOR, which corresponds to $Glu_{232}$ in *Rc*XDH) and $Arg_{880}$ (in *bm*XOR, which corresponds to $Arg_{310}$ in *Rc*XDH and $Arg_{501}$ in *Dg*AOR) [10, 14, 42]. As shown by many workers [3, 18, 31, 39, 50, 51, 52, 53], these amino acid residues are

proposed to create a hydrogen bonding micro-environment (Fig. 1.1.8, c). The fourth active site residue, that makes the secondary coordination sphere, is $Glu_{767}$ (in *bm*XOR that corresponds to $Gln_{197}$ in *Rc*XDH and $Gln_{240}$ in *Oc*Cu/Mo-CODH) [5, 6, 7, 8, 10]. Although the actual role of this amino acid residue is not known, it is believed to form a hydrogen bond with the $O_{apical}$ ligand. This residue is conserved in all XO family enzymes, except in *Dg*AOR type enzymes [8, 9, 18, 31]. The secondary coordination sphere of Cu/Mo-CODH is different from other XO family enzymes since it contains the $Cu^{I}$ ion

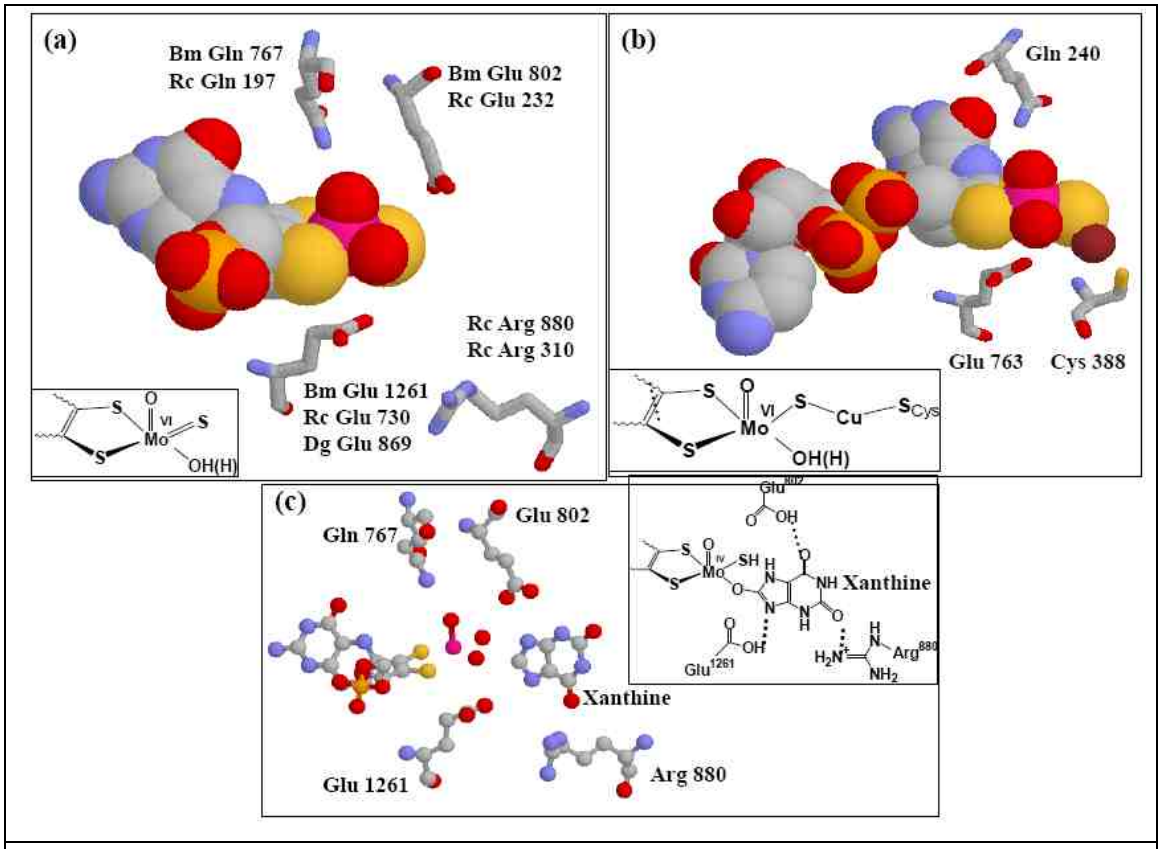


Figure 1.1.8. The secondary coordination sphere for the (a) *bm*XOR (PDB accession code of 1V97) [10] and (b) *Oc*Cu/Mo-CODH (PDB accession code of 1N5W) [8] enzymes. The position of the substrate (xanthine) inside the binding pocket (PDB accession code of 3EUB) [50] is shown in *panel (c)*. The *inset* is adapted from reference [39] to show the position of substrates (such as xanthine) inside the binding pocket. The symbols Bm, Rc, and Dg represent, respectively, the *bm*XOR, *Rc*XDH [6], and *Dg*AOR [42] enzymes. The illustration is prepared the same as Figure (1.1.1).

that is coordinated to Sγ atom of cysteine ($Cys_{388}$) residue (Fig. 1.1.8, b). The Cu-$S^{\gamma}_{Cys388}$ is part of the unique loop that surrounds the Mo-[-μ-S-]-Cu network (Fig. 1.1.9, b) [11, 16, 48, 49, 54]. Finally, in XO family enzymes, the substrate access channel is directed towards the $HO_{eq}$ and $S_{Mo}$ terminals of XOR enzymes [6, 10]. As shown in Figure (1.1.9, a), the substrate access channel is dominated by amino acid residues that are suited to accommodate the ring structures of the heterocyclic substrates. The amino acids are composed of both polar and non-polar residues that are capable of creating hydrophilic and hydrophobic micro-environments [3, 5, 10, 31, 41]. As shown in Figure (1.1.9, a), the hydrophilic amino acid residues, in XOR enzymes, are $Lys_{771}$, $Asn_{768}$, $Glu_{802}$, $Glu_{261}$, $Arg_{880}$, and $Thr_{1010}$. Similarly, the hydrophobic residues are $Phe_{914}$, $Leu_{873}$, $Ser_{876}$, $Leu_{648}$, $phe_{649}$, $Phe_{1009}$, $Val_{1011}$, $Leu_{1014}$, and $phe_{1013}$ [5, 10].

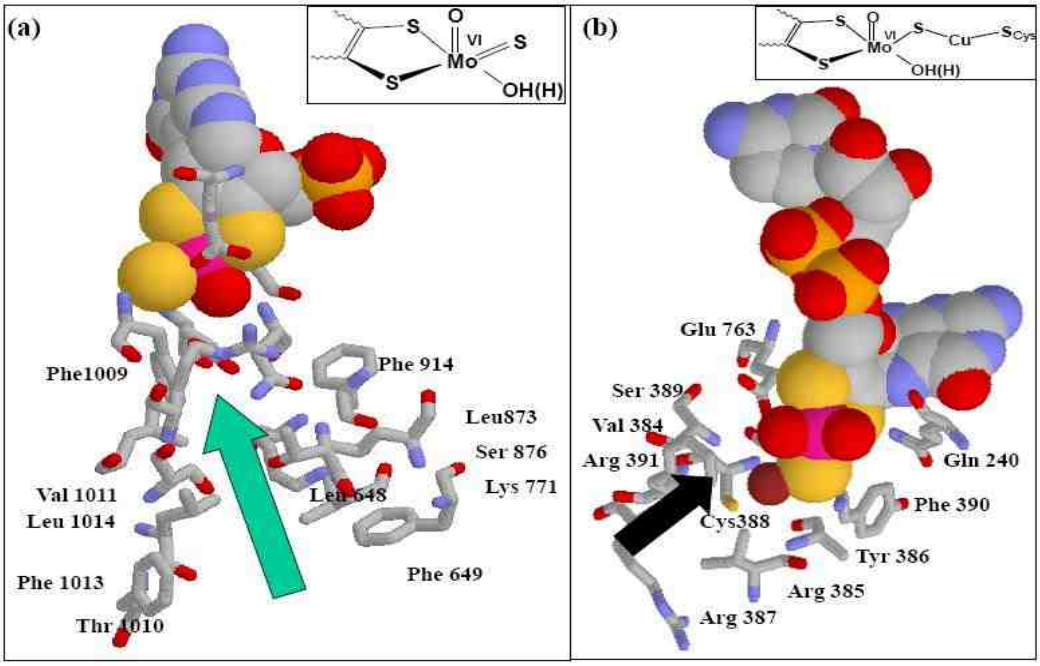


Figure 1.1.9. Interaction of substrates (represented by arrows) with the residues lining in the solvent access channel of (a) *bm*XOR (PDB accession code of 1V97) [10] and (b) and *Oc*CuMo-CODH (PDB accession code of 1N5W) [8] enzymes. The illustration is prepared the same as Figure (1.1.1).

In contrast to the reductive half-reaction, the oxidative half-reaction takes place at the flavin site [5, 6, 7, 8, 10, 49]. In eukaryotic XOR enzymes, when the enzyme is converted from the dehydrogenase to oxidase form, the largest change is localized at the flavin site [5, 38]. During the transformation, the proteolytic cleavage of the surface-exposed loops of XDH is proposed to cause a major structural and electrostatic rearrangement [5, 6, 37, 40]. The conversion of XDH to XO is proposed to alter the specificity of the oxidizing substrate by interfering with the binding of $NAD^+$ [24, 31, 32, 41, 42]. Although the dehydrogenase form of the enzymes are similar in fold and cofactor arrangements [5, 6, 10], the dehydrogenase form of the prokaryotic *Rc*XDH may not be converted to the oxidase form [32]. Finally, the intramolecular electron transfer between the reductive and oxidative half-reaction active sites is mediated by the pairs of $[Fe_2S_2](S^{\gamma}_{Cys})_4$ clusters [2, 5, 6, 37, 38] (Fig. 1.1.5). The pairs of $[Fe_2S_2](S^{\gamma}_{Cys})_4$ clusters are distinguished according to their distinct electron paramagnetic resonance (EPR) signals, designated as $[Fe_2S_2](S^{\gamma}_{Cys})_4$-I and $[Fe_2S_2](S^{\gamma}_{Cys})_4$-II [1, 5]. The pairs of $[Fe_2S_2](S^{\gamma}_{Cys})_4$-I clusters are buried beneath the protein surface, located close to the pyranopterin [5, 6, 8, 42]. Unlike $[Fe_2S_2](S^{\gamma}_{Cys})_4$-I clusters, the pairs of $[Fe_2S_2](S^{\gamma}_{Cys})_4$-II clusters are solvent-exposed and located in close proximity to the FAD cofactors (Figure 1.1.5) [5, 6, 8].

## 1.3 The reaction mechanism of xanthine oxidase enzyme

The oxidation or hydroxylation of the substrates ($C_{RH}$), by the xanthine oxidase enzymes, involves the cleavage of $C_{RH}$-$H_{RH}$ bonds of the substrates [1, 5, 10, 13, 14, 18, 29, 41, 56]. Interestingly, the reaction stoichiometries of these enzymes are unique among other hydroxylation reactions catalyzed by mono-oxygenase enzymes [1, 57]. Mono-oxygenase enzymes hydroxylate their substrates using oxygen derived from molecular oxygen and a pair of reducing equivalents. Unlike the mono-oxygenase enzymes, the XOR and Cu/Mo-CODH enzymes use oxygen derived from water [1, 18, 31, 32] although the Cu/Mo-CODH enzyme generates reducing equivalents in a reaction that doesn't involve the cleavage of $C_{CRH}$-$H_{CRH}$ bond of its substrate [8, 9, 11, 16]. As with many oxidoreductase enzymes, the XO family enzymes have components suited to interact with the reducing and oxidizing substrates [1, 5, 6, 7, 8, 10, 14, 42]. The widely accepted description of the series of events that take place in the redox sites is shown in Scheme (1.1.2) [24, 40, 55, 58]. During the reductive half-reaction, the reducing substrate ($C_{RH}$) is oxidized to a product (O-$C_R$) by donating two reducing equivalents to reduce the enzyme from $Mo^{(VI)}$ to $Mo^{(IV)}$ ions [2, 14, 18, 59]. As Olson *et al.* (in 1974) [55] described, the enzyme is proposed to function according to the ping-pong mechanism [24, 60, 61], with the $[Fe_2S_2](S^{\gamma}_{Cys})_4$ cofactors acting as electron sinks. According to the rapid equilibrium hypothesis, described by Olson and co-workers, the rate-limiting step is the release of the product followed by the re-equilibration of electrons between the redox centers. During the re-equilibration process, electrons are passed from the Moco cofactor to the FAD cofactor through the pair of $[Fe_2S_2](S^{\gamma}Cys)_4$ clusters [58]. In the oxidative half-reaction, reducing equivalents are removed from the enzyme by physiological or artificial electron acceptors (Scheme 1.1.2, a) [2, 5, 6, 7, 8, 9, 10, 14, 37, 42]. Accordingly, the FAD cofactor is responsible to pass on the hydrogen atoms and electrons to the electron acceptors. As shown in Scheme (1.1.2, b), in order for the re-oxidation steps to be completed, the fully reduced enzyme may accept up to six electrons per subunit [64]. The first four electrons are shown to depart the enzyme in the form of two equivalents of $H_2O_2$. Consequently,

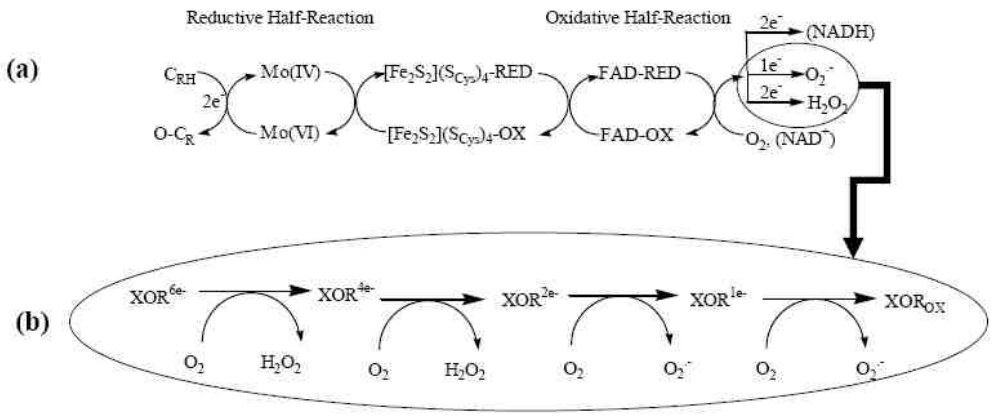


Scheme 1.1.2. The overall reaction of XOR enzymes (a) and the reactions taking place at the oxidative half-reaction (b). As shown in (b), the oxidase and dehydrogenase forms of the enzymes, respectively, use molecular oxygen and $NAD^+$ as their oxidizing substrates [2, 3, 5, 24, 37, 38, 41, 55]. The illustrations are adapted from references 2, 37, 55, 62, 63, and 64.

the final two electrons are shown to leave as two equivalents of $O_2^{\cdot-}$ [5, 13, 40]. That means, the reaction of reduced enzyme with oxidizing substrate takes place in two distinct kinetic phases. These phases involve a sequential removal of reducing equivalents by more than one oxygen molecule [1, 55, 64]. However, the extent of reduction and re-oxidation of the reduced enzyme depends on the affinity of the substrates to the enzymes and the rate of product release steps.

Although the actual catalytic mechanism of the XO family enzymes is not yet known, the oxidation or hydroxylation of substrates are believed to follow one of the alternate reaction mechanisms proposed, respectively, for XOR [1, 10, 18, 56, 59, 65, 66, 67, 68, 69] and Cu/Mo-CODH [8, 54, 70, 71] enzymes. In the mechanism proposed for XOR enzymes, as shown in Scheme (1.1.3), the common consensus is the roles of the $HO_{eq}$ terminal and the active site amino acid residues ([XOR]-$Glu_{1261/730/763/869}$). One of the postulated

mechanisms, proposed for XOR enzymes, is based on a base-assisted nucleophilic attack by the $HO_{eq}$ terminal at the electron deficient carbon of the substrates [1, 59]. As shown by

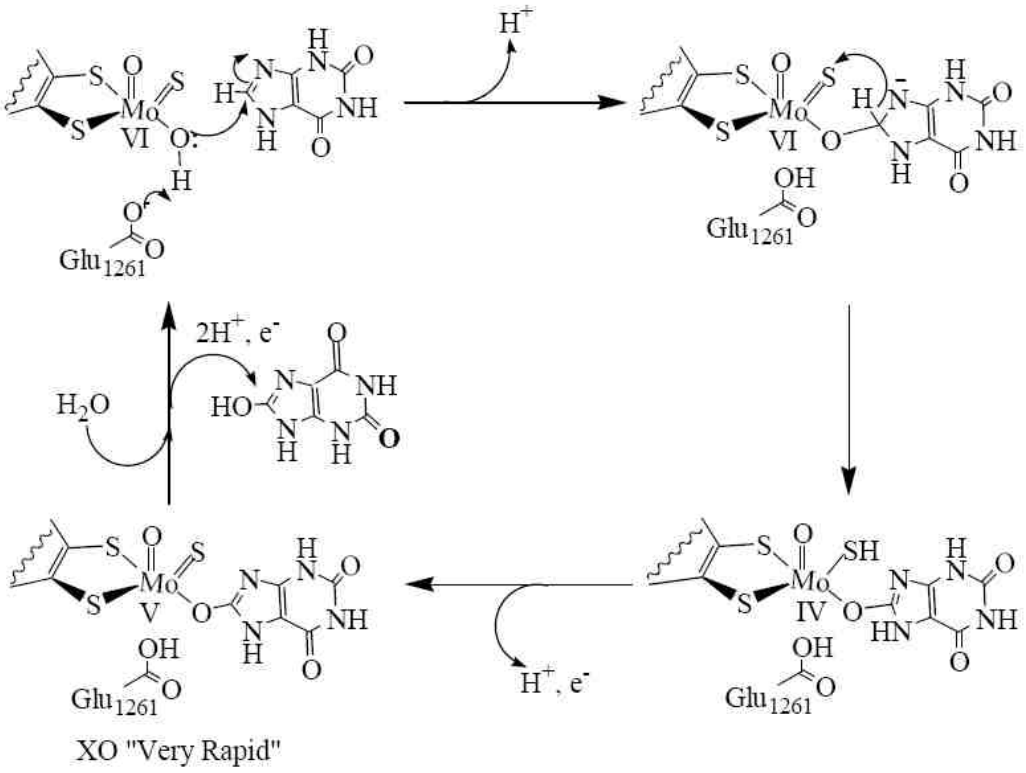


Scheme 1.1.3. A postulated base-assisted hydride transfer mechanism for the hydroxylation of xanthine by XO enzyme. In the most favorable pathway, the [XOR]-$Glu_{1261}$ is proposed to act as a general base. (Adapted from references 18, 39, 50, 51, 59, 68, and 72).

Xia *et al.* (1999) [59], R. Hille (2006) [18], Yamaguchi *et al.* (2007) [39], and in Scheme (1.1.3), the reaction is postulated to take place through a nucleophilic attack of the $HO_{eq}$ on the $C_8$ position of xanthine. The nucleophilic reaction is proposed to be followed by a formal hydride ($H^+ + 2e^-$) transfer from the substrate-binding site to the $S_{Mo}$ terminal of the active site and the allocation of the two electrons on the $Mo^{(VI)}$-center. When the enzyme reacts with xanthine, the first intermediate seen is a product (such as uric acid

bound reduced enzyme ($XOR_{RED}$). Depending on the reaction condition, this intermediate is proposed to break down by one-electron oxidation to produce the ‘very rapid’ electron paramagnetic resonance (EPR) spectroscopy signal [18, 59, 64, 68,73, 74].

## 1.4 Overview of the research projects

In order to understand the catalytic mechanism of XOR enzymes, combinations of enzymatic spectroscopic and theoretical studies were proposed. The studies were focused, on the specificity of substrates towards xanthine oxidase family enzymes (Chapter 2.0), substrate-enzyme binding cofactor reduction for XO family enzymes (Chapter 3.0), and modeling the transition state structures (Chapter 4.0). Finally, in chapters (5.0 and 6.0), the three major events of the reductive-half reaction catalytic cycle and overall reactivity of the XOR enzymes were described.

*Substrate specificity towards xanthine oxidase family enzymes:* The change in substrate specificity of the *bm*XOR enzyme to the bacterial *Rc*XDH enzyme was investigated in the presence of assay reagents and artificial electron acceptors. In addition, a mutagenic study was performed to probe the change in XOR substrate specificity to *Dg*AOR type enzyme (a type of XO family enzyme that has overlapping substrate specificity with XOR enzymes and different amino acid residues in its binding pocket) [14, 42, 78, 90, 105, 117]. The mutagenic studies were aimed to probe the roles of the binding pocket amino acid residues in substrate recognition and activation. Finally, the variation in activities and steady-state kinetic parameters (such as, $v_{max}$, $k_m$, $k_{cat}$, and $k_{cat}/k_m$) were determined in the presence of native and mutant enzymes. As shown in Scheme (1.1.3), the $HO_{eq}$ terminal of XOR enzymes was poised for nucleophilic attack on the $C_8$ position of xanthine. The same type of reaction was proposed to take place if xanthine was replaced by other heterocyclic and small molecules. The mechanistic similarity between purine substrates and small molecules such as formamide was previously evaluated through a number of theoretical studies [66, 69, 111, 112, 113, 114, 115], where formamide has been used as a basic computational model for the physiological substrates. In light of the computation data [115], an enzymatic assay was proposed to verify the existence of either direct oxidation or a group transfer mechanisms. Although the specificity of formamide towards *bm*XOR enzyme was previously described by Morpeth *et al*. (1984) [116], the binding or kinetic specificities were not given. In order to verify the specificity of formamide, formate, and

a wide range of substrates, a very sensitive assay method that probes the production of $H_2O_2$ was designed. Although the enzymes (*bm*XOR and *Rc*XDH) were shown to have similar reductive half-reaction active sites [5, 6], they were known to differ in the oxidative half-reaction. During the oxidative half-reaction, as shown in Scheme (1.1.2, c), the ROS ($O_2^{\bullet-}$ or $H_2O_2$) were expected to be produced in two distinct kinetic phases. In the past, the reactivity and steady-state kinetic parameters for XOR enzymes were probed in the presence some substrates and artificial electron acceptors. A number of artificial electron acceptors have been used as an ideal system to approximate the production of $O_2^{\bullet-}$ [79, 82, 102, 103, 104, 89, 98, 99, 105, 106, 107]. However, the activities and steady-state kinetic parameters were not fully described since the artificial electron acceptors were insensitive towards $H_2O_2$. As a result, an alternate method was developed to monitor the rate of $H_2O_2$ production in the presence of Amplex® Red reagent (10-acetyl-3, 7-dihydroxyphenoxazine) [108, 109, 110]. This assay method was used to profile the reactivity and steady-state kinetic parameters of XOR enzymes (Fig. A. 1) in the presence of a wide range of substrates (Fig. A. 2). In addition to the native XOR enzymes, a mutagenic study was also performed to identify the role of amino acid residues in substrate recognition and activation. In the past, a site directed mutagenesis has previously been used to explore the reactivity of the enzymes [37, 39, 50, 51, 52, 53]. In this work, the active site amino acid residue (known in substrate recognition, [*Rc*XDH]-$Glu_{232}$ [5, 6, 10]) was chosen as a target of investigation since it was not conserved in *Dg*AOR type enzymes [14, 42]. Upon completion of this work, the enzymatic spectroscopic approach was expected to provide relevant information regarding the overall catalytic mechanism of XOR enzymes. The assay methods were also expected to answer key questions regarding the variable activities and steady-state kinetic parameters observed. The variations were observed even when the same substrate was reacted with the oxidase and dehyderogenase forms of the same enzyme, as well as, the rate of $H_2O_2$ or $O_2^{\bullet-}$production was probed in the presence of the same enzyme and substrate. The mutants studied were expected to show slow turnover compared to the wild type *bm*XOR and *Rc*XDH enzymes. This work was expected to provide valuable information that may have a mechanistic importance since it was expected to establish the substrate preferences of *bm*XOR to *Rc*XDH and AOR type

of enzymes. Site directed mutagenesis studies on XOR and DgAOR type enzymes were also anticipated to establish the roles of the binding pocket amino acid residues.

*The substrate-enzyme binding cofactor reduction for XO family enzymes:* During the catalytic transformation, the enzymes were shown to provide similar spectral changes characterized by a decrease in absorbance (in the short wavelength region between 350 and 550 nm) [59, 81, 83, 85, 130]. The overall spectral change associated with either the oxidized or reduced enzymes were attributed to the FAD and pairs of $[Fe_2S_2](S^{\gamma}Cys)_4$ cofactors [6, 8, 11, 24, 25, 31, 32, 64, 82, 94, 98, 106, 118]. As a result, the spectral contribution from the Moco site remained ill-defined owing to the strong absorption of the prosthetic groups. Unlike the spectral changes observed in the short wavelength region, a unique spectral change (in the long wavelength region, centered at 650 nm) was reported by Davis and co-workers (1982 and 1984) [58, 130]. Although the currently accepted spectral band giving species was the (Enzyme)-$[Mo^{(IV)}\text{-}O_{violapterin}]$ intermediate, the electronic origin of the 650 nm band was not well understood. The spectral band attributed to the $E_{RED}$-violapterin intermediate has been tentatively assigned, by Davis and co-workers (1982) [130], to a metal-to-ligand-charge-transfer (MLCT) transition (more precisely, to a molybdenum-to-violapterin-charge-transfer transition) [58, 85]. Although this type of spectral band assignment was supported by previous works [58, 85, 130] and the enzymatic spectroscopic and theoretical findings [134], the detail of the spectral band assignment and description of the spectral giving species was not yet well understood. Although the characterization of the MLCT transition was consistent with the 650 nm band that was generated from the two experimental approaches, it was not well understood why the spectral band was a unique signature of $E_{RED}$-violapterin intermediate [58, 130]. Therefore, it was of a mechanistic importance to explore if the reducing substrates (other than lumazine) produce a highly covalent bonding interaction and a spectral change similar to the one shown for (Enzyme)-$[Mo^{(IV)}\text{-}O_{violapterin}]$. Although a similar mechanism was expected with other reducing substrates, it was not well understood why the long wavelength absorptions have not been observed with most substrates. However, the catalytic intermediates associated with $E_{RED}$ and other products were known to produce EPR

signals (such as $E_{RED}$-urate [18, 59, 64, 67, 68, 73, 74]). If (Enzyme)-[$Mo^{(IV)}$-$O_{violapterin}$] was the structure that gives a spectral band at 650 nm, the inhibitory (Enzyme)-[$Mo^{(IV)}$-$N_{alloxanthine}$] intermediate was expected to behave the same as (Enzyme)-[$Mo^{(IV)}$-$O_{violapterin}$]. In order to understand the spectral changes associated with the transformation of lumazine to violapterin, a combination of enzymatic spectroscopic and electronic structure calculations have been undertaken. In 1982 and 1984, Davis and co-workers reported [58, 130] the generation of spectral bands (in the long wavelength region) using two different experimental approaches (dynamic and static). The dynamic experimental approach required a direct interaction between the substrate (such as lumazine) and oxidized enzyme (*bm*$XOR_{OX}$, *Rc*$XDH_{OX}$, or *Rc*$XDH_{OX}$-$Glu_{232}$Ala mutant). In the static experimental approach, the products (or violapterin) were reacted with the reduced enzymes (*bm*$XOR_{RED}$, *Rc*$XDH_{RED}$, or *Rc*$XDH_{RED}$-$Glu_{232}$Ala mutant). The spectral band giving species were also generated in the absence and presence of artificial electron acceptors, such as $Na^{+}DCIP^{-}$. The dynamic approach was also used to probe the substrate-enzyme binding cofactor reductions. In addition, pH profiles have been constructed for XOR enzymes with a variety of substrates. Since the pH of the media was proposed to define the optimum pH for different substrates, the rate of the reaction was probed in order to locate the optimum pH and pKa values. Upon completion of this work, the unique nature of the interaction between $E_{OX}$ and lumazine or $E_{RED}$ and violapterin was expected to give insight in to the behavior of the substrate-enzyme binding cofactor reductions. The wave-function description and intensity of the charge transfer transition for the $Mo^{(IV)}$-$O_{violapterin}$ complex was expected to correlate with the degree of $Mo^{(VI)}$-$O_{OH}$-lumazine covalency. It was also expected to indicate why the reducing substrates and their respective products behave differently when reacted with the oxidized and reduced forms of the enzymes. The effect of pH on the conformation of the active site and substrates was also expected to be correlated with the electron structure description and reaction mechanism. In summary, this work was anticipated to provide additional insight into the reactions of XO family enzymes with reducing substrates and describe the origin of spectral changes associated with the formation of $E_{RED}$ species.

*Modeling the transition state structures:* As described in Scheme (1.1.3), the mechanistic transformation of the tetrahedral Michaelis-Menten type complex (($E_{OX}$)-[$Mo^{(VI)}$-$O_{eq}$-$C_{CRH}$]) to the product bound intermediate (($E_{OX}$)-[$Mo^{(IV)}$-$O_{eq}$-$C_{CR}$]) was expected to pass through the tetrahedral transition state complex (($E_{OX}$)-[$Mo^{(VI)}$(-$O_{eq}$-$C_{CRH}$---$H_{RH}$---)(=$S_{Mo}$)]$^{\#}$). At the transition state, several events were expected to take place, such as the transfer of $H_{RH}$ from substrate carbon to $S_{Mo}$, concomitant transfer of two electrons to the $Mo^{(VI)}$-center, and conversion of the substrate to product. The findings from prior studies [66, 112, 113] have been used to support a hydride transfer mechanism. The key questions were focused on the nature of the formal hydride transfer from substrate carbon to the $S_{Mo}$ terminal of the active site and a concomitant allocation of the two electrons on the $Mo^{(VI)}$-center. The findings from the electron density analysis were shown to support a hydride transfer mechanism (concerted oxidation of formamide) [112, 113], whereas the charge analysis was shown to suggest a coupled hydrogen atom and electron transfer process (stepwise oxidation of formaldehyde) [66]. In addition to these studies, several accounts were made regarding the events that took place at the transition state. However, the events that were expected to take place at the transition state have never been fully explored nor quite understood. Although the simultaneous transfer of $H_{RH}$ and two electrons was proposed to take place during catalysis, the description of the formation of $O_{eq}$-$C_{CRH}$ bond, cleavage of $C_{CRH}$-$H_{RH}$ bond, migration of $H_{RH}$ to $S_{Mo}$ terminal, and reduction of ($E_{OX}$)-$Mo^{(VI)}$ to ($E_{RED}$)-$Mo^{(IV)}$ was not well understood. In order to understand the events taking place during catalysis, new computational models have been used to perform an electronic structure calculations. The calculations were performed on the active site model compound bound to a broad range of substrates (Fig. A. 2). The substrate bound active site model structures were optimized to approximate the linear motion of $H_{RH}$ in the transition state. The migration profile for the $H_{RH}$ from the substrate carbon to $S_{Mo}$ terminal was probed between ($E_{OX}$)-[$Mo^{(VI)}$-$O_{eq}$-$C_{CRH}$] and ($E_{RED}$)-[$Mo^{(IV)}$-$O_{eq}$-$C_{CR}$)] meta-stable states (Scheme 4.1.1). The transition state structures were characterized by one imaginary negative frequency [138 (c)]. The bonding descriptions were provided in terms of atomic charges and covalency (bond order). Although the bond order profiles were used to locate the position of the transition state, they were also used to quantitate the formation of $O_{eq}$-$C_{CRH}$ and $S_{Mo}$-$H_{RH}$ and cleavage of $C_{CRH}$-$H_{RH}$ and Mo-

$O_{eq}$ bonds. Because the $C_{CRH}$-$H_{RH}$ bond distance varied significantly during the formation of $O_{eq}$-$C_{RH}$ bond, the position of $H_{RH}$ and cleavage of $C_{CRH}$-$H_{RH}$ bond were proposed to depend on the nature of the substrates. Upon completion of this work, key questions regarding the events taking place at the transition state were expected to be answered. The wave function and bonding descriptions were expected to provide insight into how electrons were transferred between the active site and substrate via an inner-sphere mechanism, possibly before or after the formation of $S_{Mo}$-$H_{RH}$ bond. The electronic structure studies were expected to provide a more complete understanding of the events leading to the formation and decay of the transition state. The proton and electron transfer process was expected to offer a mechanistic basis for the hydroxylation reaction since it affected both the oxidation state of ($E_{OX}$)-$Mo^{(VI)}$-center and the acid-base properties of the reactants. Finally, the geometry of the transition state structure was central to understanding the catalytic reaction mechanism. The pka of the substrates and active site amino acid residues and the electrostatic forces that stabilize the transition state were proposed to define the electronic structure description and turnover number ($k_{cat}$). In summary, understanding the nature of the transition state was of a prime importance in developing a deeper mechanistic insight into the enzyme catalyzed reactions.

Finally, the major objective of this work was primarily focused on relating electronic structure contributions to enzymatic catalysis. The primary goals of these studies were to help understand the orbital control of reactivity for purine hydroxylation and develop a wave-function description of enzymatic catalysis. As described in chapter 6.0, the ultimate goal of this work was to present a proper interpretation and develop a unified hydroxylation mechanism. The convergence of theoretical and enzymatic spectroscopic approaches was then expected to provide a molecular-level understanding of the mechanisms of XOR enzymes.

# Chapter 2.0

## Substrate specificity towards xanthine oxidase family enzymes

### 2.1 Introduction

The XOR enzymes, although known to catalyze the final two steps of purine metabolism (Scheme 1.1.1) [2, 10, 31, 32, 39, 41], the *in vitro* substrate specificity are very broad [1, 75, 78, 79, 81], ranging from purine [59, 62, 67, 71, 76, 77, 80, 82, 83] to pteridine derivatives [58, 84, 85] and simple aldehydes [69, 86, 87, 89, 90]. The enzymes are characterized, for the suitability of their redox sites, to undergo simultaneous interaction with both the reducing and oxidizing substrates. The reducing substrates react at the reductive and the oxidizing substrates at the oxidative half-reaction active sites. According to the classic ping-pong mechanism, designated by W. W. Cleland (1963 and 1970) [60, 61] [cited by M. P. Coughlan (1980) [24, 91]], the simplified catalytic cycle, proposed for XO family enzymes, is shown in equations (2.1.1 – 2.1.3) [46, 55, 58, 63, 70, 75, 76, 80, 92, 93, 94]. During the reductive half-reaction (eq. 2.1.1), the fully oxidized enzyme ($E_{OX}$) reacts with the substrate ($C_{RH}$) to form a Michaelis-Menten type complex ($E_{OX}$-$C_{RH}$), with rate constants $k_1$ and $k_2$ (eq. 2.1.1). Following the formation of $E_{OX}$-$C_{RH}$ complex, a catalytic transformation occurs to produce a product (O-$C_R$) bound reduced enzyme ($E_{RED}$) intermediate ($E_{RED}$-$C_R$) that dissociates to $E_{RED}$ and O-$C_R$, with rate constant $k_3$.

$$E_{OX} + C_{RH} \underset{k_2}{\overset{k_1}{\rightleftarrows}} E_{OX}-C_{RH} \xrightarrow{k_3} E_{RED} + O-C_R \qquad (2.1.1)$$

In the oxidative half-reaction, a one or two electrons oxidation of the reduced enzyme ($E_{RED}$) is expected to take place. As shown in equations (2.1.2 and 2.1.3), the $E_{RED}$ combines with the physiological oxidizing substrates ($O_2$ or $NAD^+$) to produce a reduced enzyme-substrate intermediate ($E_{RED}$-$O_2$ or $E_{RED}$-$NAD^+$), with rate constants $k_4$ and $k_5$.

As shown in equation (2.1.2), the dissociation of the intermediate yields a one electron reduced enzyme ($E'_{RED}$) and superoxide ($O_2^{\bullet-}$), with rate constant $k_6$. $E'_{RED}$ eventually undergoes a one electron oxidation to regenerate $E_{OX}$. Similarly, a catalytic transformation may take place as a result of the two electrons oxidation to form $E_{OX}$ and hydrogen peroxide ($H_2O_2$), with rate constant $k_6$ (eq. 2.1.3).

$$E_{RED} + O_2 \underset{k_5}{\overset{k_4}{\rightleftarrows}} E_{RED} - O_2 \xrightarrow{k_6} E'_{RED} + O_2^{\bullet-} \qquad (2.1.2)$$

$$E_{RED} + O_2 \underset{k_5}{\overset{k_4}{\rightleftarrows}} E_{RED} - O_2 \xrightarrow{k_6} E_{OX} + H_2O_2 \qquad (2.1.3)$$

The rates of $O_2^{\bullet-}$ or $H_2O_2$ production, in the presence of artificial electron acceptors, are used as an ideal system for enzymatic assays (Scheme 2.1.1) [76, 77, 79, 86, 92, 94, 100, 101]. The use of artificial electron acceptors, for enzymatic assay, is advantageous in a situation where a direct spectrophotometric measurement of the products and by-products is unattainable. Unlike the physiological electron acceptors (that are known to interact with the FAD cofactor), the artificial electron acceptors may interact at various redox sites (the FAD, Moco, or $[Fe_2S_2](S^{\gamma}cys)_4$ cofactors). As described in Schemes (2.1.1), the artificial electron acceptors that are proposed to interact with $O_2^{\bullet-}$ or electrons are sodium 2, 6-dichlorophenol-indophenol ($Na^+DCIP^-$) [82, 102, 103, 104], cytochrome c [89, 98, 99, 105, 106, 107], and tetranitromethane (TNM) [79]. Since the artificial electron acceptors are insensitive towards $H_2O_2$ [96, 101], an alternate method is developed to monitor the rate of $H_2O_2$ production. The method is hypothesized to provide an accurate probe for the measurement of $H_2O_2$ production, in the presence of XOR enzymes, horseradish peroxidase (HRP), and Amplex® Red reagent (10-acetyl-3, 7-dihydroxyphenoxazine) [108, 109, 110] (Schemes 2.1.1). In the presence of these assay reagents, the ability of XO family enzymes (Fig. A. 1) to oxidize or hydroxylate small molecules (Fig. A. 2) is probed. In addition, the factors that affect the initial (substrate affinity to enzymes) and final stages

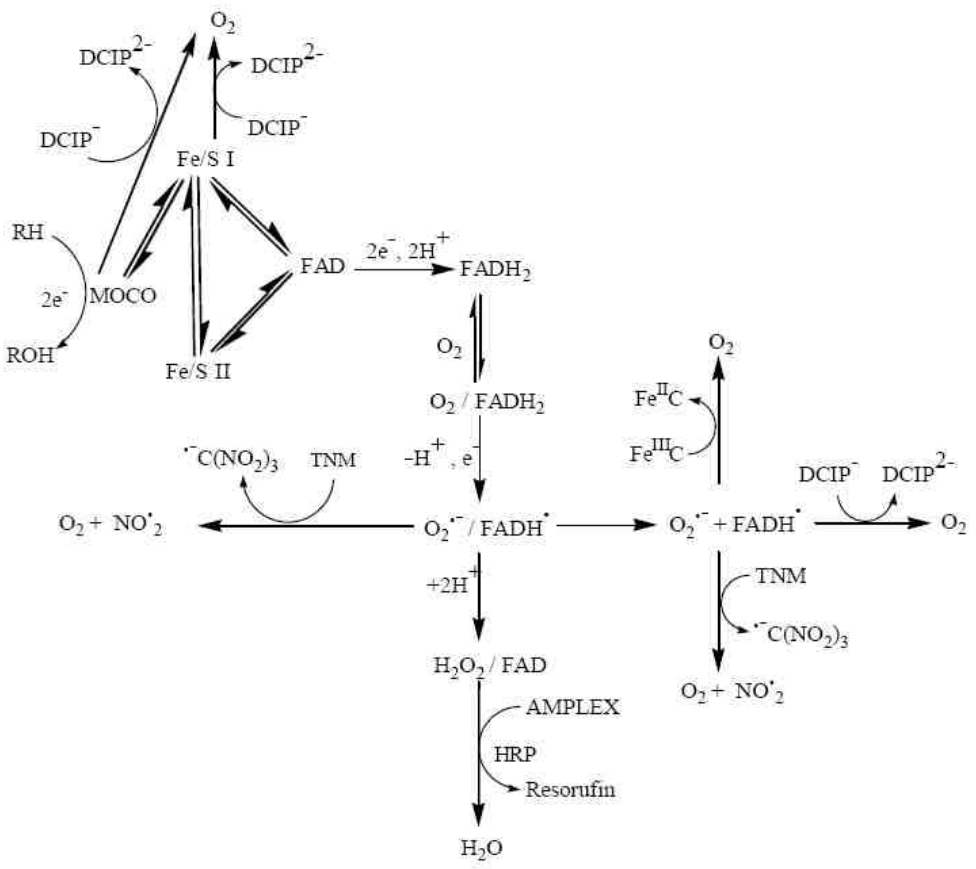


Scheme 2.1.1. A hypothetical competitive pathway, showing the role of artificial electron acceptors and assay reagent, for the reaction between XOR enzymes and reducing substrates (adapted from reference 75, 79, and 102).

of catalysis (product release) are also determined. The factors that affect the affinity of the substrates to the enzymes (such as substrate orientation) and product release (such as level of reduction or phases of catalysis) are expected to impose a combined effect on the overall catalytic transformation. The factors that affect the affinity and product release are also expected to affect the oxidative half-reaction (mainly the rates of $H_2O_2$ and $O_2^{\bullet-}$ production). The factors that affect the initial and final stages of catalysis are probed in the presence of XO family enzymes and reducing substrates (or small molecules). The choice of small molecules is based on the perception that the carbonyl carbon (of carbonyl bearing molecules, such as formamide, formate, and aldehydes) behaves the

same as $C_8$ of xanthine [69, 111, 112, 113, 114, 115]. Although the specificity of formamide towards XOR enzyme is described by Morpeth *et al.* (1984) [116], a very sensitive method is developed to verify the specificity of formamide and formate towards XOR enzymes. Similar to the formamide and formate assays, the work is extended to include the oxidation and hydroxylation of other molecules such as purine, aldehyde, and pteridine derivatives. The reactivity of these substrates is probed in the presence of native enzymes, such as *bm*XOR and *Rc*XDH. Although the enzymes (*bm*XOR and *Rc*XDH) are shown to have similar physical and spectroscopic features [5, 6, 10, 39, 50, 51, 52, 53], the change in substrate specificity of *bm*XOR enzymes to the wild type (WT) bacterial *Rc*XDH is probed. In addition to the reactivity of substrates and native XOR enzymes, a mutagenic study is also performed to identify the roles of an amino acid residue, mainly [*Rc*XDH]-$Glu_{232}$ (corresponding to [*bm*XOR]-$Glu_{802}$) (Figs. 1.1.8 and 2.1.1).

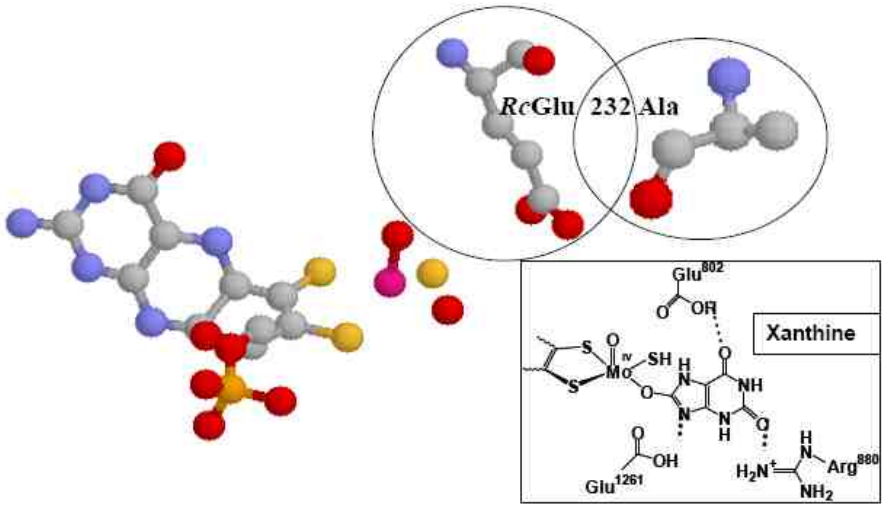


Figure 2.1.1. The position of $Glu_{232}$ in the binding pocket of *Rc*XDH (PDB accession code of 1JRO) [6] (corresponding to $Glu_{802}$ in *bm*XOR). The *inset* simulates the orientation of xanthine inside the binding pocket and the role of the residue in substrate recognition (adapted from reference 39). The replacement of $Glu_{232}$ by $Ala_{232}$ is also shown. The illustration was prepared the same as Figure (1.1.1).

The choice of this particular amino acid residue is based on the fact that this type of amino acid is not conserved in *Dg*AOR type enzyme (an enzyme that has an overlapping substrate specificity to XOR enzymes) [14, 42, 78, 90, 105, 117]. The effect of the site-directed mutagenesis, on substrate reactivity, is explored in order to probe the recognition and activation of substrates during mutation [39, 75]. The mutation is expected to reveal the change in substrate specificity of XOR enzymes to *Dg*AOR type enzymes. The effect of mutation, on the activities of XOR and *Dg*AOR type enzymes, is useful to establish the roles of the binding pocket amino acid residues (Fig. 2.1.1). The ability of XO family enzymes, to oxidize or hydroxylate reducing substrates and small molecules, is probed by monitoring the rate of electrons, $O_2^{\bullet-}$, or $H_2O_2$ production. The test principles are based on the assumption that the rate of reduction or oxidation, of the artificial electron acceptors, is proportional to the activity of XO family enzymes [75, 104]. The rate of substrate oxidation or hydroxylation is measured, spectrophotometrically, after the reaction completion is observed. The dependency of the catalytic rates of the reactions, on the concentrations of the reactants (substrates and enzymes), are also probed to describe the extent of interaction between the reactants [62, 76, 80, 93, 94, 119]. The effects of the concentrations of reactants are defined by the extent of the mole fractions of the reactants that enter the near attack conformation (before the Michaelis-Menten complex is transformed to the transition state complex). Understanding the geometric alignment of the reactants, in the near attack conformation, is mechanistically important since the extent of the mole fractions of the reactants, in the transition state, is proportional to the rate constant of the reaction. As a result, the steady-state kinetic parameters (such as $v_{max}$, $k_m$, $k_{cat}$, and $k_{cat}/k_m$) (*Definition provided in foot note*, Table 2.3.2) for the overall reaction are also determined under a catalytic turnover condition. The steady-state kinetic parameters are used to compare the properties of the enzymes as well as their specificity towards respective substrates. Upon completion of this work, the reactivity studies are expected to provide a means for characterizing the reactivity of a wide range of reducing substrates. The effect of the concentration of the reactants is expected to be correlated with the electron structure description and reaction mechanism. The mutagenic studies are also expected to prove the prediction of slow turnover towards the substrates compared to those of native enzymes.

## 2.2 Materials and methods

### Materials

*Enzymes and reagents:* The enzymes, *bm*XOR (Fig. A. 1, *upper left panel*), *Rc*XDH (Fig. A. 1, *upper right panel*), *Rc*XDH-$Glu_{232}$Ala mutant (Fig. A. 1, *lower left panel*), and *Oc*Cu/Mo-CODH (Fig. A. 1, *lower right panel*), were used to determine the reactivity of reducing substrates (Fig. A. 2) and steady-state kinetic parameters. The *bm*XOR enzyme (Fig. A. 1, *upper left panel*) was isolated from bovine milk according to the protocol developed by Massey *et al.* (1969) [46]. The isolation steps included pancreatin treatment, butanol-ammonium sulfate fractionation, and calcium phosphate-cellulose chromatography. The functionality was determined to 52% (Activity to Flavin Ratios, AFR = 102). The wild type (WT) recombinant *Rhodobacter capsulatus* XDH bacterial enzyme (*Rc*XDH WT) (Fig. A. 1, *upper right panel*) was obtained as a gift from Dr. Silke Leimkühler (Department of Plant Biology, Technical University Braunschweig, Braunschweig, Germany). The enzyme was expressed and purified from the phototropic purple bacterium *Rhodobacter capsulatus* and expressed in *E.coli*. The enzyme was purified using Ni-NTA, Qsepharose, and phenyl-sepharose columns. The functionality of the wild type *Rc*XDH was determined to 80% (AFR = 168). The *Rc*XDH-$Glu_{232}$Ala mutant enzyme (Fig. A. 1, *lower right panel*) was obtained and prepared the same as the *Rc*XDH WT enzyme. The carbon monoxide oxidizing enzyme (carbon monoxide dehydrogenase, Cu/Mo-CODH) (Fig. A. 1, *lower right panel*) was purified from *Oligotropha carboxidovorans* bacteria. The bacteria cultivation, biomass harvest, and enzyme purification were performed with the help of Prof. L. L. Barton (Department of Biology, The University of New Mexico, Albuquerque, NM, U. S. A.). *The artificial electron acceptors and assay reagents* were sodium 2,6-dichlorophenolindophenol ($Na^+$ $DCIP^-$), cytochrome c from horse heart, tetranitromethane (TNM) (Sigma-Aldrich, St. Louis, MO), and Amplex®Red reagent kit (Molecular Probes, Inc., Eugene, OR). *The buffer solutions* were prepared from sodium pyrophosphate tetrabasic decahydrate ($Na_4P_2O_7 \cdot 10H_2O$) (Sigma-Aldrich, St. Louis, MO), tris-(hydroxymethyl)-aminomethane

(J. T. Baker, Inc., Phillipsburg NJ), or 4-(2-hydroxyethyl)piperazine-1-ethanesulfonic acid (HEPES) (EMD chemicals, Inc., Gibbstown, NJ). *The molecules used for the determination of reactivity of enzymes or steady-state kinetic parameters* were, *purines* [purine (Acros organics, Fair Lawn, NJ), hypoxanthine, xanthine, allopurinol, 6-methylpurine (6MP), and 2-hydroxy-6-methylpurine (HMP) (Sigma-Aldrich, St. Louis, MO)], a*ldehydes* [formaldehyde, acetaldehyde, Propionaldehyde, butyraldehyde, trifluoroacetaldehyde, DL-glyceraldehyde, benzaldehyde, and *p*-dimethylamino cinnam-aldehyde (Sigma-Fluka, St. Louis, MO), and glycolaldehyde (MP Biomedicals LLC., Solon, OH)], and *other molecules* [sodium formate, sodium acetate, and acetonitrile (EMD chemicals, Inc., Gibbstown, NJ), formamide, methylformamide, dimethylformamide, dimethylthioformamide, trifluoroacetamide, 4-nitrophenylacetate, and 4-nitrophenylformamide (Aldrich chemical company, Inc., Milwaukee, WI), 4-nitrophenylformate and 4-nitroacetanilide (Alfa Aesar, Ward Hill, MA), $H_2O_2$, Sodium dithionite, lumazine (2,4-(1*H*,3*H*)-pteridinedione), and uracil (Sigma-Fluka, St. Louis, MO)], and CO (99.5%, v/v) (Specialty Chemical Products, Inc., South Houston, TX)].

*Instruments and program softwares:* All routine enzyme assays were performed using a Hitachi model U-3501 recording spectrophotometer (Hitachi Ltd., Tokyo, Japan) in 100 μL, 10 mm light path sub-micro Quartz spectrophotometer cell (Starna Cells, Inc., Atascadero, CA) or 1.5 mL spectrophotometer cell light path 10 mm (VWR scientific, Medis, PA). The kinetic parameters were analyzed using GraphPad® software package (GraphPad Software Inc., La Jolla, CA) by applying curve fitting (nonlinear regression) to determine the best-fit values. All experiment data were analyzed using Microsoft® Office Excel 2007 (1985 – 2003 Microsoft Corporation).

Methods

The specificity of artificial electron acceptors and assay reagents

*The detection of $H_2O_2$ in the presence of Amplex® Red reagent:* The stock solution for 10 mM Amplex®Red (10-acetyl-3, 7-dihydroxyphenoxazine) reagent was prepared by dissolving 0.26 mg Amplex®Red reagent in 100 µL DMSO. The stock solution for 100 U/mL horseradish peroxidase was prepared by mixing 20 U horseradish peroxidase and 200 µL of reaction buffer (50 mM tris buffer, pH 7.5). The *amplex working solution* was prepared, in a reaction buffer, from 100 µM Amplex® Red reagent, 0.4 U/mL horseradish peroxidase, and respective enzymes (40 µU/mL butter milk XOR or 1.7 nM *bm*XOR). A *negative control* was prepared (without substrates or enzymes) from equal amounts of reaction buffer and amplex working solution. A *positive control* was prepared (without substrates) from equal amounts of 3% $H_2O_2$ solution and an amplex working solution. All *reaction mixtures* were prepared from equal amounts of amplex working solution and 0.108 mM xanthine. All reaction mixtures and controls were incubated, under air-saturated environment, at 37°C.

*The detection of $O_2^{\bullet-}$ or electron transfer in the presence of artificial electron acceptors:* The reaction mixtures were prepared from 21 nM *bm*XOR, artificial electron acceptors (0.015 mM $Na^+$ $DCIP^-$, 10 mM TNM, or 0.02 mM cytochrome c) and 50 mM pyrophosphate buffer (pH 7.8). The reactions were initiated by adding 0.108 mM xanthine, under air-saturated environment, at 22°C ($Na^+$ $DCIP^-$), 30°C (TNM), and 25°C (cytochrome c).

The substrate specificity and mutagenic studies

*The reactivity of molecules towards XOR enzymes:* The reactivity of the molecules, in the presence of Amplex®Red reagent and $Na^+$ $DCIP^-$, was probed to screen the potential substrates for XOR enzymes. The reactions were carried out, under aerobic conditions, at 22°C. *For the determination of $H_2O_2$ production*, the working solution containing Amplex®Red (10-acetyl-3,7-dihydroxyphenoxazine) reagent was prepared as described in the previous section and in the presence of respective enzymes (40 μU/mL butter milk XOR, 1.7 nM *bm*XOR, 300 μM *Rc*XDH, or 90 μM *Rc*XDH-$Glu_{232}$Ala mutant). The negative control, positive control, and reaction mixtures were prepared as described in the previous section, by replacing xanthine with various substrates (Fig. A. 2). The reactions were initiated by adding respective molecules to the working solution. *For the determination of* $O_2^{\bullet-}$ *production,* the reaction mixtures were prepared from the respective enzymes (21 nM *bm*XOR, 300 μM *Rc*XDH, or 90 μM *Rc*XDH-$Glu_{232}$Ala mutant), 0.015 mM $Na^+$ $DCIP^-$, and 50 mM pyrophosphate buffer (pH 7.8). The reactions were initiated by adding the molecules to the working solution. All reaction mixtures and controls were incubated until the completions of the reactions were detected.

*The substrate (or enzyme) concentration dependency of the enzyme catalyzed-reactions:* The experiments were carried out under aerobic condition, at 22°C, by varying the concentrations of the substrates. *For OcCu/Mo-CODH* enzyme, the reaction mixtures were prepared by mixing 1.7 nM *Oc*Cu/Mo-CODH, 0.078 mM $Na^+DCIP^-$, and 50 mM HEPES buffer (pH 8.2). The reactions were initiated by adding varying amounts (between 0.1 mL – 5.0 mL) of CO gas. *For XOR enzymes,* the reaction mixtures were prepared by mixing respective enzymes (40 μU/mL butter milk XOR, 1.7 nM *bm*XOR, 300 μM *Rc*XDH, or 90 μM *Rc*XDH-$Glu_{232}$Ala mutant), 0.078 mM $Na^+DCIP^-$, 50 mM Tris buffer (pH 7.5), and varying amounts (between 0 – 0.3 mL) of $ddH_2O$. The reactions were initiated by adding varying amounts (between 0.3 – 0 mL) of respective substrates (0.20 M formaldehyde, 0.20 M formamide, 0.50 M acetaldehyde, 0.1 mM allopurinol, 0.128 M 6-methylpurine, 5 mM 2-hydroxy-6-methylpurine, 0.108 mM xanthine, 2.05

mM hypoxanthine, 0.20 M sodium formate, 2 mM purine, 1.3 mM lumazine, 0.20 M Propionaldehyde, 0.20 M butyraldehyde, or 1.5 mM benzaldehyde). *The enzyme concentration dependency of the enzyme catalyzed-reactions* were performed, as discussed above, by varying the concentrations of the enzymes (40 μU/mL butter milk XOR, 1.7 nM *bm*XOR, 300 μM *Rc*XDH, or 90 μM *Rc*XDH-$Glu_{232}$Ala mutant) at constant substrate, $Na^{+}DCIP^{-}$, and buffer concentrations.

## 2.3 Results

The specificity of artificial electron acceptors and assay reagents

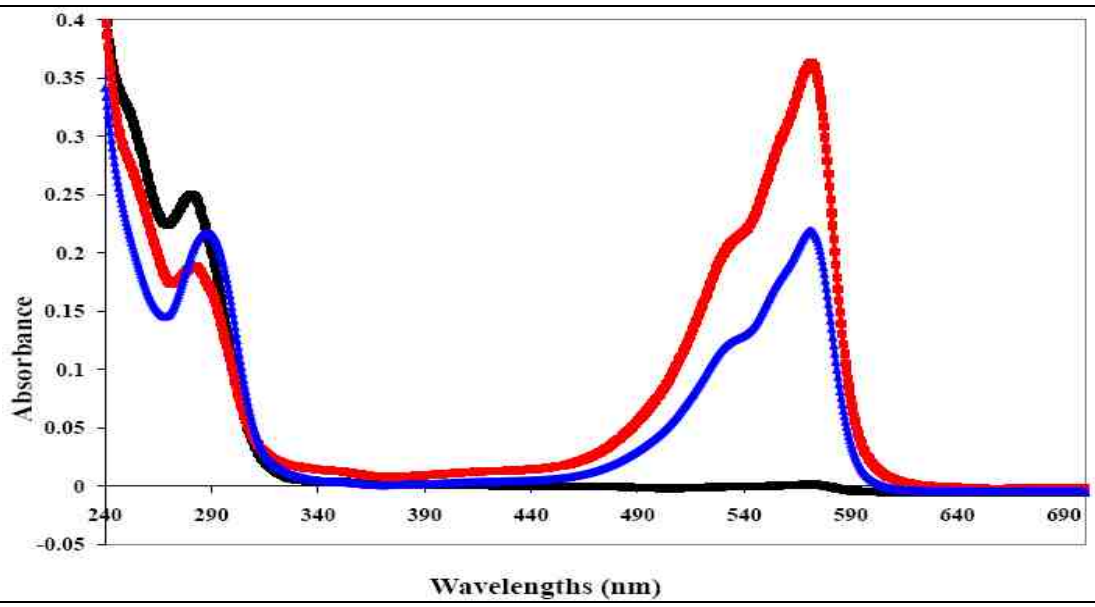


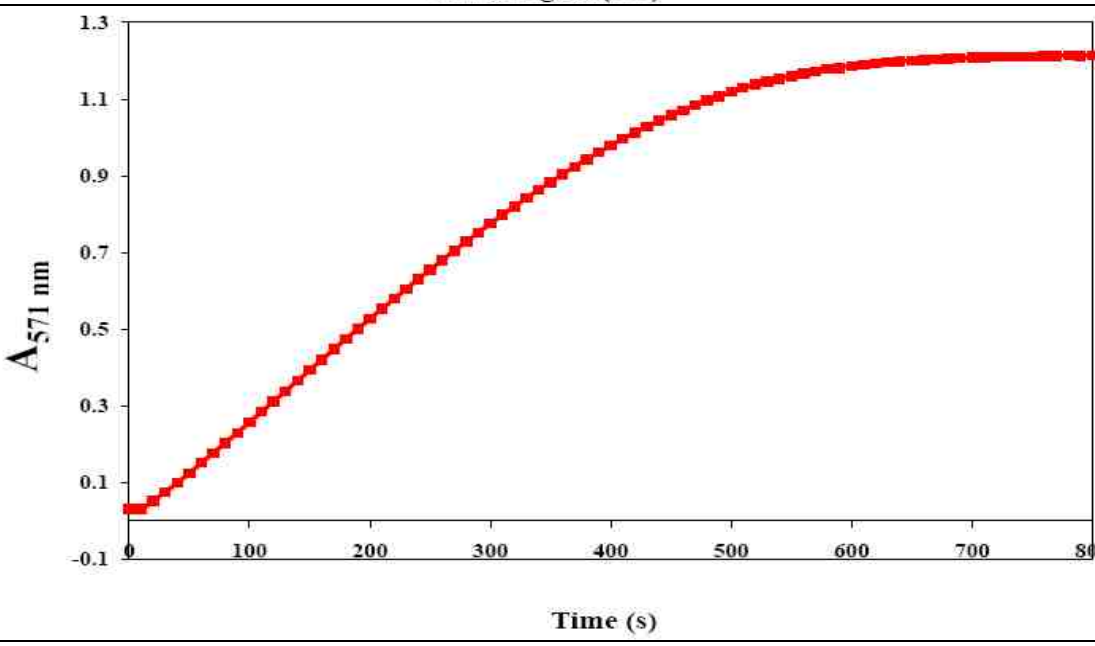


Figure 2.3.1. The UV-visible absorption spectra traces, for the rate of $H_2O_2$ production, probed in the presence of Amplex working solution. The traces, in the *upper panel from top to bottom*, represent the amplex working solution (*black or third trace*), 25 μM xanthine (*blue or second trace*), and 25 μM of 3% (v/v) $H_2O_2$ solution (*red or first trace*). The *lower panel* represents a time course progress curve for the hydroxylation of 0.20 mM xanthine by *bm*XOR enzyme.

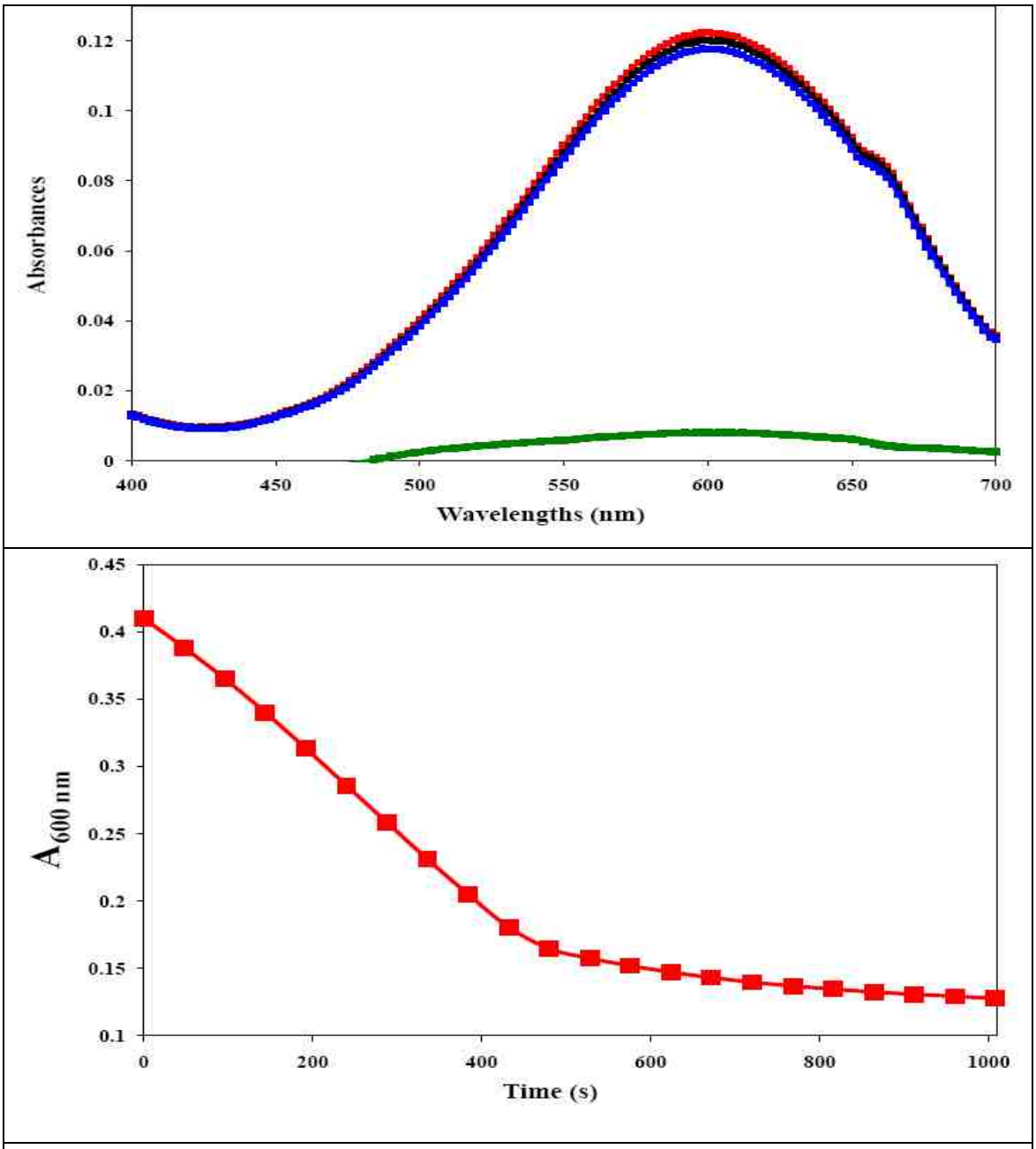


Figure 2.3.2. The UV-visible absorption spectra traces, for the rate of $O_2^{\bullet-}$ or electron production, probed in the presence of 0.064 mM $Na^+$ $DCIP^-$ and 50 mM pyrophosphate buffer, pH 7.8. The traces, in the *upper panel from top to bottom*, represent 0.064 mM $Na^+$ $DCIP^-$ and 50 mM pyrophosphate buffer, pH 7.8 (*red or first trace*), 0.108 mM xanthine (*black or second trace*), 1.5 nm *bm*XOR (*blue or third trace*), and 0.108 mM xanthine and 1.5 nm *bm*XOR (*green or fourth trace*). The *lower panel* represents a time course progress curve for the hydroxylation of 0.108 mM xanthine by *bm*XOR enzyme.

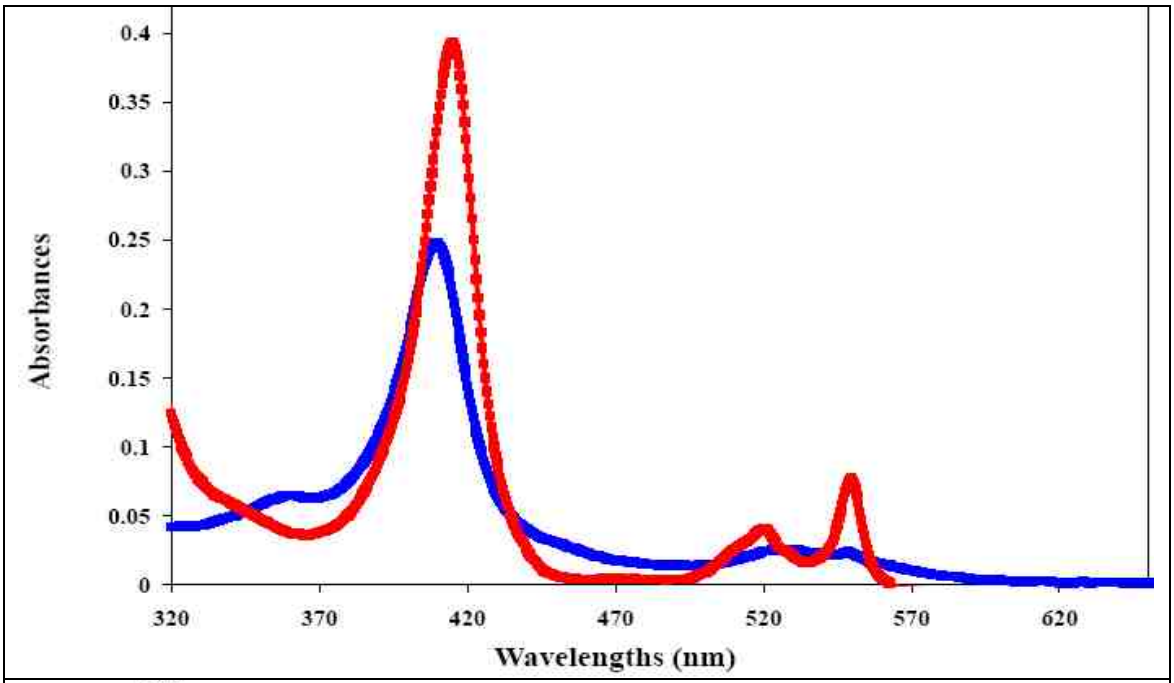


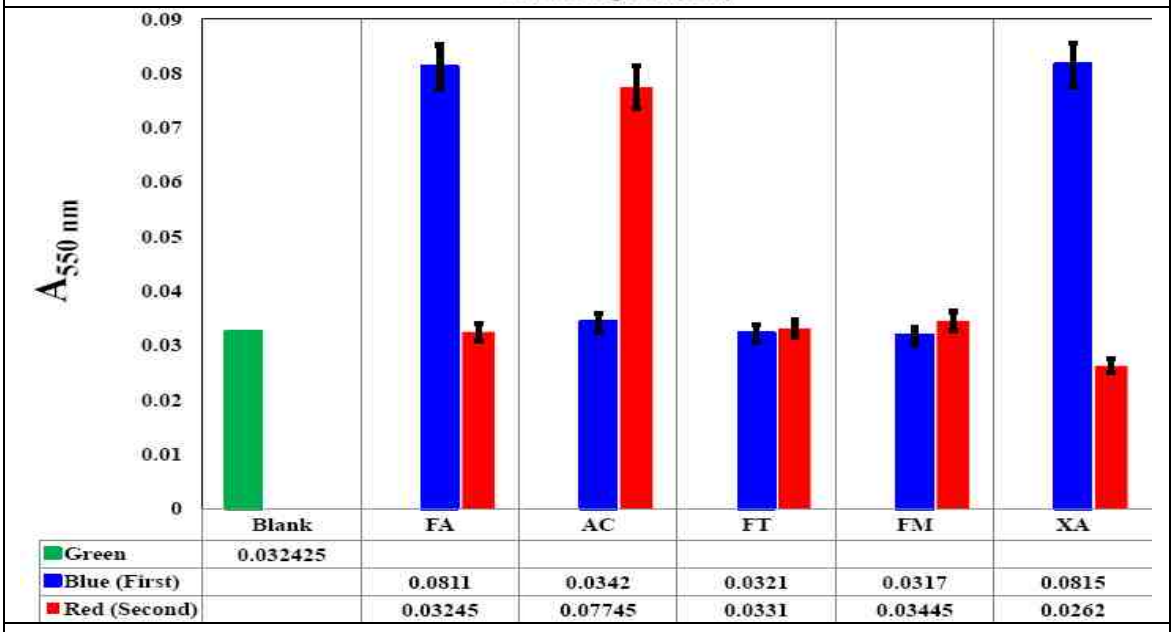


| | Blank | FA | AC | FT | FM | XA |
|---|---|---|---|---|---|---|
| Green | 0.032425 | | | | | |
| Blue (First) | | 0.0811 | 0.0342 | 0.0321 | 0.0317 | 0.0815 |
| Red (Second) | | 0.03245 | 0.07745 | 0.0331 | 0.03445 | 0.0262 |

Figure 2.3.3. The UV-visible absorption spectra traces, for the rate of $O_2^{\bullet-}$ production, probed in the presence of cytochrome c. The traces, in the *upper panel from top to bottom*, represent the reaction mixture (containing 0.02 mM cytochrome c, 1.5 mM xanthine, and 1.5 nm *bm*XOR) (*red or first trace*) and the 0.02 mM cytochrome c in 50 mM pyrophosphate buffer, pH 7.8 (*blue or second trace*). The responses, in the presence of various substrates and *bm*XOR, are also shown in the *lower panel*. The (*blue or first*) and (*red or second*) bars represent, respectively, the low and high concentrations of substrates [formaldehyde (FA), acetaldehyde (AC), formate (FT), formamdie (FM), and xanthine (XA)].

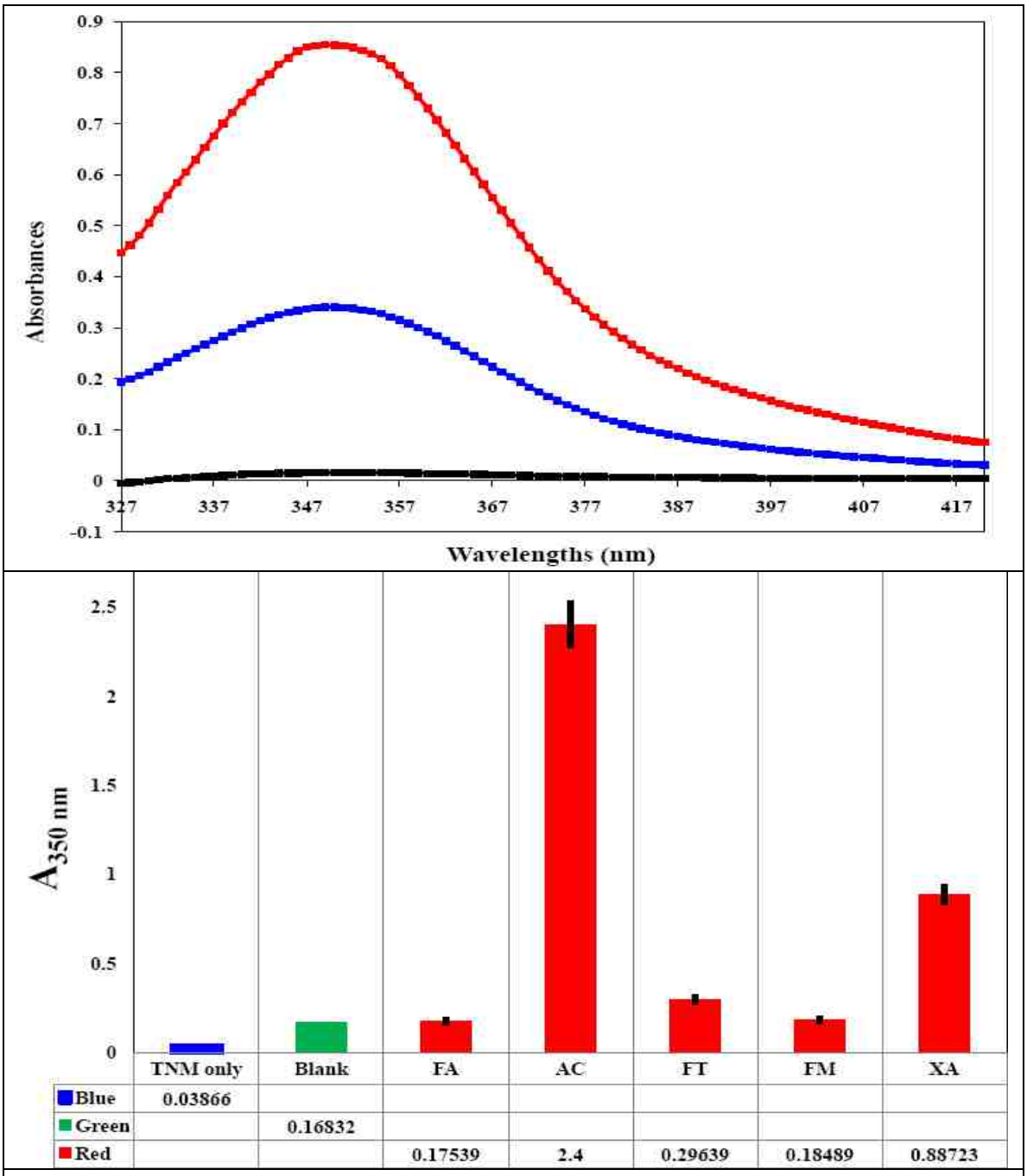


Figure 2.3.4. The UV-visible absorption spectra traces, for the rate of $O_2^{\bullet-}$ production, probed in the presence of TNM. The traces, in the *upper panel from top to bottom*, represent the reaction mixture (containing 10 mM TNM, 0.0027 mM xanthine, and 1.5 nm *bm*XOR) (*red or first trace*), 1.5 nm *bm*XOR (*blue or second trace*), and 50 mM pyrophosphate buffer (pH 7.8) (*black or third trace*). The responses, in the presence of various substrates and *bm*XOR, are also shown in the *lower panel*. The symbols of the substrates were the same as Figure (2.3.3).

Table 2.3.1. The initial rates for the hydroxylation of xanthine by *bm*XOR enzyme in the presence of assay reagents and artificial electron acceptors.

| Substrates | Initial rates ($s^{-1}$) | | | |
|---|---|---|---|---|
| | Amplex | $Na^+DCIP^-$ | Cytochrome c | TNM |
| | | | | |
| Xanthine | 7.26E-04 | 1.15E-04 | 4.92E-06 | 4.75E-05 |
| Hydrogen Peroxide | 6.03E-03 [(a)] | | | |
| Sodium Dithionite | | 7.28E-03 [(b)] | 2.28E-03 [(c)] | 0.08326 [(d)] |

The reaction mixtures were prepared from

(a) equal volumes of 3.0 % (v/v) $H_2O_2$ and amplex working solutions.

(b) 50 mM pyrophosphate buffer (pH 7.8) containing 0.06 mM $Na^+$ $DCIP^-$ and 8.0 mM sodium dithionite.

(c) 8.0 mM sodium dithionite and 10 μL of 0.036 mM cytochrome c in 50 mM phosphate buffer (pH 7.8).

(d) 10 μM TNM and 10 μL of 8.0 mM sodium dithionite in 50 mM pyrophosphate buffer (pH 7.8).

Table 2.3.2. The steady-state kinetic parameters for the hydroxylation of variable concentrations of xanthine. The determination was made in the presence of *bm*XOR and an assay reagent or artificial electron acceptors. The parameters were probed using a non-linear regression method and the curves were displayed using Lineweaver –Burk linear methods.

| Kinetic Parameters | Amplex [(a)] | $Na^+$ $DCIP^-$ [(b)] | Cytochrome c [(c)] | TNM [(d)] |
|---|---|---|---|---|
| | | | | |
| $v_0$ [(1)] | 7.26E-04 | 1.15E-04 | 4.92E-06 | 4.75E-05 |
| Activity [(2)] | 1.14E-04 | 8.69E-07 | 2.52E-07 | 3.25E-06 |
| $k_m$ [(3)] | 3.12 | 1.92E-02 | 8.30E-02 | 9.49E-01 |
| $v_{max}$ [(4)] | 2.07E-04 | 1.67E-05 | 7.98E-05 | 6.06E-06 |
| $k_{cat}$ [(5)] | 5.80E-03 | 5.29E-04 | 3.55E-04 | 1.89E-04 |
| $v_{max}/k_m$ [(6)] | 6.65E-08 | 8.70E-07 | 7.98E-08 | 6.39E-09 |
| $k_{cat}/k_m$ [(7)] | 1.85E+03 | 2.76E+04 | 4.27E+03 | 2.00E+02 |

The reaction mixtures were prepared from (0, 10, 20, 30, 40, 50, 60, and 70 μL) of 0.20 μM xanthine and working reaction mixtures containing

(a) 10 μM amplex working solution in 1X tris buffer, pH 7.5. The reaction mixtures were incubated for 105 minutes at 37°C before the measurement was taken at 571 nm.

(b) 21 nM *bm*XOR and 0.015 mM $Na^+$ $DCIP^-$ in 50 mM phosphate buffer, pH 7.81. The reaction mixtures were incubated for 60 minutes at 21°C.

(c) 0.273 mM cytochrome c and 1.18 μM *bm*XOR in 50 mM phosphate buffer, pH 7.8. The reaction mixtures were incubated for 180 minutes at 25°C.

(d) 10 mM TNM and 21 nM *bm*XOR in 50 mM phosphate buffer, pH 7.81. The reaction mixtures were incubated for 20 minutes at 30°C.

Definitions of kinetic parameters [119, 120, 121, 122 (b), 123, 124]:

1. $v_0$ (in $\mu M \bullet s^{-1}$) was the initial rate for the formation of product (d[P]/dt).
2. *Activity* (in $\mu M \bullet s^{-1} \bullet mL_{bmXOR}$) was the amount of $E_{OX}$ that converted one μM of assay reagents per second.
3. $k_m$ (in $\mu M$) was the Michaelis-Menten constant for the substrates. The parameter was used to measure the affinity of an $E_{OX}$ for the substrates. That is, the [substrate] required to get ½ of $v_{max.}$
4. $v_{max}$ (in $\mu M \bullet s^{-1}$) was the maximum rate for the $[E_{OX}]$ or the rate of a saturated enzyme used to measure how fast the enzyme could go to full speed.
5. $k_{cat}$ (in $s^{-1}$) was a molecular activity (or a turnover number of an enzyme). This was a first order rate constant that measured how tightly the substrate was bound to an enzyme or the number of substrate molecules converted to products by an enzyme.
6. $k_s$ ($v_{max}/k_m$) (in $s^{-1}$) was a first order rate constant that measured the catalytic efficiency of the substrates.
7. $k_{cat}/k_m$ (in $M^{-1} \bullet s^{-1}$) was a substrate specificity constant. This was a second order proportionality constant. It was used to compare the specificity of different substrates to the same enzyme. How fast the reaction of a given substrate was when bound to enzyme ($k_{cat}$) and how much of the substrate is required to reach maximum ($k_m$).

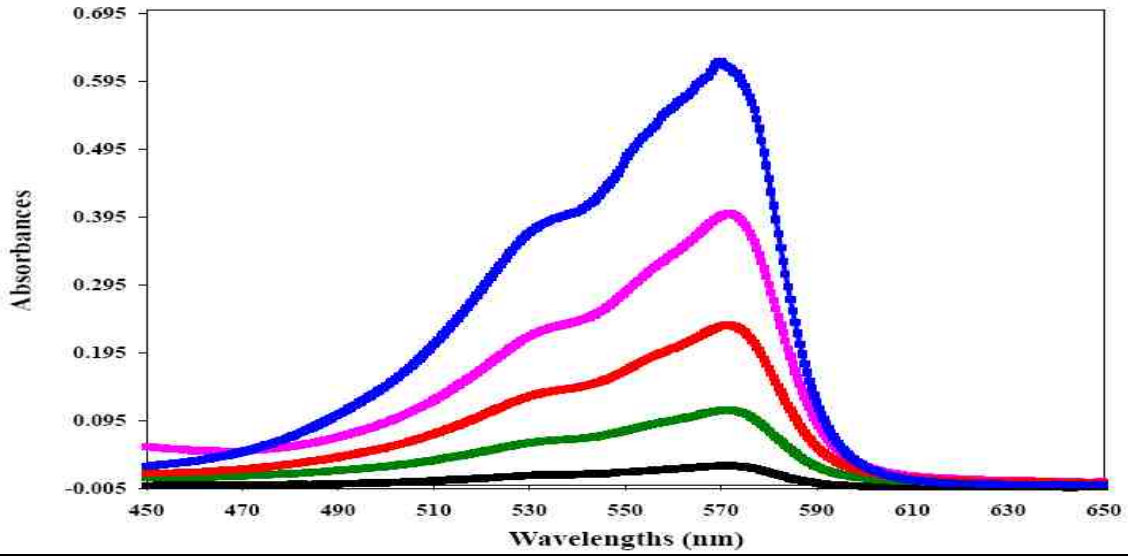


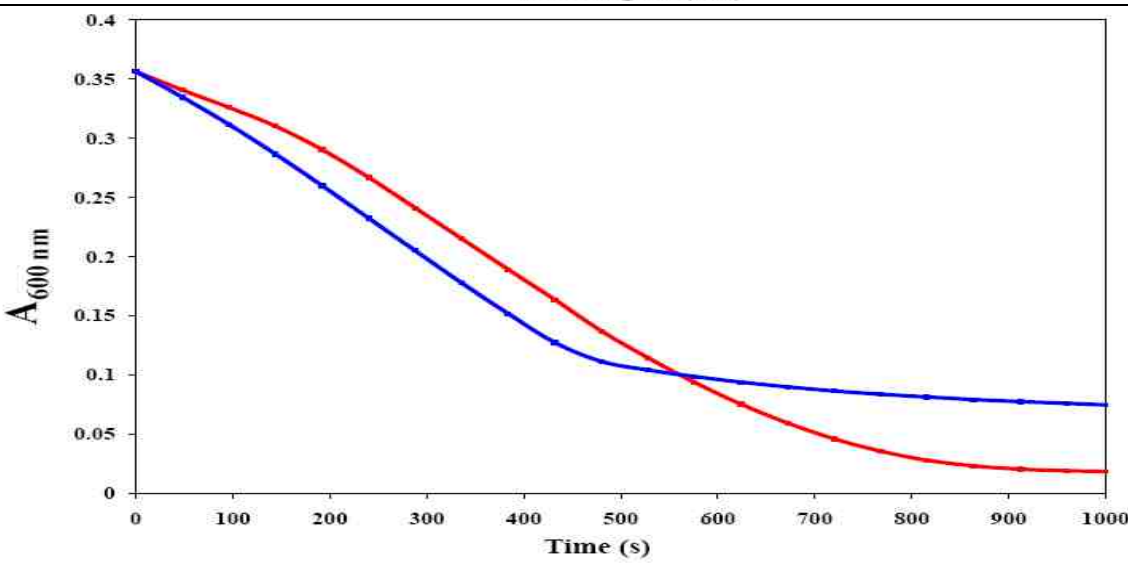


Figure 2.3.5. The UV-visible absorption spectra traces for the oxidation of substrates by *bm*XOR (*upper panel*) or *Oc*Cu/Mo-CODH (*lower panel*). The traces, in the *upper panel from top to bottom*, were determined in the presence of amplex working solution for 25 µM hypoxanthine (incubated for 2 minutes, *blue or first trace*), 25 µM xanthine (incubated for 2 minutes, *pink or second trace*), 0.20 µM formamide (incubated for 3 hours, *red or third trace*), 0.20 µM formate (incubated for 3 hours, *green or fourth trace*), or in the absence of substrates (incubated for 3 hours, *black or fifth trace*). Similarly, the traces in the (*lower panel from top to bottom*) represent a time course scan in the presence of $Na^{+}DCIP^{-}$, 1.9 nM *Oc*Cu/Mo-CODH, and substrate [either CO gas (*blue or second trace*) or buffer saturated with CO gas (*red or first trace*)].

Table 2.3.3. Activities ($\mu M \bullet s^{-1} \bullet mL_{bmXOR}$) of XO family enzymes for the oxidation and hydroxylation of the substrates. ND represents the non-convergence of the data.

| Substrates | *bm*XOR | *Rc*XDH | *Rc*XDH-$Glu_{232}$Ala |
|---|---|---|---|
| | | | |
| (a) Activities determined through the rates of $H_2O_2$ production | | | |
| Hypoxanthine (HY) | 9.23E-03 | 3.91E-04 | 1.83E-04 |
| Xanthine (XA) | 3.21E-03 | 7.48E-05 | 5.41E-05 |
| 6-methylpurine (6MP) | 7.30E-04 | 3.42E-04 | 8.47E-06 |
| 2-hydroxy-6-methylpurine (HMP) | 1.12E-03 | 1.20E-03 | 4.40E-04 |
| Allopurinol (AL) | 1.59E-03 | 9.36E-04 | 7.89E-05 |
| Formaldehyde (FA) | 1.36E-05 | 6.92E-06 | 5.38E-06 |
| Acetaldehyde (AC) | 1.24E-05 | 6.66E-06 | 3.67E-06 |
| Formate (FT) | 8.46E-06 | 7.92E-07 | ND |
| Formamide (FM) | 1.51E-05 | 2.80E-06 | 1.09E-06 |
| Methyl formamide (MF) | 7.15E-07 | ND | ND |
| Dimethylformamide (DMF) | 6.02E-08 | ND | ND |
| Dimethylthioformamide (DMT) | 3.80E-07 | ND | ND |
| Acetamide (AT) | 2.30E-08 | ND | ND |
| (b) Activities determined through the rates of $O_2^{\bullet -}$ and electron production. | | | |
| Purine (PU) | 3.43E-05 | 2.77E-03 | 5.23E-05 |
| Hypoxanthine (HY) | 9.70E-04 | 9.21E-03 | 6.02E-06 |
| Xanthine (XA) | 1.03E-05 | 9.08E-03 | 8.44E-06 |
| 6-methylpurine (6MP) | 3.31E-05 | 1.04E-04 | 9.10E-07 |
| 2-hydroxy-6-methylpurine (HMP) | 8.33E-05 | 9.32E-03 | 1.30E-05 |
| Allopurinol (AL) | 9.89E-05 | ND | ND |
| Lumazine (LU) | 7.10E-03 | 2.64E-02 | 3.64E-02 |
| Formaldehyde (FA) | 6.02E-06 | 9.50E-03 | 1.32E-06 |
| Acetaldehyde (AC) | 6.34E-06 | 1.12E-02 | 3.40E-06 |
| Propionaldehyde (PR) | ND | 2.19E-05 | 2.54E-06 |
| Butyraldehyde (BU) | ND | 4.43E-05 | 2.89E-05 |
| Benzaldehyde (BE) | 1.88E-04 | 4.20E-04 | 2.97E-05 |
| Glyceraldehyde (GL) | ND | 3.31E-05 | 3.64E-06 |
| Formate (FT) | 2.71E-07 | ND | 1.29E-08 |
| Formamide (FM) | 1.08E-07 | ND | ND |

The reactivity of substrates with *bm*XOR enzyme

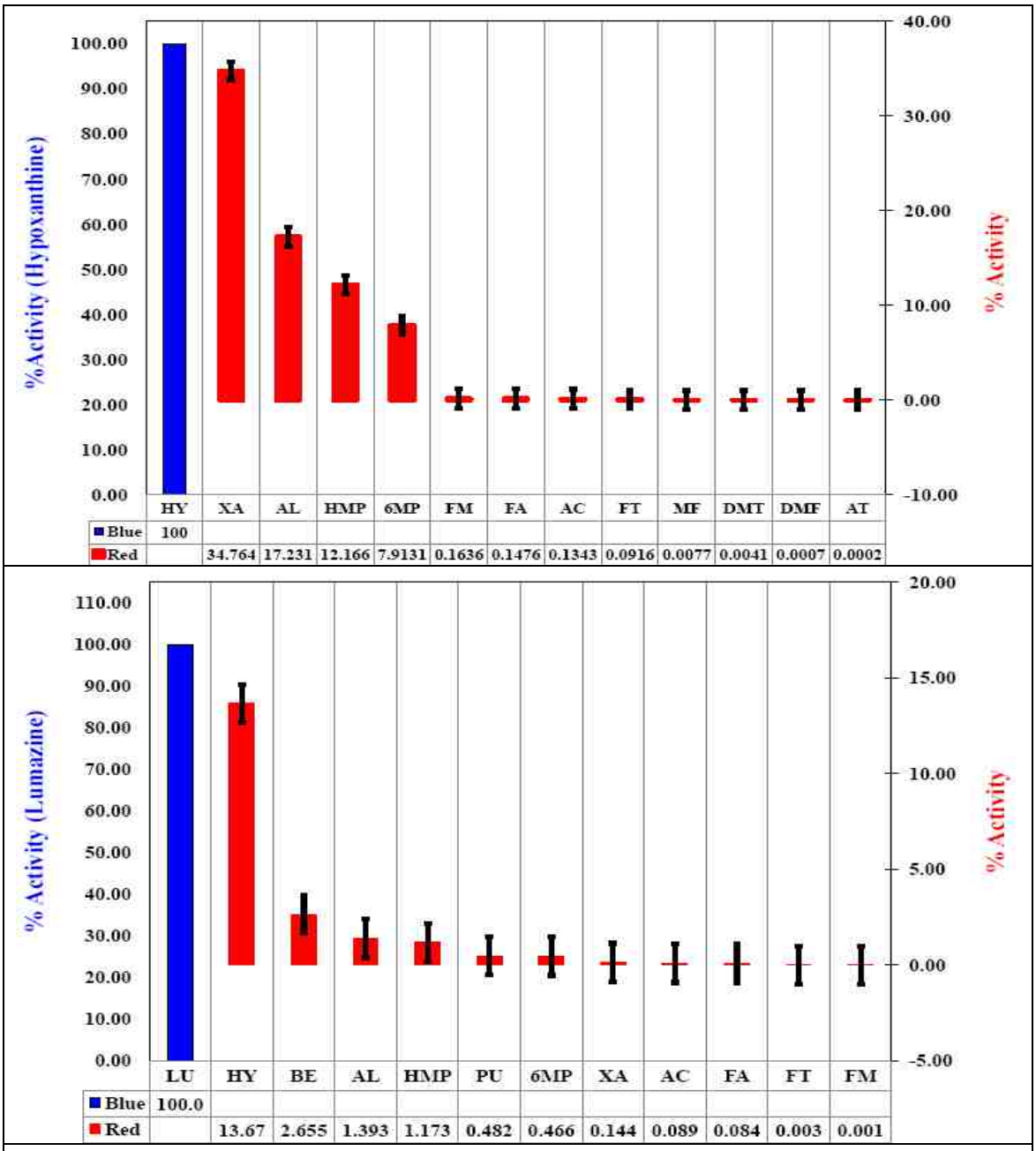


Figure 2.3.6. The percent activities of *bm*XOR enzymes probed using amplex (*upper panel*) or $Na^{+}$ $DCIP^{-}$ (*lower panel*) assay reagents. The comparison of the activities were made with respect to the substrates that gave the enzyme the highest activities, hypoxanthine (HY) (*upper panel*) and lumazine (LU) (*lower panel*). The reaction condition and activity determination were the same as Table (2.3.3).

The reactivity of substrates with *Rc*XDH enzyme

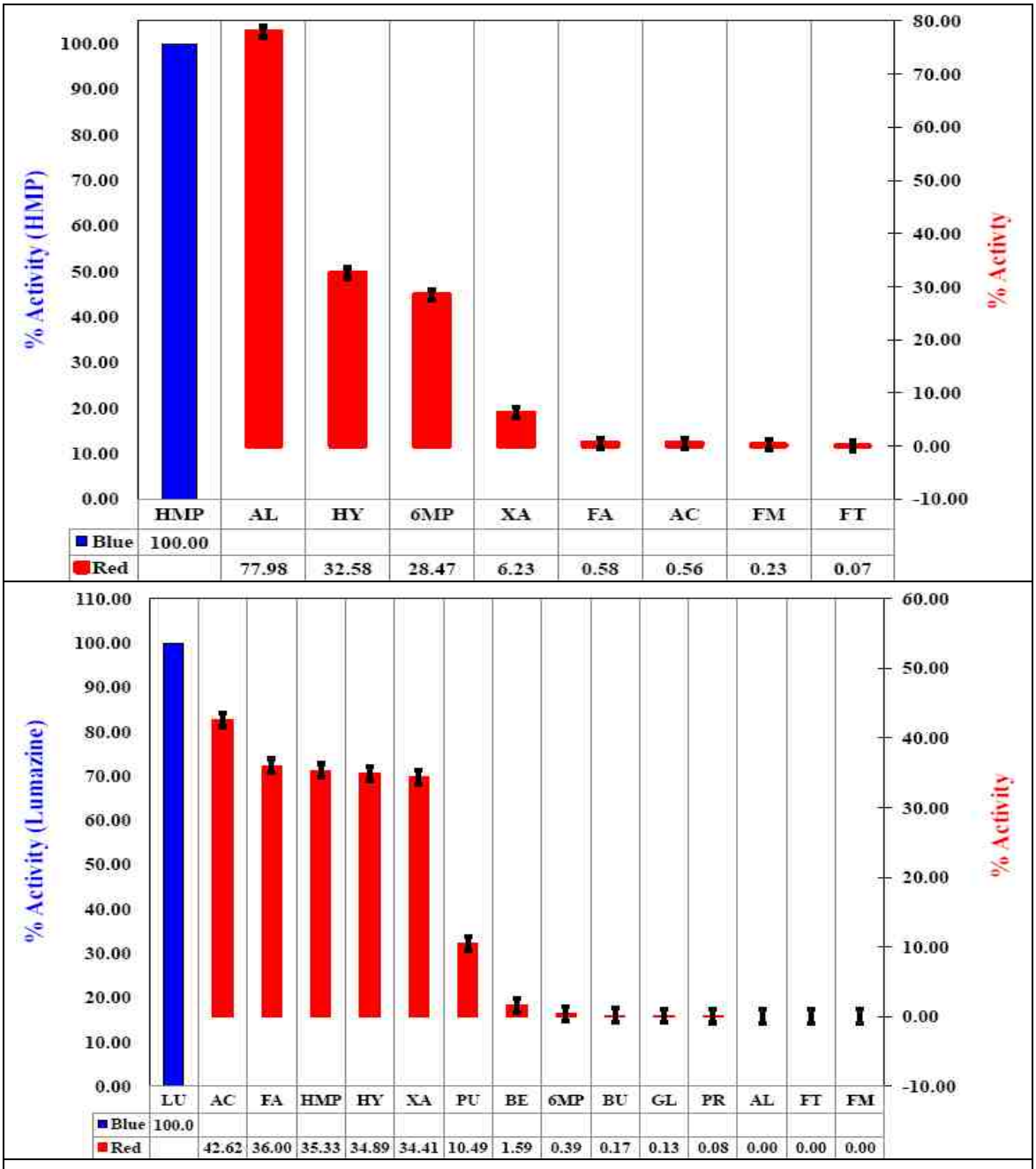


Figure 2.3.7. The percent activities of *Rc*XDH enzyme probed using amplex (*upper panel*) or $Na^{+}$ $DCIP^{-}$ (*lower panel*) assay reagents. The comparison of the activities were made with respect to the substrates that gave the enzyme the highest activities, 2-hydeoxy-6-methylpurine (HMP) (*upper panel*) and lumazine (LU) (*lower panel*). The reaction condition and activity determination were the same as Table (2.3.3).

The reactivity of substrates with *Rc*XDH-$Glu_{232}$Ala mutant enzyme

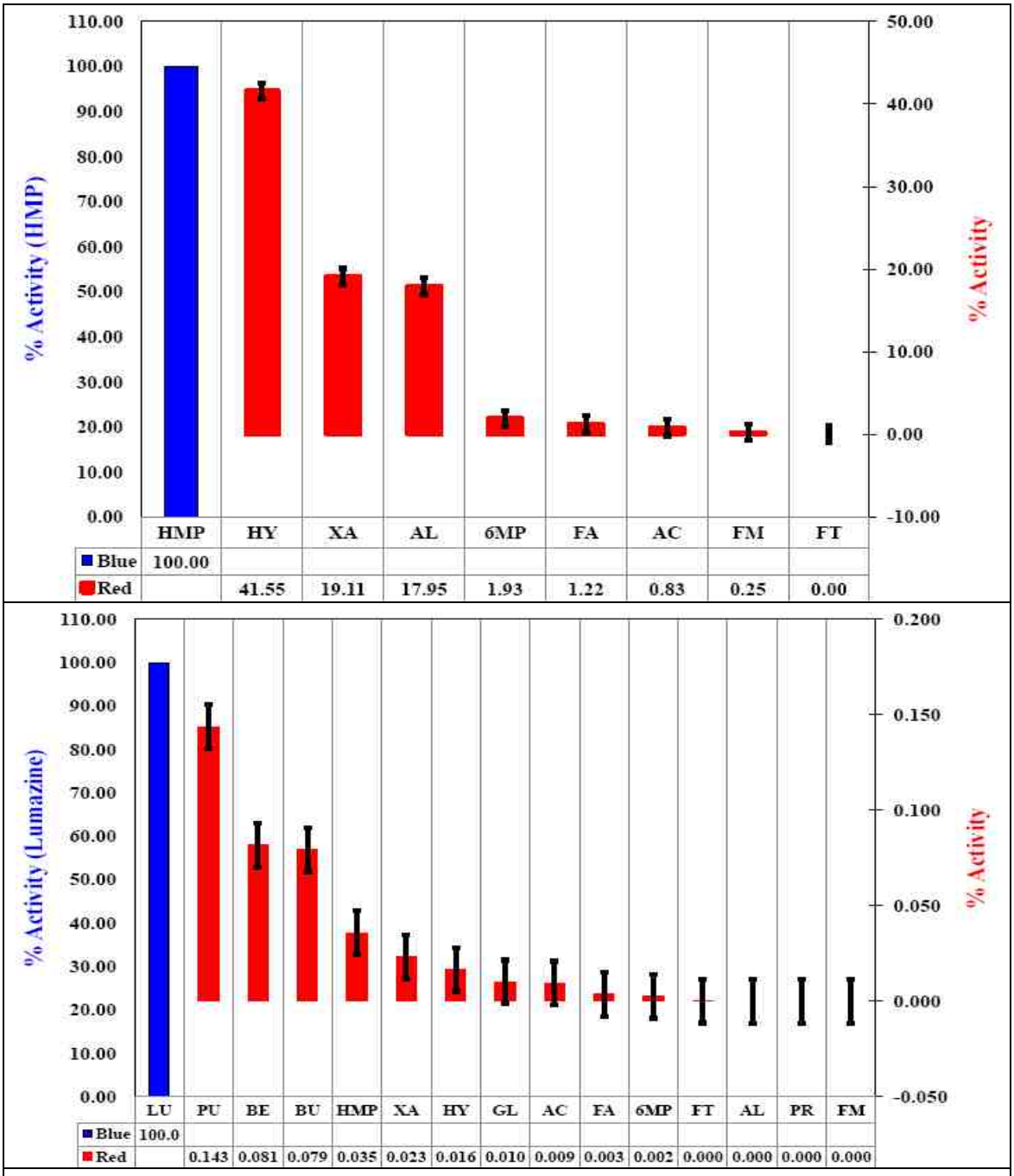


Figure 2.3.8. The percent activities of *Rc*XDH-$Glu_{232}$Ala mutant enzyme probed using amplex (*upper panel*) or $Na^+$ $DCIP^-$ (*lower panel*) assay reagents. The comparisons of the activities were made with respect to the substrates that gave the enzyme the highest activities, (HMP) (*upper panel*) and lumazine (LU) (*lower panel*). The reaction condition and activity determination were the same as Table (2.3.3).

The substrate concentration dependency of the enzyme catalyzed-reaction

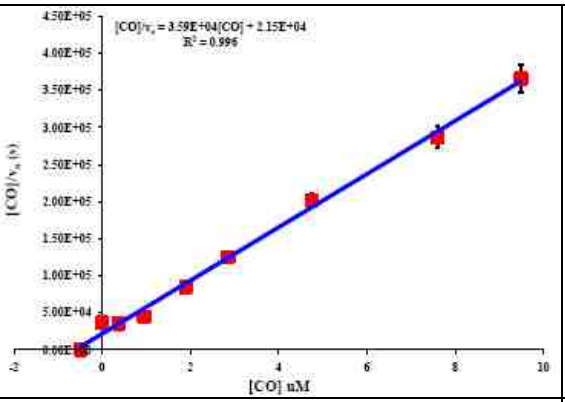


[CO]/$v_o$ versus [CO]

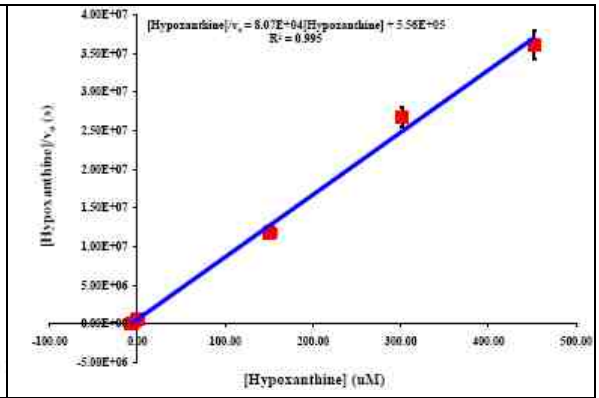


[Hypoxanthine]/$v_o$ versus [Hypoxanthine]

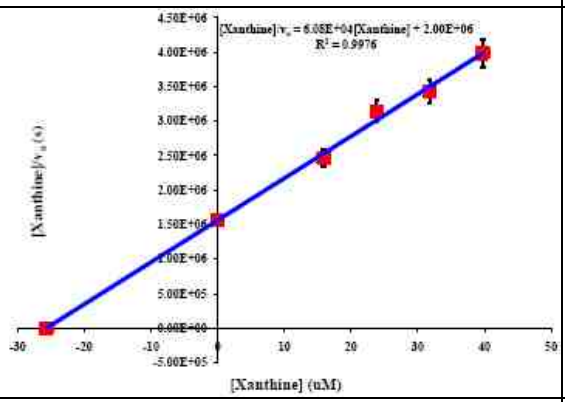


[Xanthine]/$v_o$ versus [Xanthine]

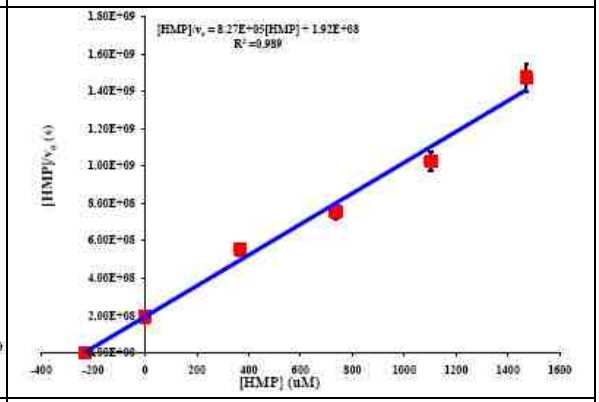


[HMP]/$v_o$ versus [HMP]

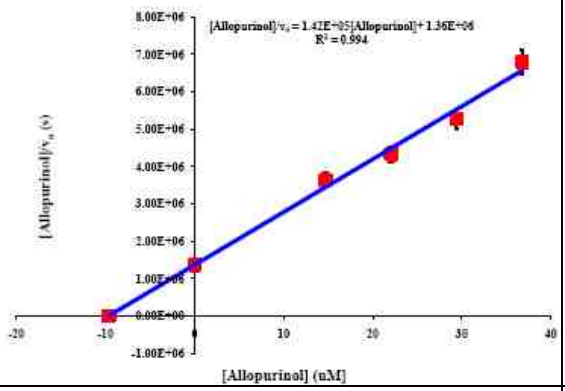


[Allopurinol]/$v_o$ versus [Allopurinol]

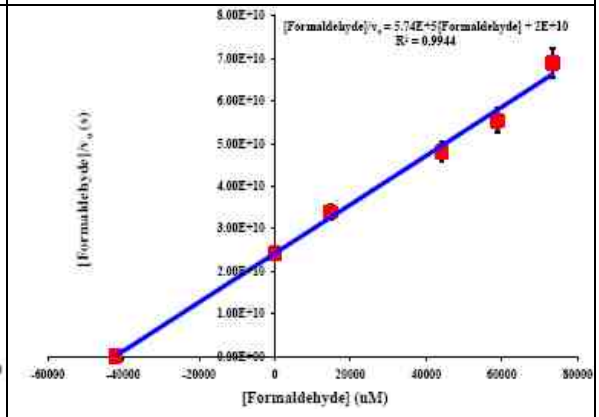


[Formaldehyde]/$v_o$ versus [Formaldehyde]

Figure 2.3.9. The effect of variable substrate concentrations on the reaction rate ($v_o$) of XO family enzymes, displayed using the Hanes-Woolf plot as shown by [Substrates]/$v_o$ against [Substrates].

The steady-state kinetic parameters for XO family enzymes

Table 2.3.4. The kinetic parameters for XO family enzymes. The parameters were probed in the presence of $Na^{+}DCIP^{-}$, as an electron acceptor. ND represents the non-convergence of the data.

| Substrates | $v_0$ ($\mu M \bullet s^{-1}$) | $k_{cat}$ ($s^{-1}$) | $v_{max}$ ($\mu M \bullet s^{-1}$) | $k_m$ ($\mu M$) | $v_{max}/k_m$ ($s^{-1}$) | $k_{cat}/k_m$ ($M^{-1} \bullet s^{-1}$) |
|---|---|---|---|---|---|---|
| (a) The steady-state kinetic parameters for *bm*XOR enzyme | | | | | | |
| Purine (PU) | 1.23E-05 | 6.5E-03 | 1.64E-05 | 270 | 6.08E-08 | 24.4 |
| Hypoxanthine (HY) | 3.49E-04 | 37.3 | 1.15E-05 | 6.90 | 1.67E-06 | 5.41E+06 |
| Xanthine (XA) | 4.23E-05 | 3.06 | 2.31E-04 | 425 | 5.45E-07 | 7.20E+03 |
| HMP | 2.78E-05 | 36.5 | 2.76E-05 | 2.08E+04 | 1.33E-09 | 17.5 |
| Allopurinol (AL) | 3.30E-05 | 2.34 | 1.33E-05 | 3.02 | 4.40E-06 | 7.75E+05 |
| Lumazine (LU) | 9.37E-03 | 1.38 | 2.33E-04 | 69.7 | 3.35E-06 | 1.98E+04 |
| Formaldehyde (FA) | 1.33E-05 | 2.31 | 1.75E-04 | 9.61E+05 | 1.82E-10 | 2.40 |
| Acetaldehyde (AC) | 1.40E-05 | 3.94 | 2.34E-05 | 3.22E+05 | 7.28E-11 | 12.2 |
| Benzaldehyde (BE) | 6.78E-05 | 164 | 4.09E-05 | 237 | 1.73E-07 | 69.3 |
| b) The steady-state kinetic parameters for *Rc*XDH enzyme | | | | | | |
| Purine (PU) | 5.53E-04 | 294 | 1.81E-04 | 1.30E+03 | 1.40E-07 | 22.7 |
| Hypoxanthine (HY) | 1.84E-03 | 19.9 | 3.37E-04 | 68.3 | 4.94E-06 | 2.91E+03 |
| Xanthine (XA) | 3.03E-03 | 91.4 | 1.55E-03 | 240 | 6.45E-06 | 3.80E+03 |
| HMP | 3.11E-03 | 146 | 2.47E-05 | 213 | 1.16E-07 | 68.5 |
| Allopurinol (AL) | ND | ND | ND | ND | ND | ND |
| Lumazine (LU) | 8.93E-03 | 11.5 | 6.25E-04 | 9.22 | 6.78E-05 | 1.25E+04 |
| Formaldehyde (FA) | 3.17E-03 | 19.2 | 3.26E-04 | 1.54E+06 | 2.13E-10 | 12.5 |
| Acetaldehyde (AC) | 3.75E-03 | 133 | 2.26E-05 | 1.03E+06 | 2.19E-11 | 129 |
| Propionaldehyde (PR) | 4.37E-06 | 142 | 3.54E-05 | 1.32E+04 | 2.68E-09 | 1.08 |
| Butyraldehyde (BU) | 8.87E-06 | 8.46E-04 | 2.11E-06 | 5.39E+03 | 3.91E-10 | 15.7 |
| Benzaldehyde (BE) | 8.41E-05 | 3.64E-03 | 9.07E-06 | 73.5 | 1.23E-07 | 49.5 |
| (c) The steady-state kinetic parameters for *Rc*XDH-$Glu_{232}$Ala enzyme | | | | | | |
| Purine (PU) | 1.92E-05 | 5.68E-03 | 1.41E-05 | 3.27E+03 | 4.32E-09 | 1.73 |
| Hypoxanthine (HY) | 5.85E-06 | 23.9 | 1.18E-05 | 103 | 1.15E-07 | 2.33E+03 |
| Xanthine (XA) | 8.19E-06 | 1.30E-03 | 3.24E-06 | 4.52 | 7.17E-07 | 288 |
| HMP | 1.26E-05 | ND | ND | ND | ND | ND |
| Allopurinol (AL) | ND | ND | ND | ND | ND | ND |
| Lumazine (LU) | 1.23E-02 | 14.0 | 2.36E-03 | 8.33 | 2.83E-04 | 1.68E+06 |
| Formaldehyde (FA) | 1.28E-06 | 1.55E-03 | 3.87E-06 | 199 | 1.95E-08 | 7.82 |
| Acetaldehyde (AC) | 3.30E-06 | 3.94E-03 | 9.80E-06 | 8.25E+04 | 1.19E-10 | 477 |
| Propionaldehyde (PR) | 1.41E-06 | 2.82E-03 | 7.01E-06 | 3.76E+04 | 1.87E-10 | 750 |
| Butyraldehyde (BU) | 1.06E-05 | 15.9 | 6.18E-06 | 4.10E+03 | 1.51E-09 | 38.8 |
| Benzaldehyde (BE) | 1.09E-05 | 2.55E-03 | 6.35E-06 | 47.2 | 1.35E-07 | 54.0 |
| (d) The steady-state kinetic parameters for *Oc*Cu/Mo-CODH | | | | | | |
| Carbon monoxide | 2.72E-02 | 2.04E-04 | 2.74E-05 | 4.84E-01 | 5.66E-05 | 4.21E+02 |

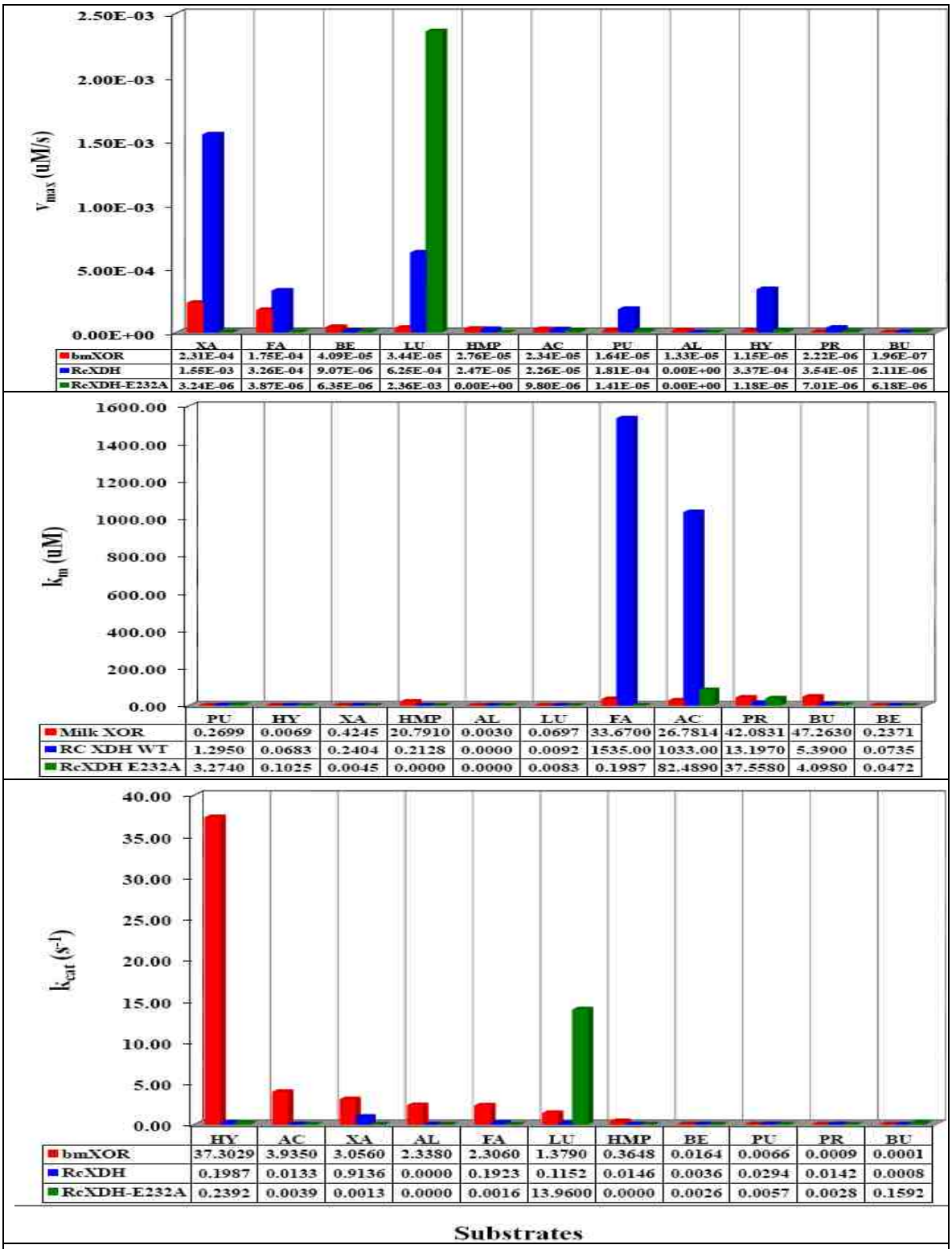


Figure 2.3.10. The kinetic parameters, $v_{max}$ (*top panel*), $k_m$ (*middle panel*), $k_{cat}$ (*bottom panel*) for the *bm*XOR, *Rc*XDH, *Rc*XDH-$Glu_{232}$Ala (*Rc*XDH-E232A) mutant enzymes. The plots were developed from Table (2.3.4).

The specificity of substrates towards XOR enzymes

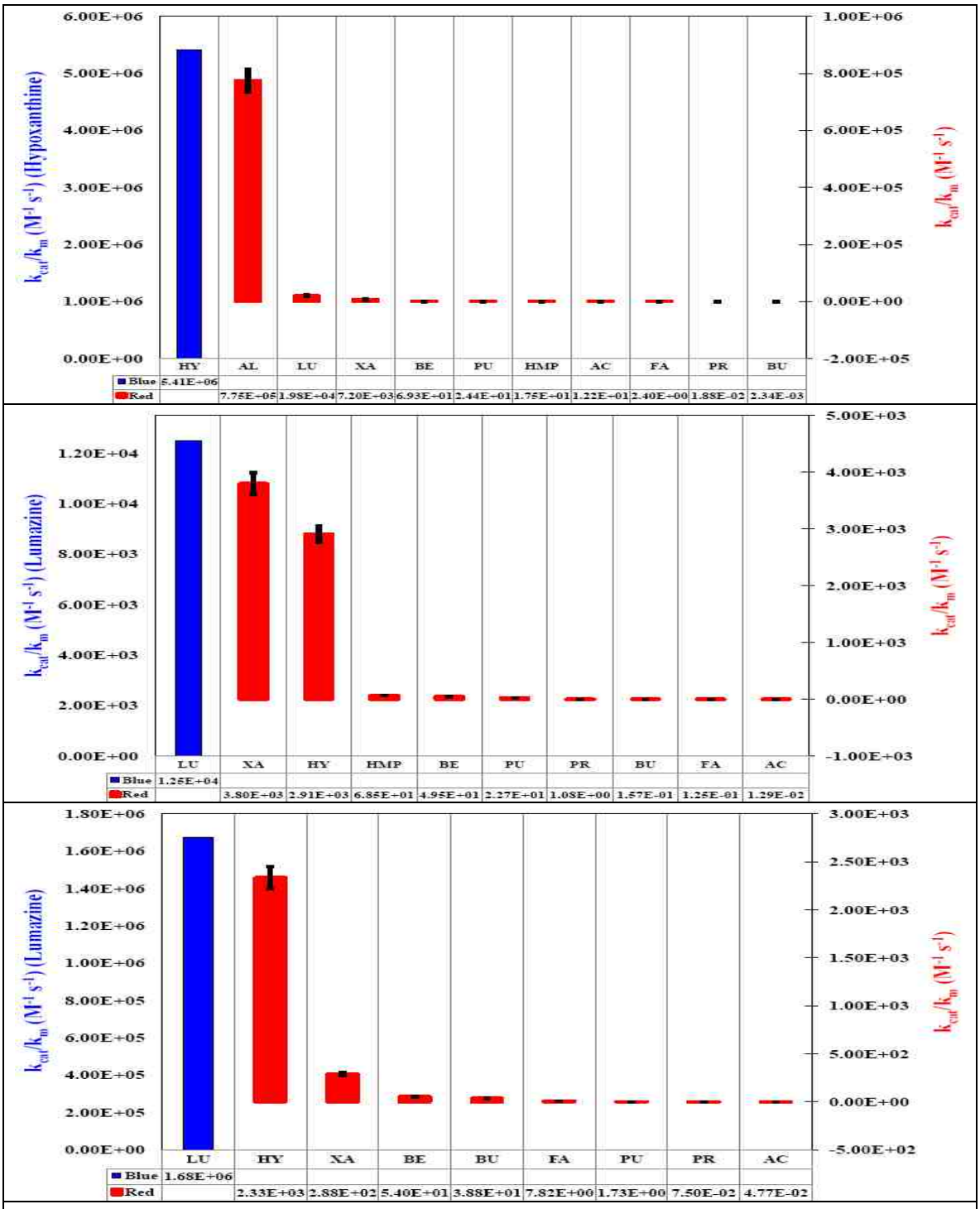


Figure 2.3.11. The $k_{cat}/k_m$ values for the *bm*XOR, *Rc*XDH, *Rc*XDH-$Glu_{232}$Ala mutant enzyme catalyzed oxidation and hydroxylation of various reducing substrates, developed from Table (2.3.4).

## 2.4 Discussion and Conclusion

### Description of results

*The specificity of artificial electron acceptors and assay reagents:* The specificity of artificial electron acceptors or assay reagent was probed in the presence of *bm*XOR enzyme and xanthine. The positive control, for the detection of the level of $H_2O_2$ production, was prepared from 3.0 % (v/v) $H_2O_2$ and amplex working solution (Fig. 2.3.1, *upper panel*). Similarly, the positive control for the detection of the level of $O_2^{\bullet-}$ production was prepared from 8.0 mM sodium dithionite ($S_2O_4^{-2}$) (used as a reducing agent) and electron acceptors (cytochrome c, TNM, or $Na^+DCIP^-$). The initial rates for the production of $H_2O_2$ and $O_2^{\bullet-}$ were shown to be in the same orders of magnitude (Table 2.3.1). The initial rates, for the hydroxylation of xanthine by *bm*XOR, was evaluated as shown in Figures (2.3.1, 2.3.2, 2.3.3, and 2.3.4), respectively, in the presence of assay reagents (amplex working solution, $Na^+DCIP^-$, cytochrome c, and TNM). The time course progress curves were also shown to obey a Michaelis-Menten type steady-state kinetics (Figs. 2.3.1 and 2.3.2, *lower panels*). The initial rates, in the presence of xanthine, were one order of magnitude lower than the initial rates determined in the presence of sodium dithionite. In the presence of sodium dithionite, the initial rate for the reduction of cytochrome c, was three orders of magnitude faster than the rates determined in the presence of *bm*XOR and xanthine (Table 2.3.1 and Fig. 2.3.3). In the presence of various substrates and *bm*XOR, the response for the rate of $O_2^{\bullet-}$ production, was shown to be concentration dependent (mainly for substrates such as formaldehyde, xanthine, and acetaldehyde) (Fig. 2.3.3, *lower panel*). Cytochrome c was shown to respond well in the presence of low concentrations of formaldehyde (6 mM) and xanthine (0.108 mM). However, cytochrome c was shown to be insensitive when high concentrations of formaldehyde (200 mM) and xanthine (1.5 mM) were used. The enzyme was shown to have similar response for high (200 mM) and low (6 mM) concentrations of formate and formamide. Similarly, the rate of $O_2^{\bullet-}$ production was measured using the spectral change

observed due to the reduction of tetranitromethane (TNM) to trinitromethane (Fig. 2.3.4). The initial rate for the reduction of TNM, in the presence of sodium dithionite, was three orders of magnitude faster than the initial rate determined in the presence of *bm*XOR enzyme and xanthine. TNM was shown to respond effectively in the presence of low concentrations of acetaldehyde (5 mM) and xanthine (0.108 mM). However, TNM was shown to interfere with acetaldehyde or *bm*XOR enzyme. TNM was also shown to exhibit poor responses for other substrates tested (Fig. 2.3.4, *lower panel*). In addition to the initial rates, the specificity of the artificial electron acceptors and assay reagent, were compared in terms of the steady-state kinetic parameters (Table 2.3.2). The parameters, for the catalytic turn over, were determined by varying the concentrations of xanthine. The initial rates for the hydroxylation of xanthine were much faster, in the presence of amplex reagent and $Na^+DCIP^-$. The turnover numbers and molecular efficiencies, in the presence of $Na^+DCIP^-$ and amplex reagent, were higher than cytochrome c and TNM. The use of $Na^+DCIP^-$, as an assay reagent, was preferred since it was presumed to interact not only with $O_2^{\bullet-}$ (at the flavin sites) but also with electrons (at the Moco and $[Fe_2S_2](S^{\gamma}_{Cys})_4$ sites). In summary, the amplex and $Na^+DCIP^-$ assay reagents were found to be the most effective assay reagents, respectively, for probing the rate of $H_2O_2$ and $O_2^{\bullet-}$ productions. The initial rates, for the hydroxylation of xanthine in the presence of amplex reagent (Fig. 2.3.1) or $Na^+DCIP^-$ (Fig. 2.3.2), were also shown to be in the same orders of magnitude (Table 2.3.2).

*The activities of XOR enzymes:* The activities of XOR enzymes were probed in the presence of amplex assay solution (Table 2.3.3, a and Figures 2.3.5 and 2.3.6 – 2.3.8, *upper panels*). The highest activity, for *bm*XOR, was observed when hypoxanthine was used as a substrate (Fig. 2.3.6, *upper panel*). Similarly, the highest activities, for *Rc*XDH (Fig. 2.3.7, *upper panel*) and *Rc*XDH-$Glu_{232}$Ala mutant (Fig. 2.3.8, *upper panel*) enzymes were observed when 2-hydroxy-6-methylpurine (HMP) was used as a substrate. The activities of *bm*XOR and *Rc*XDH enzymes, in the presence of 6-methylpurine (6MP) and HMP, were in the same order of magnitude. The activities of *Rc*XDH, in the presence of allopurinol, formaldehyde, acetaldehyde, formamide, and formate, were one order of

magnitude lower than the activities of *bm*XOR. The activities, of *Rc*XDH-$Glu_{232}$Ala mutant enzyme, were also shown to be compromised across the board. In the presence of allopurinol, HMP, and 6MP (two orders of magnitude), sever reductions in activities were observed for *Rc*XDH-$Glu_{232}$Ala mutant enzyme. In the presence of formate, there was no activity for *Rc*XDH-$Glu_{232}$Ala although formate was shown to be a slow substrate for the *bm*XOR enzyme (Fig. 2.3.5). In conclusion, the order of activities for *bm*XOR was as follows (from highest to lowest): Hypoxanthine > xanthine > allopurinol > HMP > 6MP > formamide > formaldehyde > acetaldehyde > formate. Similarly, the order of activities for *Rc*XDH was as follows (from highest to lowest): HMP > allopurinol > hypoxanthine > 6MP > xanthine > formaldehyde > acetaldehyde > formamide > formate. Finally, the order of activities for *Rc*XDH-$Glu_{232}$Ala was as follows (from highest to lowest): HMP > hypoxanthine > allopurinol > xanthine > 6MP > acetaldehyde > formaldehyde > formamide.

In addition to the activity of *Oc*Cu/Mo-CODH (Figure 2.3.5, *lower panel*), the activities of XOR enzymes were also probed in the presence of $Na^+DCIP^-$ (Table 2.3.3, b and Figs. 2.3.6 – 2.3.8, *lower panels*). The highest activities, of *bm*XOR (Fig. 2.3.6, *lower panel*), *Rc*XDH (Fig. 2.3.7, *lower panel*), and *Rc*XDH-$Glu_{232}$Ala mutant (Fig. 2.3.8, *lower panel*) enzymes, were observed in the presence of lumazine. The highest activities, of *Rc*XDH enzyme, were recorded when all substrates except allopurinol and lumazine were used as substrates (Table 2.3.3, b). The activities of *bm*XOR and *Rc*XDH-$Glu_{232}$Ala mutant enzymes, in the presence of purine, HMP, and 6MP and xanthine (for *bm*XOR), were shown to be compromised by two orders of magnitude. Similarly, in the presence of hypoxanthine, xanthne, and 6MP, the activities of *Rc*XDH-$Glu_{232}$Ala mutant enzyme were compromised by three orders of magnitude. The activities of *bm*XOR, in the presence of hypoxanthine and lumazine, were one order of magnitude lower than the activities measured for *Rc*XDH enzyme. However, in the presence of allopurinol, there were no activities for *Rc*XDH and *Rc*XDH-$Glu_{232}$Ala enzymes. The activities of *bm*XOR and *Rc*XDH-$Glu_{232}$Ala mutant enzymes, in the presence of formaldehyde and acetaldehyde, were reduced by three and four orders of magnitude (Table 2.3.3, b). The activity of *Rc*XDH-$Glu_{232}$Ala, in the presence of benzaldehyde, was shown to be reduced

by one order of magnitude. However, in the presence of formamide and formate, the activities of *Rc*XDH and *Rc*XDH-$Glu_{232}$Ala enzymes were shown to be compromised. As shown in Table (2.3.3, b), the activities of *Rc*XDH-$Glu_{232}$Ala were severely compromised across the board, by up to four orders of magnitude. In conclusion, the order of the activities for *bm*XOR enzymes were as follows (from highest to lowest): Lumazine > hypoxanthine > benzaldehyde > allopurinol > HMP > urine > 6MP > xanthine > acetaldehyde > formaldehyde > formate > formamide. Similarly, the order of the activities for *Rc*XDH enzymes were as follows (from highest to lowest): Lumazine > acetaldehyde > formaldehyde > HMP > hypoxanthine > purine > xanthine > benzaldehyde > 6MP > butyraldehyde > propionaldehyde. Finally, the order of the activities for *Rc*XDH-$Glu_{232}$Ala enzymes were as follows (from highest to lowest): Lumazine > purine > benzaldehyde > butyraldehyde > HMP > xanthine > hypoxanthine > acetaldehyde > formaldehyde > 6MP > formate. However, the activities of *Rc*XDH (formate, formamide, and allopurinol), *bm*XOR (propionaldehyde and butyraldehyde), and *Rc*XDH-$Glu_{232}$Ala (propionaldehyde, formamide, and allopurinol) were not detected, when the molecules shown in brackets were used as substrates.

*The concentration dependency of the enzyme catalyzed-reactions:* The stead-state kinetic parameters were probed in the presence of $Na^+DCIP^-$, by varying the concentrations of the substrates (Table 2.3.4). As shown in Figure (2.3.9), a Hanes-Woolf method was employed to display the steady-state plots for [Substrate]/$v_o$ against [Substrate] under constant enzyme (*bm*XOR, *Rc*XDH, or *Rc*XDH-$Glu_{232}$Ala mutant) concentrations. Similar plots were also displayed for [Enzyme]/$v_o$ against [Enzyme] under constant substrate, buffer, and $Na^+DCIP^-$ concentrations (Data not shown here). In order to determine the best-fit values, a curve fitting (nonlinear regression) was applied using GraphPad software package. As shown in Figure (2.3.9), the goodness of the fits were shown in the ranges between 0.918 - 0.994. The steady-state kinetic parameters were also evaluated within 95% confidence intervals. The initial rates were shown to vary in the lower range of the substrate concentrations (Fig. 2.3.9 and Table 2.3.4). As the concentration of substrates increased, the initial rates were shown to approach the

saturation level of the substrates. The mole fractions of substrates that were shown to saturate the enzyme, with xanthine providing the highest maximum rate, were also shown to vary from substrates' to substrates' (Figure 2.3.10, *upper panel*). However, in the presence of xanthine, a sever reduction in $v_{max}$ was observed for *Rc*XDH-$Glu_{232}$Ala mutant enzyme. In the case of *Rc*XDH-$Glu_{232}$Ala, the highest $v_{max}$ was observed in the presence of lumazine. The observed $v_{max}$, for *bm*XOR and *Rc*XDH enzymes, were lower than the $v_{max}$ values for *Rc*XDH-$Glu_{232}$Ala (except for $v_{max}$ values determined in the presence of lumazine). The highest $v_{max}$ values, in the presence of lumazine, xanthine, and formaldehyde, were also observed for *bm*XOR enzyme. In the presence of substrates (such as hypoxanthine, allopurinol, acetaldehyde, benzaldehyde, and HMP), the $v_{max}$ values were one order of magnitude higher than the $v_{max}$ values determined in the presence of other substrates. The $v_{max}$ values, for *bm*XOR, were not detected in the presence of formamide, formate, and 6MP, since there were no enough data for convergence. Similarly, in the presence of xanthine and lumazine, *Rc*XDH exhibited the highest $v_{max}$ values. As shown in Table (2.3.4), the $v_{max}$ values for *Rc*XDH were higher than the $v_{max}$ values for *bm*XOR. The enzymes (*bm*XOR, RcXDH, *Rc*XDH-$Glu_{232}$Ala) were shown to exhibit variable $v_{max}$ values depending on the affinity of substrates. In order to verify the affinity of substrates, the $k_m$ values were evaluated as shown in Figure (2.3.10, *middle panel*). Accordingly, the favourable substrate binding for *bm*XOR was shown in the presence of allopurinol and hypoxanthine. When lumazine followed by xanthine and benzaldehyde were used as substrates, the affinity for *Rc*XDH was better than the affinity determined for other enzymes. Although the $k_m$ values vary from substrate to substrate, the preference of the enzymes for specific substrates were better described using the relative ratios between $v_{max}$ and $k_m$ values ($v_{max}/k_m$ values) (Table 2.3.4). The highest relative $v_{max}/k_m$ values were observed for those substrates that exhibited preferences for the respective enzymes. The catalytic constant or a turnover number ($k_{cat}$) for *bm*XOR was higher in the presence of benzaldehyde followed by hypoxanthine and HMP (Table 2.3.3 and Fig. 2.3.10, *lower panel*). The turnover number, for *Rc*XDH, was higher in the presence of purine followed by acetaldehyde. The turnover number for *Rc*XDH-$Glu_{232}$Ala was higher in the presence of hypoxanthine. However, there was a total reduction in the turnover number for *Rc*XDH-$Glu_{232}$Ala mutant enzyme.

The turnover number determined for *Rc*XDH-$Glu_{232}$Ala, in the presence of lumazine, was lower than the turnover numbers determined in the presence of purine derivatives. However, there was a complete reduction in $v_{max}$ values when all substrates (except lumazine) were reacted with *Rc*XDH-$Glu_{232}$Ala mutant enzyme. Although the highest $v_{max}$ value for *bm*XOR was observed in the presence of xanthine, the highest $k_{cat}$ value was observed in the presence of hypoxanthine. On the other hand, the substrate binding for *Rc*XDH-$Glu_{232}$Ala was better in the presence of xanthine followed by lumazine and benzaldehyde. As shown in Table (2.3.4), the specificity of different substrates was also compared using the substrate specificity constant ($k_{cat}/k_m$). The highest $k_{cat}/k_m$ values, for *bm*XOR enzymes, were shown in the presence of hypoxanthine followed by allopurinol (Figure 2.3.10, *upper panel*). The $k_{cat}/k_m$ values, in the presence of purine derivatives (other than hypoxanthine and allopurinol) and benzaldehyde, were better than the $k_{cat}/k_m$ values determined in the presence of aliphatic aldehydes. The $k_{cat}/k_m$ value, for *Rc*XDH in the presence of purine, was higher than the $k_{cat}/k_m$ values observed for *bm*XOR and *Rc*XDH-$Glu_{232}$Ala enzymes. The *Rc*XDH enzyme was shown to have the highest specificity for lumazine followed by xanthine (Fig. 2.3.11, *middle panel*). In the presence of higher aliphatic aldehydes, the *Rc*XDH enzyme was shown to have better specificity than the specificity determined in the presence of acetaldehyde and formaldehyde. Finally, the *Rc*XDH-$Glu_{232}$Ala mutant enzyme was shown to have the highest specificity (three orders of magnitude) in the presence of lumazine (Fig. 2.3.11, *lower panel*). The $k_{cat}/k_m$ values, for *Rc*XDH, were two orders of magnitude higher than the $k_{cat}/k_m$ values for *bm*XOR and *Rc*XDH-$Glu_{232}$Ala enzymes. The variable steady-state kinetic parameters were proposed to be due to the factors that affected the initial (such as the affinity) and final (product release) stages of catalysis. The combined effects of these parameters were expected to affect the oxidative half-reaction as well as the rate of $H_2O_2$, $O_2^{\bullet-}$, or electron production. The observed differences in kinetic parameters, for *bm*XOR and *Rc*XDH enzymes, were shown to confirm the basic differences exhibited by the two enzymes.

The factors that affected the specificity of substrates

The activities and substrate specificities of the enzymes (*bm*XOR, *Rc*XDH, or *Rc*XDH-$Glu_{232}$Ala) were shown to vary even when the (1) same substrate was reacted with all enzymes, (2) native enzymes (*bm*XOR and *Rc*XDH) were reacted with the same substrate, (3) substrates from the same group were reacted with the same enzyme, and (4) same substrate and enzyme were probed using the two assay methods. The variation in activities and substrate specificities were proposed to be due to the factors that might have affected the affinity of the enzymes to the substrates (such as the orientation of substrates in the binding pocket, substrate-binding sites, and mole fractions of reactants) and the product release (the level of reduction and phases of catalysis). The combined effects of these factors are expected to affect the oxidative half-reaction as well as the rates of $H_2O_2$ and $O_2^{\bullet-}$ production and electron transfer.

*Substrate orientation inside the binding pocket:* As shown by purine hydroxylase and XDH enzymes, isolated from *Clostridium purinolyticum* [201], purine was described as the smallest heterocyclic substrate for XOR enzymes as well as an *in vitro* precursor for all purine derivatives. Purine was proposed to have up to three substrate-binding sites ($C_2$-, $C_6$-, and $C_8$-pyrimidine). Amongst the binding sites, as shown by its oxidation product (hypoxanthine), the $C_6$-pyrimidine ($\Delta q_C$ = 0.0055 au.) (Fig. A. 3) is considered to be the favoured binding site. In the presence of purine, the activity of *Rc*XDH was two orders of magnitude higher than the activities of *bm*XOR and *Rc*XDH-$Glu_{232}$Ala (Table 2.3.3, b). On the contrary, the activities of *bm*XOR and *Rc*XDH-$Glu_{232}$Ala were in the same order of magnitude although the activity of *bm*XOR was lower than the activity of *Rc*XDH-$Glu_{232}$Ala. Since the orientation of purine in the binding pocket was expected to be the same for all enzymes (with the $HO_{eq}$ terminal of the active site bound to $C_6$-pyrimidine of purine), the only obvious difference between *Rc*XDH and *Rc*XDH-$Glu_{232}$Ala was the substitution of hydrophilic amino acid ([*Rc*XDH]-$Glu_{232}$) by hydrophobic amino acid ($Ala_{232}$). Consequently, there was no evidence if purine was affected by the hydrogen

bonding network or if its reactivity was influenced by the binding pocket amino acid residues. Therefore, the decrease in activity and change in substrate specificity for XOR enzymes could have been due to the change in conformation. In order to further understand the effect of substrate orientation, the use of purine as a substrate was compared with its oxidation and methylation products, respectively, hypoxanthine and 6-Methylpurine (6MP). When purine was oxidized at its $C_6$-pyrimidine position, its oxidation product (hypoxanthine) was known to bear a carbonyl terminal at the $C_6$-pyrimidine of purine. This orientation was believed to allow the carbonyl at $C_6$-pyrimidine of hypoxanthine to be oriented towards [*bm*XOR]-$Glu_{802}$/[*Rc*XDH]-$Glu_{232}$ and [*Rc*XDH]-$Ala_{232}$ and the imidazole ring towards the substrate access channel and above the $Arg_{880/130}$ residue. The hydrogen bonds formed between the $C_6$-pyrimidine and [*bm*XOR]-$Glu_{802}$/[*Rc*XDH]-$Glu_{232}$ was expected to serve as an anchor, that allowed the $C_2$-pyrimidine ($\Delta q_C$ = 0.1612 au.) of hypoxanthine to be oriented towards the $HO_{eq}$ terminal. Similar to the $C_6$-carbonyl of hypoxanthine, the $CH_3$ at the $C_6$-pyrimidine of 6MP was expected to be oriented towards [*bm*XOR]-$Glu_{802}$/[*Rc*XDH]-$Glu_{232}$ or [*Rc*XDH]-$Ala_{232}$. As described for hypoxanthine, 6MP was presumed to assume similar substrate-binding site through its $C_2$ ($\Delta q_C$ = 0.1494 au.) position. However, the mutation was expected to allow 6MP to lose the most favorable interaction in *bm*XOR/*Rc*XDH enzymes (Table 2.3.3). The third substrate, that assumed similar orientation to that of hypoxanthine and 6MP, was allopurinol ($C_2$-pyrimidine, $\Delta q_C$ = 0.1547 au.). When allopurinol was used as a substrate, the activity for *Rc*XDH was higher than the activities for *bm*XOR and *Rc*XDH-$Glu_{232}$Ala (Table 2.3.3, b). However, the activities for *Rc*XDH and *Rc*XDH-$Glu_{232}$Ala were not detected in the presence of allopurinol. The activities of the enzymes, in the presence of allopurinol and hypoxanthine, were one order of magnitude higher than the activities measured in the presence of 6MP (Table 2.3.3, a). Although this was true for *bm*XOR, the activities for *Rc*XDH in the presence of purine, hypoxanthine, and 6MP, were in the same order of magnitude. However, the activities for *Rc*XDH-$Glu_{232}$Ala, in the presence of allopurinol and hypoxanthine, were one and two orders of magnitudes higher (Table 2.3.3, a). When hypoxanthine was oxidized at its $C_2$-pyrimidine position, its oxidation product (xanthine) was proposed to assume an inverted orientation. The $C_6$- and $C_2$-carbonyls of xanthine were expected to be oriented,

respectively, towards [*bm*XOR]-$Arg_{880}$/[*Rc*XDH]-$Arg_{130}$ and [*bm*XOR]-$Glu_{802}$/[*Rc*XDH]-$Glu_{232}$/[*Rc*XDH]-$Ala_{232}$. In a similar fashion, 6MP could also be oxidized at its $C_2$-pyrimidine position to form 2-hydroxy-6-methylpurine (HMP). Similarly, HMP was proposed to assume similar orientation to that of xanthine with the -$CH_3$ of $C_6$-pyrimidine of HMP oriented towards the [*bm*XOR]-$Arg_{880}$/[*Rc*XDH]-$Arg_{130}$ residue. This orientation was expected to allow HMP to lose the most favorable interaction with [*bm*XOR]-$Arg_{880}$/[*Rc*XDH]-$Arg_{130}$ and gain a favorable interaction with both *Rc*XDH and *Rc*XDH-$Glu_{232}$Ala. On the other hand, if the carbonyl at $C_2$-pyrimidine was able to form a hydrogen bond with [*bm*XOR]-$Glu_{802}$/[*Rc*XDH]-$Glu_{232}$, it was expected to lose the most favourable interaction when [*Rc*XDH]-$Glu_{232}$ was replaced by [*Rc*XDH]-$Ala_{232}$. That means, the $C_2$-carbonyl of xanthine was not expected to form hydrogen bonding with the [*Rc*XDH]-$Ala_{232}$ of the *Rc*XDH-$Glu_{232}$Ala mutant enzyme. Similar to xanthine, the $C_4$-pyrimidine of lumazine (equivalent to $C_6$-pyrimidine of xanthine) was expected to form a hydrogen bond with [*bm*XOR]-$Arg_{880}$/[*Rc*XDH]-$Arg_{130}$. The $C_2$-pyrimidine of lumazine was expected to be oriented towards [*bm*XOR]-$Glu_{802}$/[*Rc*XDH]-$Glu_{232}$ or [*Rc*XDH]-$Ala_{232}$. The activities of the enzymes, in the presence of lumazine, were between one and five orders of magnitude higher than the activities of the enzymes measured in the presence of other molecules. As shown in Table (2.3.3, a), the *Rc*XDH-$Glu_{232}$Ala was not shown to exhibit significance increase in activities in the presence of aldehydes.

*Substrate-binding sites:* In addition to the orientation of the substrates, the substrate-binding sites were also shown to affect the activities of the enzymes. As such, the sites of hydroxylation and oxidation of the heterocyclic molecules were located on the $C_8$-imidazole (HMP and xanthine), $C_2$-pyrimidine (hypoxanthine, allopurinol, and 6MP), $C_6$-pyrimidine (purine), and $C_7$-pyrazine (lumazine). As shown in Figure (A. 3), the substrate-binding sites were shown to bear variable Mulliken atomic charges. The Mulliken atomic charges on the $C_2$-pyrimidine of hypoxanthine/allopurinol/6MP were between 27 and 1.8 times larger than the Mulliken atomic charges on the $C_6$-pyrimidine and $C_2$-pyrimidine of the parent molecule (purine). Although xanthine ($\Delta q_C$ = 0.1330 au.) and HMP ($\Delta q_C$ = 0.1682 au.) interacted with $HO_{eq}$ through their $C_8$-imidazole, the

Mulliken atomic charges on $C_8$-imidazoles' of xanthine and HMP were about 26 times larger than the $C_2$–pyrimidines' of purines' and $C_7$-pyrazine's of lumazine ($\Delta q_C$ = 0.01707 au.). As described above, the substrate-binding sites were expected to affect the activities of the enzymes. Accordingly, the preference of the substrate-binding sites for nucleophilic reaction was predicted as follows (from highest to lowest): The $C_6$-pyrimidine (purine) > $C_2$-pyrimidine (6MP, hypoxanthine, and allopurinol) > $C_8$-imidazole (xanthine, HMP) > ($C_7$-pyrazine (lumazine). However, the Mulliken atomic charges were not consistent with the activities of the enzymes or rates of reactions. This was shown for formamide, that possessed the highest Mulliken atomic charge on its binding site ($\Delta q_C$ = 0.2314 au.). Despite the assumption that the highest positive Mulliken atomic charges were preferred for nucleophilic reaction, formamide was found to be the slowest substrate (Tables 2.3.3). Although the partial charge on the substrate-binding sites was important (to predict the nucleophilic reaction, formation of tetrahedral complex, and formation and dissociation of the transition state), there was no tangible proof for the selectivity of an interaction based on the Mulliken atomic charges.

*Mole fractions of reactants:* The $k_{cat}/k_m$ values, in the presence of hypoxanthine, 6MP, and allopurinol, were higher for *Rc*XDH than the $k_{cat}/k_m$ values for *bm*XOR and *Rc*XDH-$Glu_{232}$Ala enzymes (Fig. 2.3.11). Since the $k_{cat}/k_m$ values for *Rc*XDH-$Glu_{232}$Ala mutant were severely reduced, the reduction was proposed to be due to the mutation as proposed for the hydrophobic contact between the $C_{6\text{-}CH3}$ of 6MP and [*Rc*XDH]-$Ala_{232}$ of the *Rc*XDH-$Glu_{232}$Ala enzyme. In the presence of allopurinol, the $k_{cat}/k_m$ values for *Rc*XDH and *Rc*XDH-$Glu_{232}$Ala were not converged. However, in the presence of HMP, the $k_{cat}/k_m$ values for *Rc*XDH-$Glu_{232}$Ala were not affected. This could have been due to the fact that HMP was not shown to lose the most favorable interaction in *bm*XOR/*Rc*XDH enzymes. In the presence of lumazine and purine, the $k_{cat}/k_m$ values were similar for *bm*XOR and *Rc*XDH enzymes. However, the $k_{cat}/k_m$ value for *Rc*XDH-$Glu_{232}$Ala was two orders of magnitude higher than the $k_{cat}/k_m$ values for *bm*XOR and *Rc*XDH. As shown in Table (2.3.4), the *bm*XOR enzyme was shown to have higher specificity in the presence of hypoxanthine, allopurinol and lumazine. The $k_{cat}/k_m$ values, for RcXDH in

the presence of hypoxanthine, were lower than the $k_{cat}/k_m$ values determined for *bm*XOR. The $k_{cat}/k_m$ values, for *bm*XOR and *Rc*XDH in the presence of xanthine and lumazine, were in the same orders of magnitudes. The $k_{cat}/k_m$ values, for *Rc*XDH-$Glu_{232}$Ala, were shown to be compromised by one order of magnitude (xanthine) and increased by two orders of magnitude (lumazine). Finally, in the presence of aldehydes, formamide, and formate, the $k_{cat}/k_m$ values for all enzymes were also shown in Table (2.3.4). When aldehydes were used as substrates, the $k_{cat}/k_m$ values for *Rc*XDH-$Glu_{232}$Ala were shown to increase and behave as aldehyde oxidase (an enzyme that lacks [XOR]-$Glu_{802/232}$ type amino acid residue).

*Levels of reduction and phases of reaction:* In addition to the factors that affected the affinity of enzymes towards the substrates, the extent of reduction was also shown to affect the rate of $H_2O_2$ or $O_2^{\bullet-}$ production. In ordinary circumstances, the mechanism for the reductive half-reaction of XOR was proposed to involve the transfer of six electrons (Scheme 1.1.2, c) [54, 85]. The full reduction of the enzyme was proposed to follow the sequential order of $0 \rightarrow 2e^- \rightarrow 4e^- \rightarrow 6e^-$ (Scheme (1.2.1, c) [127]. Depending on the catalytic cycle, some substrates were proposed to reduce the enzyme fully ($6e^-$) or partially ($2e^-$ or $4e^-$). As shown in Scheme (1.1.2, c), the re-oxidation of the fully reduced enzymes ($6e^-$) with molecular oxygen was postulated to take place in $6e^- \rightarrow 4e^- \rightarrow 2e^- \rightarrow 1e^- \rightarrow 0$ order [98]. Accordingly, the formation of $H_2O_2$ was limited by the re-oxidation of $6e^-$ or $4e^-$ reduced enzyme (through the divalent steps of $6e^- \rightarrow 4e^-$ or $4e^- \rightarrow 2e^-$ oxidations). On the other hand, the $O_2^{\bullet-}$ production was proposed to occur towards the end of the fast phase and during the preceding slow phase (that included the univalent steps of $2e^- \rightarrow 1e^-$ and $1e^- \rightarrow 0$) [126, 127, 128]. If the substrate was unable to fully reduce the enzyme, the catalytic cycle was expected to occur between $2e^-$ and $4e^-$ levels of reduction. Since the level of reduction and catalytic phases varied as a function of substrates, the level of reduction and catalytic phases were expected to affect the oxidative half-reaction cycle.

The variable activities were proposed to be due to the factors that affected the reductive half-reaction (such as the affinity and product release). Although the enzymes from different sources and preparations were known to exhibit variable substrate specificities, the activities of the enzymes (*bm*XOR, *Rc*XDH, or *Rc*XDH-$Glu_{232}$Ala) were shown to vary even when the (1) same substrate was reacted with the three enzymes, (2) native enzymes (*bm*XOR and *Rc*XDH) were reacted with the same substrate, (3) substrates from the same group were reacted with the same enzyme, and (4) the reaction between the same substrate and enzyme was analyzed using the two assay methods (Amplex/$H_2O_2$ or $DCIP^-/O_2^{\bullet-}$). Although the reduction in activities of *Rc*XDH-$Glu_{232}$Ala was postulated to be due to mutation, there was no evidence whether the reductions observed were due to mutation of $Glu_{232}$Ala or conformational changes. In addition to the reduction in activities, the activities of the *Rc*XDH-$Glu_{232}$Ala enzyme were also shown to increase in the presence of some substrates. However, in the presence of purine, the activities were shown to be compromised and the change in substrate specificity was proposed to be due to conformational change. In the presence of aldehydes, the activities for *Rc*XDH-$Glu_{232}$Ala were expected to increase and behave as AOR (an enzyme that lacks the [*bm*XOR]-$Glu_{802}$/[*Rc*XDH]-$Glu_{232}$ type amino acid residue). However, the activities of the enzymes in the presence of aldehydes were not affected since aldehydes might not require an activation by the binding pocket amino acid residues. In addition, the activities of the enzymes were not affected by mutation, except when lumazine and purine were used as substrates. This indicated that, the site-directed mutagenesis was not discriminatory between purine and aldehyde substrates. Although severe reductions in activities were observed for *Rc*XDH-$Glu_{232}$Ala, in the presence of purine derivatives, there was no increase in activities in the presence of aldehydes [37]. However, the complete loss of activity shown for *bm*XOR in the presence of hypoxanthine was consistent with the data shown previously [37, 39, 50, 51, 52, 53]. As a result, the variation in activity could have been due to the factors that affected the affinity of the enzyme (orientation of substrates in the binding pocket and substrate binding-sites) and the

product release (the level of reduction and phases of catalysis). As described above, the purine derivatives were shown to exhibit different affinities towards the enzymes. This was due to the orientation of the substrates since they had functional groups as a substituent on their pyrimidine rings. Accordingly, four types of purine substrates were identified. The different types of substrates were those substrates that contained -$CH_3$ (6MP), –OH (hypoxanthine, allopurinol), -OH/-OH (xanthine, lumazine), and -$CH_3$/-OH (HMP). Accordingly, the -$CH_3$ group was proposed to create an inductive effect. On the other hand, the -OH was proposed to create an inductive effect and a resonance stabilization. The -$CH_3$ and -OH groups bound to the $C_6$-pyrimidine sites were proposed to allow the substrate to lose the most favorable interaction with the *Rc*XDH-$Glu_{232}$Ala. The replacement of the hydrophilic amino acid ([*bm*XOR]-$Glu_{802}$/[*Rc*XDH]-$Glu_{232}$) residue by a hydrophobic amino acid ([*Rc*XDH]-$Ala_{232}$) was shown to alter the orientation of the substrates (as shown for hypoxanthine and 6MP). The only difference between hypoxanthine and 6MP was the presence of the substituent groups (–$CH_3$ or –OH) on their $C_6$-pyrimidine rings. The activities and rates of reactions revealed that hypoxanthine was by far the most specific substrate for XOR enzymes. On the other hand, the 6MP and HMP (bearing –$CH_3$ bound to the $C_6$-pyrimidine ring) were shown to be less specific substrates for XOR enzymes. Since the rate limiting step was proposed to be the release of product, the product release step for *Rc*XDH was shown to be faster than the *bm*XOR enzyme. As a result, the product release steps were expected to affect the rate of ROS ($H_2O_2$ and $O_2^{\bullet-}$) production. When $O_2^{\bullet-}$ assay method was used, the activities of *bm*XOR were lower than the activities of *Rc*XDH. On the contrary, when $H_2O_2$ assay method was used, the activities of *bm*XOR were higher than the activities of *Rc*XDH (except when HMP was used as a substrate). In the presence of the same substrates and $Na^+DCIP^-$, the activities of *Rc*XDH were higher than the activities of *bm*XOR. The levels of reduction and reaction phases were also shown to affect the product release sequence and the rate of ROS production. When $DCIP^-/O_2^{\bullet-}$ assay method was used, the activities of *Rc*XDH was higher than the activities of *bm*XOR. That means, a large quantity of $O_2^{\bullet-}$ was produced when *Rc*$XDH_{RED}$ was re-oxidized to produce $O_2^{\bullet-}$. This was proposed to be due to the accumulation of the flavin semiquinone [31, 129]. The formation of $O_2^{\bullet-}$ was proposed to take place at higher oxidation states because the reaction of oxygen with

$FADH_2$ was much faster than with $FADH^{\bullet}$. The reaction of molecular oxygen with $FADH^{\bullet}$ was shown to favour the generation of a large quantity of $O_2^{\bullet-}$. In the presence of xanthine, the production of $O_2^{\bullet-}$ was 38% (for *Rc*XDH), 40–44% (chicken liver XDH), and 34% (for rat XDH) [31, 129]. Although the enzymes (*bm*XOR, *Rc*XDH and *Rc*XDH-$Glu_{232}$Ala) were shown to have similar substrate preferences, the rates of $O_2^{\bullet-}$ production were much better when *Rc*XDH was reacted with various substrates (Table 2.3.3, b). However, the activities of the enzymes in the presence of the same substrate were shown to be different from each other. As a result, the extent of $v_{max}$ was shown to depend on the type of the substrates and the binding pocket of the active site of the enzymes. The affinity of the substrates, towards the enzymes, was also shown to depend on the concentration of the substrates. When the concentrations of the substrates were much larger than the $k_m$ values, the $v_{max}$ values were shown to depend on the active sites of the free enzymes available for interaction and the rate limiting for the product release. The substrates, that were shown to give the enzymes the lowest activities, were shown to give the lowest turnover numbers. The slow substrates, unlike the fast substrates, were unable to give higher turnover numbers since their re-oxidation might have taken place during the slower phase. Therefore, the difference in turnover number between the enzymes was proposed to reflect the difference in the catalytic activities of the two enzymes (*bm*XOR and *Rc*XDH). The enzymes were shown to achieve maximum catalytic efficiency as shown by the smaller $k_m$ values. The substrates, with high $k_m$ values, were also shown to exhibit an unstable Michaelis-Menten type complex. Therefore, the substrates with the highest $k_{cat}$ values were those that exhibited less stable catalytic transformation from $E_{OX}$-$C_{RH}$ complex to $E_{RED}$-product intermediate or $E_{RED}$ and product. This was consistent with the fact that the conversion of the $E_{OX}$-$C_{RH}$ complex to $E_{RED}$-product intermediate required faster dissociation. Therefore, the kinetic parameters were influenced by several factors (such as the active site binding pocket, types of substrates, orientation of substrates in the active site binding pocket, binding-sites of substrates, formation of $E_{RED}$-product intermediates, and product release). The variations in the rates of $H_2O_2$ or $O_2^{\bullet-}$ production were also proposed to affect the levels of reduction and the stages where the re-oxidation began and ended.

# Chapter 3.0

## The substrate-enzyme binding cofactor reduction for XO family enzymes

### 3.1 Introduction

During the catalytic transformation (eqs. 2.1.1 - 2.1.3), the XOR enzymes are known to exhibit similar spectral behaviours characterized by a decrease in absorbance (in the short wavelength region, centered at 450 and 550 nm) [59, 81, 83, 85, 130]. The spectral changes are attributed to the partial reductions of the cofactors (such as Moco, $[Fe_2S_2](S^{\gamma}_{Cys})_4$, and FAD) (Fig. 1.1.5) [6, 8, 11, 24, 25, 31, 32, 64, 82, 94, 98, 106, 118]. However, the overlap of the strong absorption bands (associated with $[Fe_2S_2](S^{\gamma}_{Cys})_4$ and FAD cofactors) are known to hinder the detection of the spectral changes that may have been contributed by the Moco sites. Unlike the spectral changes observed in the short wavelength region, a unique spectral behavior (in the long wavelength region, centered at 650 nm) is reported due to the formation of a product bound intermediate ($E_{RED}$-product) [58, 80, 85, 130, 131, 132, 133]. In 1982 and 1984, Davis and co-workers [58, 130] reported the generation of a spectral bands (in the long wavelength region) using two different experimental approaches (dynamic and static). The dynamic experimental approach requires a direct interaction between the substrate (such as lumazine) and oxidized enzyme ($E_{OX}$) (Scheme 3.1.1, *upper panel*) [50]. Mechanistically, the dynamic experimental approach is similar to the catalytic transformation shown in equation (2.1.1). The dynamic experimental approach requires the participation of FAD and $[Fe_2S_2](S^{\gamma}_{Cys})_4$ cofactors, as described by the classic ping-pong mechanism designated by W. W. Cleland (1963 and 1970) [60, 61] [cited by M. P. Coughlan (1980) [24, 91]]. On the other hand, the static experimental approach requires the interaction between the reduced enzyme ($E_{RED}$) and product (such as violapterin), with or without the participation of FAD and $[Fe_2S_2](S^{\gamma}_{Cys})_4$ cofactors (Scheme 3.1.1, *lower panel*). In the static experimental approach, violapterin is allowed to interact with $E_{RED}$ (or $E'_{RED}$) in a similar way the physiological oxidizing substrates ($O_2$ and $NAD^+$) interact

with $E_{RED}$ (eqs. 2.1.2 and 2.1.3). The physiological oxidizing substrates and violapterin differ from each other, in the way they interact with the $E_{RED}$. The physiological oxidizing substrates interact with $E_{RED}$ at the flavin site. On the other hand, violapterin is

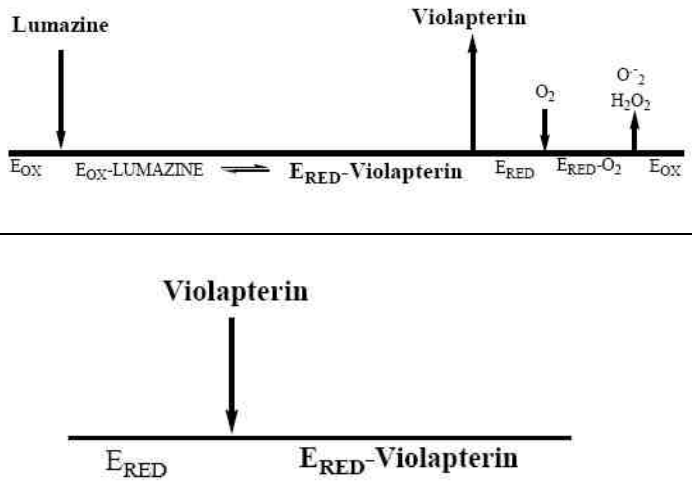


Scheme 3.1.1. A schematic representation of the dynamic (*upper panel*) and static (*lower panel*) experimental approaches. The lumazine and violapterin (an oxidation product of lumazine) are used as substrates.

proposed to interact with $E_{RED}$ (or $E'_{RED}$) at the Moco site. In contrast to the physiological oxidizing substrates, the formation of $E_{RED}$-violapterin intermediate may not require the participation of the FAD and $[Fe_2S_2](S^{\gamma}_{Cys})_4$ cofactors. However, the FAD and $[Fe_2S_2](S^{\gamma}_{Cys})_4$ cofactors may initially serve as electron sinks to assist the formation of $E_{RED}$-violapterin intermediate. Although the two approaches exhibit kinetic and mechanistic differences, they are capable of producing identical spectral bands (centered at 650 nm). However, the mechanistic and kinetic implication of the two fundamentally different experimental approaches is neither explored nor well understood.

Mechanistically, the two approaches may undergo similar transformation after the formation of $E_{RED}$-violapterin intermediate (dynamic) or the interaction between $E_{RED}$ and violapterin (static) takes place. Although the currently accepted spectral band giving species is the (Enzyme)-[$Mo^{(IV)}$-$O_{violapterin}$] intermediate, it is not well understood if there are other species (such as (Enzyme)-[$Mo^{(V)}$-$O_{violapterin}$] or (Enzyme)-[$Mo^{(VI)}$-$O_{violapterin}$]) that may possibly contribute to the spectral band (centered at 650 nm). However, the spectral band giving species are proposed to originate due to the interaction between the ($E_{RED}$)-$Mo^{(IV)}$ center and violapterin. The spectral band attributed to the $E_{RED}$-violapterin intermediate has been tentatively assigned, by Davis and co-workers (1982) [130], to a metal-to-ligand-charge-transfer (MLCT) transition (more precisely, to a molybdenum-to-violapterin-charge-transfer transition) [58, 85]. Although this type of spectral band assignment is supported by previous works [58, 85, 130] and the enzymatic spectroscopic and theoretical findings [134], the detail of the spectral band assignment and description of the spectral giving species is not yet well understood. The characterization of the charge transfer transition band as MLCT transition is consistent with the spectral band giving species generated using the two experimental approaches. Since the interaction between $E_{OX}$ and lumazine leads to the formation of $E_{RED}$-violapterin intermediate [58, 85, 130] and MLCT transition, a similar situation is expected for the $E_{RED}$-product catalytic intermediates formed by other substrates (Fig. A. 2) or their respective products. Despite this proposal, the $E_{RED}$-product intermediates (such as $E_{RED}$-alloxanthine [52, 53, 81, 83], $E_{RED}$-uric acid [59, 81], $E_{RED}$-carboxylates, $E_{RED}$-carbamate, $E_{RED}$-formate, or $E_{RED}$-$CO_2$) are not expected to exhibit similar spectral bands (centered at 650 nm). As a result, the spectral band (centered at 650 nm) is proposed to be a unique signature of $E_{RED}$-violapterin intermediate [58, 130]. If (Enzyme)-[$Mo^{(IV)}$-$O_{violapterin}$] is the structure that gives a spectral band at 650 nm, the inhibitory (Enzyme)-[$Mo^{(IV)}$-$N_{alloxanthine}$] is expected to behave the same as (Enzyme)-[$Mo^{(IV)}$-$O_{violapterin}$]. If the inhibited and spectral band giving species are the type of $E_{RED}$-product intermediates, it is important to identify the nature of the $E_{RED}$-violapterin intermediate that is not inhibitory. Although there is no reported data implicating aldehydes, formamide, and formate to form an intense charge transfer bands, it is important to identify whether their intermediates form a highly covalent bonding interaction. Therefore, it is of a mechanistic importance to explore if the reducing

substrates (other than lumazine) produce a highly covalent bonding interaction and a spectral change similar to the one shown for (Enzyme)-[$Mo^{(IV)}$-$O_{violapterin}$]. The reactions, between $E_{OX}$ and substrates or $E_{RED}$ and products, are expected to depend on the electrostatic forces and acid/base chemistry of the active sites and substrates (or their oxidation products). Therefore, the effect of the electrostatic forces and acid-base (pKa) properties on the (Enzyme)-Mo center and substrates is expected to provide a driving force for the catalytic reaction. Since the initial stage of XOR mechanism is proposed to take place through a base-assisted nucleophilic reaction (Scheme 1.1.3) [18, 39], the pH of the media is expected to affect the acid-base (pKa) properties and conformation of the active site and substrate [59, 84, 119, 122 (b), 124, 131, 135, 136].

In order to understand the spectral changes associated with the transformation of lumazine to violapterin, a combination of enzymatic spectroscopic and electronic structure calculation studies are proposed. The research is designed to closely examine the spectral changes associated with the $E_{RED}$-product catalytic intermediates. In the enzymatic spectroscopic studies, the dynamic and static experimental approaches are used to generate spectral band giving species. In the dynamic experimental approach, the substrates (or lumazine) are reacted with $E_{OX}$ (*bm*$XOR_{OX}$, *Rc*$XDH_{OX}$, or *Rc*$XDH_{OX}$-$Glu_{232}$Ala mutant) (Scheme 3.1.1, *upper panel*). In the static experimental approach, the products (or violapterin) are reacted with $E_{RED}$ (*bm*$XOR_{RED}$, *Rc*$XDH_{RED}$, or *Rc*$XDH_{RED}$-$Glu_{232}$Ala mutant) (Scheme 3.1.1, *lower panel*). The spectral band giving species are generated in the absence and presence of artificial electron acceptors such as $Na^{+}DCIP^{-}$. The dynamic approach is also used to probe the substrate-enzyme binding cofactor reductions, as well as the pH profiles of the enzymes. Upon completion of this work, the unique nature of the interaction between $E_{OX}$ and lumazine or $E_{RED}$ and violapterin is expected to give insight in to the behavior of the substrate-enzyme binding cofactor reductions. It is also expected to give a clue why the reducing substrates and their respective products behave differently. The effect of pH on the conformation of the active site and substrates is also expected to be correlated with the electron structure description and reaction mechanism. Finally, this work is expected to provide a valuable tool for characterizing the reactions of the XO family enzymes with reducing substrates.

## 3.2 Materials and methods

### Materials

*Enzymes and reagents:* The enzymes used were *bm*XOR (Fig. A. 1, *upper left panel*), commercial *bm*XOR (Sigma-Aldrich, St. Louis, MO), bacterial *Rc*XDH (Fig. A. 1, *upper right panel*), *Rc*XDH $Glu_{232}Ala$ mutant (Fig. A. 1, *lower left panel*), and *O*cCu/Mo-CODH (Fig. A. 1, *lower right panel*). *The artificial electron acceptor* used was sodium 2, 6-dichlorophenolindophenol ($Na^+DCIP^-$) (Sigma-Aldrich, St. Louis, MO). *The buffer solutions* were 4-(2-hydroxyethyl)piperazine-1-ethanesulfonic acid (HEPES) (EMD chemicals, Inc., Gibbstown, NJ), sodium pyrophosphate tetra basic decahydrate ($Na_4P_2O_7 \cdot 10H_2O$) (Sigma-Aldrich, St. Louis, MO). *The buffers for the pH profile experiments* were potassium phosphate dibasic ($K_2HPO_4$) and potassium phosphate monobasic ($KH_2PO_4$) (J. T. Baker, Inc., Phillipsburg NJ) (for pH values 2.0, 3.0 4.0, 5.0, 6.0, and 7.0), N,N-bis(2-hydroxyethyl)glycine (BICINE) (for pH values 8.0 and 9.0), and 3-(cyclohexylamino)-1-propanesulfonic acid (CAPS) (Sigma-Aldrich, St. Louis, MO) (for pH values 10.0 and 11.0). *The anaerobic reaction media* was prepared using $N_2$ (99.5%, vol/vol) (Speciality Chemical Products, Inc., South Houston, TX). *The molecules used as reactants* were *purines* [purine (Acros Organics, Fair Lawn, NJ), hypoxanthine, xanthine, uric acid sodium salt, allopurinol, 6-methylpurine, and 2-hydroxy-6-methylpurine (HMP) (Sigma-Aldrich, St. Louis, MO)], a*ldehydes* [formaldehyde, acetaldehyde, propionaldehyde, butyraldehyde, trifluoroacetaldehyde, DL-glyceraldehydes, benzaldehyde, and *p*-dimethylaminocinnamaldehyde (Sigma-Aldrich, St. Louis, MO), and glycolaldehyde (MP Biomedicals LLC., Solon, OH)], and *other molecules* [sodium formate and sodium acetate (EMD chemicals, Inc., Gibbstown, NJ), 4-nitrophenylformate and 4-nitroacetanilide (Alfa Aesar, Ward Hill, MA), and 4-nitrophenylacetate, 4-nitrophenylformamide, formamide, methylformamide, dimethylformamide, dimethylthioformamide, and trifluoroacetamide (Aldrich chemical company, Inc., Milwaukee, WI), methanol, ethanol, butanol (Sigma-Aldrich, St. Louis, MO), propanol, ethylene glycol, thiourea, and sodium nitrate (J. T. Baker, Inc.,

Phillipsburg NJ), sodium cyanide, sodium thiocyanate, N-butylisocyanide, sodium nitrite, sodium azide, urea, and lumazine (2,4-(1*H*,3*H*)-pteridinedione) (Sigma-Fluka, St. Louis, MO)]. CO (99.5%, vol/vol) (Speciality Chemical Products, Inc., South Houston, TX) was used for the *Oc*Cu/Mo-CODH binding cofactor reduction. Sodium dithionite ($NaO_2SSO_2Na$) (Sigma-Fluka/Sigma-Aldrich, St. Louis, MO) was also used to reduce the XO family enzymes.

*Instruments and program software packages:* All routine enzyme assays and UV-visible absorption spectra were performed on a Hitachi model U-3501 recording spectrophotometer (Hitachi Ltd., Tokyo, Japan) using 100 μL, 10 mm light path sub-micro Quartz spectrophotometer cell (Starna Cells, Inc., Atascadero, CA) and 1.5 mL spectrophotometer cell light path 10 mm (VWR Scientific, Medis, PA). The steady-state kinetic parameters were analyzed using GraphPad software package (GraphPad Software Inc., La Jolla, CA) by applying curve fitting (non-linear regression) to determine the best-fit values. Peak fitting and gaussian resolutions were performed using Grams/AI, version 7.02 software package (Thermo Galactic, Waltham, MA). All computation calculations were performed using Gaussian®03W (version 6.0) program software package (Gaussian, Inc., Wallingford, CT). Molecular orbital and electronic structure visualization were performed using software programs such as Molden (CAOS/CAMM center Nijmegen, Toernooiveld, Nijmegen, The Netherlands) and GaussView 3.0 (Gaussian, Inc., Pittsburgh, PA). Molecular orbital analyses for the constituent chemical fragments were performed using AOMix 2008/2009 version (revision 6.40) software package (Center for catalysis research and innovation, University of Ottawa, Ottawa, ON, Canada) [137].

## Methods

### The substrate-enzyme binding cofactor reduction for XO family enzymes

The anaerobic reduction of XO family enzymes were performed using the dynamic experimental approach at 22°C. *For XOR enzymes*, the reaction mixtures containing enzymes (40 μU/mL *bm*XOR, 95 μM *bm*$XOR_{OX}$, 26 μM *Rc*$XDH_{OX}$, or 90 μM *Rc*$XDH_{OX}$-Glu232Ala mutant, in 50 mM pyrophosphate buffer, pH 8.2) were made anaerobic by bubbling $N_2$ gas for 15 minutes. The bleaching of the enzymes was initiated by adding 8.0 mM sodium dithionite or substrates (0.20 M formaldehyde, 0.20 M formamide, 0.50 M acetaldehyde, 0.1 mM allopurinol, 0.128 M 6-methylpurine, 5 mM 2-hydroxy-6-methylpurine, 0.108 mM xanthine, 2.05 mM hypoxanthine, 0.20 M sodium formate, 2 mM purine, or 1.3 mM lumazine). *For OcCu/Mo-CODH enzyme*, the reaction mixture containing 1.9 nM *Oc*Cu/Mo-CODH and 50 mM HEPES buffer (pH 8.2) was made anaerobic by bubbling $N_2$ gas for 15 minutes. The reaction was initiated by injecting 1.0 mL of CO gas. Similar reaction was also performed by replacing CO gas with a buffer saturated with CO gas.

### The interaction of substrates or products with either *bm*$XOR_{OX}$ or *bm*$XOR_{RED}$

The interaction between substrates and enzymes were performed under aerobic conditions, at 22°C. The reaction mixtures containing blanks, standards, and reaction mixtures were incubated for 15 minutes. *For the blank solutions*, spectrophotometric scans were taken before substrates were added to the standard and reaction mixtures. A second scan was also taken after the reactions for the standard and reaction mixtures were completed. *For the standard and reaction mixtures*, spectrophotometric scans were taken before the addition of substrates and after the reactions were completed. *For OcCu/Mo-CODH enzyme, the blank solutions* were prepared from 0.35 mL water, 0.7 mL of 0.065 mM $Na^+DCIP^-$ in 20 mM HEPES buffer (pH 8.2), and 0.05 mL μM *Oc*Cu/Mo-CODH. *The standard* reaction mixtures were prepared from 0.30 mL water, 0.05 mL μM

*Oc*Cu/Mo-CODH, and 0.7 mL of 0.065 mM $Na^+DCIP^-$ in 20 mM HEPES buffer (pH 8.2). *Reaction mixtures* were prepared from 0.30 mL small molecules, 0.05 mL μM *Oc*Cu/Mo-CODH, and 0.7 mL of 0.065 mM $Na^+DCIP^-$ in 20 mM HEPES buffer (pH 8.2). The reactions for standards and reaction mixtures were initiated by injecting 2.5 mL CO. *For bmXOR enzymes*, the blank solutions were prepared from 0.35 mL water and 0.7 mL of 0.024 mM $Na^+DCIP^-$ in 50 mM tris buffer (pH 7.5). *The standard reaction mixtures* were prepared from 0.15 mL water, 0.05 mL of 1.00 nM *bm*XOR, 0.15 mL of substrates, and 0.7 mL of 0.065 mM $Na^+DCIP^-$ in 50 mM tris buffer (pH 7.5). *Reaction mixtures* were prepared from 0.15 mL small molecules, 0.05 mL XOR (1.00 nM *bm*XOR), 0.15 mL of substrates, and 0.7 mL of 0.024 mM $Na^+DCIP^-$ in 50 mM tris buffer (pH 7.5). The reactions for standards and reaction mixtures were initiated by adding 0.15 mL of substrates (0.50 M acetaldehyde, 0.1 mM allopurinol, 0.108 mM xanthine, or 2.05 mM hypoxanthine).

The pH dependency of the enzyme catalyzed-reaction

The pH profile experiments were carried out, under aerobic conditions, at 22°C. The concentrations of the enzyme and $Na^+DCIP^-$ were kept constant for the respective buffers (pH = 2.0 3.0 4.0, 5.0, 6.0, 7.0, 8.0, 9.0, 10.0, or 11.0). After the addition of variable concentrations of the substrates, the spectrophotometric scans were taken every 0.1 - 4.0 minutes of intervals. *For OcCu/Mo-CODH enzyme*, the reaction mixtures were prepared by mixing 0.95 mL of 0.078 mM $Na^+DCIP^-$ and 0.05 mL of 1.24 μM Cu/Mo-CODH in respective buffers. The reactions were initiated by injecting 1.0 mL CO gas. *For bmXOR enzyme*, the reaction mixtures were prepared by mixing 0.75 mL of 0.078 mM $Na^+DCIP^-$, 0.05 mL of respective enzymes (1.70 μM *bm*XOR, 1.09 μM *Rc*XDH, and 1.24 μM *Rc*XDH $Glu_{232}Ala$) in respective buffers. The reactions were initiated by adding 0.25 mL substrates (0.20 M formaldehyde, 0.20 M formamide, 0.50 M acetaldehyde, 0.1 mM allopurinol, 0.128 M 6-methylpurine, 5 mM 2-hydroxy-6-methylpurine, 0.108 mM xanthine, 2.05 mM hypoxanthine, 0.20 M sodium formate, 2 mM purine, 1.3 mM lumazine, 0.20 M propionaldehyde, 0.20 M butyraldehyde, or 1.5 mM benzaldehyde).

## The generation of $XOR_{RED}$-product intermediates

The $XOR_{RED}$-product intermediates were prepared, in the presence and absence of $Na^+DCIP^-$, under turnover (dynamic) (Scheme 3.1.1, *upper panel*) and static (Scheme 3.1.1, *lower panel*) conditions. *For the dynamic experiments*, the reactions were initiated by adding substrates (5.3 mM lumazine, 0.20 M formaldehyde, 0.20 M formamide, 0.50 M acetaldehyde, 0.1 mM allopurinol, 0.128 M 6-methylpurine, 5 mM 2-hydroxy-6-methylpurine, 0.108 mM xanthine, 2.05 mM hypoxanthine, 0.20 M sodium formate, or 2 mM purine) to the reaction mixtures containing enzymes (95 μM *bm*$XOR_{OX}$, 26 μM *Rc*$XDH_{OX}$, or 17 μM *Rc*$XDH_{OX}$-Glu232Ala) in 50 mM sodium pyrophosphate-HCl buffer, pH 8.3). *The controls* for the reduced enzymes were prepared, under anaerobic condition, by incubating the enzymes (95 μM *bm*$XOR_{OX}$, 26 μM *Rc*$XDH_{OX}$, or 17 μM *Rc*$XDH_{OX}$-Glu232Ala, in 50 mM sodium pyrophosphate-HCl buffer, pH 8.3) with 8 mM sodium dithionite. *The dynamic experiments, in the ab*sence of $Na^+DCIP^-$, were performed under aerobic conditions. The reactions were initiated by adding respective substrates to the reaction mixtures, containing respective enzymes. The turnover was established through the decrease in absorbance at 450 and 550 nm and increase in absorbance at 650 nm. *The dynamic experiments, in the presence of $Na^+DCIP^-$*, were performed under aerobic condition. The reaction mixtures were carried out by adding 5.3 mM lumazine to the reaction mixtures, containing enzymes and 0.45 mM $Na^+DCIP^-$. The experiments were also repeated at different pH values. *The static experiments, in the absence of artificial electron acceptors,* were performed under aerobic and anaerobic conditions. Initially, aerobic titrations were carried out by adding respective substrates to the reaction mixtures, containing respective enzymes. After the complete conversion of substrates to products, the reaction mixtures were made anaerobic by bubbling nitrogen gas for 15 minutes, at 4°C. The anaerobic reaction mixtures were titrated with 8 mM sodium dithionite, under anaerobic condition. All experiments were performed, at 22°C, by monitoring the change in absorption spectra (in the region between 200 – 800). The formation of $XOR_{RED}$-product intermediates were established through the appearance of a broad absorption bands, between 500 – 700 nm (centered at 650 nm).

Electronic structure calculations for $Mo^{(IV)}$-product intermediates

The electronic structure calculations were performed to generate Mulliken atomic charges, total electronic energies, wave-function descriptions, bonding descriptions, and oscillator strengths. The parameters were generated from the geometry optimization, time dependent density functional theory (TDDFT), and single point energy calculations [138 (c, d, j, k)]. The electronic structure calculations were performed using density functional theory (DFT) method using the Gaussian® 03W version 6.0 program software package [138 (a)]. The DFT method employing the B3LYP level of theory [138 (a, e)] was applied on the model structures derived from the initial geometries of the crystal structures of *bm*XOR [10, 14]. The calculations were performed, on the truncated analogues shown in Figure (3.2.1, b), by replacing the Mo bound water terminal with the oxidation products, such as violapterin (Fig. 3.2.2, *upper panel*). Similar calculations were also performed by replacing violapterin with other products (such as uric acid, alloxanthine, formate, and $CO_2$) (Fig. 3.2.2, *lower panel*). The 6-31G(d',p') basis set with a polarization function was used for the non-metal atoms (C, H, O, N, and S). The LANL2DZ basis set and LANL2 effective core potentials were used for molybdenum.

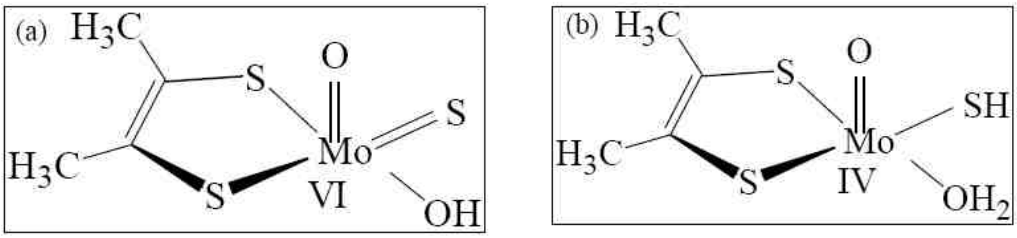


Figure 3.2.1. The truncated analogues of the structure shown in Figure (1.1.2 (a)) for the reductive half-reaction active sites of the (a) oxidized ($bm\text{XOR}_{OX}$) [10] and (b) reduced ($bm\text{XOR}_{RED}$)[1] forms.

The structures (Fig. 3.2.1) were initially optimized at $Mo^{(VI)}$ and $Mo^{(IV)}$ oxidation states using *"# b3lyp gen pseudo=read #p gfinput iop(6/7=3) opt pop=full gfprint"* theoretical model and job type [130 (j)]. The final optimized geometries were used as input files for the time dependent density functional theory (TDDFT) and single point energy calculations. The TDDFT calculations were performed using *"# td=(nstates="20) b3lyp gen pseudo=read #p gfinput iop(6/7=3)pop=full gfprint"* theoretical model and job type [138]. The single point energy calculations were performed using *"# b3lyp #p gen pseudo=read gfinput pop=full iop(3/33=1) gfprint"* theoretical model and job type [138 (h, k)].

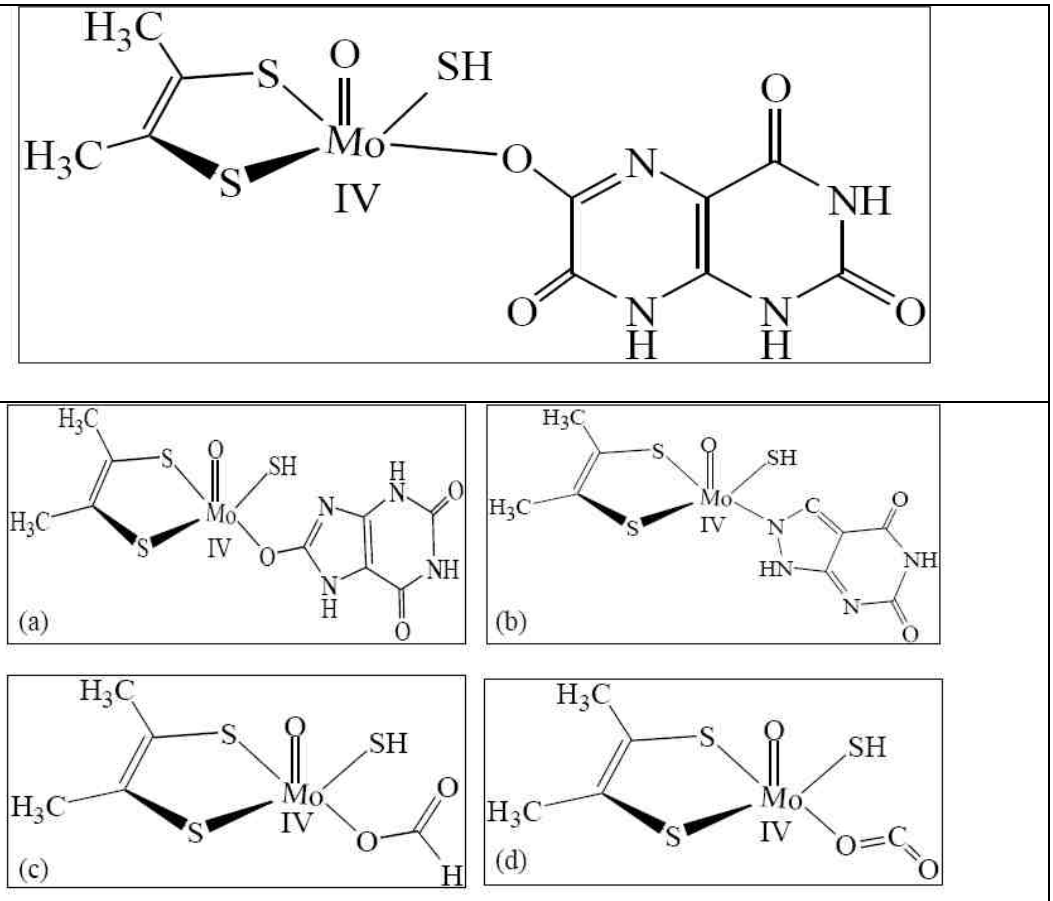


Figure 3.2.2. The geometries of the truncated Moco bound to violapterin (*upper panel*) and other products (*lower panel*): (a) uric acid, (b) alloxanthine, (c) formate, and (d) $CO_2$.

The output files from the single point energy calculations were used as input files for the AOMix analysis [137]. Molecular orbital analyses, for the constituent chemical fragments, were calculated using AOMix software package [137]. The intensity of the MLCT transition was probed by determining the energy difference between Mo($d_{xy}$) LUMO and product HOMO. The electronic transitions, for the Mo charge transfer (CT), were characterized using the contribution of individual atomic orbitals to the molecular orbital [122 (a), 139]. The Mo CT character was probed using the excitation from $HOMO_{-x}$ to $LUMO_{+y}$ using equation (3.2.1) [137, 139].

$$CT(Mo) = \%(Mo)_{HOMO-X} - \%(Mo)_{LUMO+Y} \qquad (3.2.1)$$

Gaussian resolution of the spectral bands and extinction coefficient calculation

The Gaussian resolved spectra were developed from the difference spectrum of reduced *bm*$XOR_{RED}$-violapterin intermediate *minus bm*$XOR_{RED}$. The change in maximum molar extinction coefficient ($\Delta\varepsilon_{max}$) was estimated, at 650 nm, by comparing with the $\Delta\varepsilon_{max}$ at 450 nm. The theoretical $\Delta\varepsilon_{max}$ was calculated using equation (3.2.2), where ($\Delta\nu_{1/2}$) and $f$, respectively, represent the experimental width of the peak at half height and the oscillator strength values, obtained from TDDFT calculation [122 (a), 139].

$$f = 4.6\times10^{-9}\int \Delta\varepsilon_{\max}\Delta\nu_{1/2} \qquad (3.2.2)$$

## 3.3 Results

### The substrate-enzyme binding cofactor reduction for XO family enzymes

Table 3.3.1. The initial rates for the substrate-enzyme binding cofactor spectral changes. The initial rates were calculated from Figures (A. 4 – A. 6). ND represents the non-convergence of the data.

| Substrates ($C_{RH}$) | Initial Rates ($s^{-1}$) | | | Ratio ($SD/C_{RH}$) | |
|---|---|---|---|---|---|
| | 450 nm | 550 nm | 650 nm | 450 nm | 550 nm |
| (1) *Oc*Cu/Mo-CODH enzyme | | | | | |
| Sodium Dithionite (SD) | 3.79E-03 | 1.36E-03 | ND | 1.00 | 1.00 |
| Carbon Monoxide (CO) | 1.45E-04 | 1.55E-04 | ND | 26.14 | 8.79 |
| (2) *bm*XOR enzyme | | | | | |
| Sodium Dithionite | 2.16E-02 | 1.19E-02 | ND | 1.00 | 1.00 |
| Purine (PU) | 1.37E-03 | 3.37E-04 | ND | 15.81 | 35.44 |
| Hypoxanthine (HY) | 1.52E-03 | 5.54E-04 | ND | 14.29 | 21.54 |
| Xanthine (XA) | 1.26E-03 | 1.98E-04 | ND | 17.19 | 60.45 |
| HMP | 2.11E-05 | 2.62E-05 | ND | 1023.75 | 454.78 |
| Allopurinol (AL) | 8.22E-04 | 1.59E-04 | ND | 26.34 | 75.30 |
| Lumazine (LU) | 6.93E-05 | 2.16E-05 | 5.92E-04 | 312.51 | 553.65 |
| (3) *Rc*XDH enzyme | | | | | |
| Purine (PU) | 3.12E-04 | 1.11E-04 | ND | 69.41 | 107.71 |
| Hypoxanthine (HY) | 2.80E-04 | 6.78E-05 | ND | 77.31 | 176.04 |
| Xanthine (XA) | 4.67E-04 | 2.32E-04 | ND | 46.34 | 51.42 |
| HMP | 1.87E-04 | 6.55E-05 | ND | 115.78 | 182.20 |
| Allopurinol (AL) | 2.99E-05 | 8.13E-06 | ND | 724.11 | 1469.29 |
| Lumazine (LU) | 1.66E-04 | 2.93E-05 | ND | 130.30 | 407.85 |
| Formaldehyde (FA) | 2.67E-05 | 8.02E-06 | ND | 811.80 | 1488.37 |

Table 3.3.2. The relative spectral changes (%) calculated from Table (3.3.1).

| | Native enzyme | | | Substrate activated enzyme | | |
|---|---|---|---|---|---|---|
| | 450 nm | 550 nm | 650 nm | 450 nm | 550 nm | 650 nm |
| (1) *Oc*Cu/Mo-CODH enzyme | | | | | | |
| Sodium dithionite | 0.705 | 0.639 | ND | | | |
| CO | 0.124 | 0.093 | ND | | | |
| (2) *bm*XOR enzyme | | | | | | |
| Purine | 0.208 | 0.145 | ND | 0.357 | 0.198 | ND |
| Hypoxanthine | 0.461 | 0.316 | ND | 0.121 | 0.131 | ND |
| Xanthine | 0.262 | 0.139 | ND | 0.012 | 0.006 | ND |
| HMP | 0.168 | -0.044 | ND | 0.251 | 0.126 | ND |
| Allopurinol | 0.214 | 0.106 | ND | 0.099 | 0.055 | ND |
| Lumazine | 0.137 | 0.062 | -0.217 | 0.039 | 0.200 | 0.472 |
| (3) *Rc*XDH enzyme | | | | | | |
| Purine | 0.237 | 0.180 | ND | 0.034 | 0.006 | ND |
| Hypoxanthine | 0.242 | 0.159 | ND | 0.039 | 0.024 | ND |
| Xanthine | 0.386 | 0.440 | ND | 0.050 | 0.061 | ND |
| HMP | 0.150 | 0.089 | ND | 0.032 | 0.039 | ND |
| Lumazine | 0.098 | 0.037 | ND | 0.057 | 0.003 | ND |
| Formaldehyde | 0.243 | 0.255 | ND | 0.032 | 0.021 | ND |

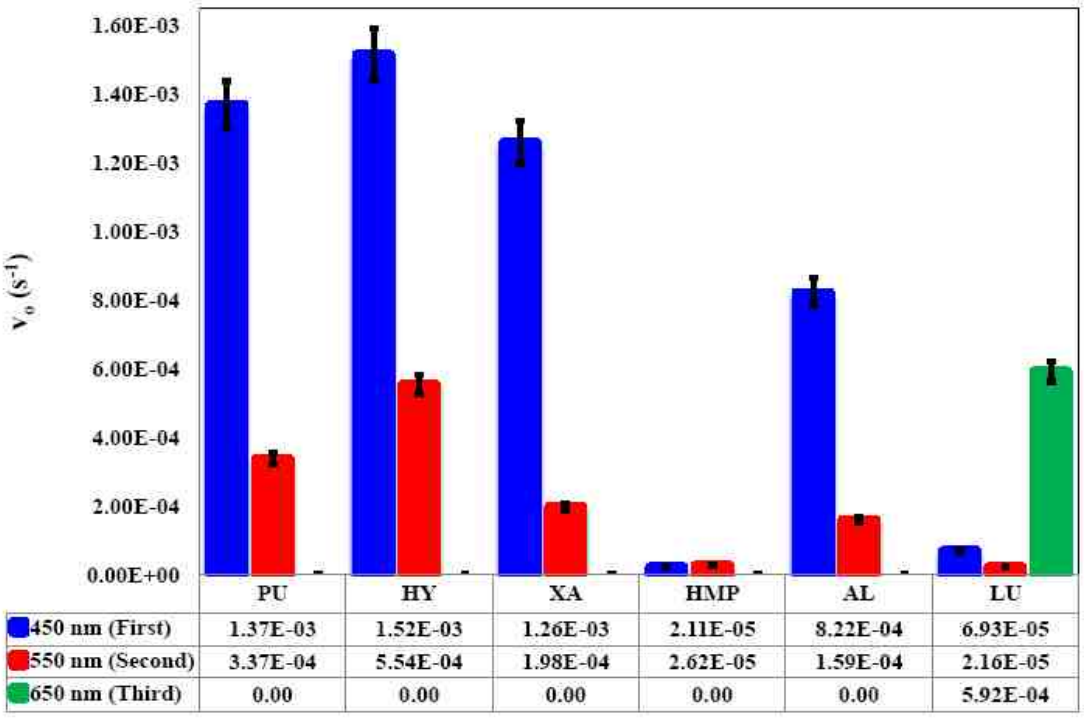


| | PU | HY | XA | HMP | AL | LU |
|---|---|---|---|---|---|---|
| 450 nm (First) | 1.37E-03 | 1.52E-03 | 1.26E-03 | 2.11E-05 | 8.22E-04 | 6.93E-05 |
| 550 nm (Second) | 3.37E-04 | 5.54E-04 | 1.98E-04 | 2.62E-05 | 1.59E-04 | 2.16E-05 |
| 650 nm (Third) | 0.00 | 0.00 | 0.00 | 0.00 | 0.00 | 5.92E-04 |

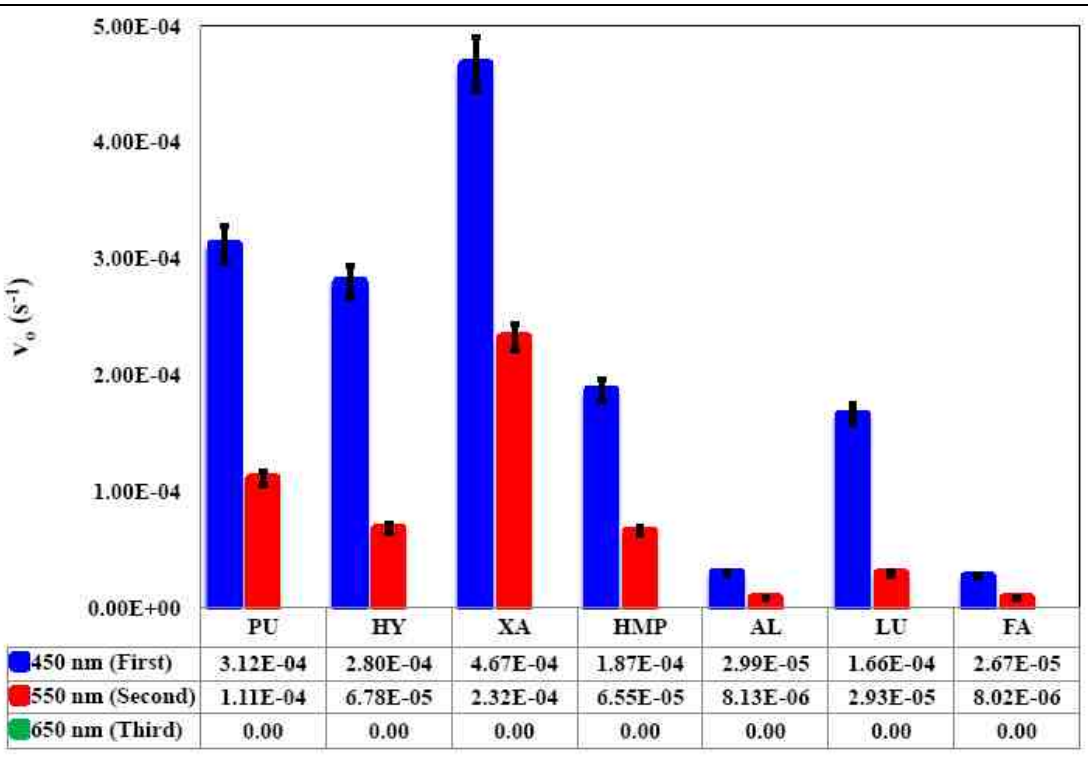


| | PU | HY | XA | HMP | AL | LU | FA |
|---|---|---|---|---|---|---|---|
| 450 nm (First) | 3.12E-04 | 2.80E-04 | 4.67E-04 | 1.87E-04 | 2.99E-05 | 1.66E-04 | 2.67E-05 |
| 550 nm (Second) | 1.11E-04 | 6.78E-05 | 2.32E-04 | 6.55E-05 | 8.13E-06 | 2.93E-05 | 8.02E-06 |
| 650 nm (Third) | 0.00 | 0.00 | 0.00 | 0.00 | 0.00 | 0.00 | 0.00 |

Figure 3.3.1. The initial rates for substrates-*bm*XOR (*upper panel*) and substrates–*Rc*XDH (*lower panel*) binding cofactors spectral changes monitored at 450, 550, and 650 nm. The rates were developed from Figures [A. 5 (*bm*XOR) and A. 6 (*Rc*XDH)].

The generation of $XOR_{RED}$-violapterin complex

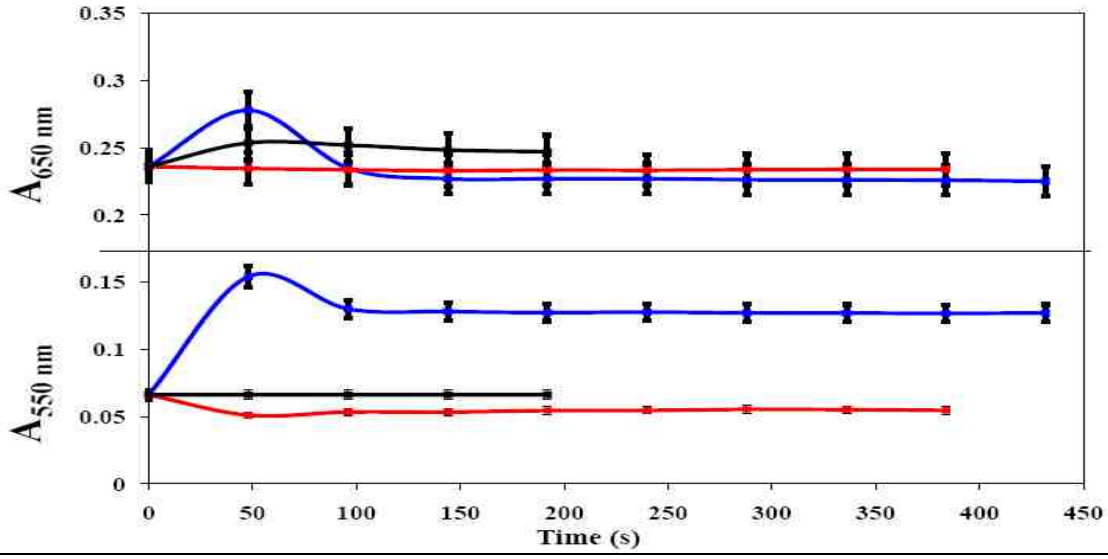


The traces from *top to bottom (at 50 s)* represent *bm*$XOR_{OX}$ (*blue or first trace*), *Rc*$XDH_{OX}$ Glu232Ala (*black or second trace*), and *Rc*$XDH_{OX}$ (*red or third trace*).

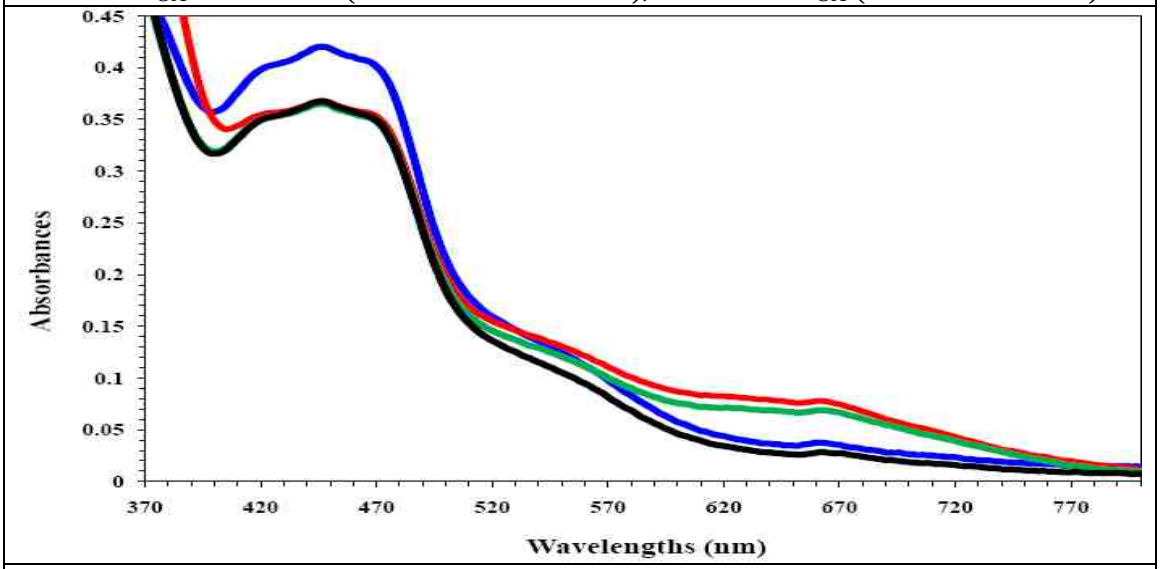


The traces from *top to bottom (at 650 nm)* represent *bm*$XOR_{OX}$ (*blue or third trace*) and *bm*$XOR_{OX}$/lumazine (5.22E-03 $s^{-1}$) (*red or first trace*). After incubation of 8 s (5.92E-04 $s^{-1}$) (*green or second trace*) and 32 s (1.53E-03 $s^{-1}$) (*black or fourth trace*).

Figure 4.3.2. The dynamic experimental approach in the absence of artificial electron acceptors. The *upper panel* represents the interaction between lumazine and enzymes (95 μM $bmXO_{OX}$, 26 μM $RcXDH_{OX}$, or 17 μM $RcXDH_{OX}$ Glu232Ala mutant in 50 mM sodium pyrophosphate-HCl, pH 8.3). The *bottom panel* represents the generation of long wavelength spectra (centered at 650 nm) in the presence of lumazine and 95 μM *bm*$XOR_{OX}$ in 50 mM sodium pyrophosphate-HCl, pH 8.3.

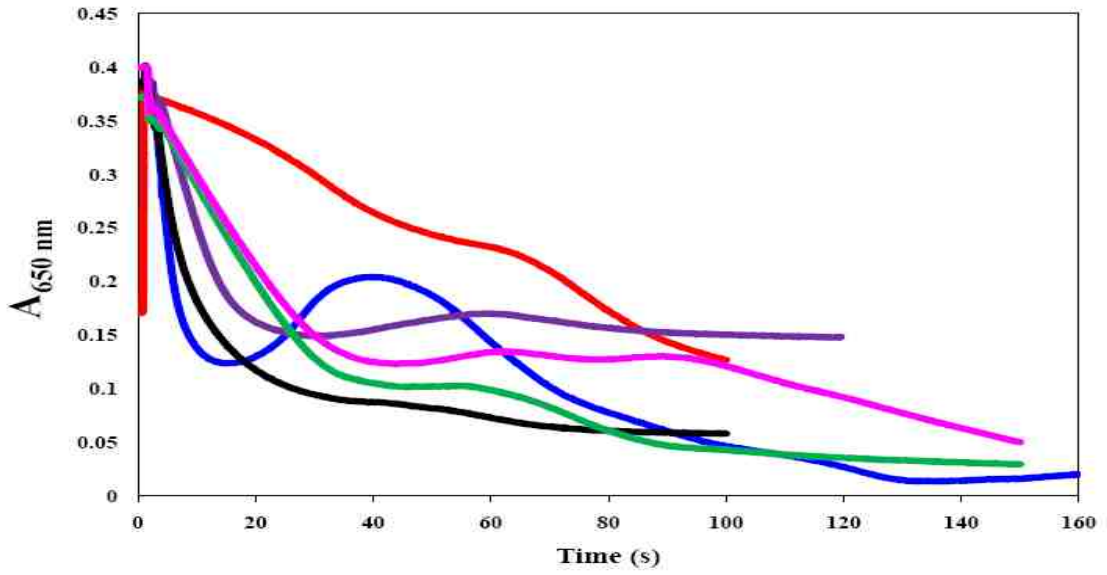


The traces from *top to bottom (at 40 s)* represent 250 µM lumazine with *bm*XOR at pH 5.0 (*red or first trace*), 50 µM lumazine with *Rc*XDH at pH 7.0 (*blue or second trace*), 50 µM lumazine with *Rc*XDH at pH 9.0 (*purple or third trace*), 100 µM lumazine with *Rc*XDH $Glu_{232}Ala$ at pH 9.0 (*pink or fourth trace*), 50 µM lumazine with *Rc*XDH $Glu_{232}Ala$ at pH 9.0 (*green or fifth trace*), and 250 µM lumazine with *Rc*XDH at pH 6.0 (*black or sixth trace*).

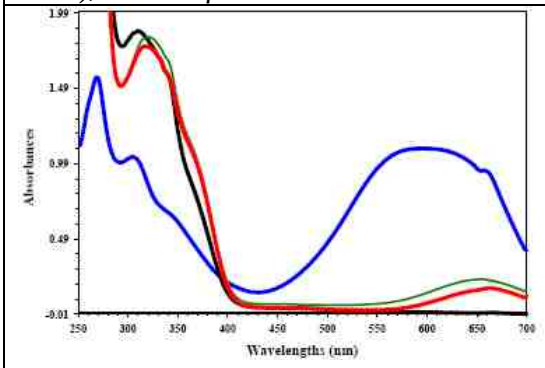


The traces from *top to bottom (at 650 nm)* represent $Na^+DCIP^-$ only (*blue or first trace*), first (*green or second trace*) and second (*red or third trace*) scans after incubation. The *black or fourth trace* represent *Rc*XDH only.

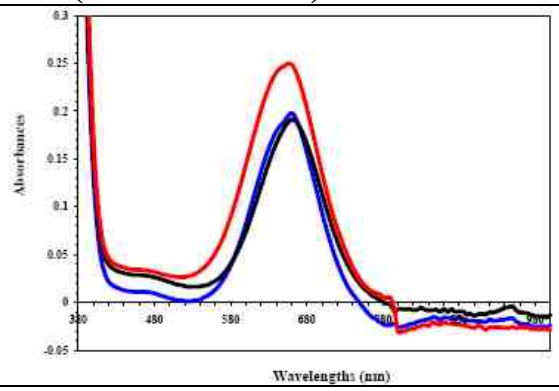


Repeated scans in the presence of *Rc*XDH, lumazine, and $Na^+DCIP^-$

Figure 3.3.3. The dynamic experimental approach in the presence of artificial electron acceptor ($Na^+DCIP^-$). The time course scan was monitored at 650 nm in the presence of different concentrations and pH values (*upper panel*). The *bottom left panel* represents the generation of the long wavelength spectra in the presence of *Rc*XDH, lumazine, and $Na^+DCIP^-$. The *bottom right panel* represents the reproducibility of the traces shown in the *bottom left panel*.

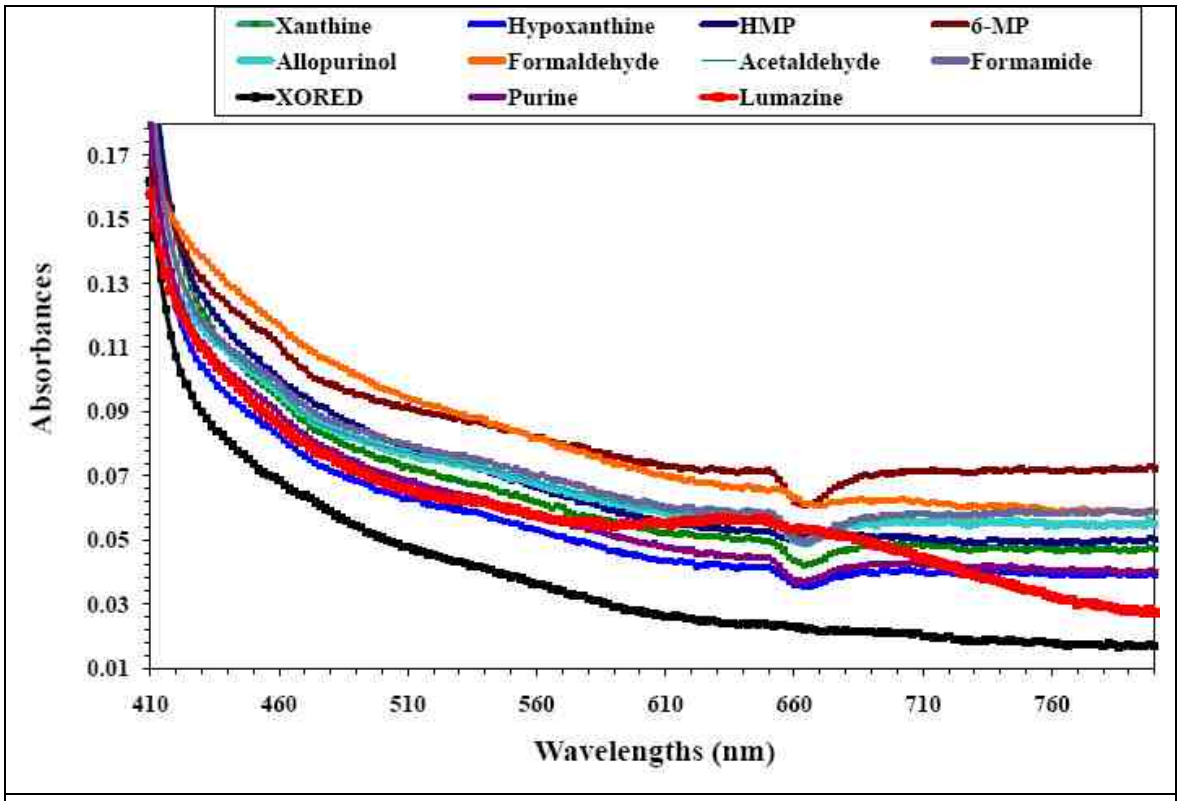


Figure 3.3.4. The static experimental approach in the absence of artificial electron acceptors. The static experimental approach was used to generate the long wavelength spectra (centered at 650 nm) in the presence of sodium dithionite reduced *bm*$XOR_{OX}$ (*bm*$XOR_{RED}$) and various substrates (0.20 M formaldehyde, 0.20 M formamide, 0.50 M acetaldehyde, 0.1 mM allopurinol, 0.128 M 6-methylpurine, 5 mM 2-hydroxy-6-methylpurine, 0.108 mM xanthine, 2.05 mM hypoxanthine, 0.20 M sodium formate, 2 mM purine, or 1.3 mM lumazine). The only spectral band was observed in the presence of 1.3 mM lumazine. The trace for the reaction between violapterin and *bm*$XOR_{RED}$ is the (*red or second trace from bottom to top at 780 nm*).

Charge transfer complexes from the dynamic and static experimental approaches

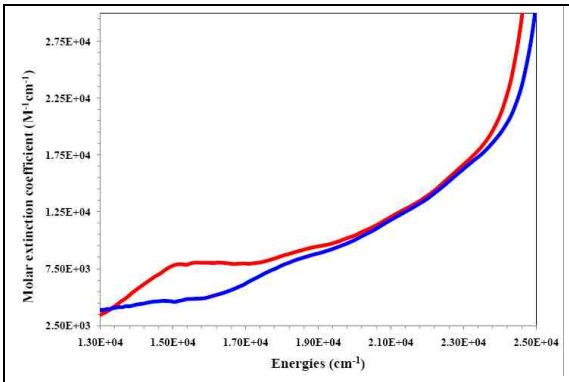


The traces from *top to bottom* represent native (*blue or second trace*) and activated (*red or first trace*) enzymes.

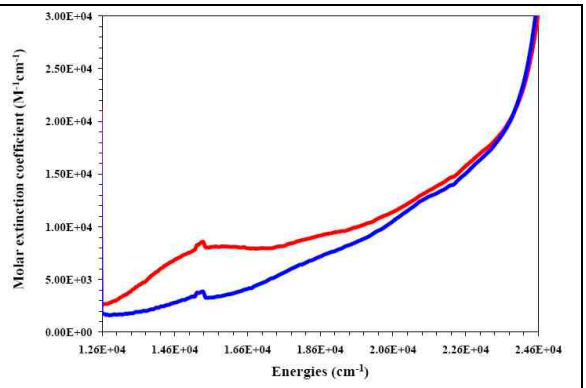


The traces from *top to bottom* represent reduced (*blue or second trace*) and activated reduced (*red or first trace*) enzymes.

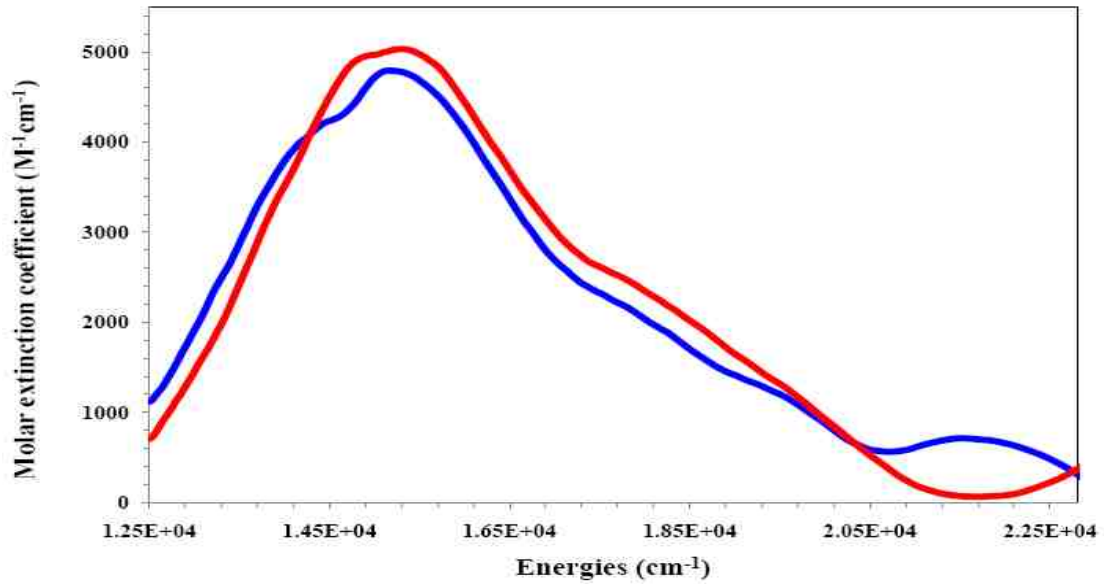


The traces from *top to bottom* represent difference spectra generated from the dynamic (*red or first trace*) and static (*blue or second trace*) approaches.

Figure 3.3.5. The long wavelength spectra (centered at 650 nm) generated using the dynamic (*upper left panel*) and static (*upper right panel*) experimental approaches. The *bottom panel* represents an overlap of the difference spectra developed from the *top panels*. The difference spectra of reduced $XO_{RED}$-violapterin complex minus $XO_{RED}$ displayed a broad peak centered at 650 nm with an even broader shoulder beginning at 550 nm and continuous below 450 nm.

Gaussian resolution of the spectral bands and extinction coefficient calculation

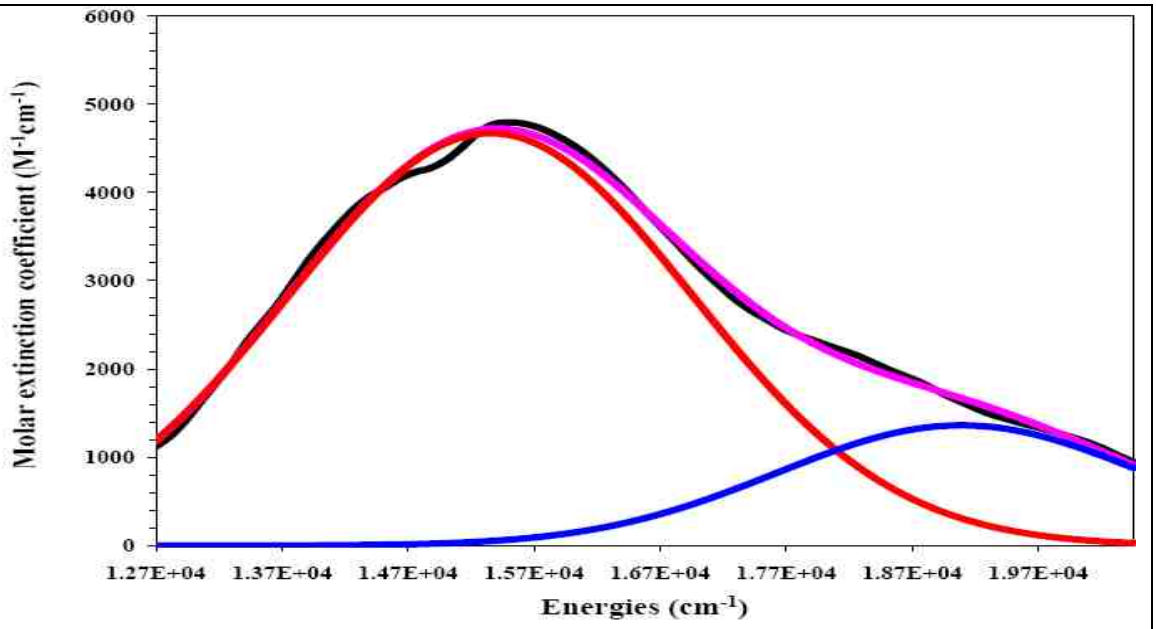


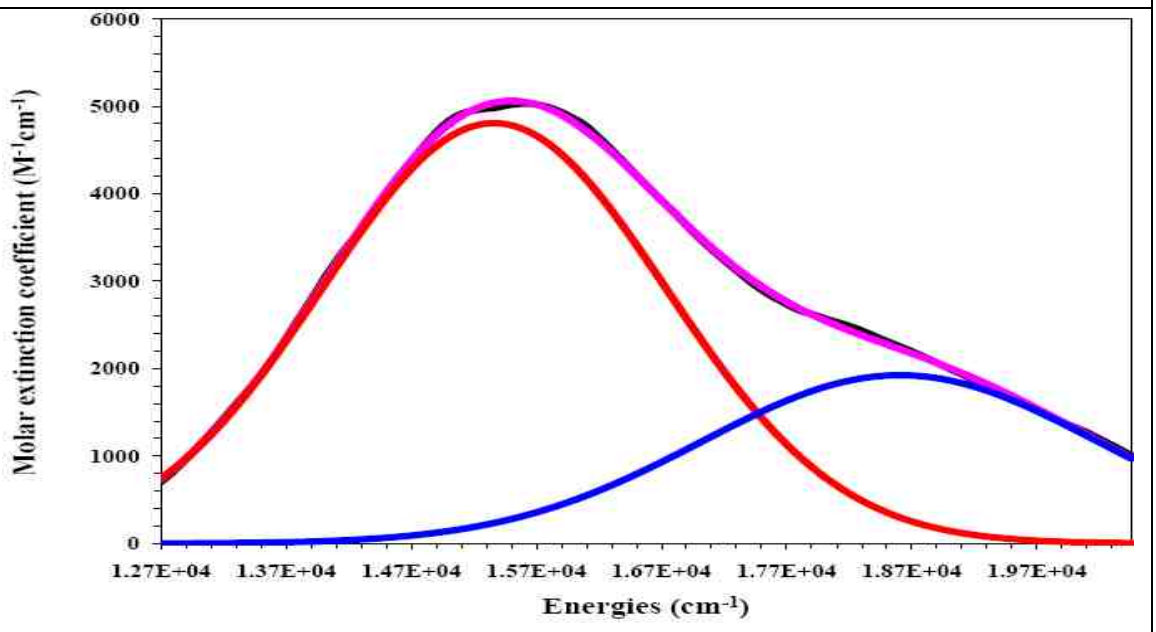


Figure 3.3.6. The Gaussian resolution of the difference spectra representing the traces obtained from the dynamic (*upper panel*) and static (*bottom panel*) experimental approaches. The difference spectra obtained from Figure (3.3.5, *bottom panel*) was fitted to two gaussian peaks. The initial difference spectra (*black or first trace*) was fitted as shown with the fitted spectra (*pink or second trace*) to produce the two Gaussian peaks centered around 650 nm (Peak 1, *Red or third trace*) and 550 nm (Peak 2, *Blue or fourth trace*).

Table 3.3.3. The molar extinction coefficients (in units of $M^{-1}$ $cm^{-1}$) ($\Delta\varepsilon_{max}$) were determined to probe the total strength of an absorption bands at 550 and 650 nm. The theoretical extinction coefficient was calculated using equation (3.2.2). The oscillator strength (*f*) values (from TDDFT calculation) and the width of the peak at half height ($\Delta\nu_{1/2}$) from Figure (3.3.6) were used to determine the $\Delta\varepsilon_{max}$.

| Oscillator strengths (*f*) | Extinction Coefficients, $\Delta\varepsilon_{max}$ ($M^{-1}$ $cm^{-1}$) | | | | | |
|---|---|---|---|---|---|---|
| | Experimental | | | Theoretical | | |
| | Overall | Peak 1 | Peak 2 | Overall | Peak 1 | Peak 2 |
| *(a) Static Experimental Approach* | | | | | | |
| | 4762.32 | 4760 | 2204.76 | | | |
| 0.1767 | | | | 9227.25 | 9905.37 | 11992.83 |
| 0.1158 | | | | 6047.06 | 6491.46 | 7859.47 |
| 0.0384 | | | | 2005.24 | 2152.61 | 2606.25 |
| *(b) Dynamic Experimental Approach* | | | | | | |
| | 4978.75 | 4970 | 2506.17 | | | |
| 0.1767 | | | | 9053.27 | 10567.54 | 12194.61 |
| 0.1158 | | | | 5933.04 | 6925.42 | 7991.71 |
| 0.0384 | | | | 1967.43 | 2296.51 | 2650.10 |

Table 3.3.4. The intensity of the MLCT transition was probed by determining the energy differences between Mo($d_{xy}$) LUMO and violapterin HOMO to relate the closeness of the frontier orbitals. The electronic transitions, as partial charge transfer for the Mo charge transfer (CT), was characterized using the contribution of individual atomic orbitals to the molecular orbital [122 (a), 140]. The Mo CT character was probed using the excitation from $HOMO_{-x}$ to $LUMO_{+y}$ using equation (3.2.1) [133].

| Electronic transitions | | | MLCT | Oscillator strengths (*f*) calculated from | | |
|---|---|---|---|---|---|---|
| | | | | TDDFT | Dynamic | Static |
| HOMO | → | LUMO, 0, 1 | 31.3036 | 0.1767 | 0.0971 | 0.0912 |
| HOMO | → | LUMO, 0, 1 | 34.8260 | 0.1158 | 0.0831 | 0.0849 |
| HOMO, 4, 5 | → | LUMO, 0 | 2.1866 | 0.0384 | 0.0363 | 0.0324 |

The pH dependency of the enzyme catalyzed-reaction

The pH profile for *bm*XOR enzyme

<table>
<tr><td> 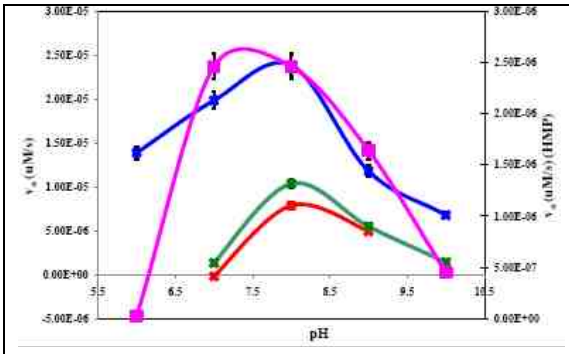 </td><td> 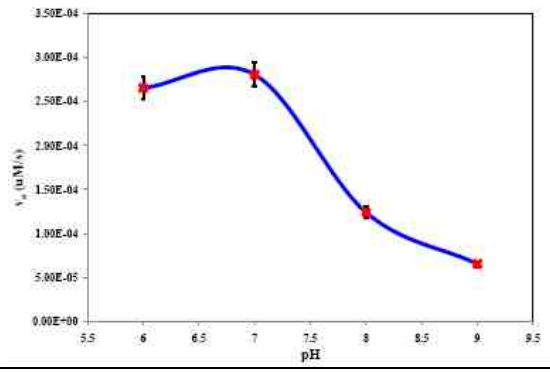 </td></tr>
<tr><td>The traces from top to bottom represent 5 mM HMP (pink or first trace), 0.108 mM xanthine (blue or second trace), 2.0 mM purine (green or third trace), and 2.05 mM hypoxanthine (red or fourth trace).</td><td>1.0 mM allopurinol</td></tr>
<tr><td> 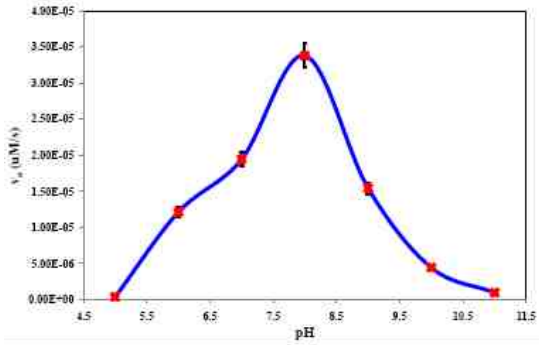 </td><td> 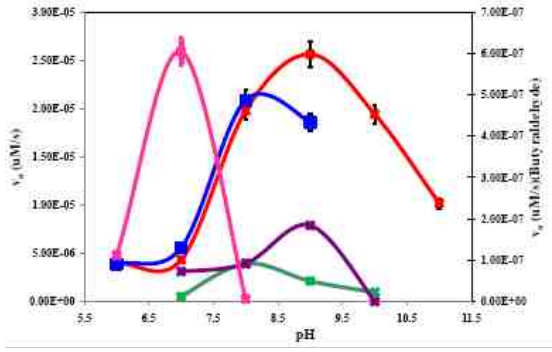 </td></tr>
<tr><td>1.36 mM Lumazine</td><td>The traces from top to bottom represent 0.50 M acetaldehyde (red or first trace), 0.20 M formaldehyde (blue or second trace), 1.5 mM benzaldehyde (purple or third trace), 0.20 M propionaldehyde (green or fourth trace), and 0.20 M butyraldehyde (pink or left trace).</td></tr>
<tr><td colspan="2">Figure 3.3.7. The pH profile for 1.7 µM bmXOR catalyzed hydroxylation and oxidation of various substrates. The profiles were developed from the data shown in Table (A. 1).</td></tr>
</table>

The pH profile for *Rc*XDH enzyme

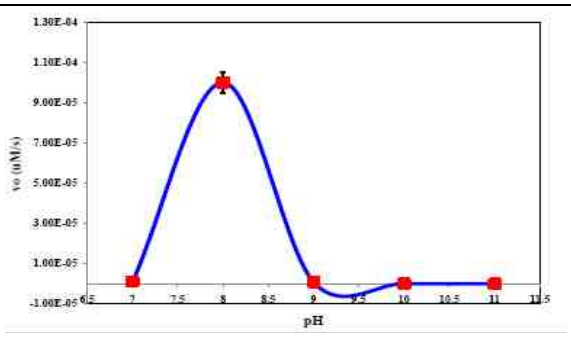


0.108 mM xanthine

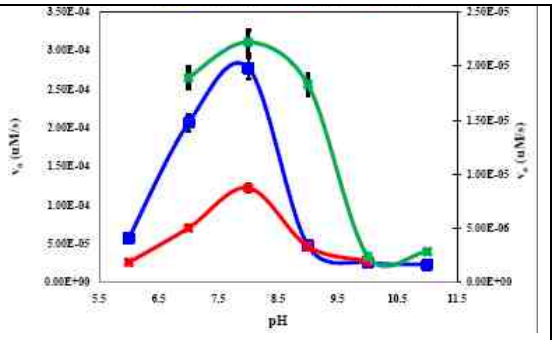


The traces from *top to bottom* represent 5 mM HMP (*green or first trace*), 2.05 mM hypoxanthine (*blue or second trace*), and 2.0 mM purine (*red or third trace*).

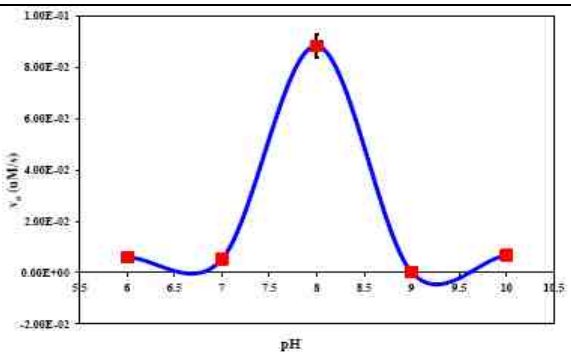


1.36 mM lumazine

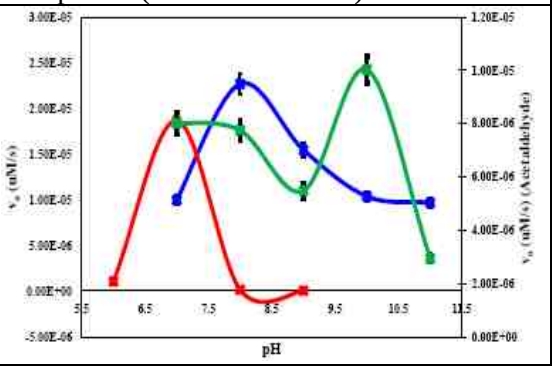


The traces from *left to right* represent 1.5 mM benzaldehyde (*red or left trace*), 20 M formaldehyde (*blue or middle trace*), and 0.50 M acetaldehyde (*green or right trace*).

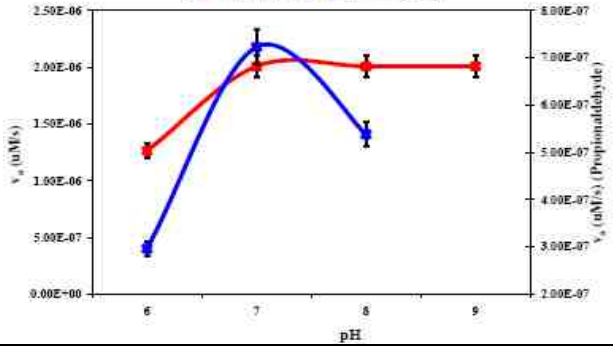


The traces from *top to bottom* (at pH 7.0) represent 0.20 M propionaldehyde (*blue or first trace*) and 0.20 M butyraldehyde (*red or second trace*).

Figure 3.3.8. The pH profile for 1.09 nM *Rc*XDH catalyzed hydroxylation and oxidation of various substrates. The profiles were developed from the data shown in Table (A. 1).

The pH profile for *Rc*XDH-$Glu_{232}$Ala mutant enzyme

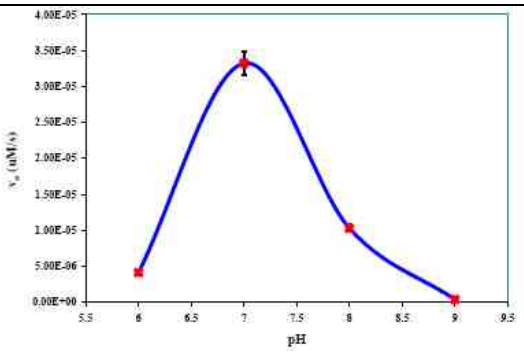


0.108 mM xanthine

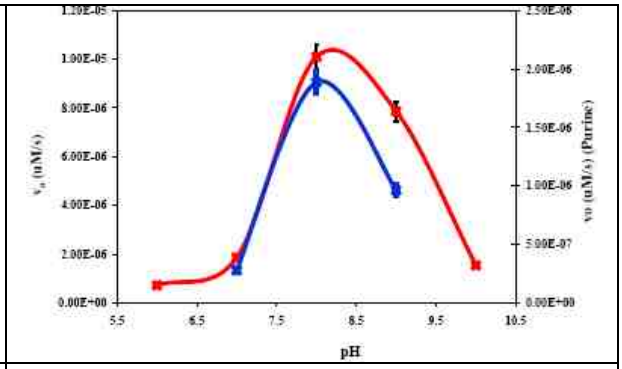


The traces from *top to bottom* represent 2.05 mM hypoxanthine (*red or first trace*) and 2.0 mM purine (*blue or second trace*).

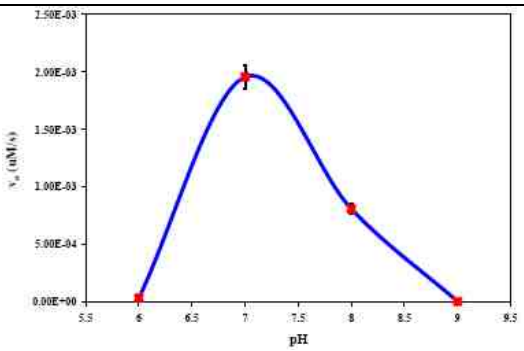


1.36 mM lumazine

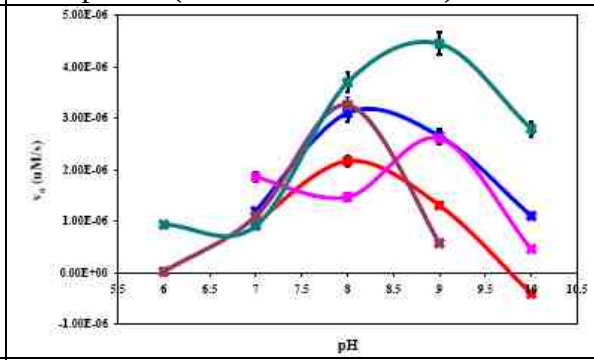


The traces from *top to bottom* (at pH 8.0) represent 0.50 M acetaldehyde (*green or first trace*), 0.20 M formaldehyde (*brown or second trace*), 0.20 M butyraldehyde (*blue or third trace*), or 1.5 mM benzaldehyde (*red or fourth trace*), and 0.20 M propionaldehyde (*pink or fifth trace*).

Figure 3.3.9. The pH profile for 1.24 µM *Rc*XDH $Glu_{232}$Ala catalyzed hydroxylation and oxidation of various substrates. The profiles were developed from the data shown in Table (A. 1).

The pH profile for OcCu/Mo-CODH enzyme

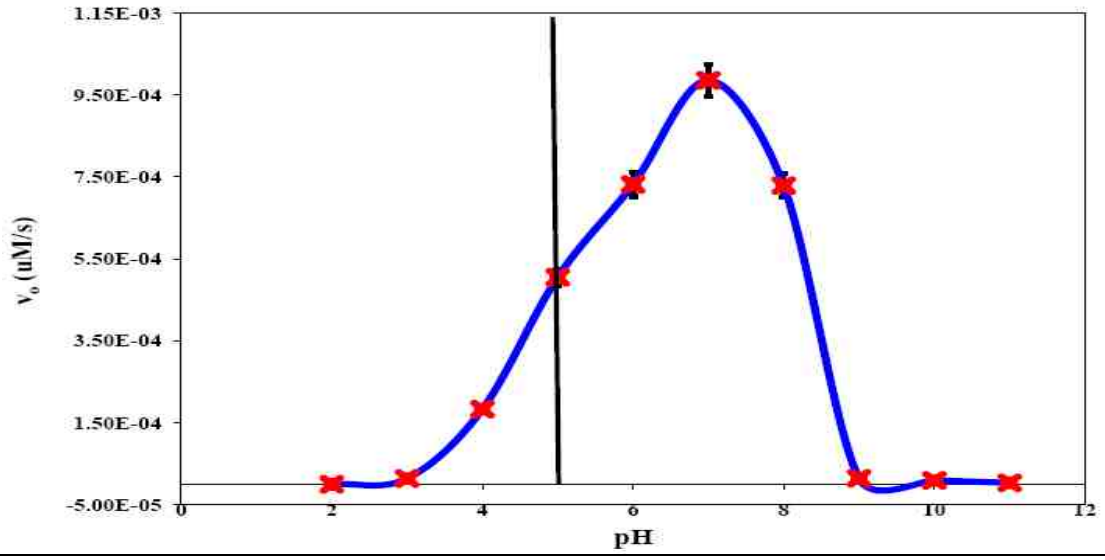


Figure 3.3.10. The pH profile for the *Oc*Cu/Mo-CODH enzyme catalyzed oxidation of CO. The vertical line demarcates the pH change observed for $DCIP^-$. Below pH 5.0, the colour of $DCIP^-$ was observed to change from sky blue to pink.

The optimum pH and pKa values

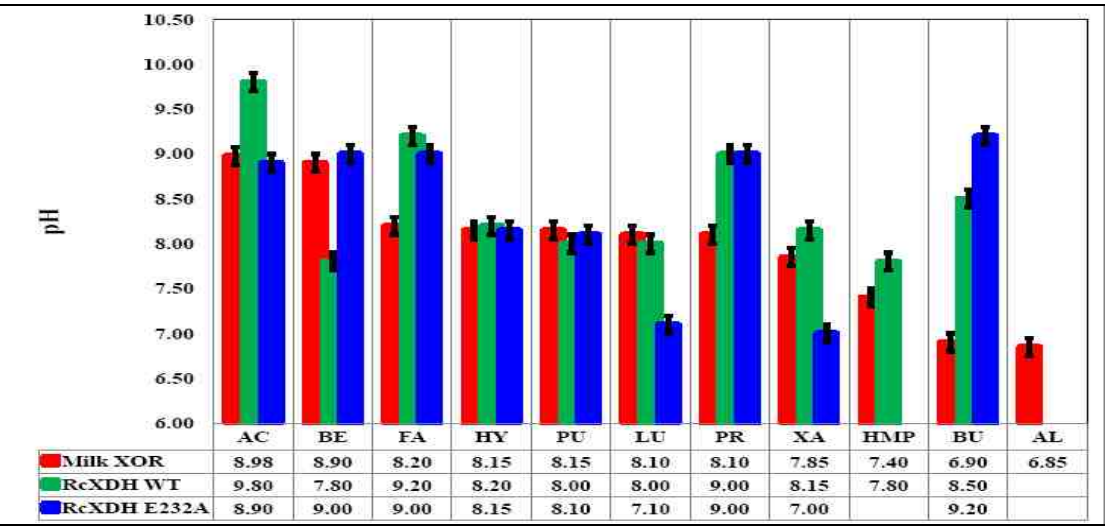


| | AC | BE | FA | HY | PU | LU | PR | XA | HMP | BU | AL |
|---|---|---|---|---|---|---|---|---|---|---|---|
| Milk XOR | 8.98 | 8.90 | 8.20 | 8.15 | 8.15 | 8.10 | 8.10 | 7.85 | 7.40 | 6.90 | 6.85 |
| RcXDH WT | 9.80 | 7.80 | 9.20 | 8.20 | 8.00 | 8.00 | 9.00 | 8.15 | 7.80 | 8.50 | |
| RcXDH E232A | 8.90 | 9.00 | 9.00 | 8.15 | 8.10 | 7.10 | 9.00 | 7.00 | | 9.20 | |

Figure 3.3.11. The optimum pH values for the hydroxylation and oxidation of various substrates. The plots were developed from Table (3.3.5) and *bm*XOR (Figure 3.3.7), *Rc*XDH (Figure 3.3.8), and RcXDH-E232A (*Rc*XDH-$Glu_{232}$Ala) (Figure 3.3.9).

Table 3.3.5. The optimum (OPT) pH and pKa (pKa-L and pKa-R, represent, the left and right limbs) values for *bm*XOR, *Rc*XDH WT, and *Rc*XDH-$Glu_{232}$Ala enzymes. ΔpKa [pKa(D) – pKa(A)] is also shown to verify the accuracy of the pKa values. The optimum pH and pka values were calculated from Figures (3.3.7 - 3.3.10).

| Substrates | $v_{max}$ | pka-L | Optimum pH | pKa-R | ΔpKa |
|---|---|---|---|---|---|
| *Oc*Cu/Mo-CODH | | | | | |
| Carbom Monoxide | 9.85E-5 | 4.97 | 7.20 | 8.37 | 3.40 |
| *bm*XOR | | | | | |
| Xanthine (XA) | 2.38E-05 | 5.21 | 7.85 | 8.97 | 3.76 |
| Lumazine (LU) | 1.71E-04 | 7.46 | 8.10 | 8.96 | 1.50 |
| Acetaldehyde (AC) | 2.56E-05 | 7.53 | 8.98 | 10.73 | 3.20 |
| Allopurinol (AL) | 2.80E-4 | 3.66 | 6.85 | 7.91 | 4.25 |
| Formaldehyde (FA) | 2.08E-05 | 7.33 | 8.20 | 11.65 | 4.32 |
| Butyrlaldehyde (BU) | 6.04E-07 | 6.40 | 6.90 | 7.46 | 1.06 |
| Propionaldehyde (PR) | 3.91E-06 | 7.67 | 8.10 | 9.23 | 1.56 |
| Benzaldehyde (BE) | 7.87E-06 | 8.07 | 8.90 | 9.46 | 1.39 |
| HMP | 2.45E-06 | 6.53 | 7.40 | 9.37 | 2.83 |
| Hypoxanthine (HY) | 7.87E-06 | 7.53 | 8.15 | 9.43 | 1.90 |
| Purine (PU) | 1.03E-05 | 7.43 | 8.15 | 9.13 | 1.70 |
| *Rc*XDH | | | | | |
| Xanthine (XA) | 9.99E-05 | 7.49 | 8.15 | 8.40 | 0.91 |
| Lumazine (LU) | 0.0889 | 7.47 | 8.00 | 8.55 | 1.08 |
| Acetaldehyde (AC) | 1.00E-05 | 8.84 | 9.80 | 10.71 | 1.87 |
| Formaldehyde (FA) | 2.26E-05 | 7.11 | 9.20 | 9.82 | 2.71 |
| Butyrlaldehyde (BU) | 2.00E-06 | 5.49 | 8.50 | 11.66 | 6.17 |
| Propionaldehyde (PR) | 7.22E-07 | 6.13 | 9.00 | 9.23 | 3.10 |
| Benzaldehyde (BE) | 1.86E-05 | 6.47 | 7.80 | 7.49 | 1.02 |
| HMP | 3.73E-04 | 6.24 | 7.80 | 9.45 | 3.20 |
| Hypoxanthine (HY) | 4.57E-3 | 6.35 | 8.20 | 8.66 | 2.32 |
| Purine (PU) | 5.00E-06 | 6.82 | 8.00 | 8.81 | 1.99 |
| *Rc*XDH-$Glu_{232}$Ala | | | | | |
| Xanthine (XA) | 3.32E-05 | 6.45 | 7.00 | 7.71 | 1.26 |
| Lumazine (LU) | 2.68E-03 | 6.51 | 7.10 | 7.73 | 1.22 |
| Acetaldehyde (AC) | 4.44E-06 | 7.46 | 8.90 | 10.40 | 2.94 |
| Formaldehyde (FA) | 5.83E-06 | 7.83 | 9.00 | 9.51 | 1.68 |
| Butyrlaldehyde (BU) | 5.21E-06 | 8.51 | 9.20 | 10.51 | 2.00 |
| Propionaldehyde (PR) | 3.79E-06 | 7.38 | 9.00 | 10.61 | 3.23 |
| Benzaldehyde (BE) | 3.30E-05 | 8.47 | 9.00 | 9.45 | 0.98 |
| Hypoxanthine (HY) | 9.94E-06 | 7.41 | 8.15 | 9.16 | 1.75 |
| Purine (PU) | 1.88E-06 | 7.46 | 8.10 | 9.03 | 1.57 |

## 3.3 Discussion and conclusion

### Description of results

*The substrate-enzyme binding cofactor reduction for XOR enzymes:* The anaerobic reduction of *Oc*Cu/Mo-CODH by sodium dithionite, after 2 s of incubation, was about 68 % (at 450 nm) and 70 % (at 550 nm) (Figure A. 4). Similar reduction, in the presence of sodium dithionite and various substrates, was also observed for XOR enzymes (Figure 3.3.1 and Table 3.3.1). The ratios of the reductions were calculated with respect to the reduction initiated by sodium dithionite (Table 3.3.1). Accordingly, the reductions initiated by sodium dithionite (at 450 nm) were 26 times higher than the reduction initiated by carbon monoxide. The ratio of the initial rates of reduction initiated by sodium dithionite was between 3197 (with respect to formate and *bm*XOR) and 2 (with respect to buffer saturated with CO and *Oc*Cu/Mo-CODH) times higher than the reductions initiated by the substrates (Table 3.3.1). The percent reductions, at 450 and 550 nm in the presence of substrates and *bm*XOR or *Rc*XDH enzymes, were also provided in Table (3.3.2). The percent reductions were calculated with respect to the native enzymes and after the initial interaction between the enzymes and substrates took place. Similarly, the highest reductions for *bm*XOR were observed in the presence of purine derivatives (except HMP). Unlike the reduction initiated by purine derivatives, the reduction initiated by HMP was about 1023 times smaller than the reduction initiated by sodium dithionite. The rate of reduction, in the presence of HMP, was similar to the rates of reductions in the presence of aldehydes. The reduction for *bm*XOR, in the presence of lumazine, was about 22 and 312 times lower than the reductions initiated, respectively, in the presence of hypoxanthine and sodium dithionite. In the presence of hypoxanthine, the reduction for *Rc*XDH was about 5 times smaller than the reduction observed for *bm*XOR. The percent reduction for *bm*XOR, in the presence of the smallest heterocyclic substrate (purine), was reported to be between 20% - 35%. Similarly, the percent reduction for *Rc*XDH in the presence of purine substrates was between 23% - 34%. The initial rates, at 450 nm for the reduction of *bm*XOR by purine (1.37E-03 $s^{-1}$), was one order of

magnitude lower than the reduction initiated by sodium dithionite (2.16E-02 $s^{-1}$) (Table 3.3.1). The reduction for *Rc*XDH, in the presence of purine, was also one order of magnitude lower than the reduction for *bm*XOR. When purine was methylated or oxidized, at the $C_6$-pyrimidine position, the extent of reduction was shown to vary. As a result, there was no detectable reduction, when 6MP was used as a substrate. However, there was a significant reduction in the presence of hypoxanthine (Fig. 3.3.1, *upper panel*). The reduction at 450 nm, in the presence of hypoxanthine, was about 12% - 41%. Similar reductions, for the *bm*XOR enzyme, were also observed in the presence of xanthine. Unlike the reduction for the *bm*XOR enzyme, in the presence of purine, hypoxanthine, and xanthine, there was no significant reduction for *Rc*XDH (Fig. 3.3.1, *lower panel*). The initial rates for the reduction of the enzymes, in the presence of allopurinol, were much lower than the reductions initiated by purine derivatives. Similarly, the initial rate for the reduction of the *bm*XOR enzyme by lumazine, at 450 nm, was two orders of magnitude lower than the reduction initiated by purine derivatives. In the case of *Rc*XDH, the highest reduction was observed in the presence of lumazine followed by xanthine and hypoxanthine.

*The generation of $XOR_{RED}$-violopterin and stable complexes:* In the absence of artificial electron acceptors, a unique spectral change (centered at 650 nm) was observed when *bm*XOR was reacted with lumazine (Fig. 3.3.1, *upper panel*). The initial rates (rise and decay) for the spectral bands (centered at 650 and 550 nm) were calculated from Figure (3.3.2, *right panel*). The overall initial rate, after the activation of *bm*$XOR_{OX}$ to form *bm*$XOR_{RED}$-violopterin complex, was 5.22E-03 $s^{-1}$. The rise in spectral band, at 650 nm, was 5.92E-04 $s^{-1}$. On the other hand, the decay of the spectral band was 5.92E-04 $s^{-1}$. A complete decay was observed at a rate of 1.53E-03 $s^{-1}$. An attempt was also made to generate the spectral band (centered at 650 nm) by reacting lumazine with $E_{OX}$ (*Rc*$XDH_{OX}$ or *Rc*$XDH_{OX}$-$Glu_{232}$Ala mutant) (Fig. 3.3.2, *left panel*). Although similar transformation was expected to take place, the only spectral band observed at long wavelength region (centered at 650 nm) was attributed to the unique $XOR_{RED}$-violapterin intermediate. As discussed above, the only spectral change (centered at 650 nm) was

observed for the reaction between lumazine and *bm*XOR. Since the long wavelength spectral bands (centered at 650 nm) was not detected for *Rc*XDH and RcXDH-$Glu_{232}$Ala enzymes (Fig. 3.3.2, upper panel), the use of an artificial electron acceptor was made to develop the spectral band (Fig. 3.3.3, *upper panel*). As shown from the time course traces, the reaction between 50 µM lumazine with *Rc*XDH (at pH 7.0) was shown to provide a well pronounced spectral band (centered at 650 nm). The experiment was performed, in the presence of $Na^{+}DCIP^{-}$, by reacting *Rc*XDH with lumazine. After the total bleaching of the blue color (a decrease in absorbance at 600 nm, for the conversion of $DCIP^{-}$ to $DCIP^{-2}$), the reaction mixture was re-scanned repeatedly in order to observe the reproducibility of the spectral bands at 650 nm (Fig. 3.3.3, *lower right panel*). Similar spectral bands, although less intense, were also observed for the interaction between *bm*XOR and *Rc*XDH-$Glu_{232}$Ala enzymes with lumazine (Fig. 3.3.3, *upper panel*). Although the increase in absorbance was generated using the dynamic experimental approach, similar spectral band was also generated using the static approach (Fig. 3.3.4). Initially, the reaction for the turnover of substrates by *bm*$XOR_{OX}$ was initiated by adding respective substrates to the reaction mixtures, containing respective enzymes. After the catalytic turnover, the *bm*$XOR_{RED}$-product complexes were prepared by adding 8 mM sodium dithionite to the anaerobic vial (containing the reaction mixtures of *bm*$XOR_{RED}$ and products). As shown in Figure (Fig. 3.3.4), the only spectral change (at long wavelength) was observed for the interaction between *bm*$XOR_{RED}$ and violapterin (that was proposed to be the $XOR_{RED}$-violapterin complex).

*Generation of stable complexes using small molecules:* The formation of stable (or inhibitory) complexes were probed by initiating the reaction mixtures (pre-incubated with small molecules) by the specific substrates (such as 0.50 M acetaldehyde, 0.1 mM allopurinol, 0.108 mM xanthine, or 2.05 mM hypoxanthine) (Table A. 2). The highest inhibition (greater than 50% inhibition), for the hydroxylation of hypoxanthine, was observed in the presence of cyanide (2.65%), formamide (30.53%), and formate (23.84%). The highest inhibition (greater than 50% inhibition), for the hydroxylation of xanthine, was observed in the presence of 6MP (31.79%), formamide (24.63%), HMP (16.10%), formate (0.85%), ethanol (0.07%), cyanide (0.03%), methanol (0%), and

formaldehyde (0%). The highest inhibition (greater than 50% inhibition), for the hydroxylation of allopurinol, was observed in the presence of cyanide (0%). Finally, the highest inhibition (greater than 50% inhibition), for the oxidation of acetaldehyde, was observed in the presence of HMP (50.70%), formate (38.66%), and cyanide (0%). The data for *bm*XOR was compared with the reactivity of *Oc*Cu/Mo-CODH enzyme, as shown in Table (A. 2). Accordingly, the highest inhibition (greater than 50% inhibition) was observed in the presence of formamide (30.60%), formate (46.04%), cyanide (0.71%), benzaldehyde (11.55%), acetaldehyde (29.46%), methanol (18.14%), thiocynate (19.77%), acetonitrile (0.06%), butylisocyanide (0.11%), and formaldehyde (37.77%).

*The pH dependency of the enzyme catalyzed-reaction:* In addition to the XOR enzymes, the pH profile for the *Oc*Cu/Mo-CODH enzyme catalyzed oxidation of CO was generated by varying the pH values (Figure 3.3.10). The optimum pH was calculated to 7.20. The ascending (left limb) and descending (right limb) pka values were determined, respectively, 4.97 and 8.37 (Table 3.3.5). The pH profile, for *Oc*Cu/Mo-CODH (Fig. 3.3.10), was shown to have similar shape to the pH profiles shown for XOR enzymes (Fig. 3.3.7 – 3.3.9). The optimum pH values, for *bm*XOR in the presence of various substrates, were also provided in Figure (3.3.11). Accordingly, the optimum pH range for *bm*XOR was between 6.85 - 8.98 (Fig. 3.3.11 and Table 3.3.5). The pH profile for the *Rc*XDH enzyme, in the presence of various substrates, was provided in Figure (3.3.8). Accordingly, the optimum pH range was between 7.80 - 9.80 (Fig. 3.3.11 and Table 3.3.5). The pH profile for the *Rc*XDH-$Glu_{232}$Ala mutant enzyme, in the presence of various substrates, was provided in Figure (3.3.9). Accordingly, the optimum pH range was between 7.00 - 9.20 (Fig. 3.3.11 and Table 3.3.5). The bell shaped pH profiles revealed that the acidic and basic pKa values were in the range, respectively, between (3.66) and (11.65) (Fig. 3.3.11 and Table 3.3.5). The acidic pKa values (left limbs) were assumed for the active site amino acid residue ([*bm*XOR]-$Glu_{1261}$, [*Rc*XDH]-$Glu_{736}$, or [*Oc*Cu/Mo-CODH]-$Glu_{736}$). The abstraction, of proton from the active site (right limb), was expected to facilitate the nucleophilic reaction. On the other hand, the basic pKa values were assigned for the free substrates needed to interact with the active site.

*Spectral bands at the short and long wavelength regions:* The spectral bands obtained for the $XOR_{RED}$-violapterin were shown in Figure (3.3.5). The difference spectra for the *bm*$XOR_{RED}$-violapterin complex *minus bm*$XOR_{RED}$ were shown to display a broad peak (centered at 650 nm). The overlap of the spectral bands, in the energy regions between 12500 through 22500 $cm^{-1}$, were displayed for the spectra obtained from both the dynamic and static approaches (Fig. 3.3.5, *lower panel*). The difference spectra were fitted to two gaussian peaks using Grams/AI, version 7.02 software packages (Thermo Galactic, Waltham, MA). The two Gaussian peaks (centered at 550 and 650 nm), for the bands originated from the dynamic (*upper panel*) and static (*lower panel*) preparations, were shown in Figure (3.3.6). The bands were consistent with the oscillator strengths obtained from the TDDFT results. Accordingly, the transitions from HOMO to LUMO and HOMO to LUMO+1, respectively, were 0.1769 and 0.1167 at 580 and 460 nm (Table 3.3.4). In addition to the energy similarities, the intensities of the bands were also identical (Fig. 3.3.6). The intensities of the bands were correlated with the experimental molar extinction coefficients (in units of $M^{-1}$ $cm^{-1}$), as shown in Table (3.3.3). The maximum experimental molar extinction coefficient changes ($\Delta\varepsilon_{max}$), at 650 nm, were estimated with respect to the molar absorbance coefficient changes, at 450 nm. The decrease in absorbance at 450 nm was approximately equal to the corresponding increase at 650 nm. The $\Delta\varepsilon_{650}$ for the *bm*$XOR_{RED}$-violopterin was 4978.75 $M^{-1}cm^{-1}$per active *bm*XOR (dynamic preparation). On the other hand, for the static preparation, the $\Delta\varepsilon_{650}$ complex was 4762.32 $M^{-1}cm^{-1}$ per active *bm*XOR. The oscillator strength (*f*) values (from TDDFT calculation) and the width of the peak at half height ($\Delta\nu_{1/2}$) for the charge transfer complex were calculated using (eq. 3.2.2). The theoretical $\Delta\varepsilon_{max}$ were 9053.27 $M^{-1}$ $cm^{-1}$ (for the dynamic preparation) and 9227.25 $M^{-1}$ $cm^{-1}$ (for the static preparation). The electronic transitions, as partial charge transfer for the Mo charge transfer (CT), were characterized using the contribution of individual atomic orbitals to the molecular orbital. The Mo CT character was probed using the excitation from $HOMO_{-x}$ to $LUMO_{+y}$ using equation (eq. 3.2.1). The metal character at the HOMO was 75.66 % and LUMO was 2.94 % (data not shown here). The intensity of the MLCT transition was also probed by determining the energy difference between Mo($d_{xy}$) LUMO and other products HOMO.

As shown in Table (3.3.4), the % Mo CT characters were 31.3036 % and 34% for the transition from HOMO to LUMO, 0, +1. The % Mo CT characters were compared with the % Mo MLCT character for $E_{RED}$-alloxanthine (12.38% and 1.71%), $E_{RED}$-uric acid (25.97%, 15.51%, 0.28%, and LMCT 5.99%), and $E_{RED}$-formate (LMCT 5.51%, 32.17%, and 29.10%), or $E_{RED}$-$CO_2$ (MLCT 7.66% and 9.26% and LMCT 14.68% and 6.86%).

Survey of the substrate-enzyme binding cofactor reduction for XOR enzymes

The number of equivalents required for the maximum bleaching of the cofactors of *Rc*XDH or *bm*XOR enzymes was shown to depend on several factors, such as the affinity of the substrate and product release. The substrate-binding cofactors reduction, associated with the cofactors (Moco, FAD, or $[Fe_2S_2](S^{\gamma}_{Cys})_4$), were shown through a complete bleaching in the presence of sodium dithionite ($NaO_2SSO_2Na$). Since the reduction wasn't related to the individual cofactors, an assumption was made to relate the reductions to the cofactors that were most significantly affected. The reduction of the redox sites (or cofactors) that were expected to respond independently, as shown by the stepwise reduction titration. In the absence of artificial electron acceptors, the unique spectral change (centered at 650 nm) was observed by reacting *bm*XOR with lumazine. This unique spectral behavior was attributed to the formation of the $E_{RED}$-violapterin catalytic intermediate. Although similar transformation was expected to take place, when lumazine was replaced by other substrates and *bm*XOR was replaced by *Rc*XDH or *Rc*XDH $Glu_{232}Ala$, the only spectral band observed was for the $XOR_{RED}$-violapterin intermediate. This spectral behavior was found to be a very unique signature of $E_{RED}$-violapterin, not shown with other catalytic intermediates. In addition to the experiments performed, in the absence of electron acceptors, the reaction between lumazine and *Rc*XDH was also carried out in the presence of $Na^{+}DCIP^{-}$. This was shown to provide a well pronounced spectral band (centered at 650 nm). Although spectral changes were not observed in the presence of substrates other than lumazine, some of the aldehydes (such

as acetaldehyde) were shown to interact at the Moco site. Since acetaldehydes could exist, in equilibrium with their hydrated forms, it is not known whether the aldehydes or their hydrates interacted with Moco. This is consistent with the fact that benzaldehyde was not shown to act like aliphatic aldehydes. The failure of benzaldehyde to act as an inhibitor could have been due to the fact that the inhibitory action of the aliphatic aldehydes was due to the formation of equilibrium with the hydrated form of an aldehyde. Therefore, the aldehydes that interacted with the $E_{RED}$ were proposed to be due to the hydrated form of acetaldehyde and formaldehyde. Similarly, methanol was also shown to interact with the enzymes in the same way formaldehyde and formamide interacted. However, the hydrogen bonding patterns of methanol was different from those of formamide and formaldehyde. The assignment of the hydrogen bonds was two sites for methanol, three sites for formamide, and four sites for the hydrated-formaldehyde. According to the inhibitory action, the molecules were categorized into four main classes. The first groups of molecules were those that were independent of turnover and unable to give progressive inhibition. These reagents (such as cyanide) were presumed to interact with the active site to yield an inactive Moco. Upon interaction with cyanide, the enzymes were rendered non-functional since cyanide was believed to interact with the $S_{Mo}$ group of the active site. The second class of reagents included those that were structurally similar to the physiological substrates of XO family enzymes. These reagents (methanol, ethanol, thiocynate, acetonitrile, and butylisocyanide) were able to provide progressive inhibition with or without the turnover condition of the enzymes. The third classes of reagents were similar to the second class of molecules. Unlike the second class of reagents, these reagents (formamide, formate, benzaldehyde, acetaldehyde, formaldehyde, 6MP, HMP, and allopurinol) were shown to provide progressive inhibition by depending on the turnover of the enzymes. The fourth class of reagents included molecules that interacted at the flavin site of the FAD cofactor. These reagents (such as nitrite and nitrate) were shown to inhibit by blocking the electron transfer chain at the flavin site. The interaction of the molecules with the enzymes and generation of the $E_{RED}$-product intermediates were shown to depend on the pH of the media. The initial rates, as a function of pH values, were shown to exhibit a bell-shaped pH dependence. The bell shape profile was shown to indicate the need for protonated and deprotonated forms of an

ionizable groups. The pKa (around 7.4 on the acidic limb) agreed with fact that the neutral form of the substrate was the one that reacted with the enzymes. The ionizable groups on the enzyme were shown to influence the $HO_{eq}$ assisted nucleophilic reaction. The interaction between $E_{OX}$ and $C_{RH}$ was facilitated by (Enzyme)-$Glu_{1261/730/736}$ after the proton was abstracted from $HO_{eq}$ and followed by a nucleophilic attack of the oxyanion group on the substrate-binding sites. Therefore, in order for the nucleophilic reaction to take place, the neutral form of the substrate and an ionizable group of the active site were required. The variation in pKa and optimum pH values were shown to reflect the changes that could have taken place in the binding pockets of the enzymes. Finally, the formation and decay of $E_{RED}$-product intermediate was shown to exhibit a bell shaped pH dependence.

# Chapter 4.0

## Modeling the transition state structures

### 4.1 Introduction

The currently accepted catalytic mechanism, for XOR enzymes, is postulated to take place through a base-assisted nucleophilic reaction (Scheme 1.1.3) [1, 18, 39, 51, 52, 62, 68, 70, 72, 76, 80]. The proposed nucleophilic reaction is presumed to proceed after the substrate enters the binding pocket and the substrate-binding site and $HO_{eq}$ terminal are re-aligned in a close proximity. On the basis of the orientation of the $HO_{eq}$ terminal, the mechanism is proposed to begin with the abstraction of a proton ($H_{OH}$) from the $HO_{eq}$ terminal by the active site amino acid residue ([XOR]-$Glu_{1261}$) (Fig. 1.1.8). This is proposed to be followed by a nucleophilic attack of the oxyanion ($Ö^{-}_{eq}$) on the carbon center ($C_{CRH}$) of the substrate ($C_{RH}$) to yield a tetrahedral species (a tetrahedral intermediate or tetrahedral transition state). As shown in Scheme (4.1.1), depending on the type of the substrate ($C_{RH}$), the transition state structure (c) is proposed to dissociate into Structure (j) with or without forming a stable intermediate (Structure d). The Structure (d) is presumed to undergo a two electron or a stepwise one electron oxidation to form Structure (j). The tetrahedral transition state complex is expected to undergo dissociation, following a transfer of substrate ($C_{RH}$) bound hydrogen ($H_{RH}$) to the $S_{Mo}$ terminal and simultaneous allocation of two electrons on the ($E_{OX}$)-$Mo^{(VI)}$ center. In principle, the transfer of $H_{RH}$ and flow of electrons is proposed to take place along a separate (Scheme 4.1.2, a) or the same (Scheme 4.1.2, b) coordinates, or a hydrogen atom transfer (Scheme 4.1.2, c). The path, shown in Scheme (4.1.2, a), suggests the transfer of $H_{RH}$ from $C_{RH}$ to $S_{Mo}$ as a proton and flow of electrons through the ($C_{CRH}$-$O_{eq}$)-$Mo^{(VI)}$ super-exchange pathway. In this case, a sequential electron and proton transfer is proposed to take place in the opposite direction since the proton motion may serve as a driving force for the flow of electrons.

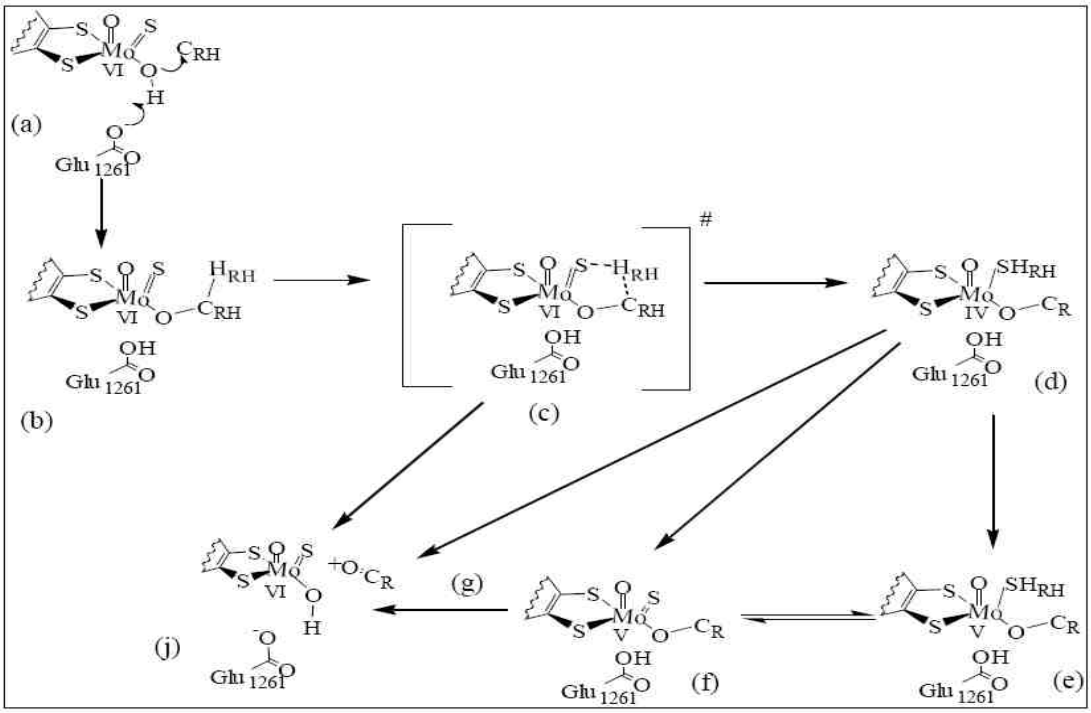


Scheme 4.1.1. A hypothetical schematic model for the catalytic transformation of the oxidation and hydroxylation of the substrates ($C_{RH}$) by XOR enzymes. The major structural features for the meta-stable and transition state structures are shown.

As shown in Scheme (1.1.3), the currently supported pathway for the $H_{RH}$ and two electrons transfer is the hydride transfer [1, 10, 18, 39, 51, 66, 68, 69, 112, 113, 114]. This type of transfer (Scheme 4.1.2, b) is similar to the outer sphere electron transfer mechanism that may or may not support a simultaneous electron transfer and $C_{RH}$-$H_{RH}$ bond cleavage. The transfer of an electron from the substrate to the ($E_{OX}$)-[Mo($d_{xy}$)] is proposed to take place through the $C_{CRH}$-($H_{RH}$-$S_{Mo}$)-$Mo^{(VI)}$ super-exchange pathway (Scheme 4.1.2, b). The third alternate, shown in Scheme (4.1.2, c), suggests the transfer of $H_{RH}$ and flow of an electron in the same coordinate. This alternate process is not similar to the hydride transfer mechanism, where the flow of two electrons and transfer of a proton are proposed to takes place in the same or opposite directions. In the hydrogen atom transfer, like the first two paths, the transfer of electrons and a proton are kinetically uncoupled.

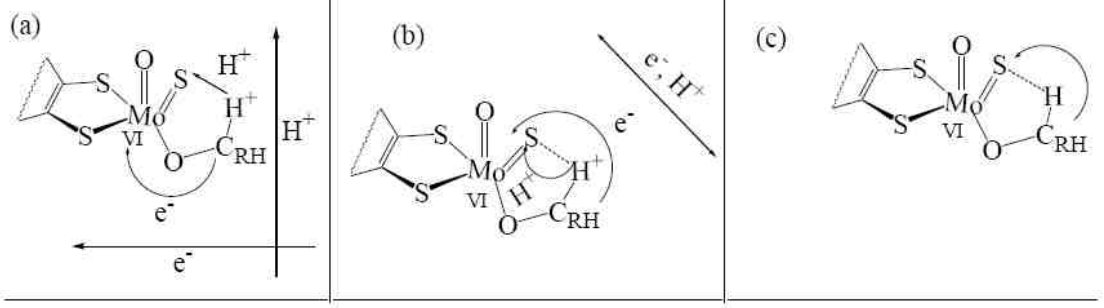


Scheme 4.1.2. A hypothetical description for the nature of the proton and electron transfer process. The possibilities are the transfer of proton and flow of electron in a separate (a) and the same (b) coordinates. The third path describes the coupled hydrogen atom transfer (c).

That means, the migration of a hydrogen and the flow of an electron may take place at different time scales. In this case, both the electrons and proton are proposed to originate from the same atom. In any case, the migration of electrons and proton might take place in one of the three alternate ways, depending on the kinetics and thermodynamics of the electron flow and the position of $H_{RH}$, at any time scale. The proton and electron transfer process is expected to offer a mechanistic basis for the hydroxylation reaction since it affects both the oxidation state of $(E_{OX})$-$Mo^{(VI)}$ center and the acid-base properties of the reactants ($E_{OX}$ and $C_{RH}$). The substrates and active sites of the enzymes are affected by this process since the electrons reside on the $(E_{OX})$-$Mo^{(VI)}$ center and the proton on the substrates or $S_{Mo}$ terminal. Although the transfer of $H_{RH}$ from $C_{RH}$ to the $S_{Mo}$ terminal and allocation of two electrons on the $(E_{OX})$-$Mo^{(VI)}$ center are proposed to take place during the initial stage of catalysis [1, 10, 18, 39, 68, 69, 76, 106], the description the events (such as, the formation of $O_{eq}$-$C_{CRH}$ bond, cleavage of $C_{CRH}$-$H_{RH}$ bond, migration of $H_{RH}$ to $S_{Mo}$, and reduction of $(E_{OX})$-$Mo^{(VI)}$ to $(E_{RED})$-$Mo^{(IV)}$) taking place at the transition state is not well understood. In order to understand the events taking place during the mechanistic transformation, computation models are developed to evaluate the bonding and wave-

function descriptions. As a result, the substrate bound active site model structures are optimized to approximate the linear motion of $H_{RH}$ at the transition state. The migration profile for the $H_{RH}$ from the $C_{RH}$ to $S_{Mo}$ is quantitated between $(E_{OX})$-$[Mo^{(VI)}$-$O_{eq}$-$C_{CRH}]$ and $(E_{RED})$-$[Mo^{(IV)}$-$O_{eq}$-$C_{CR}]$ meta-stable states (Scheme 4.1.1). Since the postulated transition state complex (Structure c) is located above the two meta-stable states (Structures b and d), an electronic structure calculation is performed on the active site model compound bound to a broad range of substrates (Fig. A. 1). The transition state structure is characterized by one imaginary negative frequency, in order to distinguish the minimum characterized by all other positive frequencies [138 (c)]. The imaginary negative frequencies and linear motions of the $H_{RH}$, at the transition state, is also proposed to vary depending on the affinity of the substrates (orientation of substrates and substrate-binding sites). In addition to the linear transit scans, the bond order indices are also used to describe the transition state structures. The bond order indices are expected to approximate the weakening and strengthening of the bonds. Although the bond order profiles are used to characterize the transition state, they are also used to quantitate the formation of $O_{eq}$-$C_{CRH}$ and $S_{Mo}$-$H_{RH}$ and cleavage of $C_{CRH}$-$H_{RH}$ and Mo-$O_{eq}$ bonds. Because the $C_{CRH}$-$H_{RH}$ bond distance varies significantly, when $O_{eq}$-$C_{RH}$ bond is formed, the position of $H_{RH}$ and cleavage of $C_{CRH}$-$H_{RH}$ bond is proposed to depend on the nature of the substrate. Therefore, understanding the coordination geometry of the active site is of a prime importance in developing a deeper mechanistic insight into the enzyme catalyzed reactions. Upon completion of this work, the theoretical approach is expected to provide an insight whether the electron transfer takes place through an inner sphere mechanism, possibly before or after the formation of $S_{Mo}$-$H_{RH}$ bond. Finally, in the presence of structurally different substrates, the theoretical work is expected to provide a new mechanistic handle that should prove useful in understanding the behavior of XO family enzymes.

## 4.2 Materials and methods

### Materials

*Programs and software packages:* All computation calculations were performed using Gaussian®03W (version 6.0) program software package (Gaussian, Inc., Wallingford, CT). Molecular orbital and electronic structure visualization were performed using software programs such as Molden (CAOS/CAMM center Nijmegen, Toernooiveld, Nijmegen, The Netherlands) and GaussView 3.0 (Gaussian, Inc., Pittsburgh, PA). Molecular orbital analyses for the constituent chemical fragments were performed using AOMIX 2008/2009 (revision 6.40) version software package (Center for catalysis research and innovation, University of Ottawa, Ottawa, ON, Canada) [137].

### Methods

#### General computation methods

Electronic structure calculations were performed to generate Mulliken atomic charges ($\Delta q_{Mo}$, $\Delta q_{S,}$ etc.), total electronic energies, wave-function descriptions, bonding descriptions, and bond orders. The parameters were generated from the geometry optimization, single point energy, frequency, and linear transit calculations [138 (c, d, j, k)]. All calculations were carried out using Gaussian® 03W (version 6.0) program software package using density functional theory (DFT) method of the B3LYP [132, 137, 138 (a)] correlation functional formalism (DFT-B3LYP) [138 (e)]. The DFT method employing the B3LYP level of theory [138 (a, e)] was applied on the truncated analogues shown in Figure (3.2.1, a). The truncated model structures were bound to respective substrates through their $HO_{eq}$ terminals. The 6-31G (d', p') basis set with a polarization function was applied for non-metal atoms (C, H, O, N, and S) [138 (g)]. Similarly, the LANL2DZ basis set and LANL2 effective core potentials were applied for Mo atoms [149 (i)]. The structures were

fully optimized using *"# b3lyp gen pseudo=read #p gfinput iop(6/7=3) opt pop=full gfprint"* theoretical model and job type [138 (j)]. The linear transit calculations were used to explore potential energy surfaces. The transition state structures were located using the quadratic synchronous transit method (QST3) [138 (b)]. The final optimized geometries were used as input files for the single point energy and frequency calculations [138 (c, h, k)]. The single point energy calculations were performed using *"# b3lyp #p gen pseudo=read gfinput pop=full iop(3/33=1) gfprint"* theoretical model and job type [138 (h, k)]. The frequency calculations were also carried out using *"# b3lyp gen freq pseudo=read #p gfinput iop(6/7=3) pop=full gfprint"* theoretical model and job type [138]. The bond distances were computed from the output files of the optimized structures using Molden and GaussView 3.0 software programs. The pictorial views, for the frontier (HOMO and LUMO) orbitals, were generated from the checkpoint files using GaussView 3.0 software program. The output files, from the single point calculations, were used as input files for the AOMix analysis [137]. The percentage contributions of different molecular fragments and Mayer bond orders were generated using AOMix software package [137].

## Predicting the transition state structures

The linear motion of $H_{RH}$, during the migration of $H_{RH}$ from $C_{RH}$ to $S_{Mo}$, was approximated to probe the position of $H_{RH}$ in the transition state structure. The geometries, representing the tetrahedral transition state structures (Fig. A. 7), were modeled by placing the substrate bound hydrogen ($H_{RH}$) between the $S_{Mo}$ terminal and the carbon center ($C_{CRH}$) of the substrate ($C_{RH}$). The $C_{RH}$ in Figure (A. 7) was replaced by various substrates (Fig. A. 2). The substrates were bound to the $HO_{eq}$ terminal of the truncated Moco, as shown in Figures (A. 8 – A. 18). *A linear transit optimization scans* were performed on the substrate bound complexes. The scans were performed at the $Mo^{(VI)}$ and $Mo^{(IV)}$ states, respectively, representing the initial and final meta-stable structures (Scheme 4.1.1). The input files for the linear transit optimization scans were developed using the $H_{RH}$–$S_{Mo}$ distance, as a constraint. The difference in $H_{RH}$–$S_{Mo}$ distance, between the initial ($H_{RH}$–$C_{CRH}$ distance, when $H_{RH}$ was bound to $C_{CRH}$) and the

final distance ($H_{RH}$–$S_{Mo}$ distance, when $H_{RH}$ was bound to $S_{Mo}$), were used to develop the intervals for the linear transit scans. A series of geometry optimizations were carried out by stepping up the $H_{RH}$–$S_{Mo}$ bond distance, at constant intervals. All linear transit calculations were carried out at $Mo^{(VI)}$ oxidation state using *"# opt=modredundant b3lyp gen pseudo=read #p gfinput iop(6/7=3) pop=full gfprint"* theoretical model and job type [138]. Once a series of structures were optimized, the total energies from each optimization steps were plotted against respective $H_{RH}$–$S_{Mo}$ distances. From the plot, the structure with the highest energy was considered as an initial guess for the transition state structure. The input files containing the three geometries (the initial, final, and initial guesses) were optimized using *"# b3lyp gen pseudo=read #P gfinput iop(6/7=3) opt=QST3"* theoretical model and job type [138]. This job type was used to generate a guess for the transition state structure, in terms of redundant internal coordinates [137], that were midway between $Mo^{(VI)}$ and $Mo^{(IV)}$ meta-stable states. A frequency calculation was performed, on the final geometries, using *"# b3lyp gen freq pseudo=read #p gfinput iop(6/7=3) pop=full gfprint"* theoretical model and job type [138 (c)]. The position of $H_{RH}$ at the transition state structure was characterized by one imaginary negative frequency. After the transition state structure was identified, a single point energy calculation was performed using *"# b3lyp #p gen pseudo=read gfinput pop=full iop(3/33=1) gfprint"* theoretical model and job type [138 (h, k)]. The output files from the single point energy calculations were used as input files for AOMix analysis [137]. *Vibrational frequency optimization calculations* were also used, as a one step optimization, to locate the transition state structures. In this approach, the $H_{RH}$ was placed between the $C_{CRH}$ and $S_{Mo}$ terminal and optimized without additional constraints. The structures shown in Figures (A. 8 – A. 18) were optimized using *"#p freq b3lyp nosymm iop(6/7=3) gen pseudo=read gfinput opt=(ts,noeigen,calcfc)"* theoretical model and job type [138 (c)]. A single point energy calculations were performed on the optimized structures as described above. The output files from the single point energy calculation were used for AOMIX analysis [137]. *Bond order profile scans* [137] were performed using the geometries from the single point energy calculations and AOMix analysis [137]. The Mayer bond order indices for $H_{RH}$-$S_{Mo}$ (or $C_{CRH}$-$H_{RH}$) were plotted against $H_{RH}$-$S_{Mo}$ ($C_{RH}$-$H_{RH}$) bond distances.

## 4.3 Results

Characterization of the transition state structures

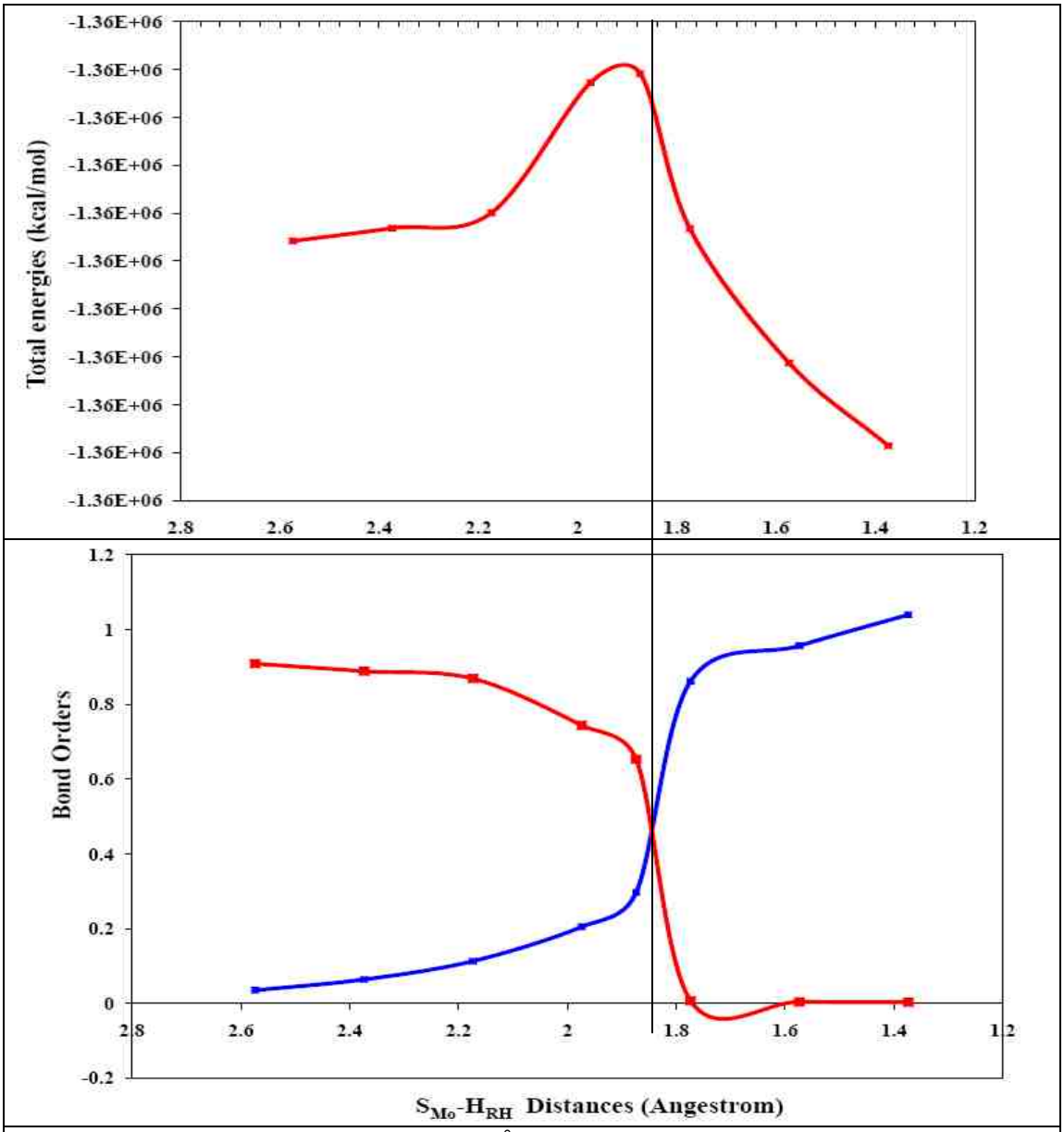


The traces from *top to bottom (at 2.58 Å)* represent $C_{RH}$-$H_{RH}$ (*red or first trace*) and $S_{Mo}$-$H_{RH}$ (*blue or second trace*) bond distances.

Figure 4.3.1. A sample representation for the characterization of the transition state structure ($[C_{CRH}---H_{RH}---S_{Mo}]^{‡}$). The linear transit scan was performed, for the truncated active site model compound bound to lumazine, to monitor the migration of $H_{RH}$ from $C_{RH}$ to $S_{Mo}$. The total energy, *top panel* (Tables A. 3) and Mayer bond order profiles, *bottom panel* (Table A. 6) were plotted as a function of $S_{Mo}$-$H_{RH}$ bond distances.

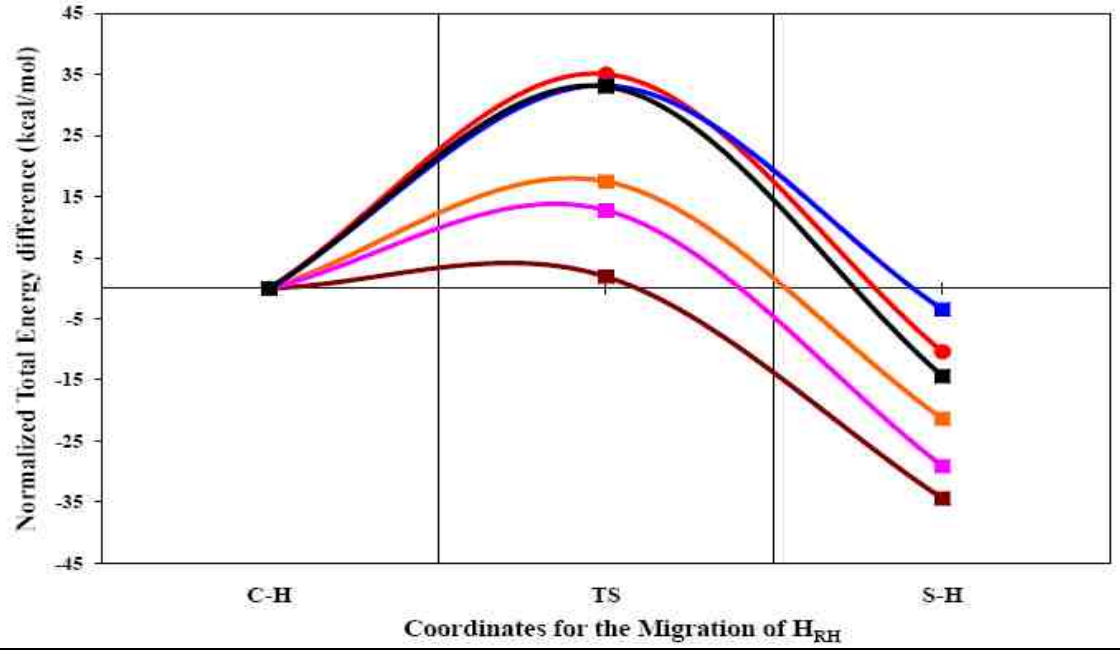


The traces from *top to bottom (at S-H side)* represent complexes bound to formate (*blue or first trace*), allopurinol (*red or second trace*), formamide (*black or third trace*), lumazine (*orange or fourth trace*), formaldehyde (*pink or fifth trace*), and xanthine (*brown or sixth trace*).

| Structures | $\Delta H^{\ddagger}$ ($E_{TS}$-$E_{CH}$) (kcal/mol) | $\Delta H^{0}$ ($E_{CH}$-$E_{SH}$) (kcal/mol) |
|---|---|---|
| | | |
| Purine C2 (PU C2) | 0.332392 | -34.4748 |
| Purine C8 (PU C8) | 15.86263 | -21.7679 |
| 6MP C2 | 19.01812 | -21.0767 |
| 6MP C8 | 2.390498 | -38.2396 |
| HMP | 2.805407 | -34.4421 |
| Xanthine (XA) | 1.898718 | -34.4357 |
| Hypoxanthine (HY) | 18.24911 | -21.0533 |
| Allopurinol (AL) | 1.118159 | -37.1119 |
| Lumazine (LU) | 17.48022 | -21.3833 |
| Formaldehyde (FA) | 12.75137 | -29.1651 |
| Acetaldehyde (AC) | 18.38685 | -25.1695 |
| Formate (FT) | 33.20115 | -3.45846 |
| Formamide (FM) | 35.70705 | -12.9303 |

Figure 4.3.2. The normalized energies, for selected substrates, were plotted as a function of the reaction coordinates (C-H, TS, and S-H). The symbols (C-H, TS, and S-H) represent, respectively, the $Mo^{(VI)}$-$O_{eq}$-$C_{CRH}$ meta-stable, transition ([$C_{CRH}$---$H_{RH}$---$S_{Mo}$]$^{\ddagger}$), and $Mo^{(IV)}$-$O_{eq}$-$C_{CR}$(-SH) meta-stable states. The energy normalization was calculated with respect to the Michaelis-Menten type structure ($Mo^{(VI)}$-$O_{eq}$-$C_{CRH}$ meta-stable) from the raw data provided in Figure (4.3.1, *upper panel*).

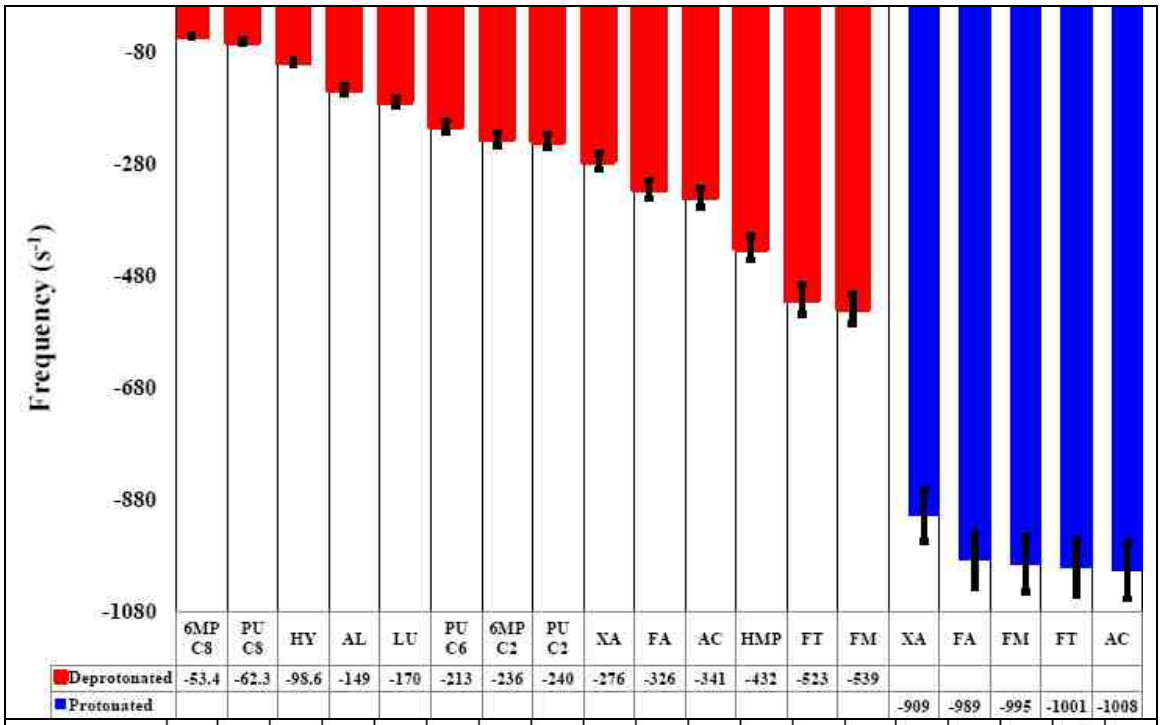


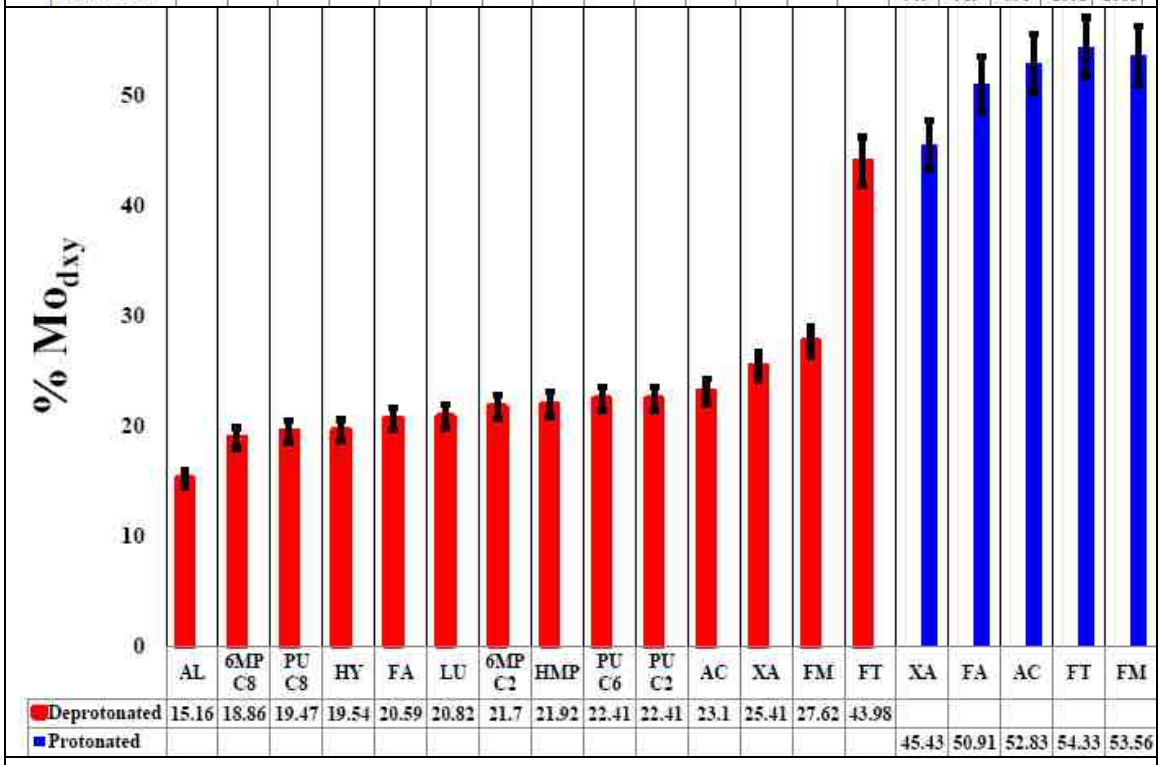


Figure 4.3.3. The frequencies (*upper panel*) and % Mo $d_{xy}$ (*lower panel*) were plotted as a function of substrates, respectively, used to locate the transition state structures and % composition of Mo $d_{xy}$ at the transition state structures. The plots were generated from the raw data provided in Table (A. 4).

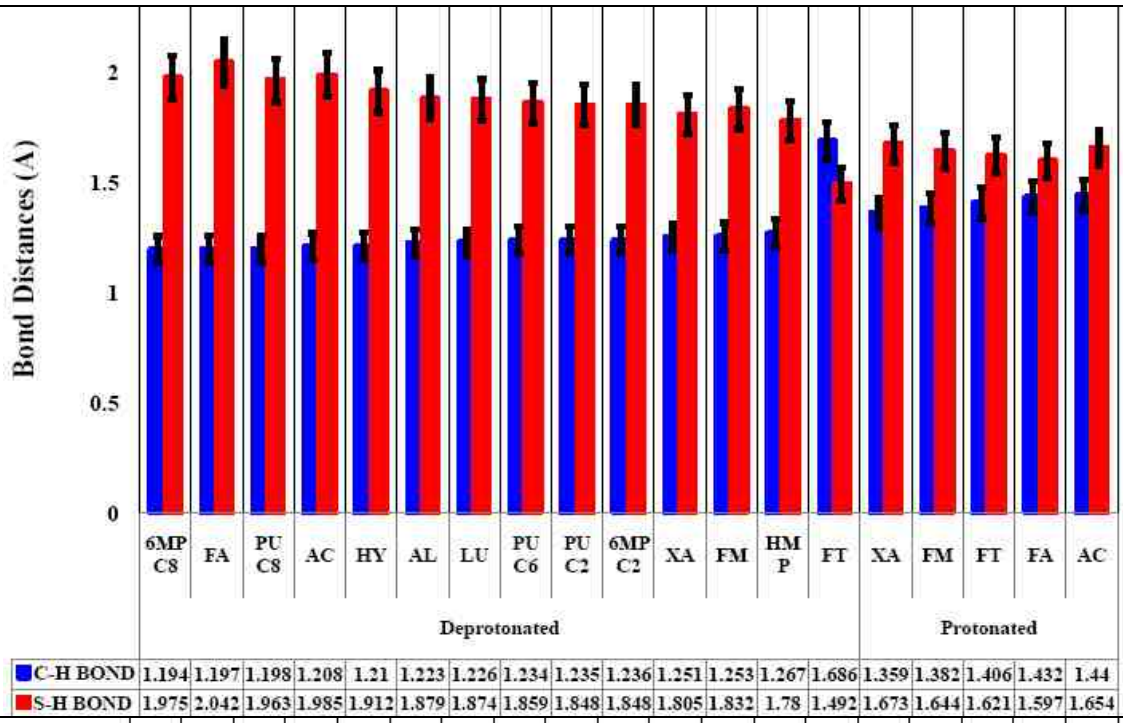


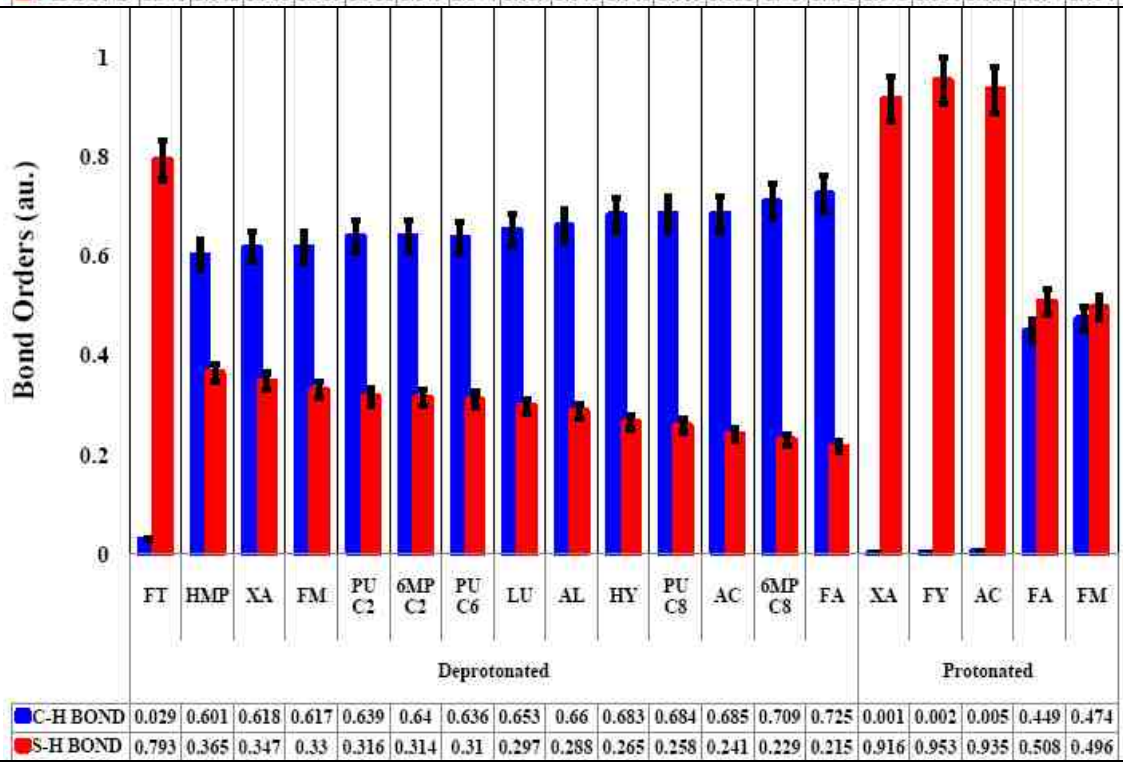


Figure 4.3.4. The bond distances (*upper panel*) and bond orders (*lower panel*) for the $S_{Mo}$-$H_{RH}$ (S-H) and $C_{CRH}$-$H_{RH}$ (C-H) bonds, at the transition state structures, were plotted as a function of the substrates. The symbols for the substrates were the same as Figure (4.3.2). The plots were developed from the raw data provided in Table (A. 6). The *blue or first (rear)* and *red or second (front)* bars of the respective substrate bound complex represent, respectively, the C-H and S-H bonds.

The change of the Mulliken atomic charges on $H_{RH}$, $C_{RH}$, Mo, $O_{eq}$, and $S_{Mo}$ groups

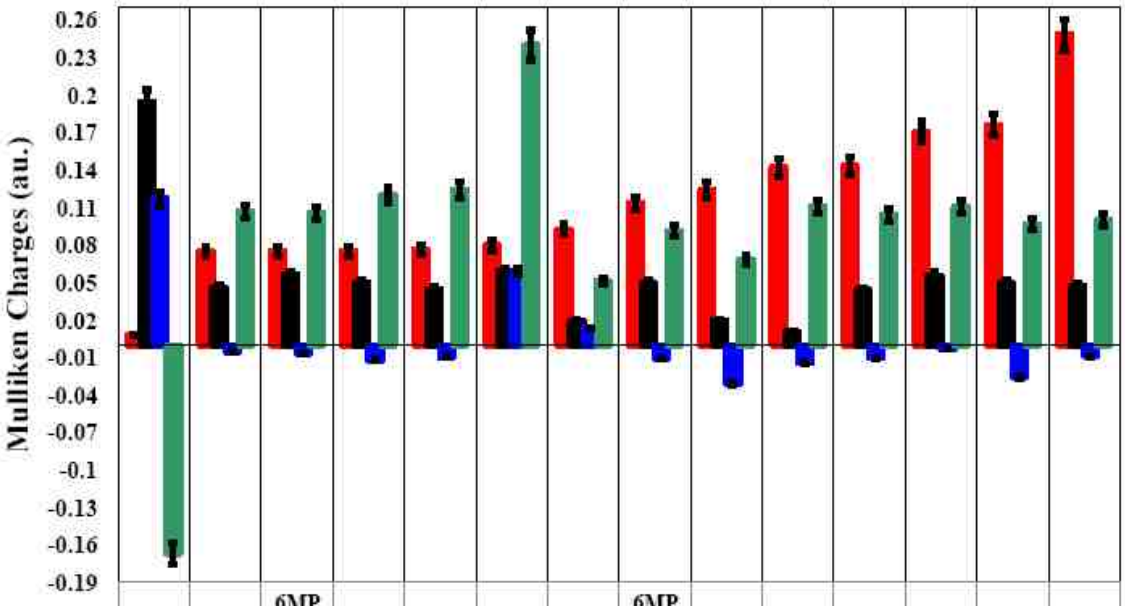


| | FT | XA | 6MP C8 | AL | HMP | PU C8 | FM | 6MP C2 | FA | AC | LU | HY | PU C2 | PU C6 |
|---|---|---|---|---|---|---|---|---|---|---|---|---|---|---|
| C-H | 0.008 | 0.0749 | 0.0751 | 0.0752 | 0.0762 | 0.0798 | 0.0925 | 0.1134 | 0.1241 | 0.1422 | 0.1436 | 0.1705 | 0.1761 | 0.2486 |
| TS | 0.1946 | 0.0461 | 0.0564 | 0.05 | 0.0448 | 0.0591 | 0.019 | 0.0492 | 0.0197 | 0.0107 | 0.0438 | 0.0556 | 0.0494 | 0.0472 |
| S-H | 0.117 | -0.005 | -0.007 | -0.012 | -0.01 | 0.0591 | 0.0137 | -0.011 | -0.031 | -0.014 | -0.01 | -0.003 | -0.025 | -0.009 |
| CRH | -0.167 | 0.1069 | 0.1057 | 0.1201 | 0.1241 | 0.24 | 0.0509 | 0.0913 | 0.0683 | 0.111 | 0.1042 | 0.1106 | 0.0966 | 0.1005 |

Figure 4.3.5. The mulliken atomic charges on the hydrogen ($\Delta q_H$) group was plotted as a function of the substrates (the symbols of the substrates were the same as Figure (4.3.2)). The Mulliken atomic charges on $H_{RH}$ were calculated, when $H_{RH}$ was at different locations ($C_{RH}$, C-H, TS, and S-H). The Mulliken atomic charges on $H_{RH}$, when $H_{RH}$ was bound to the substrate-binding site of unbound or free substrate, were represented by $C_{RH}$ (*shown by the green or fourth bars of respective substrate bound complexes*). The C-H represents, when $H_{RH}$ was still bound to the active site bound substrate (the $Mo^{(VI)}$-$O_{eq}$-$C_{CRH}$ meta-stable, *shown by the red or first bars of respective substrate bound complexes*). The TS represents, when $H_{RH}$ was on the transition state ($[C_{RH}$---$H_{RH}$---$S_{Mo}]^{\ddagger}$) structure (*shown by the black or second bars of respective substrate bound complexes*). The S-H represents, when $H_{RH}$ was completely transferred to the $S_{Mo}$ terminal ($Mo^{(IV)}$-$O_{eq}$-$C_{CR}$(-SH) meta-stable state, *shown by the blue or third bars of respective substrate bound complexes*). The plot was developed from the raw data provided in Table (A. 5).

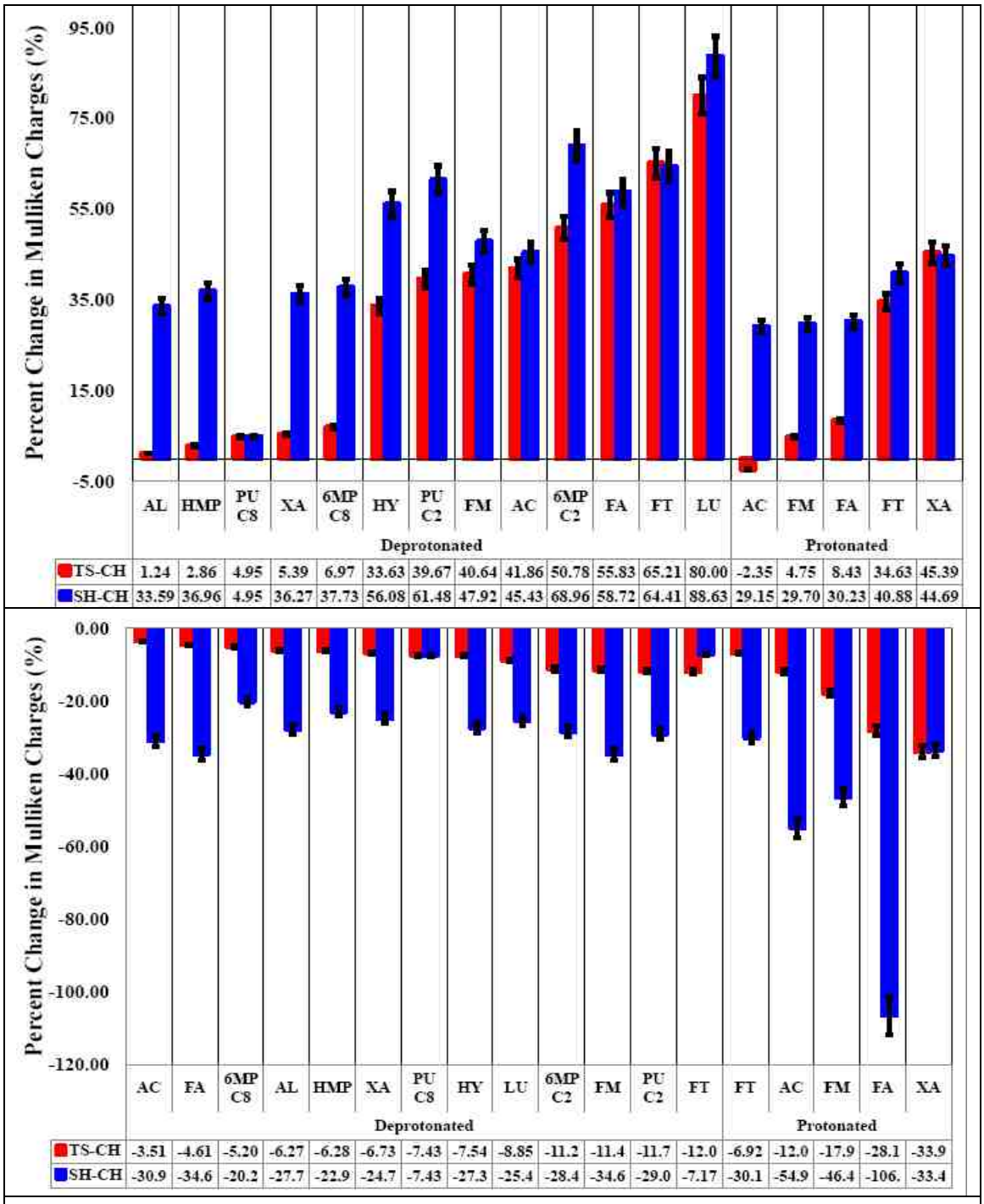


Figure 4.3.6. The percent change in Mulliken atomic charges, on the substrate carbon ($C_{RH}$) (*upper panel*) and $O_{eq}$ of $HO_{eq}$ terminal (*lower panel*), were plotted as a function of substrates. TS-CH represents [($\Delta q_{CRH}$) or ($\Delta q_{Oeq}$)] at the TS minus [($\Delta q_{CRH}$) or ($\Delta q_{Oeq}$)] at the C-H side. Similarly, SH-CH represents [($\Delta q_{CRH}$) or ($\Delta q_{Oeq}$)] at the S-H side minus [($\Delta q_{CRH}$) or ($\Delta q_{Oeq}$)] at the C-H side. The *red or first (rear)* and *blue or second (front)* bars of the respective substrate bound complex represent, respectively, the TS-CH and SH-CH. The charges were analyzed the same as Figure (4.3.5).

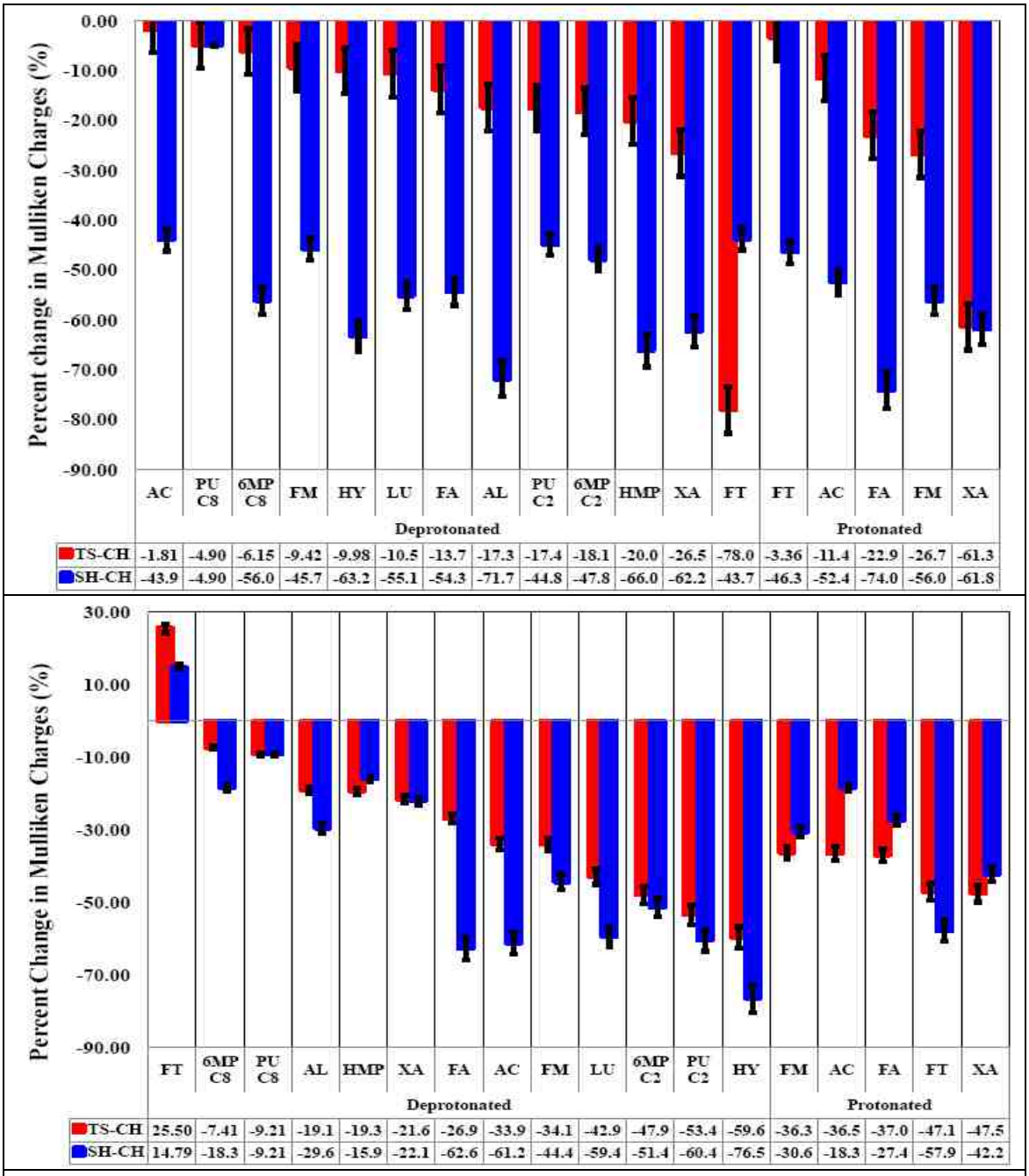


Figure 4.3.7. The percent change in Mulliken atomic charges, on the Mo ion (*upper panel*) and the sulfido ($S_{Mo}$) terminal (*lower panel*), were plotted as a function of substrates. TS-CH represents [($\Delta q_{Mo}$) or ($\Delta q_S$)] at the TS minus [($\Delta q_{Mo}$) or ($\Delta q_S$)] at the C-H. Similarly, SH-CH represents [($\Delta q_{Mo}$) or ($\Delta q_S$)] at the S-H minus [($\Delta q_{Mo}$) or ($\Delta q_S$)] at the C-H. The *red or first (rear)* and *blue or second (front)* bars of the respective substrate bound complex represent, respectively, the TS-CH and SH-CH. The charges were analyzed the same as Figure (4.3.6).

The bond order indices for the $O_{eq}$-$C_{RH}$, $S_{Mo}$-$H_{RH}$, $C_{RH}$-$H_{RH}$, and Mo-$O_{eq}$ bonds

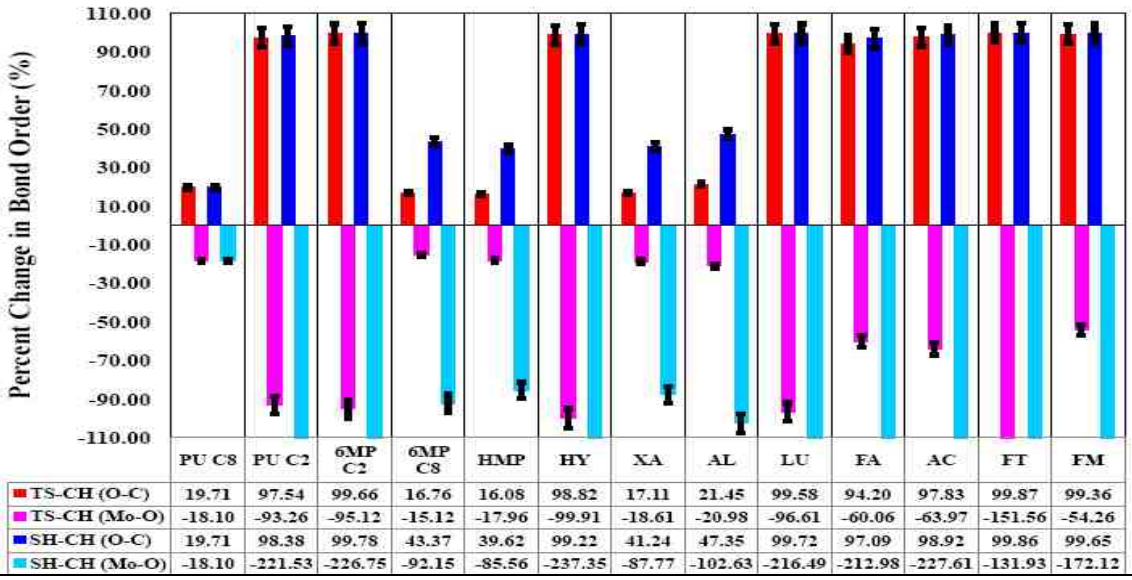


| | PU C8 | PU C2 | 6MP C2 | 6MP C8 | HMP | HY | XA | AL | LU | FA | AC | FT | FM |
|---|---|---|---|---|---|---|---|---|---|---|---|---|---|
| TS-CH (O-C) | 19.71 | 97.54 | 99.66 | 16.76 | 16.08 | 98.82 | 17.11 | 21.45 | 99.58 | 94.20 | 97.83 | 99.87 | 99.36 |
| TS-CH (Mo-O) | -18.10 | -93.26 | -95.12 | -15.12 | -17.96 | -99.91 | -18.61 | -20.98 | -96.61 | -60.06 | -63.97 | -151.56 | -54.26 |
| SH-CH (O-C) | 19.71 | 98.38 | 99.78 | 43.37 | 39.62 | 99.22 | 41.24 | 47.35 | 99.72 | 97.09 | 98.92 | 99.86 | 99.65 |
| SH-CH (Mo-O) | -18.10 | -221.53 | -226.75 | -92.15 | -85.56 | -237.35 | -87.77 | -102.63 | -216.49 | -212.98 | -227.61 | -131.93 | -172.12 |

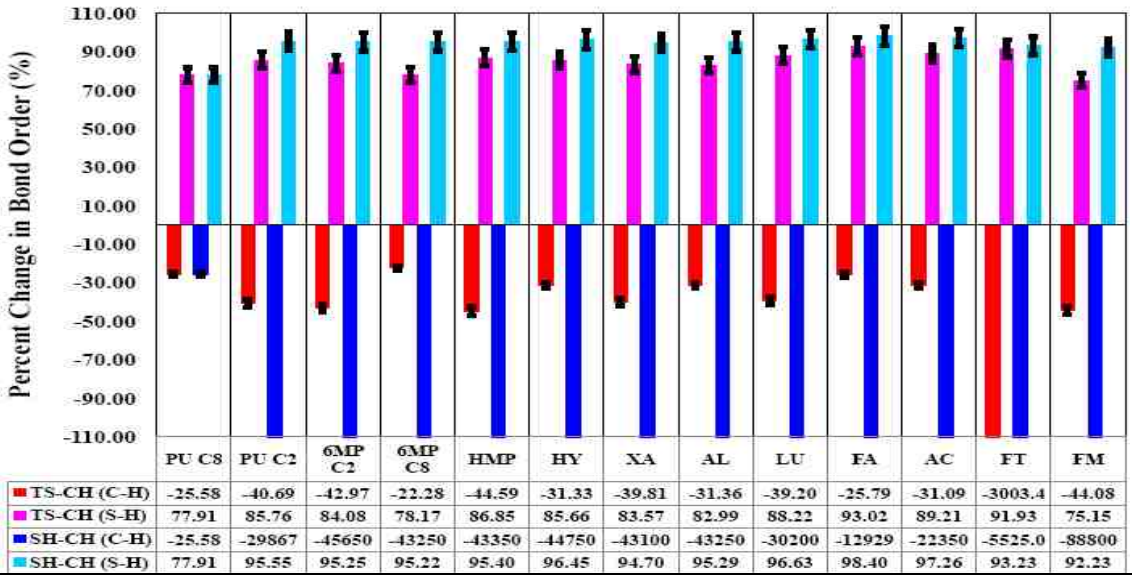


| | PU C8 | PU C2 | 6MP C2 | 6MP C8 | HMP | HY | XA | AL | LU | FA | AC | FT | FM |
|---|---|---|---|---|---|---|---|---|---|---|---|---|---|
| TS-CH (C-H) | -25.58 | -40.69 | -42.97 | -22.28 | -44.59 | -31.33 | -39.81 | -31.36 | -39.20 | -25.79 | -31.09 | -3003.4 | -44.08 |
| TS-CH (S-H) | 77.91 | 85.76 | 84.08 | 78.17 | 86.85 | 85.66 | 83.57 | 82.99 | 88.22 | 93.02 | 89.21 | 91.93 | 75.15 |
| SH-CH (C-H) | -25.58 | -29867 | -45650 | -43250 | -43350 | -44750 | -43100 | -43250 | -30200 | -12929 | -22350 | -5525.0 | -88800 |
| SH-CH (S-H) | 77.91 | 95.55 | 95.25 | 95.22 | 95.40 | 96.45 | 94.70 | 95.29 | 96.63 | 98.40 | 97.26 | 93.23 | 92.23 |

Figure 4.3.8. The percent change in Mayer bond orders, for the strengthening of [$O_{eq}$-$C_{RH}$ (or O-C)] and weakening of [Mo-$O_{eq}$(or Mo-O)] (*upper panel*) and strengthening of [$S_{Mo}$-$H_{RH}$ (or S-H)] and weakening of [$C_{RH}$-$H_{RH}$ (or C-H)] (*lower panel*) bonds, plotted as a function of substrates. The bond orders were calculated for the bonds, when $H_{RH}$ was at $C_{RH}$ (CH), $S_{Mo}$ (SH), and TS sides. TS-CH represents (Mo-O, O-C, C-H, or S-H) at the TS minus (Mo-O, O-C, C-H, or S-H) at the C-H. Similarly, SH-CH represents (Mo-O, O-C, C-H, or S-H) at the S-H minus (Mo-O, O-C, C-H, or S-H) at the C-H. The *red (first), pink (second), blue(third),* and *light blue (fourth)* bars of the respective substrate bound complex represent, respectively, the TS-CH (O-C or C-H), TS-CH (Mo-O or S-H), SH-CH (O-C or C-H), and SH-CH (Mo-O or S-H). The bond orders were analyzed the same as Figure (4.3.4).

## 4.4 Discussion and conclusion

### Description of results

*Characterization of the transition state structures:* The migration profile of the $H_{RH}$ from the $C_{RH}$ to $S_{Mo}$, through the transition state ((Enzyme)-[$Mo^{(VI)}$-$O_{eq}$-$C_{CRH}$---$H_{RH}$---($=S_{Mo}$)]$^{\#}$), was quantitated between (Enzyme)-[$Mo^{(VI)}$-$O_{eq}$-$C_{CRH}$] and (Enzyme)-[$Mo^{(IV)}$-$O_{eq}$-$C_{CR}$)] meta-stable states (Scheme 4.1.1). The structures between the meta-stable states were fully optimized to locate the position of $H_{RH}$ at the transition state structures, by replacing the $C_{RH}$ shown in Figure (A. 7) with various substrates (Figs. A. 8 – A. 18). The linear transit optimization scan was performed using a series of geometry optimizations at $Mo^{(VI)}$ oxidation state. The total energies (Table A. 3), from each optimization steps, were plotted against the respective ($H_{RH}$–$S_{Mo}$) distances (Fig. 4.3.1, *upper panel*). The total energy profile, analyzed for lumazine (Fig. 4.3.1), was a sample representation for the linear transit optimization scans (*upper panel*) and bond order profiles (*lower panel*). Similar profiles were also developed for the complexes, in the presence of other substrates using the data shown in Table (A. 3). The optimized structures from the linear transit optimization scans were used to compute the bond order profiles (Table A. 6). The bond order profiles were constructed to provide a rough estimate for the location of $H_{RH}$ at the transition state. From the bond order profile plot (Fig. 4.3.1, *lower panel*); the inflection point was regarded as an indicator for the location of $H_{RH}$ at the transition state. From the energy profile curve, the transition state was defined as a point at which the two energy curves cross each other. The position of $H_{RH}$, at the transition state, was also defined by the highest normalized energies. The energies, along the reaction coordinates, were shown for various substrates (Fig. 4.3.2). The energies were shown to vary depending on the type of substrates and the substrate-binding sites. Although the substrates were bound to the same active site terminal ($HO_{eq}$), the difference in binding sites was shown to allow the complexes to exhibit different energies. This could have been due to the covalency difference and the charges

transferred due to the binding of the $HO_{eq}$ terminal to the carbon centers of the substrates. In the presence of purine, the stabilization energies were shown to vary depending on the binding sites. The $C_6$-purine bound complex was shown to be more stable than the $C_2$-purine and $C_8$-purine bound complexes. The data indicated that, the transition state was stabilized by energies ($\Delta H^{\ddagger}$ ($E_{TS}$-$E_{CH}$)) ranging between 0.33 - 19.0 kcal/mol) (Fig. 4.3.2). The location of the highest energies was confirmed by performing frequency calculations. The electronic structure description, for the transition state structure, was characterized by one imaginary negative frequency (Fig. 4.3.3, *upper panel*). The protonated analogues were shown to have higher frequencies than the de-protonated analogues. In general, the frequencies were shown to depend on the conformation and binding sites of the substrates. As shown in Figure (4.3.3, *upper panel*), the positions and linear motions of the $H_{RH}$ were shown to vary from substrates' to substrates'. This was shown for all substrates, mainly, for those substrates that were bound to the active site model compound, through their $C_2$-pyrimidine (such as hypoxanthine and allopurinol). The extent of the metal characters, described by the percent ($Mo_{dxy}$), was provided in Figure (4.3.3, *lower panel*). With the exception of the complexes bound to the de-protonated substrates, all complexes bound to the protonated substrate and formamide, were shown to have their highest metal characters at their HOMO-1. On the other hand, all complexes bound to the de-protonated analogous had their highest metal characters at the HOMO. The data, therefore, revealed that the % $Mo_{dxy}$ of the HOMO for the unbound active site was about (2.5 %) and HOMO-1 was (3.9 %). This was consistent with the % $Mo_{dxy}$ values calculated for the tetrahedral Michaeli-Menten type complexes. At the transition state, the %$Mo_{dxy}$ for the complexes bound to the de-protonated and protonated substrates, respectively, were shown to change in the ranges between (15 – 28%) and (35 % – 55 %). The migration of $H_{RH}$ from $C_{RH}$ to $S_{Mo}$, through the transition state, was shown to cause some parametric changes. As shown in Figure (4.3.4, *upper panel*), the bond distances for $C_{CRH}$-$H_{RH}$ were much shorter than the $S_{Mo}$-$H_{RH}$ bonds. The optimized structures, from the linear transit optimization scans, were also used to compute the bond order indices (Table A. 6). As shown in Figure (4.3.4, *lower panel*), the bond orders for the $C_{CRH}$-$H_{RH}$ bonds were stronger for all substrates, with the exception to the complexes bound to the de-protonated formate, protonated acetaldehyde, xanthine, formaldehyde,

and formamide. The bond orders, in the presence of all substrates, revealed that the transition states were shown to exhibit a substrate type structure. That means, at the transition state, the bond orders for $C_{RH}$-$H_{RH}$ bonds were much stronger (Fig. 4.3.4). The bond orders for the $C_{CRH}$-$H_{RH}$ bonds, in the presence of the protonated analogues, were weaker than the bond orders for the complexes bound to the de-protonated substrates. On the other hand, the $S_{Mo}$-$H_{RH}$ bonds were shown to exhibit stronger bond orders for the complexes bound to the de-protonated substrates.

*The change of the Mulliken atomic charges on $H_{RH}$, $C_{RH}$, Mo, $O_{eq}$, and $S_{Mo}$ groups:* The changes in Mulliken atomic charges were computed in order to characterize the redox reactions and the paths of electron transfer from the substrate to Mo-center (Figs. 4.3.5 – 4.3.7). The change in Mulliken atomic charges were computed by calculating how much the charges on selected groups ($C_{RH}$, Mo, $O_{eq}$, and $S_{Mo}$) changed as $H_{RH}$ migrated from the $C_{CRH}$ (C-H) to the $S_{Mo}$ (S-H) terminal (Scheme 4.1.1). The Mulliken atomic charges on substrate bound hydrogen ($H_{RH}$), when $H_{RH}$ was at different locations ($C_{RH}$, C-H, TS, and S-H), was evaluated for all complexes (Fig. 4.3.5). The charges on $H_{RH}$ were small positive, when $H_{RH}$ was bound to the unbound (or free) substrates. The Mulliken atomic charge on $H_{RH}$ became more positive after the tetrahedral complex was formed. This was true for substrates that were bound through their $C_8$-imidazole sites (such as xanthine, 6MP, HMP, and purine). As the $H_{RH}$ moved closer to the transition state, the charges were shown to decrease (close to neutral). When $H_{RH}$ was at the transition state, the charges on $H_{RH}$ were positive (for all complexes bound to the de-protonated substrates) or small negative (for all complexes bound to the protonated substrates). The charges on $H_{RH}$, when $H_{RH}$ was on the S-H side, were also small negative or close to neutral (for all complexes bound to the protonated substrates, with the exception to formate, $C_8$-purine, and formamide). The percent change in Mulliken atomic charges, on the substrate ($C_{RH}$) carbon ($C_{CRH}$), was provided in Figure (4.3.6, *upper panel*). The Mulliken atomic charges on the substrate carbon ($C_{CRH}$), when ($H_{RH}$) was on the (C-H) side, were positive. The departure of $H_{RH}$ from the substrate carbon was accompanied by a buildup of more positive charges on its carbon center. The buildup of positive charges was expected to

serve as a driving force for the transfer of electrons via the $S_{Mo}$ or $HO_{eq}$ terminals. For some substrates (allopurinol, HMP, $C_8$-purine, xanthine, $C_8$-6MP, and protonated), the changes in charges were small positive. Similarly, the charges on $C_{CRH}$ were shown to increase progressively during the migration of $H_{RH}$ to the $S_{Mo}$ terminal. The percent changes in Mulliken atomic charges, on Mo ion, were provided in Figure (4.3.6, *lower panel*). The charge on Mo ion, when $H_{RH}$ was on C-H side, was large positive and shown to decrease during the migration of $H_{RH}$. When $H_{RH}$ was on the $S_{Mo}$ terminal, the charges became less positive, indicating the transfer of electron from the substrate to the ($Mo^{(VI)}$ center). The percent changes in Mulliken atomic charges, on the $O_{eq}$ group, were provided in Figure (4.3.7, *upper panel*). The charges on $O_{eq}$ were shown to increase progressively as $H_{RH}$ moved through the transition state to the $S_{Mo}$ terminal. That means the charges that were lost from the substrate carbon were transferred to $O_{eq}$. Finally, the percent change in Mulliken charges, on the $S_{Mo}$ terminal, was provided in Figure (4.3.7, *lower panel*). When $H_{RH}$ moved from C-H to TS, the charges on $S_{Mo}$ became more negative. In the presence of some substrates (allopurinol, HMP, $C_8$-purine, xanthine, $C_8$-6MP, and protonated), the changes in charges were shown to be small negative.

*The bond order indices for the $O_{eq}$-$C_{CRH}$, $S_{Mo}$-$H_{RH}$, $C_{CRH}$-$H_{RH}$, and Mo-$O_{eq}$ bonds:* The change in bond order indices, for the formation of an $O_{eq}$-$C_{CRH}$ bond (with concomitant weakening of Mo-$O_{eq}$ bond) and the dissociation of a $C_{CRH}$-$H_{RH}$ bond (concomitant formation of $S_{Mo}$-$H_{RH}$ bond), were computed by calculating how much the bond strength changed as $H_{RH}$ moved from C-H side to the $S_{Mo}$ terminal (S-H side) (Fig. 4.3.8). The change in bond orders, for the $O_{eq}$-$C_{CRH}$ and Mo-$O_{eq}$ bonds were provided in Figure (4.3.8, *upper panel*). The percent change in bond order for the $O_{eq}$-$C_{CRH}$ bond, when $H_{RH}$ was on the TS side, was shown by an increase in bond order strength. On the other hand, the percent changes for the weakening of Mo-$O_{eq}$ bond was shown by a decrease in bond order strengths. The bond order for Mo-$O_{eq}$ started as a strong bond and became weaker than the bond order for Mo-$O_{eq}$ after $H_{RH}$ was at the TS. After $H_{RH}$ was transferred to the S-H side, the Mo-$O_{eq}$ bond was weaker. As the $H_{RH}$ was moving towards the transition state, the $O_{eq}$-$C_{CRH}$ bond strength was shown to increase. Eventually, the bond order was

shown to become much stronger after $H_{RH}$ was completely transferred to the $S_{Mo}$ terminal. However, the extent of the bond order was lower for allopurinol and those substrates that were bound through their $C_8$-imidazole. Similarly, the percent change in bond orders for $C_{CRH}$-$H_{RH}$ and $H_{RH}$-$S_{Mo}$ were provided in Figure (4.3.8, *lower panel*). The bond orders, for $H_{RH}$-$S_{Mo}$ bonds, were shown to become stronger after $H_{RH}$ migrated from C-H to TS side. The weaker bond orders shown for the $C_{CRH}$-$H_{RH}$ bonds, after $H_{RH}$ moved from C-H to TS side, were proposed to indicate the tendency of the $C_{CRH}$-$H_{RH}$ bond to rupture.

Survey of the transition state structures

The electronic structure description for the transition state, when $H_{RH}$ migrated from $C_{CRH}$ to $S_{Mo}$, was characterized by one imaginary negative frequency. The frequencies and intensities were shown to depend on the conformation and binding-sites of the substrates. The variation in the activation energy for all complexes was due to the absence of the factors that were supposed to stabilize the charge accumulation. Some purine derivatives were shown to provide the complexes much lower barriers than the aldehydes, formamide, and formate. The highest barriers on the complexes were due to the charge delocalization on the carbonyl carbons of the aldehydes, formamide, and formate. The large increase, in the activation energy, was shown for some complexes (in the presence of less reactive substrate). The bond distances, at the transition state, revealed that the $C_{CRH}$-$H_{RH}$ bond distances were much shorter compared to the $S_{Mo}$-$H_{RH}$ bonds. This indicated that, the transition state structure was a substrate type rather than a product type. The bond order profile was also constructed to provide a rough estimate for the location of $H_{RH}$ at the transition state. Accordingly, the bond order for $C_{CRH}$-$H_{RH}$ bond (when $H_{RH}$ was on the C-H side) was shown to become much stronger, indicating the substrate type nature of the transition states. However, the bond orders for the $C_{CRH}$-$H_{RH}$ bonds were weaker for the complexes bound to the protonated substrates. The charge flow was also monitored in order to characterize the redox reactions and the transfer of electrons from substrates to the $(E_{OX})$-$Mo^{(VI)}$ center. As a result, the oxidation or

hydroxylation of the substrates were shown to be accompanied by the charge transfer and change in the oxidation state of the $(E_{OX})$-$Mo^{(VI)}$ center. The charge on $(E_{OX})$-$Mo^{(VI)}$ center was shown to decrease by accepting the electrons transferred from the substrates. During the formation of the tetrahedral complex, the carbon on the substrate became more positive by losing electrons to the $(E_{OX})$-$Mo^{(VI)}$ center via the $O_{eq}$ or $H_{RH}$ group. The charge on $O_{eq}$ group was shown to increase and became more positive by receiving a partial charge from the substrate carbon. During the formation of a tetrahedral complex, the $S_{Mo}$ terminal was shown to exhibit a buildup of partial charges transferred from $(E_{OX})$-$Mo^{(VI)}$ center. When the Michaelis-Menten type tetrahedral complex was formed, the $H_{RH}$ started as a small positive (when bound to the $C_{RH}$) and became neutral (when $H_{RH}$ was at the transition state). Finally, the charge on $H_{RH}$ became less positive (or close to neutral) after $H_{RH}$ was transferred to the $S_{Mo}$ terminal. That means $H_{RH}$ was shown to depart from the substrate as a positively charged entity. The complexes were shown to spend most of their time, at the transition state, by behaving as a substrate bound rather than product bound entities. At the transition state, the formation of $O_{eq}$-$C_{CRH}$ bond was shown to be nearly completed. The transfer of $H_{RH}$ from $C_{RH}$ to $S_{Mo}$ was proposed to take place after the formation of the tetrahedral transition state. The $O_{eq}$-$C_{CRH}$ and $C_{CRH}$-$H_{RH}$ bond orders were also shown to be more substrate like for the complexes that were bound to the substrates with higher $k_{cat}$ values. However, the rate of the formation of the tetrahedral transition state species was predicted to be higher for complexes that were bound to those substrates that were shown to have higher $k_{cat}/k_m$ values. In summary, the variations in bonding descriptions were shown to be dictated by the position of $H_{RH}$ at the transition state. Because the $C_{CRH}$-$H_{RH}$ bond distances varied significantly (after $O_{eq}$-$C_{CRH}$ bond was formed), the position of $H_{RH}$ and cleavage of $C_{CRH}$-$H_{RH}$ bonds (at the transition state) were proposed to depend on the type of substrates and the substrate-binding sites.

Chapter 5.0

Overview of the reductive half-reaction catalytic cycle

The catalytic transformation of the substrates ($C_{RH}$) to their products (O-$C_{CR}$), as shown in Scheme (5.1.1), were expected to pass through the Michaelis-Menten type (Structure b) and transition state (Structure c) complexes. The transformation was expected to take place with or without the formation of Structure (d). The intermediate (Structure d) may then undergo a transformation (a stepwise one electron or two electrons oxidation) to form a Structure (j). During the catalytic transformation, the three major events described in Scheme (5.1.1) were expected to take place.

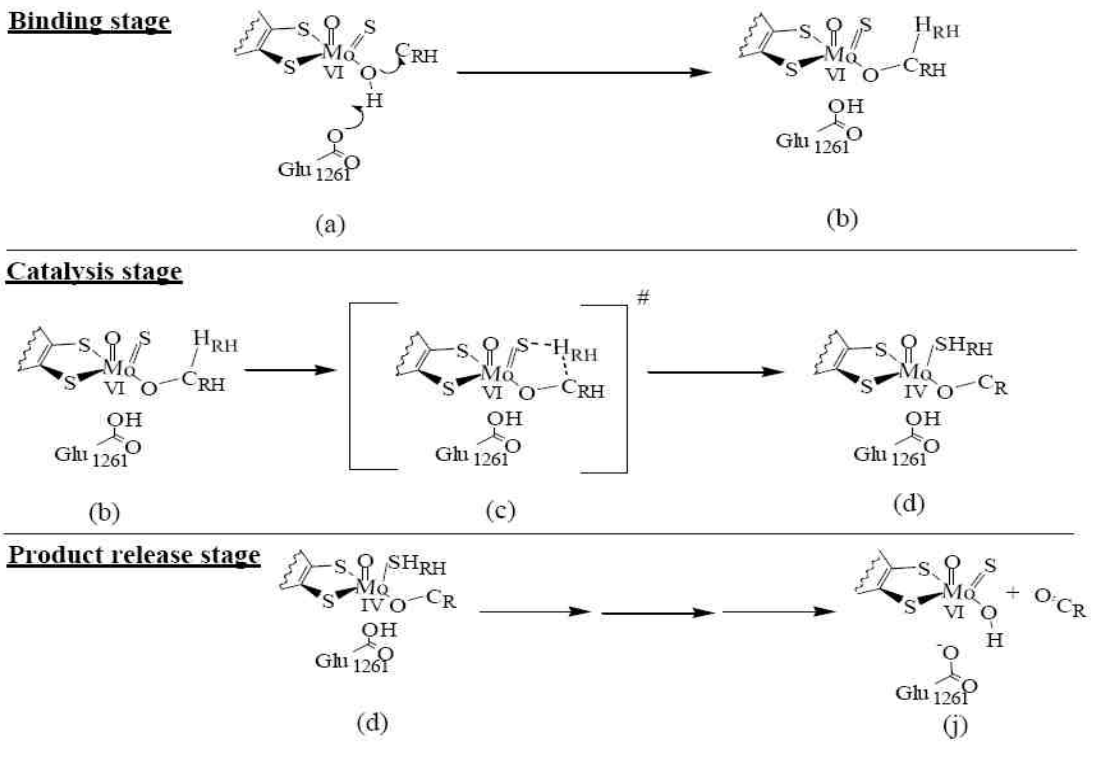


$$E_{OX} + C_{RH} \underset{}{\overset{Binding}{\rightleftarrows}} E_{OX} - C_{RH} \xrightarrow{Catalysis} E_{RED} - C_R \xrightarrow{Release} E_{RED} + O{-}C_R$$

Scheme 5.1.1. A hypothetical schematic model for the oxidation of substrates ($C_{RH}$) by XOR enzymes. The model represents the catalytically crucial elements of the reductive-half reaction.

*The substrate-enzyme binding stage:* In order for the interaction between the reactants ($C_{RH}$ and $E_{OX}$) to take place, the substrates were expected to enter the binding pocket and attain a proper orientation (Scheme 5.1.1, Structure a). The binding pocket amino acid residues were expected to assist the near attack conformation (NAC), by promoting a hydrogen bonding micro-environment. As shown in Scheme (5.1.2), the substrate-binding site of lumazine ($C_7$-pyrazine) was orientated in a close proximity to the $HO_{eq}$

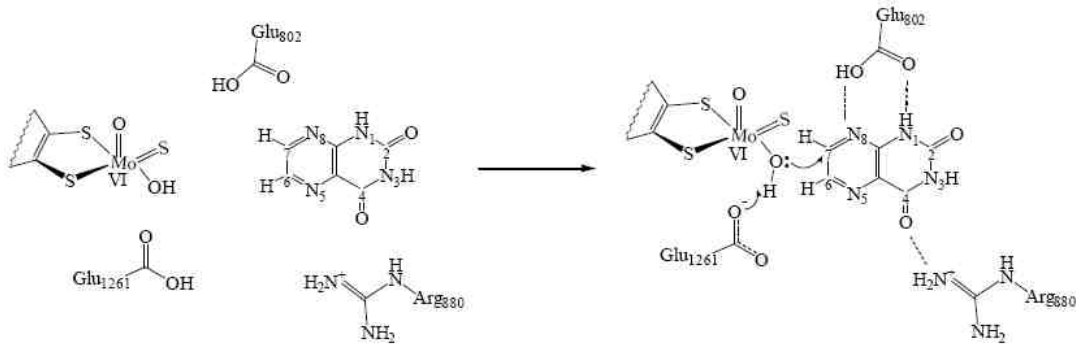


Scheme 5.1.2. A hypothetical representation of the NAC and hydrogen bonding micro-environment, in the presence of lumazine, modulated by the binding pocket amino acid residues.

terminal of the active site. The carbonyl oxygen on the $C_4$ of the pyrimidine ring of lumazine was oriented towards [XOR]-$Arg_{880/130}$, similar to the orientation of xanthine. Once the substrates were modulated to attain the proper orientation, the activation of the $HO_{eq}$ terminal took place after the $H_{OH}$ was abstracted from the $HO_{eq}$ terminal. The abstraction of the $H_{OH}$ from $HO_{eq}$, by [XOR]-$Glu_{1261/730}$, was proposed to take place in one of the three routes (Fig. 5.1.1, *left panel*). If the abstraction was to take place before the nucleophilic attack (Structure i-b), the unstable oxyanion ($Ö^{-}_{eq}$) was expected to lead to the formation of either Structures (c or d). In this case, the unstable $Ö^{-}_{eq}$ was shown to undergo a nucleophilic attack, on the substrate carbon ($C_{CRH}$), to form Structure (d). On the other hand, Structure (c) was not feasible due to the likely formation of an unrealistic

equatorial oxo ligand ($Mo^{(VI)}=O_{eq}$). If a nucleophilic attack was to take place before the abstraction of $H_{OH}$, a high energy barrier was created due to the formation of a positive

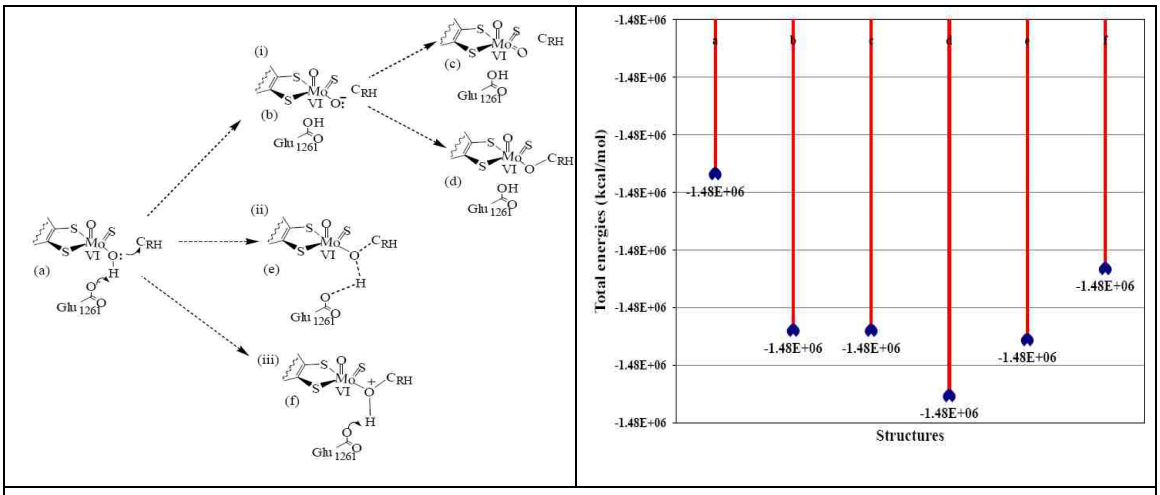


Figure 5.1.1. A hypothetical scheme for the de-protonation of $H_{OH}$ from $OH_{eq}$ by [XOR]-$Glu_{1261}$ (*left panel*). The de-protonation of $H_{OH}$ was proposed to take place before (i-b), during (ii-e), and after (iii-f) the nucleophilic reaction took place. The total energies (*right panel*) were described for the structures shown in the *left panel*. The structures were optimized by replacing $C_{RH}$ with xanthine.

charge density (Structure f). Similarly, the concerted formation of Structure (e) was shown to be less favorable due to the charge neutralization on the nucleophile ($Ö^{-}_{eq}$). As shown in Figure (5.1.1, *right panel*), higher energy barriers were observed for Structures (c, e, and f). Therefore, in the most favorable pathway, the [XOR]-$Glu_{1261}$ was expected to act as a general base. Therefore, as shown in Scheme (5.1.3), the abstraction of $H_{OH}$ from $HO_{eq}$ terminal was essential in enhancing the nucleophilicity of the $Ö^{-}_{eq}$ terminal. In addition to the orientation of the substrates, the substrate-binding sites were also shown to affect the activities of the enzymes. As such, the binding sites of the heterocyclic molecules were located on the $C_8$-imidazole (HMP and xanthine), $C_2$-pyrimidine (hypoxanthine, allopurinol, and 6MP), $C_6$-pyrimidine (purine), and $C_7$-pyrazine (lumazine). Unlike the purine derivatives, mainly directed by recognition of the 1, 3-diazine ($N_1$ or $N_3$) of pyrimidine or 7, 9-imidazole ($N_7$ or $N_9$) imidazole, the binding

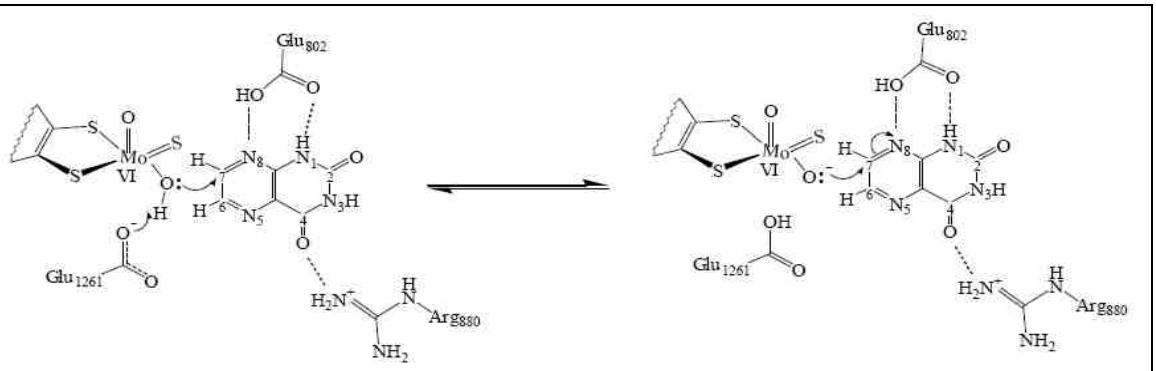

Scheme 5.1.3. The abstraction of $H_{OH}$ by the de-protonated (XOR)-$Glu_{1261}$ and nucleophilic attack of the oxyanion ($\ddot{O}^{-}_{eq}$) on the $C_7$-lumazine.

of lumazine (at $C_7$ position) was not directed by recognition of the 5, 8-diazine ($N_5$ or $N_8$) of the pyrazine ring. When $\ddot{O}^{-}_{eq}$ was bound to the $C_7$ of lumazine, a negative charge density was proposed to be created on the $N_8$ of 5, 8-diazine (Scheme 5.1.4). The Mulliken atomic charges on the $C_{CRH}$ site of the unbound (free) substrate were shown to increase after the $\ddot{O}^{-}_{eq}$ was bound to $C_{CRH}$. The abstraction of an acidic proton by [XOR]-$Glu_{1261}$ was expected to lower the activation barrier for the formation of a tetrahedral Michaelis-Menten type complex (Scheme 5.1.4). On the contrary, the charges on Mo-

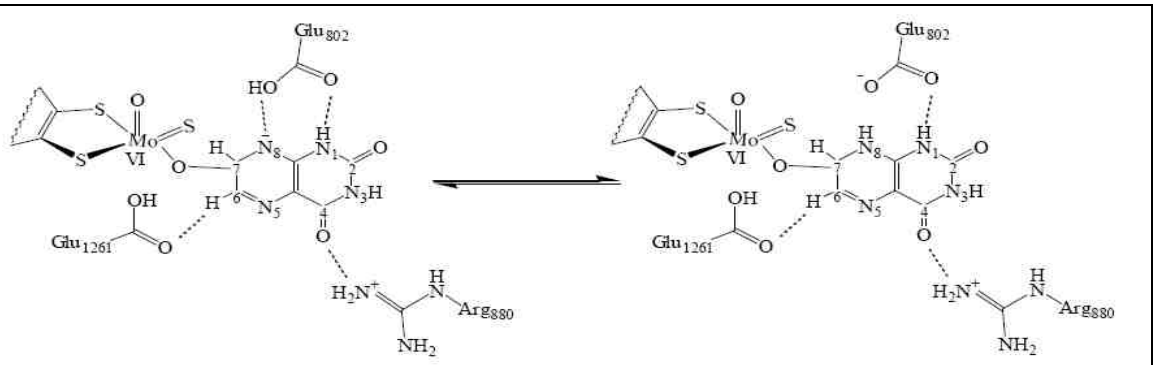

Scheme 5.1.4. The formation of the Michaelis-Menten type complex, resulting the nucleophilic reaction and formation of $O_{eq}$-$C_7$-lumazine bond.

centers were shown to maintain the same oxidation number and exhibit a very small decrease in Mulliken atomic charges. Therefore, the transfer of $H_{OH}$ to the de-protonated [XOR]-$Glu_{1261}$ was proposed to be a key element that lowered the activation barrier for the formation of tetrahedral Michaelis-Menten type and transition state complexes.

*The catalysis stage:* As shown by the overall catalytic mechanism (Scheme 5.1.1), the mechanistic transformation of the tetrahedral Michaelis-Menten type complex (Structure b) to the product bound intermediate (Structure d) was expected to pass through the tetrahedral transition state (Structure c). Following the $sp^2 \rightarrow sp^3$ re-hybridization of the carbon atom of the substrate-binding site, the events that took place at the transition state (such as the transfer of $H_{RH}$ from $C_{RH}$ to $S_{Mo}$, the reduction of $Mo^{(VI)}$ into $Mo^{(IV)}$, and the conversion of the substrate to product) were evaluated using a DFT level calculations (as described in Appendix VI (Figs. A. 7 – A. 18). Since the postulated transition state complex (Structure c) was located above the two meta-stable states (Structures b and d), the transfer of $H_{RH}$ from $C_{RH}$ to $S_{Mo}$ and allocation of two electrons at Mo-center were probed. The bonding descriptions for the consumption of the substrates were provided in terms of ionicity (Mulliken atomic charges) and covalency (bond multiplicity). The changes in Mulliken atomic charges ($\Delta q$), on the selected groups ($H_{RH}$, $C_{CRH}$, Mo, $O_{eq}$, and $S_{Mo}$), were shown to exhibit similar trends. As described in Figure (5.1.2, *first panel*), the charge on Mo ion (when $H_{RH}$ was on the C-H side) was a large positive (about +0.648557 au.). After the $H_{RH}$ was transferred to the $S_{Mo}$ terminal (S-H side), the charge was shown to decrease to about +0.399709 au. As shown by the linear motion of $H_{RH}$, the charge landscape was shown to change by +0.248848 au. The charge at the transition state (TS) complex (or, the inflection point) was +0.512712 au., a decrease of +0.135845 au. Similarly, after $H_{RH}$ was transferred to the $S_{Mo}$ terminal, the charge on Mo ion was also shown to decrease by about +0.113003 au. The charge reduction, shown on the Mo-center, was proposed to be driven by the charge variation observed on the substrate carbon ($C_{CRH}$). As a result, when $H_{RH}$ was at the C-H side, the Mulliken atomic charge on the substrate carbon ($C_{CRH}$) was small positive (+0.289713 au.). The charge was also

shown to increase, progressively, as $H_{RH}$ migrated through the transition complex to the $S_{Mo}$ terminal. When $H_{RH}$ moved from the C-H side to the TS side, a positive charge buildup was observed on $C_{CRH}$. Similarly, when $H_{RH}$ was on S-H side, the charges on $C_{CRH}$ were shown to increase. After $H_{RH}$ was transferred to the $S_{Mo}$ terminal, the charge

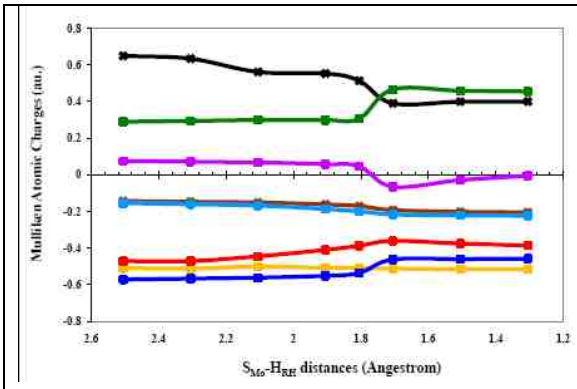


Xanthine

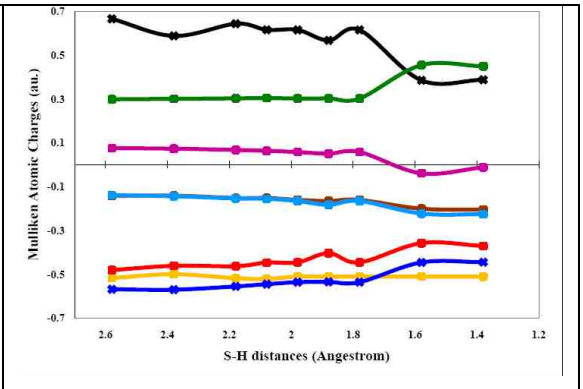


Allopurinol

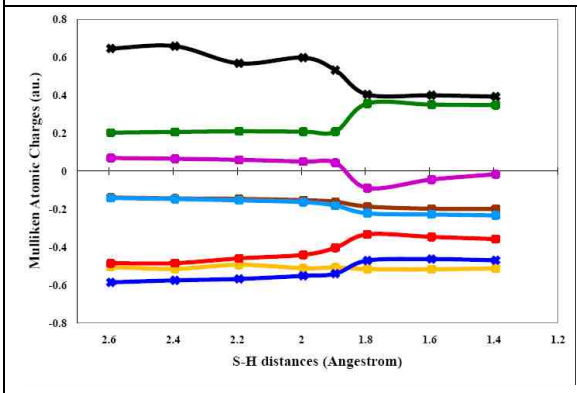


Lumazine

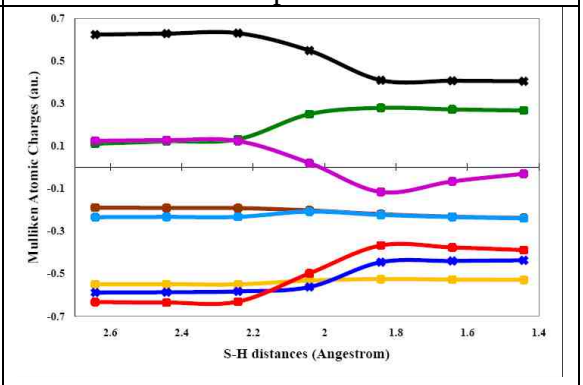


Formaldehyde

Figure 5.1.2. The changes in Mulliken atomic charges ($\Delta q$) on the selected groups: $H_{RH}$ (*purple or third traces, at 1.4 Å from top to bottom* ), $C_{CRH}$ (*green or second traces, at 1.4 Å from top to bottom*), Mo (*black or first traces, at 1.4 Å from top to bottom*), $O_{eq}$ (*blue or second traces, at 1.4 Å from bottom to top*), $S_{Mo}$ (*red or third traces, at 1.4 Å from bottom to top*), $O_{apical}$ (*yellow or first traces, at 1.4 Å from bottom to top*), $S_{dithiolene\ trans\ to\ sulfido\ terminal}$ (*light blue or fourth traces, at 1.4 Å from bottom to top*), and $S_{dithiolene\ trans\ to\ water\ terminal}$ (*brown or fourth traces, at 1.4 Å from bottom to top*). The Mulliken atomic charges were calculated during the linear motion of $H_{RH}$ from $C_{RH}$ (C-H) through the transition state (TS) to the $S_{Mo}$ terminal (S-H). The plots were developed from the raw data provided in Table (A . 9).

landscape was shown to change by +0.16492 au. As shown by the charge profile plots, when $H_{RH}$ was at the transition state, the change in Mulliken atomic charges on Mo ion was shown to decrease by 20%. Correspondingly, the changes on $C_{CRH}$ sites were shown to increase by about 5.69%. When $H_{RH}$ moved from TS to the $S_{Mo}$ terminal, the charges on Mo and $C_{CRH}$ groups were shown, respectively, to decrease by about 22% and increase by about 48%. Although the changes in Mulliken atomic charges were shown to indicate the charge variation on the respective groups, the changes were not able to indicate the direction of electron flow. The direction of electron flow, through one of the two possible super-exchange pathways ($C_{CRH}$-$O_{eq}$-$Mo^{(VI)}$ or $C_{CRH}$---$H_{RH}$---$S_{Mo}$-$Mo^{(VI)}$), were then described using the behavior of Mulliken atomic charges on the three groups ($H_{RH}$, $O_{eq}$, and $S_{Mo}$). At the transition state, the Mulliken atomic charge on $O_{eq}$ was shown to increase by about 6%. That means, some portion of the charges that were lost from the substrate carbon were proposed to be transferred to the $O_{eq}$ group. Similarly, when $H_{RH}$ was on the $S_{Mo}$ terminal, the percent reduction of the charges on $O_{eq}$ group was shown to increase by about 14%. The increase in Mulliken atomic charge, on $O_{eq}$ group, was shown to reflect the buildup of negative charges. The buildup of negative charges, after the formation of the tetrahedral complex, was proposed to be a driving force for the allocation of electrons on Mo-center. After $H_{RH}$ was completely transferred to $S_{Mo}$, the charges on $O_{eq}$ group were shown to decrease by about 19%. That means some of the charges that were lost from the substrate carbon must have been allocated on the Mo-centers, through the bridging $O_{eq}$ group. In addition to $O_{eq}$ group, when $H_{RH}$ was in the transition state, the charge on $H_{RH}$ group was shown to decrease by about 38%. The charge on the $H_{RH}$ group, when $H_{RH}$ was on the C-H side, was small positive. However, when $H_{RH}$ migrated to the transition state, the charges became less positive (close to neutral and small negative). The charges on $H_{RH}$ group, when $H_{RH}$ was on the S-H side, became negative or close to zero (for almost all protonated substrates with the exception to formate, $C_8$-purine, and formamide). If electrons were transferred from the $C_{CRH}$, through the $H_{RH}$ group, a buildup of small partial charge was observed on the $H_{RH}$ group. Similarly, when $H_{RH}$ was at the transition state, the Mulliken charges on the $S_{Mo}$ terminal was shown to increase by about 17%. However, when $H_{RH}$ was on the $S_{Mo}$ terminal, there was no significant change on the $S_{Mo}$ group. This reflected the inability of the $S_{Mo}$ group

to serve as a nucleophile. As described above, at the transition state, the charges on the Mo-center was shown to decrease by about 0.2486 au., $C_{CRH}$ group to increase by about 0.16492 au., and $O_{eq}$ group to decrease by about 0.113251 au. The net change on the $O_{eq}$ and $C_{CRH}$ groups was about +0.2815 au. Since the net change on $H_{RH}$ was +0.028715 au., the actual charge that was unaccounted was about +0.136205 au. After the de-protonation of $H_{OH}$ from $HO_{eq}$ by [XOR]-$Glu_{1261}$, one electron was made available for the substrate carbon ($C_{CRH}$). The remaining two electrons were shown to account for the Mo-$O_{eq}$ bond formation. That means, there were no additional electrons available to allocate two electrons on $Mo^{(VI)}$-center, as ($H^+ + 2e^-$), through the $C_{CRH}$-$H_{RH}$-$S_{Mo}$-$Mo^{(VI)}$ super-exchange pathway. The difference between the two proposed pathways, shown in Schemes (4.1.2, a and b), was the direction of electron flow. The neutral charge on $H_{RH}$, at the transition state (Figs. 4.3.5), was shown to favor the hydrogen atom transfer mechanism (Schemes 4.1.2, c and 5.1.5). Since the high oxidation state on Mo-center was expected to create a decrease in electron density on $S_{MO}$, the effect was expected to serve as a driving force for the transfer of $H_{RH}$ atom from $C_{RH}$ to the $S_{Mo}$ terminal. If this was the case, one of the electrons was expected to be transferred from the substrate to the $Mo^{(VI)}$-center through $\ddot{O}^{-}_{eq}$ group. The second electron was expected to be transferred to the Mo-center from $S_{Mo}$ terminal. The $S_{Mo}$ terminal was then expected to regenerate the electron that was lost to $Mo^{(VI)}$-center, from the hydrogen atom that was transferred from the substrate. Unlike the hydride transfer ($H^+ + 2e^-$), that was proposed to favor an outer-sphere mechanism, the transfer of a hydrogen atom was proposed to take place through an inner-sphere mechanism. The hydride transfer mechanism, proposed in Schemes (1.1.3 and 4.1.2 (b)), was not feasible since the $H_{RH}$ was proposed to behave as a leaving group. If electron transfer was proposed to occur by an outer-sphere mechanism, the electron- and proton-transfer steps were expected to be uncoupled kinetically. As a result, the migration of a proton and flow of an electron were expected to take place, at different time scale, through the $C_{CRH}$-($H_{RH}$-$S_{Mo}$)-$Mo^{(VI)}$ super-exchange pathway. In the case of a hydride transfer ($H^+ + 2e^-$), the electron and proton were expected to originate from different orbitals. On the other hand, in hydrogen atom transfer process, the proton and an electron were expected to originate from the same atom and orbitals. In the hydrogen atom transfer, as shown in Scheme (5.1.5), the transfer of $H_{RH}$ and an electron were

expected to depend on the kinetics and thermodynamics of the electron flow and the position of $H_{RH}$, at any time scale. As a result, it was suitable to label the hydrogen and electron transfer as shown in Scheme (4.1.1, c) rather than Scheme (4.1.1, a or b).

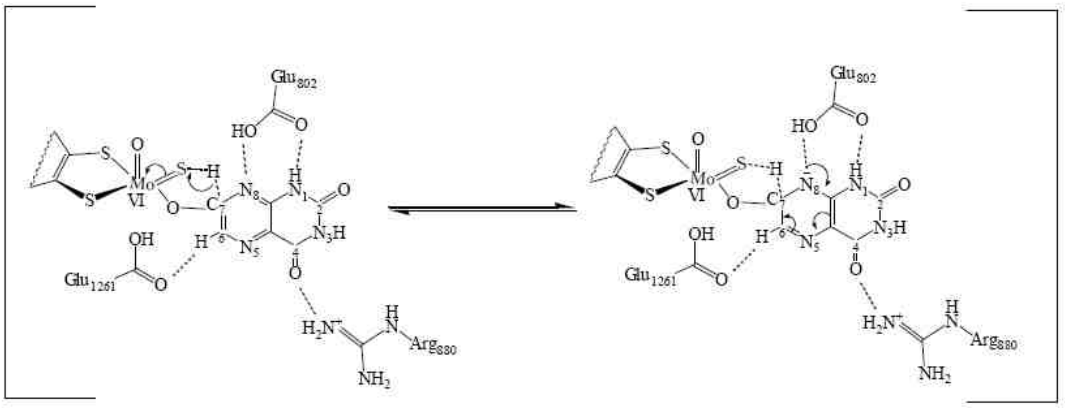


Scheme 5.1.5. A hypothetical description for the transition state structure that involved the transfer of substrate proton ($H_{RH}$) from $C_{RH}$ to $S_{Mo}$ terminal.

Therefore, in the course of the reaction, an electron was proposed to be transferred from the $C_{CRH}$ of the substrate to Mo-center, through the $C_{CRH}$-$O_{eq}$-$Mo^{(VI)}$ super-exchange pathway, with concomitant transfer of a hydrogen atom. The effect of ionicity and consumption of charges, on the major groups (Mo, $C_{CRH}$, $H_{RH}$, $O_{eq}$, and $S_{Mo}$), were associated with the respective covalent bonds. The weakening or strengthening of the covalent bonds was described using the Mayer bond order indices. The bond order indices were also used to locate the position of $H_{RH}$ at the transition state, using the inflection point as an indicator (Fig. 4.3.1). The bond order profile was also used to relate the formation of $O_{eq}$-$C_{CRH}$ to the cleavage of Mo-$O_{eq}$ bond and the cleavage of $C_{CRH}$-$H_{RH}$ bond to the formation of $S_{Mo}$-$H_{RH}$ bond (Fig. 4.3.8 - 4.3.9). The bond order profile, for the immediate bonds associated during the transformation of Structure (b) to (d) through (c) (shown in Scheme (5.1.1), was described in Figure (5.1.3). During the formation of the transition state tetrahedral species, the first bond formed was the $O_{eq}$-$C_{CRH}$ bond. As

shown in Scheme (5.1.3, *first panel*), when $O_{eq}$ was bound to $C_{CRH}$, the bond order for $O_{eq}$-$C_{CRH}$ was 1.08 au. This was about 17% weaker than the bond order for $O_{eq}$-$C_{CRH}$ (1.303 au.), when $H_{RH}$ was at the transition state. Similarly, the bond strength for the $O_{eq}$-$C_{CRH}$ bond, when $H_{RH}$ was at the $S_{Mo}$ terminal, was about 41% stronger. The $O_{eq}$-$C_{CRH}$

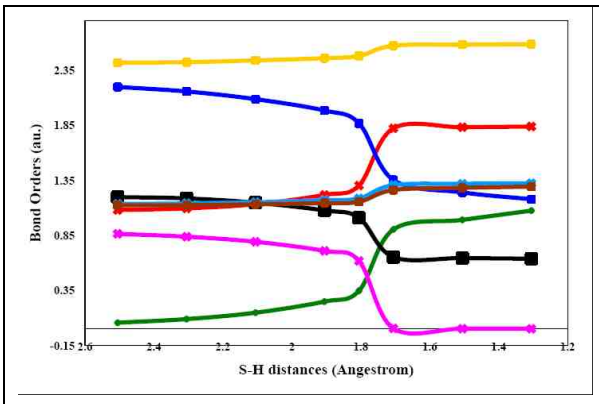


Xanthine

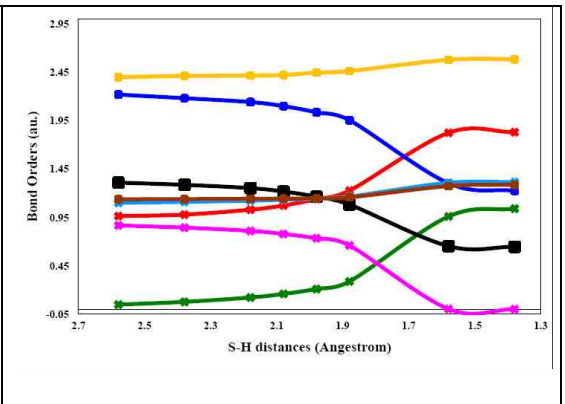


Allopurinol

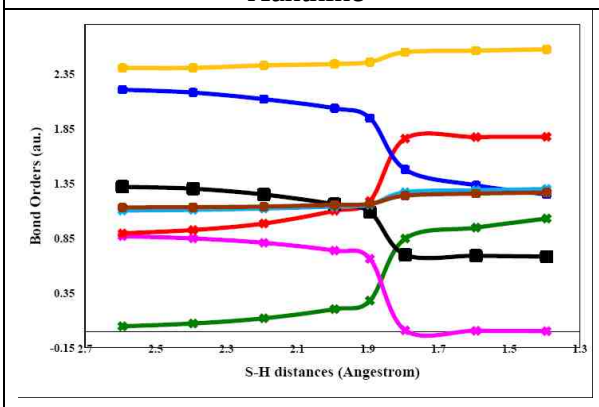


Lumazine

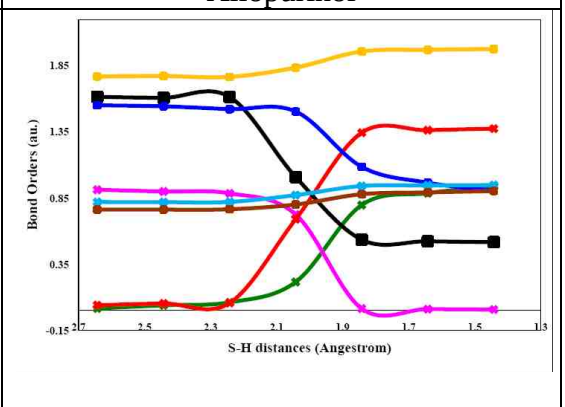


Formaldehyde

Figure 5.1.3. The bond order profile for the transformation of Structure (b) to (d) through (c) (Scheme 5.1.1). The profile was used to relate the formation of $O_{eq}$-$C_{CRH}$ (*red or second traces, at 1.4 Å from top to bottom*) to the cleavage of Mo-$O_{eq}$ (*black or second traces, at 1.4 Å from bottom to top*) bonds and the cleavage of $C_{CRH}$-$H_{RH}$ (*pink or first traces, at 1.4 Å from bottom to top*) to the formation of $S_{Mo}$-$H_{RH}$ (*green or third traces, at 1.4 Å from bottom to top*) bonds. The bond order profile for the bonds that were not directly associated with the formation and cleavage of bonds was also described, such as Mo-$S_{Mo}$ (*blue or second traces, at 2.6 Å from top to bottom*), Mo-$O_{apical}$ (*yellow or first traces, at 1.4 Å from top to bottom*), Mo-$S_{dithiolene\ trans\ to\ sulfido\ terminal}$ (*brown or fourth traces, at 1.4 Å from bottom to top*), and Mo-$S_{dithiolene\ trans\ to\ water\ terminal}$ (*light blue or fourth traces, at 1.4 Å from bottom to top*). The bond orders were computed to determine how much the bond strengths changed as $H_{RH}$ migrated from $C_{RH}$ (C-H) through the transition state (TS) to the $S_{Mo}$ terminal (S-H).

bond formation was expected to be accompanied by the cleavage of Mo-$O_{eq}$ bond. The bond order for Mo-$O_{eq}$, when $H_{RH}$ was at C-H side, was stronger by about 1.198 au. The bond order then decreased by about 16% and 46%, respectively, after $H_{RH}$ migrated to the TS side and $S_{Mo}$ terminal. When $H_{RH}$ was at transition state, the $O_{eq}$-$C_{CRH}$ and Mo-$O_{eq}$ bonds were described, respectively, by stronger and weaker bonds. Similarly, when $H_{RH}$ was at the C-H side, the initial bond order for the $C_{CRH}$-$H_{RH}$ bond was shown to start as a strong bond (0.864 au.). The bond order for the $C_{CRH}$-$H_{RH}$ bond, when $H_{RH}$ was at the TS, was about 39% weaker than the initial bond order. The bond order for the $C_{CRH}$-$H_{RH}$ bond, when $H_{RH}$ was at the S-H side, was about 69% weaker than the initial bond order. The weakening of $C_{CRH}$-$H_{RH}$ bond was accompanied by the formation of $S_{Mo}$-$H_{RH}$ bond. The $S_{Mo}$-$H_{RH}$ bond, when $H_{RH}$ was at the C-H side, was shown to start weaker (with bond order of 0.057 au.). The bond order for $S_{Mo}$-$H_{RH}$, when $H_{RH}$ was at the transition state, was shown to increase by about 17%. The bond order for the $S_{Mo}$-$H_{RH}$ bond, when $H_{RH}$ was at S-H side, was shown to increase by about 65%. At the transition state, the $C_{CRH}$-$H_{RH}$ bond distances were shown to considerably lengthen and eventually rupture. Similarly, the $S_{Mo}$-$H_{RH}$ distances were shown to be longer than the bond distance for the $S_{Mo}$-$H_{RH}$ bonds (described for the reduced enzyme). Similarly, at the transition state, the Mo-$O_{eq}$ bond distances were shown to moderately lengthen with a subsequent shortening of the $O_{eq}$-$C_{CRH}$ bond distances. This combination was expected to serve as a driving force for the release of the product as a keto analogous.

*The product release stage:* This stage of catalysis, usually described by the spectroscopic behaviors of the $E_{RED}$-$C_R$ intermediate, was expected to follow several paths as shown in Scheme (5.1.6). The spectral changes, centered on 450 and 550 nm, were characterized by the substrate-enzyme cofactors reduction. On the other hand, the spectral changes, centered on 650 nm, were characterized by the charge transfer due to the formation of $E_{RED}$-product intermediate. As shown in Scheme (5.1.6), the reduction of the cofactors and formations of the charge transfer complexes were described using the two approaches. The dynamic approach was described as shown in Scheme (5.1.6, path A;

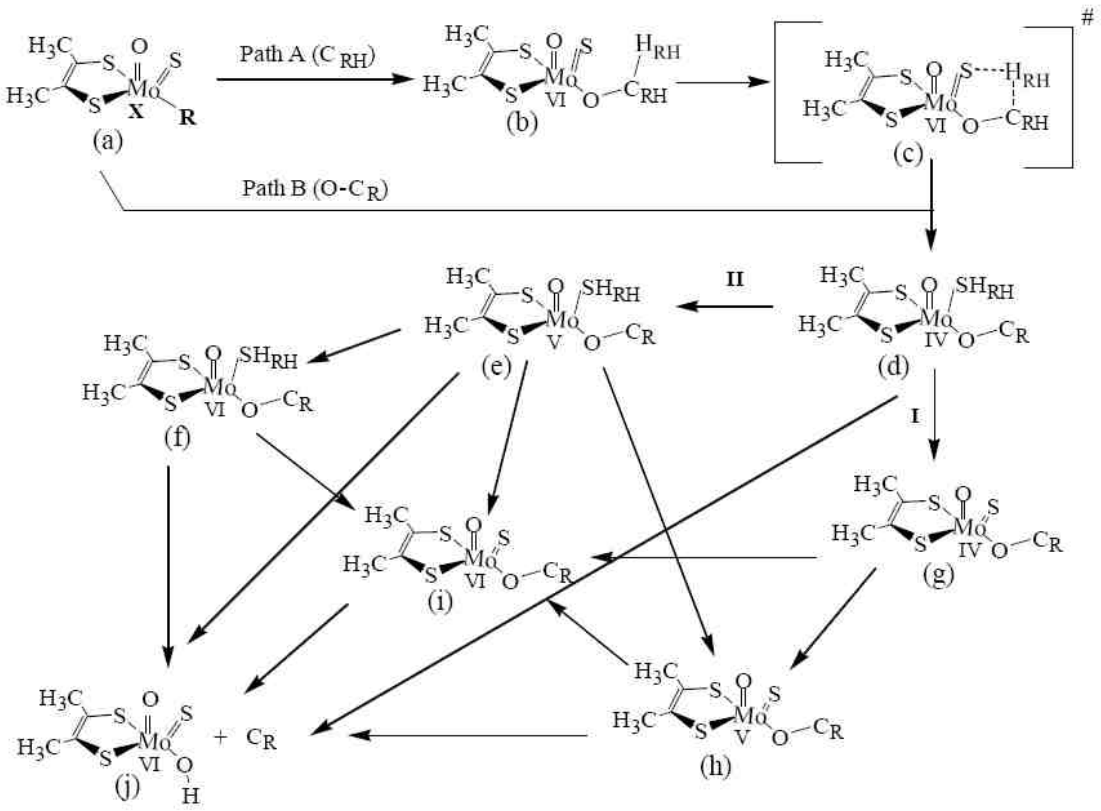


Scheme 5.1.6. A hypothetical postulated schematic model showing the major structural features of the equilibrium and spectral giving species. The mechanistic routes were shown for the dynamic (when R = OH, X = (VI) oxidation state, and $C_{RH}$ = lumazine or other substrates) and static (when R = no ligand or water, X = (IV) oxidation state, and O-$C_R$ = violapterin or other products). The currently accepted signal giving intermediate (Structure d) was shown to undergo a step wise oxidation through the immediate routes: (I) or (II). Route (I) was described by a loss of a proton to form Structure (g) followed by step-wise one electron oxidation, through Structure (h), involving one of the several routes. Or, two electrons oxidation to form Structure (j). Route (II) was described by an electron oxidation to form Structure (e). Structure (e) was proposed to dissociate to structure (j), via one electron oxidation, followed by a loss of a proton. It may also take different routes by losing one electron and a proton, respectively, to form Structure (j) directly or through Structure (h). Finally, Structure (e) may dissociate to form Structure (j) through Structure (h) or by losing a proton and two electrons, without forming an intermediate.

where $C_{CRH}$ was replaced by lumazine). And, the static approach was described as shown in path B (where O-$C_{CR}$ was replaced by violapterin). The two paths were shown to

follow different mechanistic paths, where path A was similar to equation (2.1.1) and path B was similar to equation (2.1.2 and 2.1.3). In path B, the oxidation products (such as violapterin) were reacted with $E_{RED}$, in the same way the elemental oxygen or $NAD^+$ were reacted with $E_{RED}$. The two paths (A and B) were shown to provide similar spectral changes, mainly centered at 650 nm (Figs. 3.3.1 – 3.3.6). Although the currently accepted spectral band giving complex was Structure (d), it was not well understood if there were other species (such as Structures g, e, f, h, i, or j) that were expected to contribute to the spectral band, centered at 650 nm. In order to understand the spectral bands associated with the transformation of lumazine to violapterin, a combination of enzymatic spectroscopic and electronic structure studies were performed. The model structures, bound to either lumazine (Path A) or violapterin (Path B) shown in Scheme (5.1.6), were optimized across the three oxidation states ($Mo^{(VI)}$, $Mo^{(V)}$, $Mo^{(IV)}$) by replacing $C_{RH}$ or O-$C_R$,

respectively, with lumazine or violapterin. The energetic for the reaction coordinates, described by the two paths, were developed as described in Figure (5.1.4, *upper panel*).

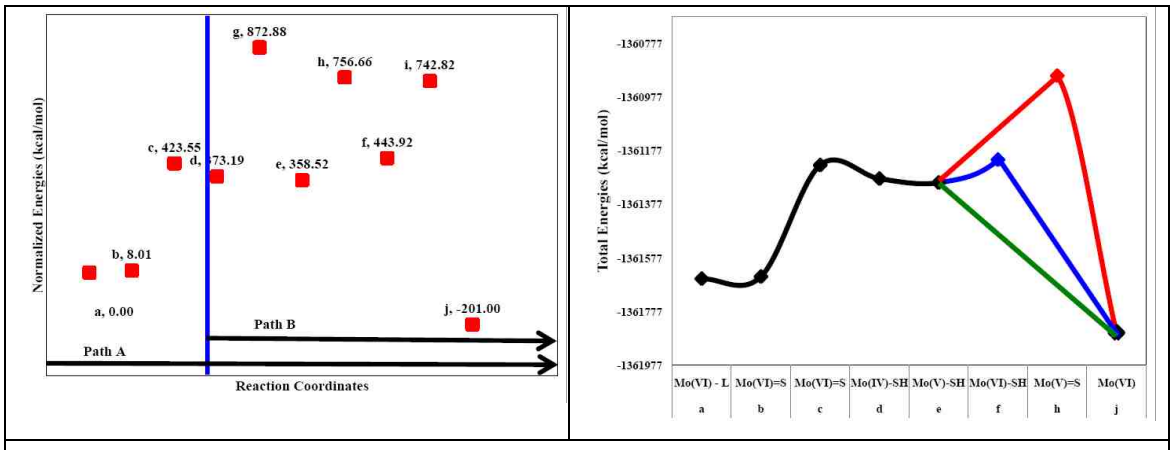


Figure 5.1.4. Relative energies of the equilibrium and transition state structures (*left panel*). Path (A) was shown to begin from Structure (a) and Path (B) from Structure (d). In the *right panel*, the total energies for the favorable reaction paths of the product release stage were shown.

The reaction paths for the product release, involving structures (d, e, and f) were shown to reveal similar energies (Fig. 5.1.4, *lower panel*). Although the paths involving structures (d, e, or f) were favorable, the paths involving Structures (d, e, h, and j) or (d, e, h, i, and j) were consistent with the very rapid signal giving species described for purine derivatives [18, 59, 64, 67, 68, 73, 74]. A time dependent DFT (TDDFT) calculations, on the equilibrium structures shown in Scheme (5.1.6), were applied to probe the oscillator strengths. The intensity of the bands was described using the oscillator strengths and correlated with the experimental extinction coefficients. The intensity of the MLCT transitions was probed from the overlap of Structure (d) by determining the energy difference between $Mo_{dxy}$ LUMO and violapterin HOMO (Appendix VIII, Table A. 7). The transition energies were shown to relate the closeness of the frontier orbitals to the strength of $Mo^{(VI)}$-$O_{eq}$-lumazine covalency. The % Mo charge transfer characters, for Structure (d), were shown in Table (3.3.1 and Table A. 7). Unlike Structure (d), the Structures (e and f) were shown to exhibit negative MLCT (Table A. 7). The characterization of the charge transfer transition band, as MLCT transition, was consistent with the spectral band giving species generated using the two experimental approaches. In order for MLCT transition (M to L*) to take place, the Mo-center was expected to be oxidized. Since the only oxidation was expected to take place, when Structure (d) was oxidized to either Structures (e or f), the Structure (d) was expected to undergo a one or two electron oxidations, respectively, to either Structures (e) or (f) (Scheme 5.1.7). Therefore, in order for MLCT transition to exist, Structure (d) was proposed to be oxidized from its (Enzyme)-[$Mo^{(IV)}$-violapterin] to either (Enzyme)-[$Mo^{V}$-violapterin] or (Enzyme)-[$Mo^{(VI)}$-violapterin] states. The accumulation of Structure (d), throughout the reaction time, was proposed to be a major source of the spectral band (centered at 650 nm). This was consistent with the fact that the complex couldn't be re-oxidized, as shown by the static experimental approach, due to the anaerobicity of the reaction. That means, the formation of $E_{RED}$-violapterin intermediate didn't require the participation of the FAD and $[Fe_2S_2](S^{\gamma}_{Cys})_4$ cofactors, unless the cofactors were able to serve as electron sinks when violapterin was reacted with the reduced enzyme. In this case, Structure (d) was proposed to be transformed to either Structure (e) or (g). Since Structure (g) was similar to the 'Very rapid' EPR signal giving species (shown for the

(Enzyme)-[$Mo^{(V)}$-uric acid] complex [18, 59, 64, 67, 68, 73, 74], it was ruled out as a long wavelength signal giving species (due to the lack of reported data for a 'Very rapid' EPR signal in the presence of lumazine). If the spectral band giving species were due to the species other than Structure (d), the charge transfer complex was proposed to be formed

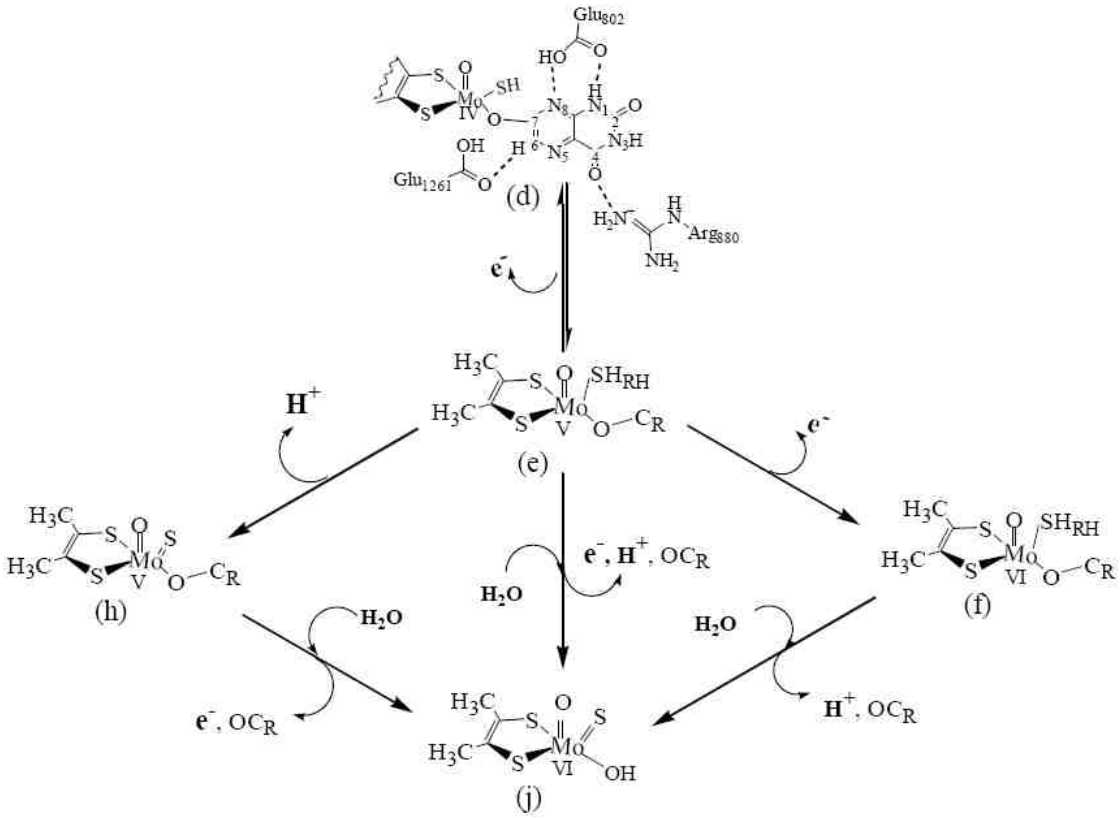


Scheme 5.1.7. A hypothetical schematic pathway proposed for the product release of a violapterin bound complex. The Mo-center of Structure (d) was proposed to be oxidized to Structure (e) upon giving a spectral band centered at 650 nm.

due to the accumulation of Structures (d and e). The spectral band giving species, as demonstrated by the static experimental approach, was proposed to occur on a much longer time scales due to the accumulation of structures (d), (e), or both (d and e). These structures were expected to significantly shift the electron density from the Mo($d_{xy}$) onto violapterin by placing the Mo($d_{xy}$) in greater proximity to violapterin.

# Chapter 6.0

## Overview of the overall reaction mechanism for XOR enzymes

The XOR enzymes, as with many oxidoreductase enzymes, were known to have components suited to interact with the reducing (at their Moco sites) and oxidizing (at their flavin sites) substrates [1, 5, 6, 7, 8, 10, 14, 42]. They also interact, at their redox sites or the pairs of $[Fe_2S_2](S^{\gamma}_{Cys})_4$ clusters (Fig. 1.1.5), with exogenous artificial electron acceptors. The widely accepted description of the series of events that took place, at the redox sites, were shown in Scheme (1.1.2) [24, 40, 55, 58]. The three major events that took place, during the catalytic cycle, were also described in Scheme (5.1.1). The binding stage was described by the transformation of the reactants (Structure a) to the Michaelis-Menten type complex (Structure b). The Structure (a) was described by the near attack conformation (NAC) when substrates entered the binding pocket and re-aligned themselves for nucleophilic reaction. The catalysis stage was described by the events that took place during the conversion of the Michaelis-Menten type complex (Structure b) to the product bound intermediate (Structure d). The catalytic conversion from Structure (b) to Structure (d) was expected to pass through the transition state (Structure c). Finally, the product release stage was described by the events that led to the formation of the products (Structure j). The formation of Structure (j) was expected to take place in two electrons or a stepwise one electron oxidation. In order to provide a greater understanding, on the overall unified catalytic mechanism, the three major events of the reductive half-reaction catalytic cycle were summarized in Scheme (6.1.1). In the presence of a wide range of substrates, the binding and catalysis stages were proposed to behave the same although the orientation of the substrates in the binding pocket were expected to vary. However, the dissociation of Structure (d) was proposed to follow different routes outlined in Scheme 6.1.1 (as described by the Paths A, B, or C).

As shown in Scheme (6.1.1), lumazine was modulated by geometric and electrostatic complementarity with the aid of the binding pocket amino acid residues. The amino acid

residues were proposed to promote a hydrogen bonding micro-environment, so that the reactants could achieve the proper orientation and activation. Similar to lumazine, all other substrates were also expected to share similar patterns of hydrogen-bond interactions. As described in Table (3.3.1), the pKa values for the acidic limb were shown to reflect the changes that were expected to take place in the [XOR]-$Glu_{1261/730}$ residue. Accordingly, in order for the reaction to take place, the neutral form of the substrate and an ionizable group of the [XOR]-$Glu_{1261/730}$ residue were required. That means, the [XOR]-$Glu_{1261/730}$ was expected to be de-protonated prior to the binding stage (formation of Substrate b). The abstraction of an acidic proton by [XOR]-$Glu_{1261/730}$ was expected to lower the activation barrier for the formation of a tetrahedral Michaelis-Menten and transition state complexes. In general, the [XOR]-$Glu_{1261/730}$ was proposed to activate $HO_{eq}$ terminal and facilitate the nucleophilic reaction that allowed the interaction between $E_{OX}$ and $C_{RH}$ and formation of Structure (b). When the unstable oxyanion ($\ddot{O}^{-}_{eq}$) was bound to the $C_7$ of lumazine or ($C_8$, $C_2$, or $C_6$) of purine derivatives, a negative charge density was created on the $N_8$ of 5, 8-diazine of the pyrazine, $N_9$ of 7, 9-diazole of the imidazole, or $N_1$ of 1, 3-diazine of pyrimidine rings. As shown in Scheme (6.1.1), the binding of lumazine at the $C_7$ position was not directed by recognition of the 5, 8-diazine ($N_5$ or $N_8$) of the pyrazine ring, as was the case for the binding of substrate at position $C_2$ of allopurinol or hypoxanthine, mainly directed by recognition of the 1, 3-diazine ($N_1$ or $N_3$) of pyrimidine rings. Unlike the purine derivatives, the binding-site for lumazine was not expected to have the donor/acceptor capabilities since its binding site ($C_7$) was bound to only one nitrogen ($N_8$) and a carbon ($C_6$) atoms. As shown by the overall catalytic mechanisms (Scheme 6.1.1), the transformation of the tetrahedral Michaelis-Menten type complex (Structure b) to the product bound intermediate (Structure d) was proposed to pass through the tetrahedral transition state (Structure c). Following the $sp^2 \rightarrow sp^3$ re-hybridization of the carbon atom of the substrate-binding site, some parametric changes were shown to take place. The parametric changes were expected to be influenced by several factors (such as the orientation of substrates in the binding pocket, geometric distortion of the active site, tautomeric nature of substrates, transfer of $H_{OH}$ from $HO_{eq}$ to [XOR]-$Glu_{1261}$, allocation of electrons on Mo-center, transfer of $H_{RH}$ from $C_{RH}$ to $S_{Mo}$

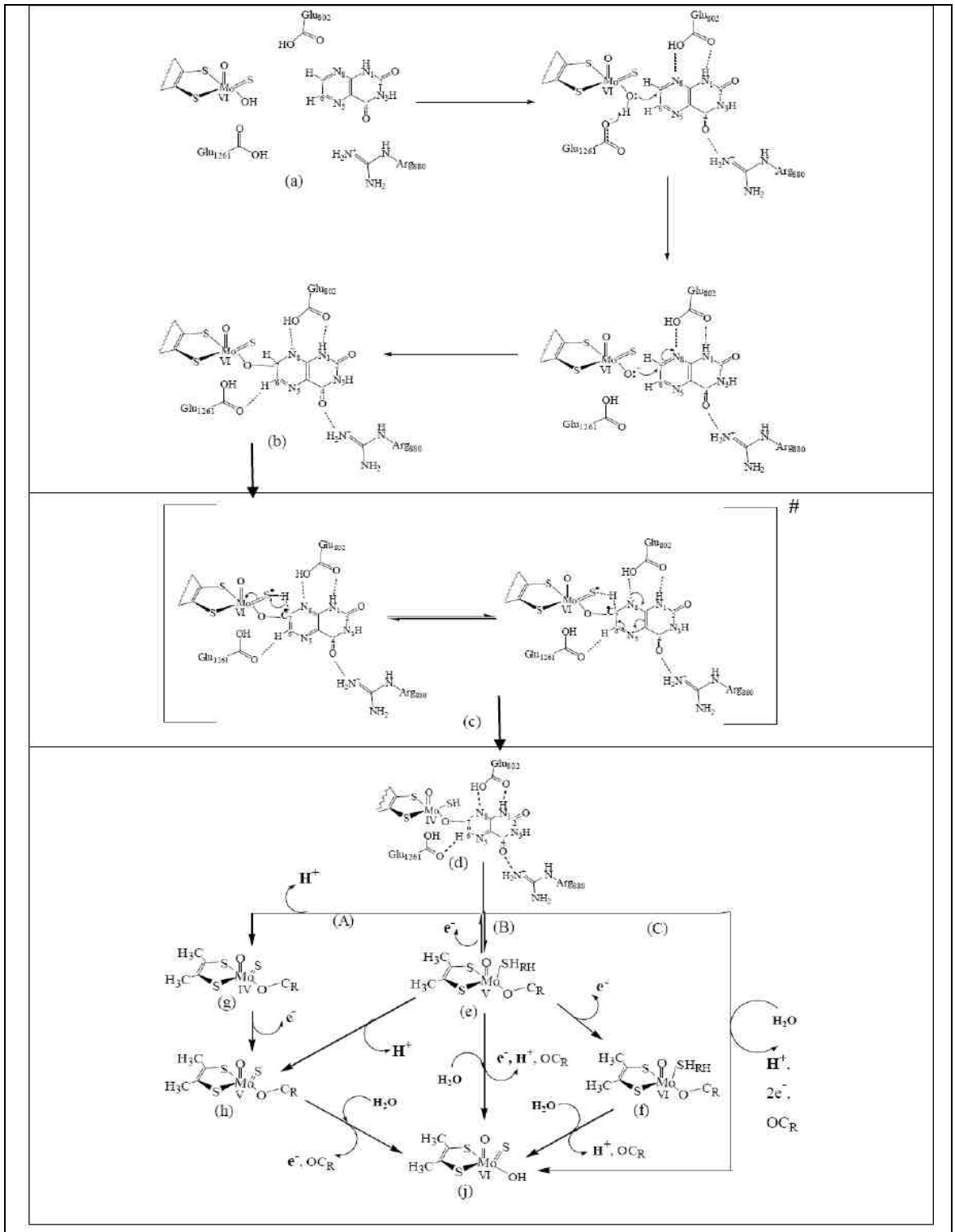


Scheme 6.1.1. A hypothetical schematic model showing the major structural features of the equilibrium and transition state structures. Paths (A), (B), and (C), respectively, represented the proposed routes for purine derivatives, pteridine derivatives, and aldehydes, formate, or formamide.

terminal, and release of products). When the charges at the major groups (Mo, $C_{CRH}$, $H_{RH}$, $O_{eq}$, and $S_{Mo}$) were consumed, the bonds associated with these groups were also shown to either weaken or strengthen. According to the bonding and wave-function descriptions, the transfer of an electron from the substrate to the Mo-center was proposed to take place through the $C_{CRH}$-$H_{RH}$-$S_{Mo}$-$Mo^{(VI)}$ rather than the $C_{CRH}$---$H_{RH}$---$S_{Mo}$-$Mo^{(VI)}$ super-exchange pathway. The transfer of $H_{RH}$ to $S_{MO}$ was expected to take place as a hydrogen atom, in a separate coordinate to the flow of an electron (Scheme 5.1.5). In this case, the reduction of $Mo^{(VI)}$-center was expected to take place through an inner-sphere mechanism, before the formation of $S_{Mo}$-$H_{RH}$ bond. Since the proton and electrons originated from the same atom and orbitals, their transfer were proposed to be coupled kinetically and depended on the position of $H_{RH}$ atom. At the transition state (Figure 6.1.1), the Mulliken atomic charges on the $H_{RH}$ atom was between + 0.05558 au. and + 0.010651 au.(in the presence of de-protonated substrates) and + 0.019345 au. and -0.037137 au. (in the presence of protonated substrates). As a result, it was suitable to label the hydrogen and electron

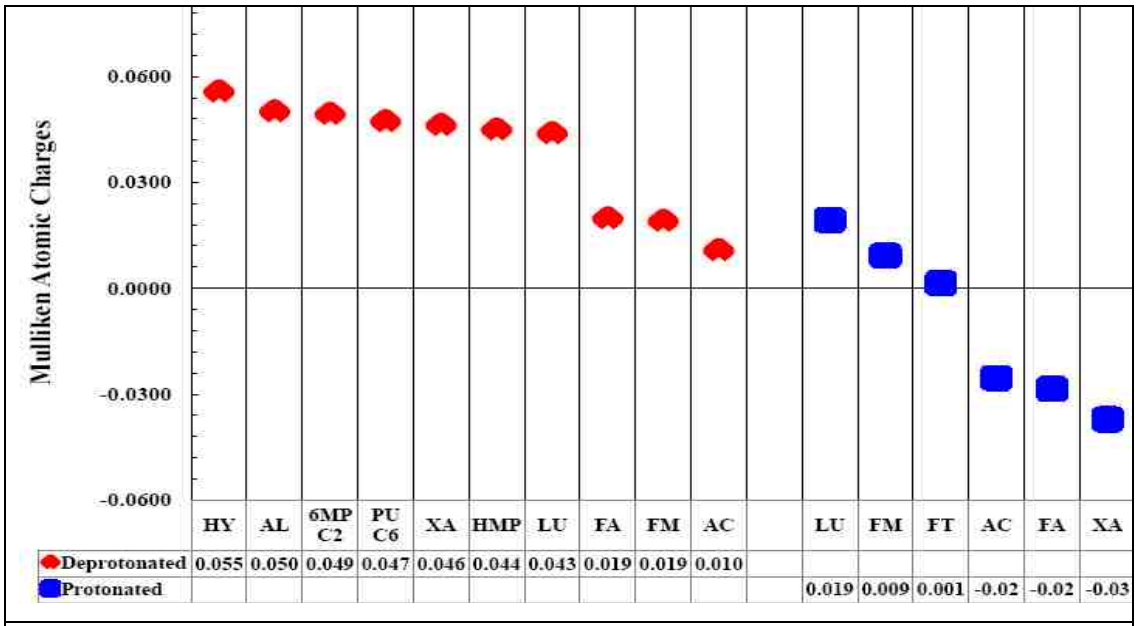


Figure 6.1.1. The Mulliken atomic charges on $H_{RH}$ atom, when $H_{RH}$ was at the transition state (Structure c). The designation "protonated" and "de-protonated" referred, respectively, to the enol and keto forms of the substrates.

transfer as described in Scheme (4.1.1 (c)) instead of the hydride transfers ($H^+ + 2e^-$) (Schemes 4.1.1 (a) or (b)). Therefore, in the course of the reaction, an electron was transferred from the $C_{CRH}$ of the substrate to Mo-center, through the $C_{CRH}$-$O_{eq}$-$Mo^{(VI)}$ super-exchange pathway, with concomitant transfer of hydrogen atom. The most important feature of the enzymatic reaction was the transfer of hydrogen atom from the

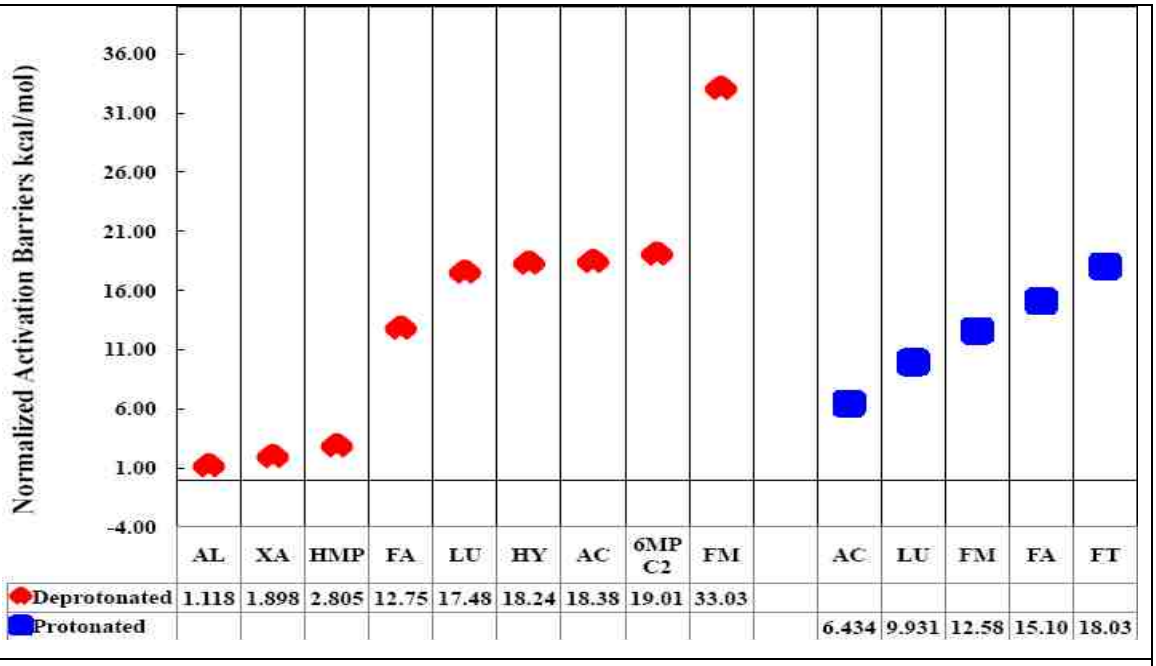


Figure 6.1.2. The normalized activation energy barriers ($\Delta H^{\ddagger}$ ($E_{TS}$-$E_{CH}$)) for the active site model compound bound to selected substrates. The energies were computed for the migration of $H_{RH}$ from $C_{RH}$ to $S_{Mo}$ terminal. The energy normalization was calculated with respect to the Michaelis-Menten type structure ($Mo^{(VI)}$-$O_{eq}$-$C_{CRH}$ meta-stable) and the Figure was developed from Figure (4.3.2).

substrate-binding site to the $S_{Mo}$ terminal. In order to understand this process, the activation barrier for the transfer of hydrogen atom was described in Figure (6.1.2). The activation barrier for the hydrogen atom transfer, from the substrate carbon of the substrate-binding site to the $S_{Mo}$ terminal of the active site, was in the range between 6.43 – 18.03 kcal/mol (in the presence of protonated substrates) and 1.12 – 33.03 kcal/mol (in the presence of de-protonated substrates). The behavior of the transition state was also

described by the % $Mo_{dxy}$, as described in Figure (6.1.3), where the metal character was shown to reveal the behavior of the transition state complex. The metal characters were shown to be higher in the presence of the protonated substrates (Fig. 4.3.3, *lower panel*). The highest $Mo_{dxy}$ character, in the presence of the protonated substrates, was shown in the highest occupied molecular orbital (HOMO-1). As a result, in the presence of the de-protonated substrates, the $H_{RH}$ atom was shown to spend most of the time at the transition state, behaving as a substrate bound rather than product bound.

In general, the parametric changes were shown to dictate the position of $H_{RH}$ at the transition state. Along the reaction pathway, in the presence of the protonated substrates, the transition states were shown to occur during the late transition state that resembled the products. On the other hand, in the presence of the de-protonated substrates, the transition states were shown to occur during the early transition state that resembled the reactants. Although all substrates had the same profile, the bond order indices were shown to vary from substrate to substrate. The $O_{eq}$-$C_{CRH}$ bond formation was followed by a simultaneous cleavage of Mo-$O_{eq}$ bond. The Mo-$O_{eq}$ bond cleavage was shown to represent the transfer of $O_{eq}$ terminal to the substrate and departure as an oxidized product. The frequencies for the movement of $H_{RH}$ from $C_{RH}$ to $S_{Mo}$ terminal were also shown to vary depending the type of the substrates (Figure 4.3.3, *upper panel*). At the transition state, the $O_{eq}$-$C_{CRH}$ bond order was 17% formed while the $C_{CRH}$-$H_{RH}$ bond was only about 28% broken. That means the $O_{eq}$-$C_{CRH}$ and $C_{CRH}$-$H_{RH}$ bond lengths were more substrate-like. Once the transition state (Structure c) was transformed to Structure (d), the product release stage was shown to follow one of the several paths (Scheme (6.1.1). Since the last stage of the reductive half-reaction catalytic cycle was proposed to be a rate limiting, the accumulation of Structure (d, shown in Scheme 6.1.1) and its slow decay to structure (e, shown in Scheme 6.1.1) was monitored at slower time scale. Therefore, the accumulation of the intermediates (d, e, or both) was proposed to be the major contributors for the spectral bands, centered at 650 nm. Since the interaction between $E_{OX}$ and lumazine was shown to form the $E_{RED}$-violapterin [58, 81, 85, 130] and MLCT transition, a similar situation was expected for the $Mo^{(IV)}$-$O_{eq}$-$C_{CR}$ catalytic intermediates (such as

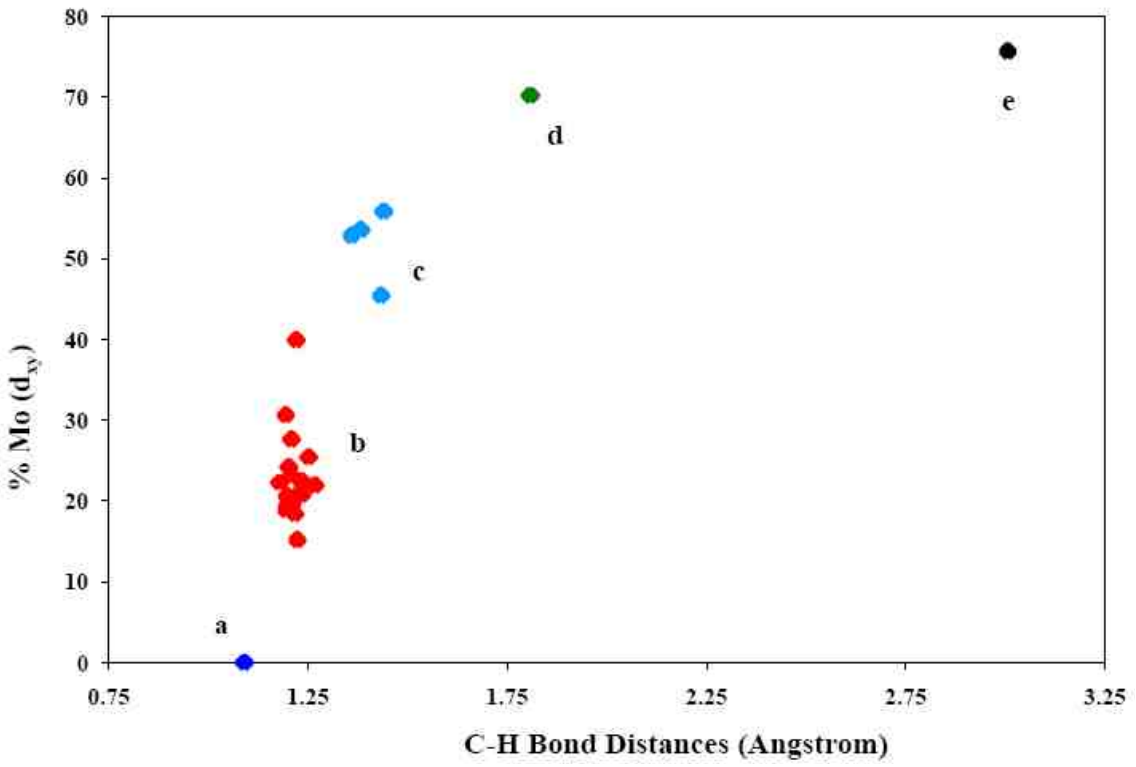


| | C-H Bond Distances | Mo(dxy) |
|---|---|---|
| C-H (bond distance from methanol) | 1.090 | 0 |
| Lumazine *enol* form | 1.179 | 22.27 |
| Formamide | 1.194 | 30.62 |
| 6-Methylpurine (bound at $C_8$ imidazole) | 1.194 | 18.86 |
| Purine (bound at $C_8$ imidazole) | 1.198 | 19.47 |
| Formaldehyde | 1.197 | 20.59 |
| Xanthine | 1.202 | 24.18 |
| Acetaldehyde | 1.208 | 23.1 |
| Hypoxanthine | 1.210 | 19.54 |
| Lumazine *keto* form | 1.217 | 18.4 |
| Formate de-protonated | 1.220 | 39.91 |
| Allopurinol | 1.223 | 15.16 |
| Purine (bound at $C_6$ imidazole) | 1.234 | 20.75 |
| Purine (bound at $C_2$ imidazole) | 1.235 | 22.41 |
| 6-Methylpurine (bound at $C_2$ pyrimidine) | 1.236 | 21.7 |
| 2-hydroxy-6-methylpurine | 1.267 | 21.92 |
| Xanthine protonated | 1.359 | 52.83 |
| Formamide protonated | 1.382 | 53.56 |
| Formaldehyde protonated | 1.432 | 45.43 |
| Acetaldehyde protonated | 1.440 | 55.85 |
| Formate (product bound) | 1.808 | 70.22 |
| Violapterin | 3.006 | 75.66 |

Figure 6.1.3. The % $Mo_{dxy}$, that described the metal character at the transition state, with respect to the C-H bond distance (*blue or a*). The % $Mo_{dxy}$ for the active site model compounds were evaluated in the presence of protonated (between 40% - 60%, *light blue or c*) and de-protonated (below 30%, *red or b*) substrates. Formate (*green or d*) and violapterin (*black or e*) were shown to represent the product bound.

$E_{RED}$-alloxanthine [52, 53, 81, 83], $E_{RED}$-uric acid [59, 81], $E_{RED}$- carboxylates (carboxylic acids), $E_{RED}$-carbamate, $E_{RED}$-formate, or $E_{RED}$-$CO_2$), as shown in Paths (A) and (C) (Scheme 6.1.1). If Structures (d) or/and (e) were the structures that contributed to the spectral band (centered at 650 nm), the inhibitory (Enzyme)-[$Mo^{(IV)}$-alloxanthine] was expected to behave the same as (Enzyme)-[$Mo^{(IV)}$-violapterin]. However, $E_{RED}$-alloxanthine was not known to give spectral bands similar to $E_{RED}$-violapterin [52, 81, 83]. Although the inhibited signal giving species were the type of $E_{RED}$-product complexes [52], the $E_{RED}$-violapterin complexes were identified to give complexes that were not inhibitory. As shown in Scheme (6.1.1), catalysis was proposed to be completed when the product was displaced by hydroxide from solvent water (Structure j). The displacement was proposed to be followed by concomitant transfer of an electron, out of the Moco center, to the flavin site and de-protonation of the $S_{Mo}$–$H_{RH}$ terminal (Scheme 6.1.1). If the transfer of electrons took place, prior to the release of products (Path A, shown in Scheme 6.1.1), a transient species characterized by the "very rapid" EPR signal (Structure h, shown in Scheme 6.1.1) was expected to be generated.

Although the mechanism proposed, in Scheme (6.1.1), was expected to serve as a benchmark for all XOR enzymes (*bm*XOR, *Rc*XDH, and *Rc*XDH-$Glu_{232}$Ala), the enzymes were shown to exhibit significantly different catalytic activities (when the same assay method, enzyme, and substrate were used). The enzymes were shown to exhibit different reaction phases and product release steps that were shown to affect the rate of ROS ($H_2O_2$ and $O_2^{\bullet-}$) production. The catalytic activity of the enzymes was also described by the two different types of flavin reactivities (involving the reaction between molecular oxygen with $FADH_2$ or $FADH^{\bullet}$). The variable activities were proposed to be due to the factors that affected the reductive half-reaction catalytic cycle (such as the affinity and product release). The extent of the $v_{max}$ was shown to depend on the type of the substrates and the binding pocket of the active site of the enzymes. The affinity of the substrates, towards the enzymes, was also shown to depend on the concentration of the substrates. The substrates, that were shown to give the enzymes the lowest activities, were shown to give the lowest turnover numbers. The slow substrates, unlike the fast substrates, were unable to give higher turnover numbers since their re-oxidation was

proposed to have taken place during the slower phases. Therefore, the difference in the turnover number between the enzymes reflected the difference in the catalytic activities of the two enzymes (*bm*XOR and *Rc*XDH). The substrates, with high $K_m$ values, were also shown to exhibit an unstable Michaelis-Menten type complex. Therefore, the substrates with the highest $k_{cat}$ values were those that exhibited less stable catalytic transformation from $E_{OX}$-$C_{RH}$ complex to $E_{RED}$-product intermediate. This was consistent with the fact that the conversion of the $E_{OX}$-$C_{RH}$ complex to $E_{RED}$-product intermediate required faster dissociation. The levels of reduction and reaction phases were shown to affect the product release. The variation in the rates of $H_2O_2$ or $O_2^{\bullet-}$ production were also expected to reflect the levels of reduction and the stages where the re-oxidation began and ended.

Finally, the progression of substrates to products were expected to be influenced by several factors (such as the orientation of substrates in the binding pocket, geometric distortion of the active site, tautomeric nature of substrates, transfer of $H_{OH}$ from $HO_{eq}$ to [XOR]-$Glu_{1261}$, electron allocation on Mo-center, transfer of $H_{RH}$ from $C_{RH}$ to $S_{Mo}$ terminal, and release of products). This was significant, since the factors that stabilize the products also stabilize the transition state. Therefore, the geometry of the transition state structure was shown to offer a mechanistic implication although the smallest fraction of the catalytic cycle was spent at the transition state. Since the formation and dissociation of the transition state complex required the participation of the enzymatic forces needed to oxidize the substrates, the events that took place at the transition state were central in understanding the catalytic reaction mechanism of XOR enzymes.

# Appendices

## Appendix I: Survey of the xanthine oxidase family enzymes

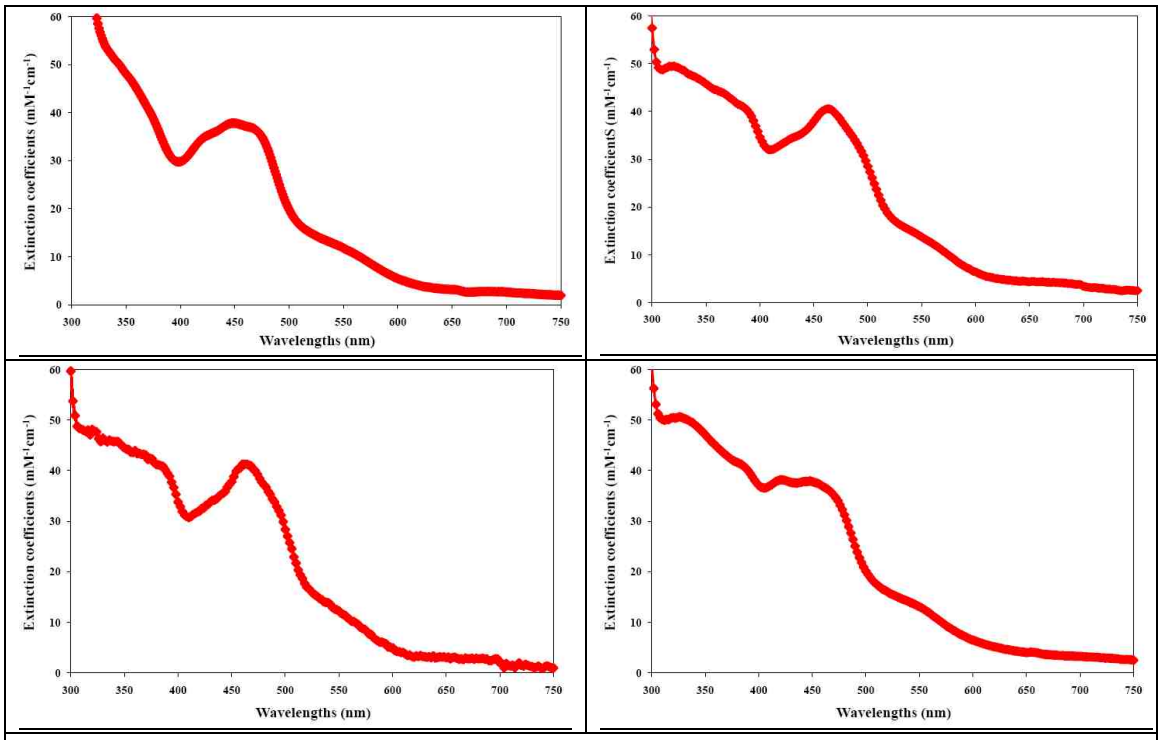


Figure A. 1. The UV-visible absorption spectra for XO family enzymes: *Upper left panel* was for 32 mM *bm*XOR in 50 mM pyrophosphate buffer, pH 7.5. *Upper right panel* was for 300 µM *Rc*XDH in 20 mM Tris buffer, pH 7.2. *Lower right panel* was for 90 µM *Rc*XDH-$Glu_{232}$Ala mutant enzyme in 20 mM Tris buffer, pH 7.2. And, *lower right panel* was for 20 µM *Oc*Cu/Mo-CODH in 50 mM HEPES buffer, pH 7.2.

Appendix II: Survey of the reducing substrates

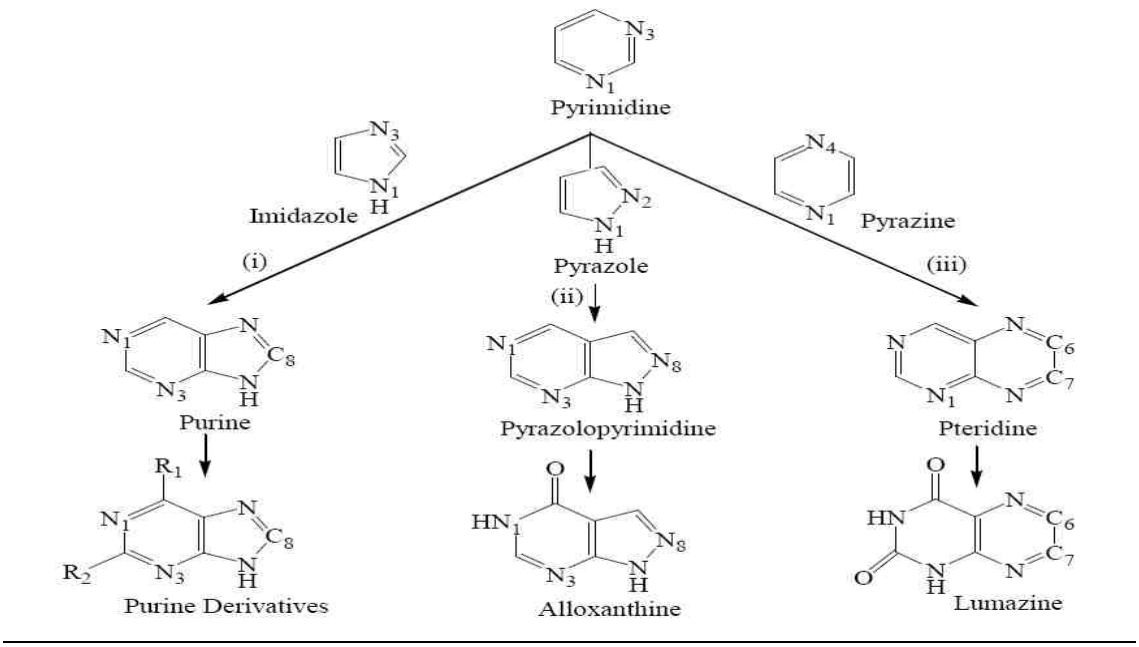


Purine derivatives: purine ($R_1$ and $R_2$ = H), hypoxanthine ($R_1$ = OH and $R_2$ = H), 6-methylpurine ($R_1$ = $CH_3$ and $R_2$ = H), 2-hydroxy-6-methylpurine ($R_1$ = $CH_3$ and $R_2$ = OH), and xanthine ($R_1$ = OH and $R_2$ = OH)

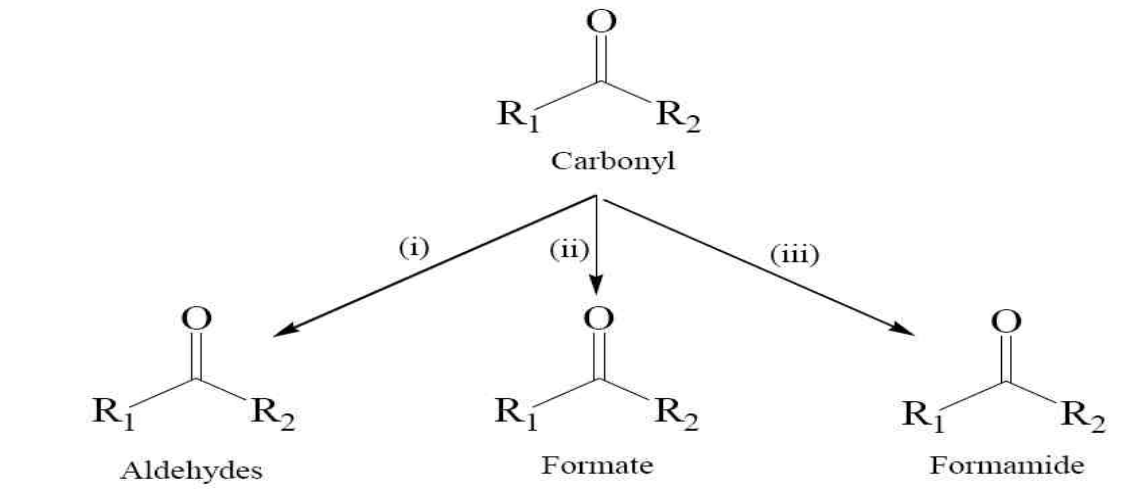


$R_1$ or $R_2$ = H for all substrates, and $R_1$ or $R_2$ could be H (formaldehyde), $CH_3$ (acetaldehyde), $CH_2CH_3$ (propionaldehyde) $CH_3(CH_2)_2$ (butyraldehyde), phenyl (benzaldehyde), OH (formate), and $NH_2$ (formamide)

Figure A. 2. The classification of reducing substrates. *Upper panel (i*) represents the purine derivatives, *upper panel (ii*) represents the pyrazolopyrimidine derivatives (such as allopurinol), and *upper panel (iii*) represents the pteridine derivatives (such as lumazine). The *lower panel (i*) represents aldehydes, *lower panel (ii*) represents formate, and *lower panel (iii*) represents formamide.

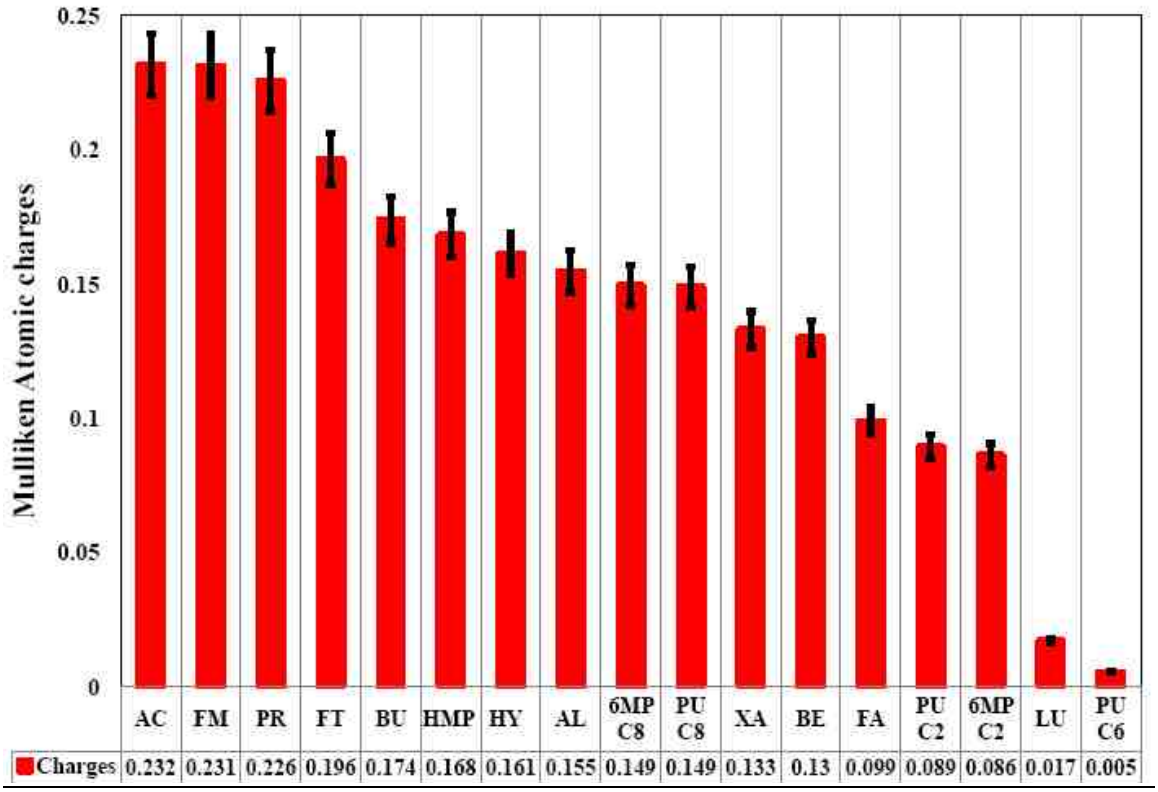


Figure A. 3. The Mulliken atomic charges calculated for the substrate-binding sites of the substrates [acetaldehyde (AC), formamide (FM), propionaldehyde (PR), formate (FT), butyraldehyde (BU), 2-hydroxy-5-methylpurine (HMP), hypoxanthine (HY), allopurinol (AL), 6-methylpurine (6MP-$C_8$ or 6MP-$C_2$), purine (PU-$C_8$, PU-$C_2$, or PU-$C_6$), xanthine (XA), benzaldehyde (BE), formaldehyde (FA), and lumazine (LU)].

The geometry optimization of the molecules were performed using the Gaussian® 03W version 6.0 software package. The 6-31G (d', p') basis set with a polarization function were used for the atoms (C, H, O, N, and S) [138 (g)]. The full optimization was performed using *"# b3lyp gen #p opt pop=full gfprint gfinput"* theoretical model and job type [138 (a, e, j)]. The Mulliken charges were computed from the output files of the optimized structures.

## Appendix III: The data for the steady-state kinetic parameters

Table A. 1. The data for the steady-state kinetic parameters, of XO family enzymes, determined from the pH profile. The kinetic parameters were not converged *bm*XOR, in the presence of (formate, formamide, 6-methylpurine, and glyceraldehyde), for *bm*XOR, *Rc*XDH (in the presence of allopurinol), *Rc*XDH-$Glu_{232}$Ala (in the presence of allopurinol and 2-hydroxy-6-methylpurine).

| Substrates | pH | $k_{cat}$ ($s^{-1}$) | $v_{max}$ ($\mu M \bullet s^{-1}$) | $k_m$ ($\mu M$) | $v_{max}/k_m$ ($s^{-1}$) | $k_{cat}/k_m$ ($M^{-1} \bullet s^{-1}$) |
|---|---|---|---|---|---|---|
| (a) The steady-state kinetic parameters for *Oc*Cu/Mo-CODH | | | | | | |
| Carbon Monoxide | 5 | 2.5721E-04 | 3.4980E-05 | 1.0460E-01 | 3.3442E-04 | 2.4589E+03 |
| | 6 | 4.0801E-04 | 5.5490E-05 | 6.0530E-02 | 9.1674E-04 | 6.7407E+03 |
| | 7 | 4.2949E-04 | 5.8410E-05 | 6.9970E-02 | 8.3479E-04 | 6.1381E+03 |
| | 8 | 1.4169E-04 | 1.9270E-05 | 1.2260E-01 | 1.5718E-04 | 1.1557E+03 |
| | 9 | 3.4743E-05 | 4.7250E-06 | 1.1540E-16 | 4.0945E+10 | 3.0106E+17 |
| | 10 | 1.3088E-05 | 1.7800E-06 | 1.2880E-16 | 1.3820E+10 | 1.0162E+17 |
| | | | | | | |
| (b) The steady-state kinetic parameters for *bm*XOR enzyme | | | | | | |
| Purine | 6 | 5.0060E-03 | 1.2460E-05 | 1.1890E+02 | 1.0479E-07 | 4.2103E+01 |
| | 7 | 2.5740E-03 | 6.4060E-06 | 8.5130E+02 | 7.5250E-09 | 3.0236E+00 |
| | 8 | 6.5890E-03 | 1.6400E-05 | 2.6990E+02 | 6.0763E-08 | 2.4413E+01 |
| | 9 | 3.0950E-03 | 7.7040E-06 | 8.4600E+01 | 9.1064E-08 | 3.6584E+01 |
| | 10 | 7.0060E-02 | 1.6840E-06 | 4.0980E+01 | 4.1093E-08 | 1.7096E+03 |
| Hypoxanthine | 6 | 5.9934E-01 | 4.5370E-05 | 2.4930E+02 | 1.8199E-07 | 2.4041E+03 |
| | 7 | 2.1493E-01 | 1.6270E-05 | 5.4390E-10 | 2.9914E+04 | 3.9516E+14 |
| | 8 | 1.5218E-01 | 1.1520E-05 | 4.4550E-10 | 2.5859E+04 | 3.4159E+14 |
| | 9 | 1.4161E-01 | 1.0720E-05 | 4.0270E-10 | 2.6620E+04 | 3.5166E+14 |
| Xanthine | 6 | 4.9990E-01 | 3.6340E-05 | 7.6960E+01 | 4.7219E-07 | 6.4956E+03 |
| | 7 | 3.2500E-01 | 2.4600E-05 | 1.1650E+01 | 2.1116E-06 | 2.7897E+04 |
| | 8 | 3.0560E+00 | 2.3140E-04 | 4.2450E+02 | 5.4511E-07 | 7.1991E+03 |
| | 9 | 6.9960E-01 | 5.2960E-05 | 1.6210E+02 | 3.2671E-07 | 4.3159E+03 |
| | 10 | 1.2900E+00 | 9.7660E-05 | 7.6700E+02 | 1.2733E-07 | 1.6819E+03 |
| 2-hydroxy-6-methylpurine | 6 | 2.1268E-03 | 1.6100E-07 | 1.0510E-09 | 1.5319E+02 | 2.0236E+12 |
| | 7 | 3.6473E-01 | 2.7610E-05 | 2.0791E+04 | 1.3280E-09 | 1.7543E+01 |
| | 8 | 3.6473E-01 | 2.7610E-05 | 2.0791E+04 | 1.3280E-09 | 1.7543E+01 |
| | 9 | 6.0938E-01 | 4.6130E-05 | 5.4561E+04 | 8.4548E-10 | 1.1169E+01 |
| | 10 | 2.1770E+25 | 1.6480E+21 | 2.9080E+30 | 5.6671E-10 | 7.4863E+00 |
| Allopurinol | 6 | 2.2220E-01 | 1.6820E-05 | 7.5890E-01 | 2.2164E-05 | 2.9279E+05 |
| | 7 | 2.3380E+00 | 1.3290E-05 | 3.0180E+00 | 4.4036E-06 | 7.7469E+05 |
| | 8 | 2.8230E-01 | 2.1370E-05 | 5.4090E+01 | 3.9508E-07 | 5.2191E+03 |
| | 9 | 9.3350E-01 | 3.1010E-06 | 4.2530E+02 | 7.2913E-09 | 2.1949E+03 |
| Lumazine | 5 | 7.8680E-04 | 2.1790E-04 | 1.1480E+00 | 1.8981E-04 | 6.8537E+02 |
| | 6 | 5.8020E-04 | 1.6070E-04 | 1.5880E+01 | 1.0120E-05 | 3.6537E+01 |
| | 7 | 2.1470E-04 | 5.9480E-05 | 6.6880E+01 | 8.8935E-07 | 3.2102E+00 |
| | 8 | 1.2400E-04 | 3.4360E-05 | 3.2830E+00 | 1.0466E-05 | 3.7770E+01 |
| | 9 | 1.6740E-02 | 1.9740E-05 | 9.2210E+00 | 2.1408E-06 | 1.8154E+03 |
| | 10 | 2.4270E-04 | 6.7230E-05 | 1.2950E+02 | 5.1915E-07 | 1.8741E+00 |

| | | | | | | |
|---|---|---|---|---|---|---|
| | 11 | 1.4540E-04 | 4.0280E-05 | 8.1820E+02 | 4.9230E-08 | 1.7771E-01 |
| Formaldehyde | 6 | 8.1770E-02 | 6.1900E-06 | 1.4113E+05 | 4.3860E-11 | 5.7939E-01 |
| | 7 | 1.2910E+00 | 9.7720E-05 | 9.2322E+04 | 1.0585E-09 | 1.3984E+01 |
| | 8 | 2.3060E+00 | 1.7460E-04 | 9.6056E+05 | 1.8177E-10 | 2.4007E+00 |
| | 9 | 9.9250E-01 | 7.5130E-05 | 3.5641E+05 | 2.1080E-10 | 2.7848E+00 |
| | 10 | 3.2680E-01 | 2.4740E-05 | 2.7688E+04 | 8.9353E-10 | 1.1803E+01 |
| | 11 | 5.5080E-01 | 4.1700E-05 | 8.7808E+04 | 4.7490E-10 | 6.2728E+00 |
| Acetaldehyde | 6 | 1.1640E+00 | 4.3990E-06 | 1.3770E+06 | 3.1946E-12 | 8.4532E-01 |
| | 7 | 1.2820E+00 | 5.1270E-06 | 6.4902E+05 | 7.8996E-12 | 1.9753E+00 |
| | 8 | 3.3430E+00 | 2.3440E-05 | 3.5728E+05 | 6.5607E-11 | 9.3569E+00 |
| | 9 | 3.9350E+00 | | 3.2201E+05 | | 1.2220E+01 |
| | 10 | 3.3040E+00 | | 3.6000E+05 | | 9.1777E+00 |
| Propionaldehyde | 6 | 9.3930E-09 | 2.3380E-05 | 1.7515E+05 | 1.3349E-10 | 5.3628E-08 |
| | 7 | 2.6250E-01 | 1.3650E-05 | 4.0980E+03 | 3.3309E-09 | 6.4056E+01 |
| | 8 | 8.9030E-04 | 2.2160E-06 | 4.7263E+04 | 4.6887E-11 | 1.8837E-02 |
| | 9 | 4.6300E-02 | 8.6420E-07 | 1.2294E+04 | 7.0294E-11 | 3.7661E+00 |
| | 10 | 2.7670E-03 | 6.8880E-06 | 2.3910E+03 | 2.8808E-09 | 1.1573E+00 |
| Butyraldehyde | 6 | 3.7560E-03 | 9.3490E-06 | 2.5700E+04 | 3.6377E-10 | 1.4615E-01 |
| | 7 | 7.8900E-05 | 1.9640E-07 | 3.3670E+04 | 5.8331E-12 | 2.3433E-03 |
| | 8 | 8.3710E-04 | 2.0830E-06 | 1.2597E+05 | 1.6536E-11 | 6.6454E-03 |
| | 9 | 3.1010E-02 | 4.7670E-07 | 1.6392E+04 | 2.9081E-11 | 1.8918E+00 |
| | 10 | 5.4390E-03 | 1.3540E-05 | 2.7199E+04 | 4.9781E-10 | 1.9997E-01 |
| Benzaldehyde | 7 | 1.5640E-03 | 3.8920E-06 | 5.2770E+00 | 7.3754E-07 | 2.9638E+02 |
| | 8 | 2.1230E-02 | 5.2840E-05 | 6.2290E+02 | 8.4829E-08 | 3.4083E+01 |
| | 9 | 1.6440E-02 | 4.0920E-05 | 2.3710E+02 | 1.7259E-07 | 6.9338E+01 |
| | | | | | | |
| (c) The steady-state kinetic parameters for *Rc*XDH enzyme | | | | | | |
| Purine | 6 | 1.9050E+11 | 1.1480E+23 | 6.9380E+16 | 1.6547E+06 | 2.7457E+00 |
| | 7 | 5.9130E-02 | 5.9450E-05 | 4.7470E+03 | 1.2524E-08 | 1.2456E+01 |
| | 8 | 2.9370E-02 | 1.8130E-04 | 1.2950E+03 | 1.4000E-07 | 2.2680E+01 |
| | 9 | 1.5140E-02 | 8.0120E-05 | 1.9930E+03 | 4.0201E-08 | 7.5966E+00 |
| Hypoxanthine | 6 | 9.1630E-01 | 6.7500E-05 | 5.7280E+01 | 1.1784E-06 | 1.5997E+04 |
| | 7 | 2.5120E-01 | 4.2630E-04 | 3.3100E+02 | 1.2879E-06 | 7.5891E+02 |
| | 8 | 1.9870E-01 | 3.3720E-04 | 6.8270E+01 | 4.9392E-06 | 2.9105E+03 |
| | 9 | 6.0780E-01 | 3.5210E-05 | 1.1460E+02 | 3.0724E-07 | 5.3037E+03 |
| | 10 | 3.4060E-02 | 5.7800E-05 | 8.1790E+02 | 7.0669E-08 | 4.1643E+01 |
| Xanthine | 6 | 3.4470E-02 | 5.8500E-05 | 1.2080E-01 | 4.8427E-04 | 2.8535E+05 |
| | 7 | 1.4020E-01 | 8.8520E-07 | 3.0180E+00 | 2.9331E-07 | 4.6455E+04 |
| | 8 | 9.1360E-01 | 1.5500E-03 | 2.4040E+02 | 6.4476E-06 | 3.8003E+03 |
| | 9 | 6.2440E-04 | 1.0600E-06 | 1.0240E+01 | 1.0352E-07 | 6.0977E+01 |
| | 10 | 1.0400E+20 | 1.1210E+12 | 5.0210E+20 | 2.2326E-09 | 2.0713E+05 |
| | 11 | 2.3100E+28 | 5.6710E+10 | 1.3080E+19 | 4.3356E-09 | 1.7661E+15 |
| 2-hydroxy-6-methylpurine | 6 | 8.7220E-02 | 1.4800E-04 | 1.1040E+03 | 1.3406E-07 | 7.9004E+01 |
| | 7 | 1.0550E-02 | 1.7900E-05 | 2.1520E+01 | 8.3178E-07 | 4.9024E+02 |
| | 8 | 1.4580E-02 | 2.4730E-05 | 2.1280E+02 | 1.1621E-07 | 6.8515E+01 |
| | 9 | 4.8110E-01 | 2.4310E-05 | 1.3970E+02 | 1.7402E-07 | 3.4438E+03 |
| | 10 | 1.2550E-01 | 2.8880E-06 | 3.4930E+02 | 8.2680E-09 | 3.5929E+02 |
| | 11 | 2.7930E-03 | 4.7400E-06 | 4.3350E+02 | 1.0934E-08 | 6.4429E+00 |

| | | | | | | |
|---|---|---|---|---|---|---|
| Lumazine | 5 | 3.8620E-03 | 1.6250E-03 | 4.6660E+01 | 3.4826E-05 | 8.2769E+01 |
| | 6 | 7.9540E-04 | 3.3460E-04 | 3.8570E+01 | 8.6751E-06 | 2.0622E+01 |
| | 7 | 1.0160E-02 | 4.2740E-03 | 5.0260E+01 | 8.5038E-05 | 2.0215E+02 |
| | 8 | 1.1520E-01 | 6.2490E-04 | 9.2210E+00 | 6.7769E-05 | 1.2493E+04 |
| | 9 | 1.6300E-01 | 1.0840E-03 | 1.8440E+01 | 5.8785E-05 | 8.8395E+03 |
| | 10 | 1.4450E-03 | 6.0780E-04 | 2.5170E+02 | 2.4148E-06 | 5.7410E+00 |
| Formaldehyde | 6 | 2.3030E+12 | 3.8110E+16 | 1.0830E+26 | 3.5189E-10 | 2.1265E-08 |
| | 7 | 1.5730E-02 | 2.6690E-05 | 4.8926E+04 | 5.4552E-10 | 3.2151E-01 |
| | 8 | 6.5180E-02 | 1.1060E-04 | 5.5992E+05 | 1.9753E-10 | 1.1641E-01 |
| | 9 | 1.9230E-01 | 3.2630E-04 | 1.5350E+06 | 2.1257E-10 | 1.2528E-01 |
| | 10 | 6.8680E+21 | 3.5720E+09 | 5.4620E+19 | 6.5397E-11 | 1.2574E+08 |
| | 11 | 5.3740E+12 | 1.2210E+25 | 1.9070E+35 | 6.4027E-11 | 2.8180E-17 |
| Acetaldehyde | 6 | 7.1050E-02 | 1.2060E-04 | 1.3343E+05 | 9.0382E-10 | 5.3247E-01 |
| | 7 | 3.0180E-02 | 5.1210E-05 | 1.5530E+06 | 3.2975E-11 | 1.9433E-02 |
| | 8 | 3.7160E-02 | 6.3060E-05 | 2.1400E+06 | 2.9467E-11 | 1.7364E-02 |
| | 9 | 1.3300E-02 | 2.2580E-05 | 1.0330E+06 | 2.1859E-11 | 1.2875E-02 |
| | 10 | 1.0150E+10 | 1.4410E+17 | 5.7960E+27 | 2.4862E-11 | 1.7512E-12 |
| | 11 | 3.2470E+38 | 1.5650E+16 | 1.2160E+27 | 1.2870E-11 | 2.6702E+17 |
| Propionaldehyde | 6 | 1.4140E-02 | 1.0990E-07 | 1.2294E+04 | 8.9393E-12 | 1.1502E+00 |
| | 7 | 8.8990E-02 | 2.4510E-06 | 4.0980E+03 | 5.9810E-10 | 2.1715E+01 |
| | 8 | 3.8980E-02 | 6.3780E-07 | 8.1960E+03 | 7.7818E-11 | 4.7560E+00 |
| | 9 | 1.4220E-02 | 3.5400E-05 | 1.3197E+04 | 2.6824E-09 | 1.0775E+00 |
| Butyraldehyde | 6 | 2.9390E-03 | 7.3160E-06 | 2.6976E+04 | 2.7120E-10 | 1.0895E-01 |
| | 8 | 8.4610E-04 | 2.1060E-06 | 5.3900E+03 | 3.9072E-10 | 1.5698E-01 |
| | 9 | 8.4610E-04 | 2.1060E-06 | 5.3900E+03 | 3.9072E-10 | 1.5698E-01 |
| Benzaldehyde | 6 | 1.0310E+12 | 1.6300E+19 | 1.4370E+26 | 1.1343E-07 | 7.1747E-09 |
| | 7 | 1.4070E-03 | 3.5030E-06 | 5.2770E+00 | 6.6382E-07 | 2.6663E+02 |
| | 8 | 3.6420E-03 | 9.0660E-06 | 7.3520E+01 | 1.2331E-07 | 4.9538E+01 |
| | 9 | 2.3930E+11 | 3.2650E+08 | 8.4890E+16 | 3.8462E-09 | 2.8189E+00 |
| | | | | | | |
| (d) The steady-state kinetic parameters for *Rc*XDH-Glu$_{232}$Ala enzyme | | | | | | |
| Purine | 7 | 2.4590E-02 | 3.3100E-07 | 1.0250E+02 | 3.2293E-09 | 2.3990E+02 |
| | 8 | 5.6800E-03 | 1.4140E-05 | 3.2740E+03 | 4.3189E-09 | 1.7349E+00 |
| | 9 | 6.2100E-04 | 1.5460E-06 | 3.3520E+02 | 4.6122E-09 | 1.8526E+00 |
| Hypoxanthine | 6 | 3.1470E-01 | 7.8320E-04 | 2.9924E+05 | 2.6173E-09 | 1.0517E+00 |
| | 7 | 9.7290E-04 | 2.4220E-06 | 1.1450E+02 | 2.1153E-08 | 8.4969E+00 |
| | 8 | 2.3920E-01 | 1.1780E-05 | 1.0250E+02 | 1.1493E-07 | 2.3337E+03 |
| | 9 | 2.2260E-03 | 5.5410E-06 | 2.5220E+02 | 2.1971E-08 | 8.8263E+00 |
| | 10 | 2.6760E-03 | 6.6620E-06 | 9.1820E+02 | 7.2555E-09 | 2.9144E+00 |
| Xanthine | 6 | 4.0100E-03 | 9.9800E-06 | 2.8430E+00 | 3.5104E-06 | 1.4105E+03 |
| | 7 | 1.3020E-03 | 3.2400E-06 | 4.5200E+00 | 7.1681E-07 | 2.8805E+02 |
| | 8 | 4.5770E-03 | 1.1390E-05 | 3.3770E+00 | 3.3728E-06 | 1.3553E+03 |
| Lumazine | 6 | 4.8850E+00 | 9.5480E-05 | 1.8440E+01 | 5.1779E-06 | 2.6491E+05 |
| | 7 | 1.3960E+01 | 2.3590E-03 | 8.3320E+00 | 2.8313E-04 | 1.6755E+06 |
| | 8 | 6.6300E+00 | 8.4080E-04 | 1.4030E+01 | 5.9929E-05 | 4.7256E+05 |
| | 9 | 1.5070E+01 | 5.7170E-04 | 1.8440E+01 | 3.1003E-05 | 8.1725E+05 |
| Formaldehyde | 6 | 4.8480E+20 | 1.7470E+07 | 1.5940E+18 | 1.0960E-11 | 3.0414E+08 |
| | 7 | 7.3980E-04 | 1.8410E-06 | 7.8235E+04 | 2.3532E-11 | 9.4561E-03 |

| | | | | | | |
|---|---|---|---|---|---|---|
| | 8 | 1.5540E-03 | 3.8680E-06 | 1.9870E+02 | 1.9467E-08 | 7.8208E+00 |
| Acetaldehyde | 6 | 4.6510E-04 | 1.1580E-06 | 1.0190E+05 | 1.1364E-11 | 4.5641E-03 |
| | 7 | 3.9120E-04 | 9.7380E-07 | 2.8913E+04 | 3.3680E-11 | 1.3530E-02 |
| | 8 | 1.9160E-03 | 4.7690E-06 | 3.5360E+03 | 1.3487E-09 | 5.4186E-01 |
| | 9 | 3.9380E-03 | 9.8030E-06 | 8.2489E+04 | 1.1884E-10 | 4.7740E-02 |
| | 10 | 2.8050E-03 | 6.9810E-06 | 2.6305E+04 | 2.6539E-10 | 1.0663E-01 |
| Propionaldehyde | 7 | 8.3250E-02 | 2.2070E-06 | 4.0980E+03 | 5.3856E-10 | 2.0315E+01 |
| | 8 | 8.6300E-04 | 2.1480E-06 | 3.8240E+03 | 5.6172E-10 | 2.2568E-01 |
| | 9 | 2.8150E-03 | 7.0060E-06 | 3.7558E+04 | 1.8654E-10 | 7.4951E-02 |
| | 10 | 9.5490E-03 | 2.0620E-06 | 1.7786E+04 | 1.1593E-10 | 5.3688E-01 |
| Butyraldehyde | 7 | 4.4270E-02 | 8.2990E-07 | 4.0980E+03 | 2.0251E-10 | 1.0803E+01 |
| | 8 | 1.1470E-01 | 3.6750E-06 | 2.0490E+04 | 1.7936E-10 | 5.5979E+00 |
| | 9 | 1.5920E-01 | 6.1790E-06 | 4.0980E+03 | 1.5078E-09 | 3.8848E+01 |
| | 10 | 1.2870E-03 | 3.2040E-06 | 4.4520E+03 | 7.1968E-10 | 2.8908E-01 |
| | 7 | 1.9840E-02 | 2.1110E-07 | 1.1270E+01 | 1.8731E-08 | 1.7604E+03 |
| | 8 | 8.6490E-02 | 2.3510E-06 | 4.5080E+00 | 5.2152E-07 | 1.9186E+04 |
| Benzaldehyde | 9 | 2.5520E-03 | 6.3530E-06 | 4.7220E+01 | 1.3454E-07 | 5.4045E+01 |

Appendix IV: The data for the substrate-enzyme binding cofactor reduction

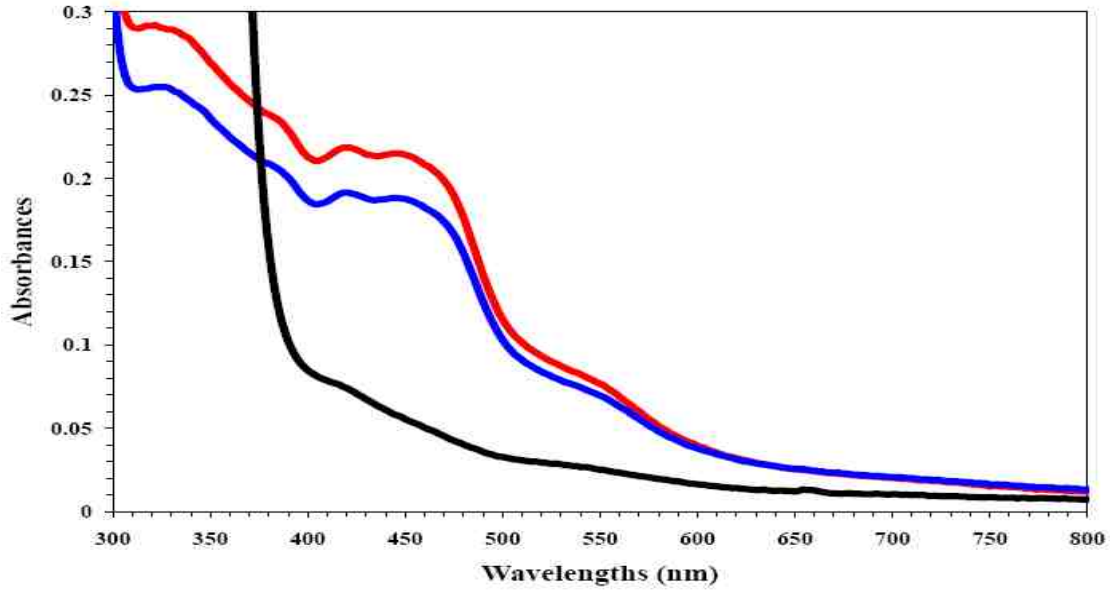


The traces from *top to bottom* represent the native enzyme (*red or first trace*) and *Oc*Cu/Mo-CODH reduced with CO (*blue or second trace*) and sodium dithionite (*black or third trace*).

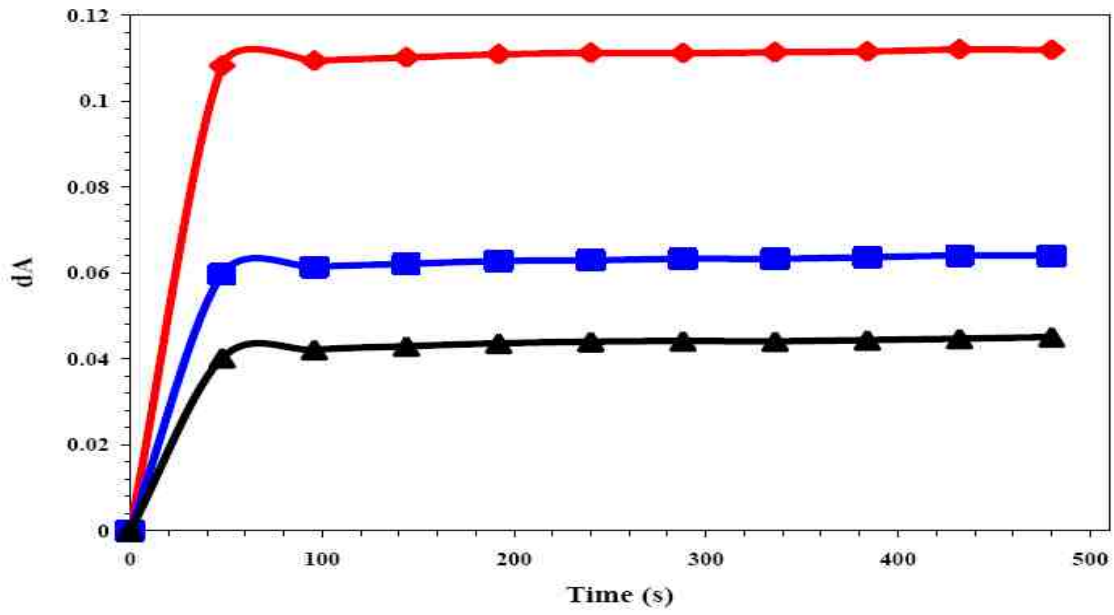


The traces from *top to bottom* represent the oxidized *bm*XOR enzyme reduced with sodium dithionite monitored at 450 nm (*red or first trace*), 550 nm (*blue or second trace*), and 650 nm (*black or third trace*).

Figure A. 4. The anaerobic substrate-enzyme cofactor reduction for *Oc*Cu/Mo-CODH (*upper panel*) and *bm*XOR (*lower panel*) enzymes.

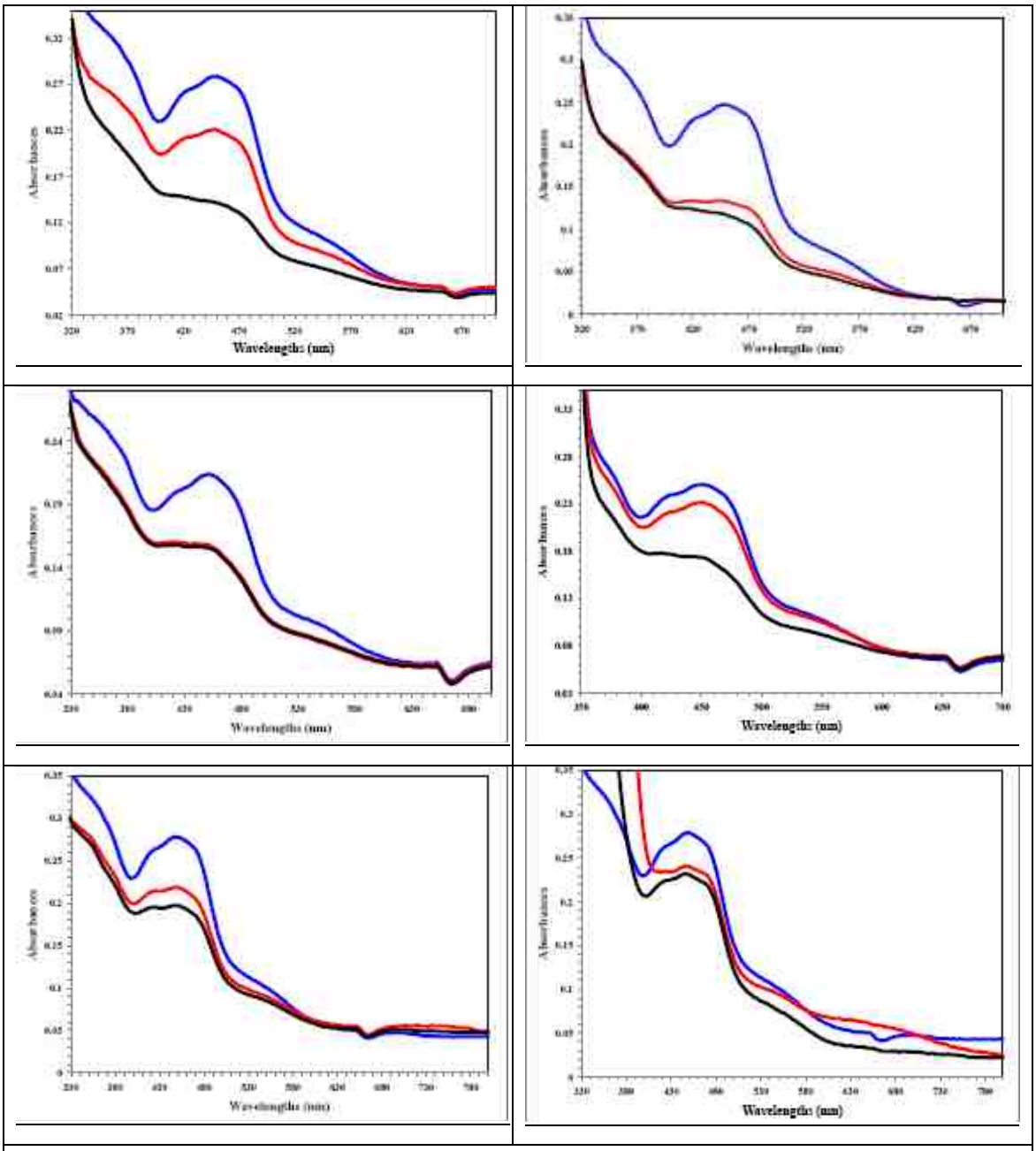


Figure A.5. The anaerobic substrate-enzyme cofactor reduction of *bm*XOR enzyme, in the presence of various substrates [purine (*upper left panel*), hypoxanthine (*upper right panel*), xanthine (middle *left panel*), HMP (*middle right panel*), allopurinol (*lower left panel*), and lumazine (*lower right panel*)]. The traces from *top to bottom* represent the partial reduction of the oxidized *bm*XOR enzyme (*black or third traces*), in the presence of various substrates, were compared with respect to the native enzymes (*blue or first traces*) and the activated enzyme (after the reaction mixture was activated by the substrates, *red or second traces*).

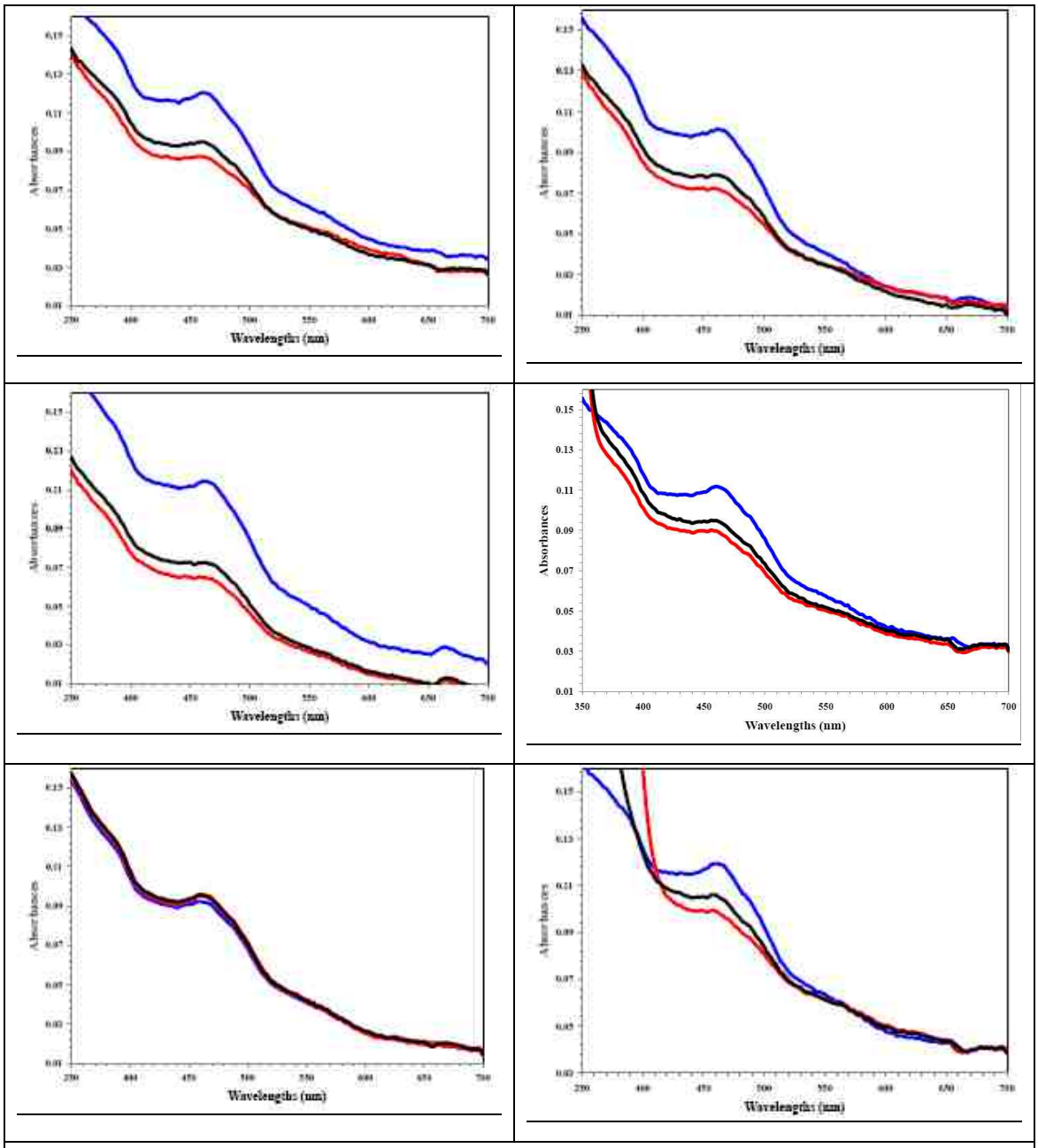


Figure A.6. The anaerobic substrate-enzyme cofactor reduction of *Rc*XDH enzyme, in the presence of various substrates [purine (*upper left panel*), hypoxanthine (*upper right panel*), xanthine (middle *left panel*), HMP (*middle right panel*), allopurinol (*lower left panel*), and lumazine (*lower right panel*)]. The traces from *top to bottom* represent the partial reduction of *Rc*XDH enzyme (*red or third traces*), in the presence of various substrates, were compared with respect to the native enzymes (*blue or first traces*) and the activated enzyme (after the reaction mixture was activated by the substrates, *black or second traces*).

Appendix V: The data for the inhibitors screening of the catalyzed-reaction

Table A. 2. The percent (%) inhibition of physiological substrates [carbon monoxide (CO), xanthine (XA), hypoxanthine (HY), allopurinol (AL), and acetaldehyde (AC)] in the presence of various molecules. Other symbols represent for 2-Hydroxy,6-methylpurine (HMP) and N,N-Dimethylthioformamide (DMTF)

| Substrates | *Oc*Cu/Mo-CODH | *bm*XOR in the presence of | | | |
|---|---|---|---|---|---|
| | CO | 4.5 mM XA | 0.1 mM HY | 0.1 mM AL | 50 mM AC |
| 0.2 M Methanol | 18.14 | 0.00 | 115.50 | 67.91 | 60.27 |
| 0.2 M Ethanol | 61.07 | 0.07 | 96.89 | 64.20 | 96.27 |
| 0.1 mM Propanol | 128.09 | 85.29 | 85.06 | 82.88 | |
| 0.1 mM Butanol | 104.48 | 100.17 | 95.74 | 84.28 | |
| 0.2 M Ethylene glycole | 77.40 | 98.33 | 89.01 | 76.51 | |
| 2.0 mM Glyceraldehyde | | 76.13 | 98.21 | 74.63 | |
| 0.2 M Formaldehyde | 37.77 | | | | 69.13 |
| 2.0 mM Formaldehyde | 68.46 | 0.00 | 79.14 | | |
| 2.0 mM Acetaldehyde | 71.62 | 76.93 | 79.34 | 53.88 | |
| 0.2 M Acetaldehyde | 29.46 | | | 98.33 | |
| 0.1 mM Propionaldehyde | 94.62 | 79.41 | 86.42 | 98.13 | |
| 0.1 mM Butyraldehyde | 92.81 | 76.52 | 92.72 | 73.58 | |
| 0.1 mM Trifluoroacetaldehyde | 104.01 | 81.22 | 98.63 | 73.49 | |
| 0.1 mM Benzaldehyde | 104.56 | | | | |
| 0.2 M Benzaldehyde | 11.55 | | | | |
| 0.1 mM Purine | 103.54 | | | | |
| 0.1 mM Hypoxanthine | 91.65 | | | | |
| 0.1 mM 6-Methylpurine | 97.38 | 31.79 | 115.12 | 110.54 | 78.77 |
| 0.1 mM Xanthine | 113.14 | | | | |
| 0.1 mM HMP | 96.28 | 16.10 | 92.83 | 70.54 | 50.70 |
| 0.1 mM Allopurinol | 108.86 | | | | |
| 0.2 M Formamide | 30.60 | 24.63 | | | 83.38 |
| 2.0 mM Formamide | 51.55 | | 30.53 | 139.52 | |
| 0.1 mM N-Methylformamide | 93.15 | 93.27 | 93.63 | 78.53 | |
| 0.1 mM N,N-Dimethylformamide | 136.17 | 100.42 | 101.14 | 77.77 | |
| 0.1 mM DMTF | 96.59 | 97.69 | 87.81 | | |
| 0.1 mM Nitrophenyl-formamide | 98.51 | | | | |
| 2.0 mM Trifluoroacetamide | | 94.59 | 105.93 | 85.88 | |
| 0.1 mM Thiourea | 118.05 | | | | |
| 2.0 mM Formate | 74.91 | | 23.84 | 137.29 | 38.66 |
| 0.2 M Formate | 46.04 | 0.85 | | | |
| 0.1 mM Acetate | 85.69 | 113.99 | 94.82 | 89.54 | |
| 0.2 M Cyanide | 0.71 | 0.03 | 2.65 | 0.00 | 0.00 |
| 0.2 M Thiocynate | 19.77 | 69.75 | 113.16 | 152.35 | |
| 0.2 M Nitrite | 16.35 | 66.49 | 113.26 | 149.98 | |
| 0.2 M Nitrate | 45.86 | 5.30 | 114.94 | 135.74 | |

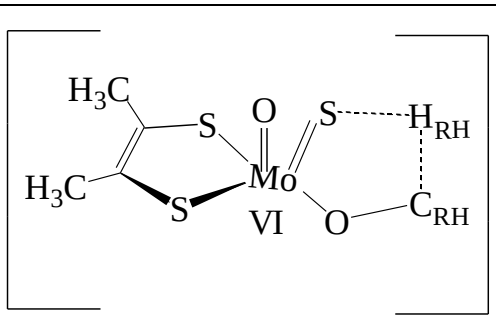


Figure A.7. A general structure for the transition state. The structures, representing the tetrahedral transition state structures, were modeled by placing the substrate bound hydrogen ($H_{RH}$) between the Mo bound sulfido ($S_{Mo}$) terminal and the substrate ($C_{RH}$) bound carbon center. The $C_{RH}$ was replaced by various substrates (Fig. A. 2, as shown below).

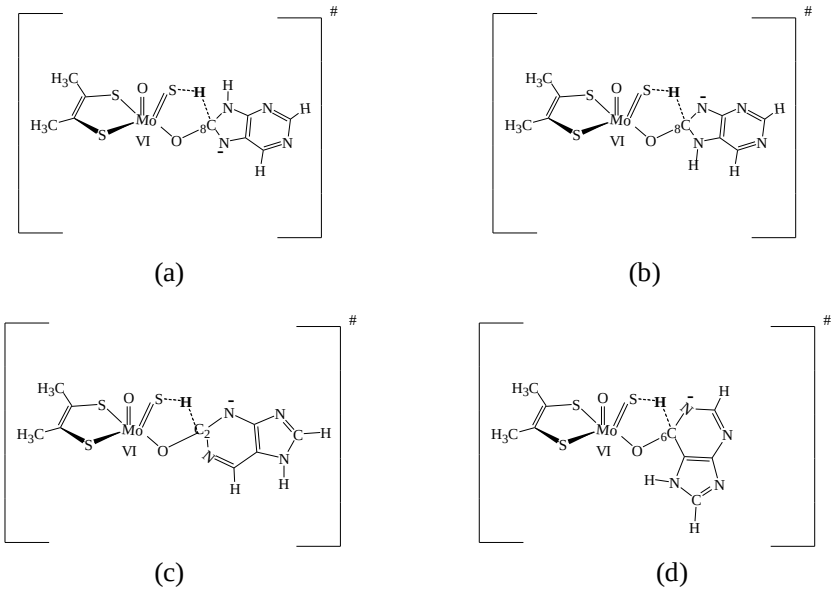


Figure A. 8. The geometries represent the transition state structures, modeling the $Mo^{(VI)}$ state of Moco bound to (a) and (b) $C_8$-purine, (c) $C_2$-purine, and (d) $C_6$-purine. The geometries were modeled in (a) N-down, (b) N-up, (c) N-up, and (d) N-up conformations.

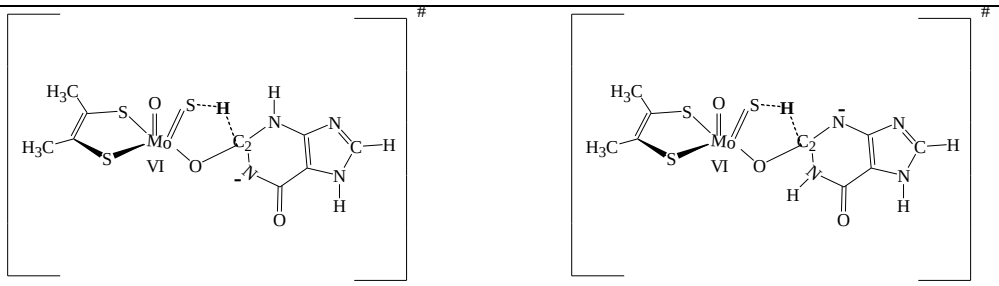


Figure A. 9. The geometries represent the transition state structures, modeling the $Mo^{(VI)}$ state Moco bound to $C_2$-hypoxanthine. The geometries were probed in (a) N-down and (b) N-up conformations.

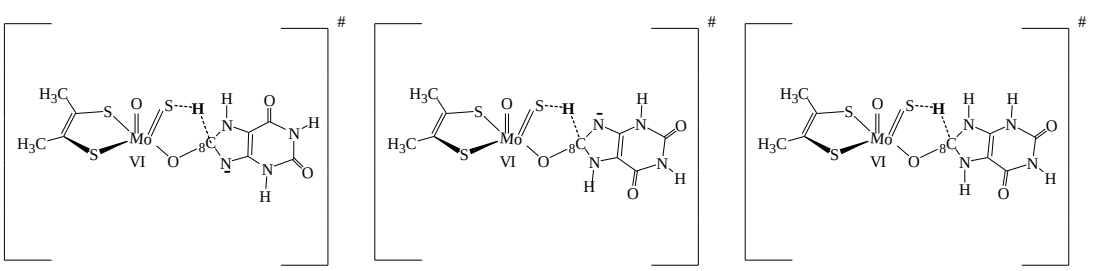


Figure A. 10. The geometries represent the transition state structures, modeling the $Mo^{(VI)}$ state of truncated Moco bound to $C_8$-xanthine. The geometries were probed in (a) N-down, (b) N-up, and (c) N-protonated conformations.

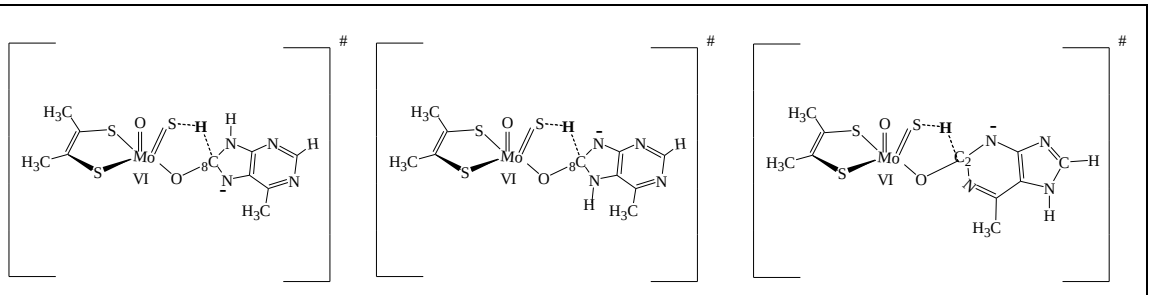


Figure A. 11. The geometries representing the transition state structures, modeling the $Mo^{(VI)}$ state of Moco bound to (a) and (b) $C_8$-6-methylpurine and (c) $C_2$-6-methylpurine. The geometries were probed in (a) N-down, (b) N-up, and (c) N-up conformations.

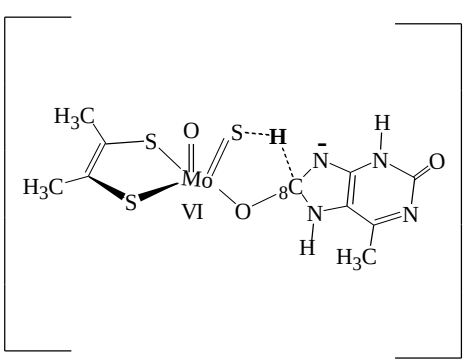

Figure A. 12. The geometries represent the transition state structures, modeling the $Mo^{(VI)}$ state of truncated Moco bound to $C_8$-2-hydroxy-6-methylpurine. The geometry was probed in N-up conformation.

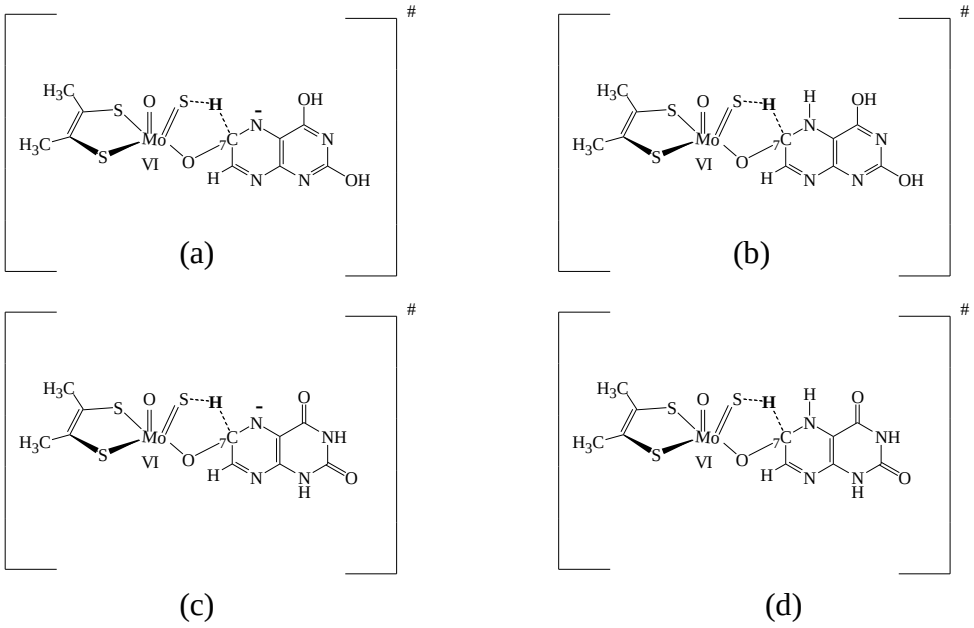


Figure A. 13. The geometries represent the transition state structures, modeling the $Mo^{(VI)}$ state of Moco bound to $C_7$-lumazine. The geometries were probed for the enolic ((a) and (b)) and phenolic ((c) and (d)) forms in (a) N-up, (b) N-protonated, (c) N-up, and (d) N-protonated conformations.

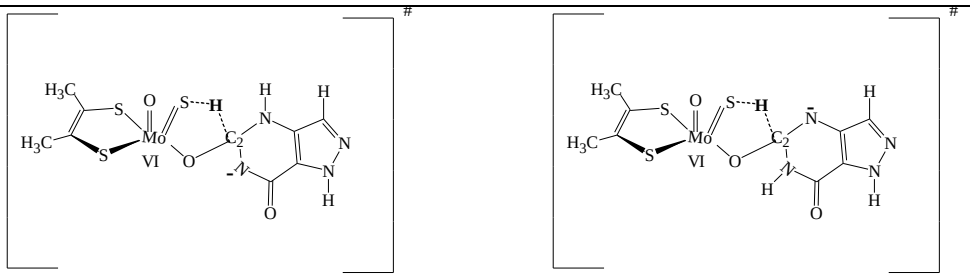

(a) (b)

Figure A. 14. The geometries represent the transition state structures, modeling the $Mo^{(VI)}$ state of Moco bound to $C_2$-allopurinol. The geometries were probed in (a) N-down and (b) N-up conformations.

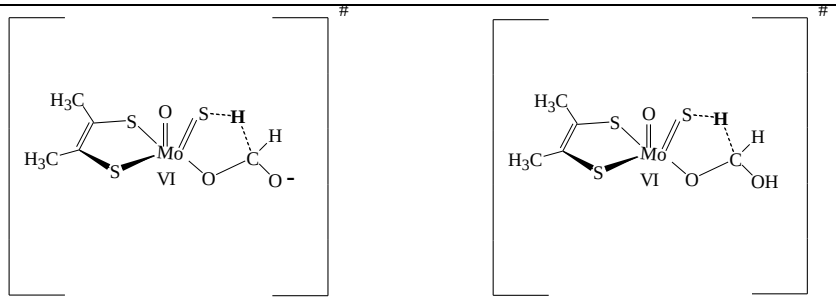

(a) (b)

Figure A. 15. The geometries represent the transition state structures, modeling the $Mo^{(VI)}$ state of Moco bound to formaldehyde. The geometries were probed in (a) un-protonated and (b) protonated conformations of the carbonyl oxygen of formaldehyde.

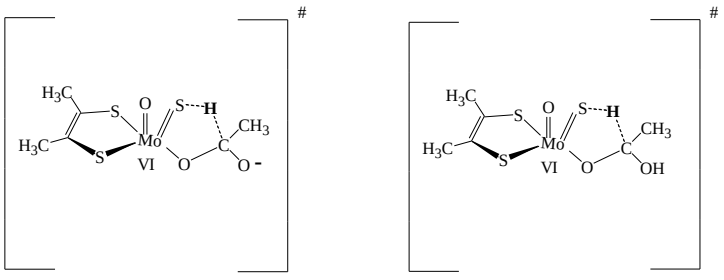

(a) (b)

Figure A. 16. The geometries represent the transition state structures, modeling the $Mo^{(VI)}$ state of Moco bound to acetaldehyde. The geometries were probed in (a) un-protonated and (b) protonated conformations of the carbonyl oxygen of acetaldehyde.

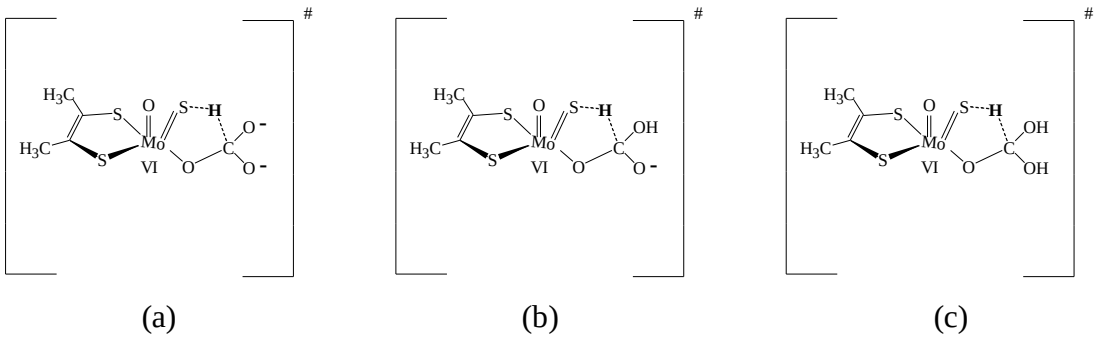


Figure A. 17. The geometries represent the transition state structures, modeling the $Mo^{(VI)}$ state of Moco bound to formate. The geometries were probed in (a) doubly un-protonated, (b) singly protonated, (c) doubly protonated conformations of the carbonyl oxygen of formate.

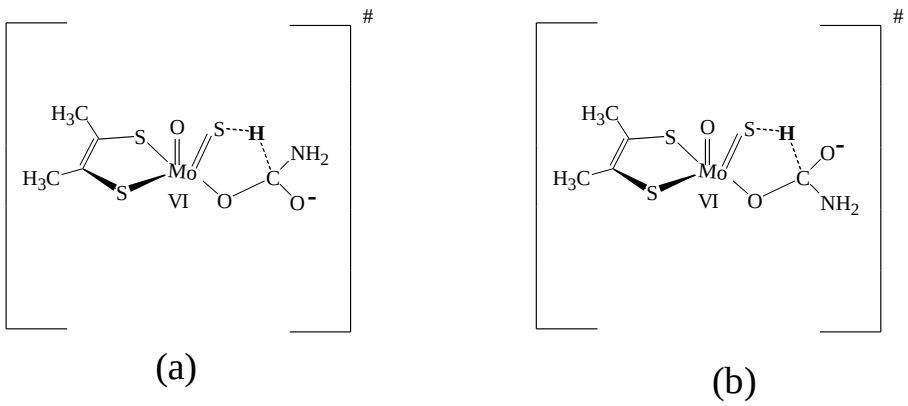


Figure A. 18. The geometries representing the transition state structures modeling the $Mo^{(VI)}$ state of Moco bound to formamide. The geometries were probed in two conformations, when the carbonyl oxygen of formamide was (a) below and (b) above the equatorial plane of the truncated Moco.

Appendix VII: The raw data for the transition state characterization

Table A. 3. The raw data obtained from the linear transit calculations. The total energies are shown for the $S_{Mo}$-$H_{RH}$ (S-H) bond distances (in angestrom). The calculations were performed for the geometries described in Appendix (VI).

| S-H | E (kcal/mole) | S-H | E (kcal/mole) | S-H | E (kcal/mole) | S-H | E (kcal/mole) |
|---|---|---|---|---|---|---|---|
| H (Down conformation) for deprotonated substrates | | | | | | | |
| | Purine-$C_6$ | | 6MP-$C_2$ | | 6MP-$C_8$ | | HMP |
| 1.3587 | -1.2429114E+06 | 1.3482 | -1.2675758E+06 | 1.3875 | -1.2676065E+06 | 1.3799 | -1.3148233E+06 |
| 1.5587 | -1.2429035E+06 | 1.5482 | -1.2675688E+06 | 1.5875 | -1.2675978E+06 | 1.5799 | -1.3148143E+06 |
| 1.7587 | -1.2428890E+06 | 1.6482 | -1.2675621E+06 | 1.7747 | -1.2675833E+06 | 1.7799 | -1.3147861E+06 |
| 1.8587 | -1.2428749E+06 | 1.7482 | -1.2675543E+06 | 1.8747 | -1.2675663E+06 | 1.8799 | -1.3147865E+06 |
| 1.9587 | -1.2428752E+06 | 1.8482 | -1.2675357E+06 | 1.9747 | -1.2675659E+06 | 1.9799 | -1.3147858E+06 |
| 2.0587 | -1.2428697E+06 | 1.9482 | -1.2675367E+06 | 2.0747 | -1.2675659E+06 | 2.0799 | -1.3147876E+06 |
| 2.1587 | -1.2428644E+06 | 2.1482 | -1.2675495E+06 | 2.1747 | -1.2675678E+06 | 2.1799 | -1.3147886E+06 |
| 2.3587 | -1.2428553E+06 | 2.3482 | -1.2675514E+06 | 2.3747 | -1.2675682E+06 | 2.3799 | -1.3147891E+06 |
| 2.5587 | -1.2428493E+06 | 2.5482 | -1.2675547E+06 | 2.5747 | -1.2675683E+06 | 2.5799 | -1.3147889E+06 |
| | | | | | | | |
| | Hypoxanthine | | Xanthine | | Allopurinol | | Lumazine enol |
| 1.3118 | -1.2901389E+06 | 1.3052 | -1.3373694E+06 | 1.3792 | -1.2901378E+06 | 1.3941 | -1.3612562E+06 |
| 1.5118 | -1.2901346E+06 | 1.5052 | -1.3373657E+06 | 1.5792 | -1.2901288E+06 | 1.5941 | -1.3612465E+06 |
| 1.7118 | -1.2901210E+06 | 1.7052 | -1.3373522E+06 | 1.7792 | -1.2901000E+06 | 1.7941 | -1.3612321E+06 |
| 1.8118 | -1.2901137E+06 | 1.8052 | -1.3373331E+06 | 1.8792 | -1.2900996E+06 | 1.8941 | -1.3612196E+06 |
| 1.9118 | -1.2900996E+06 | 1.9052 | -1.3373328E+06 | 1.9792 | -1.2901000E+06 | 1.9941 | -1.3612207E+06 |
| 2.1312 | -1.2901002E+06 | 2.1052 | -1.3373340E+06 | 2.1792 | -1.2901005E+06 | 2.1941 | -1.3612208E+06 |
| 2.3312 | -1.2901162E+06 | 2.3052 | -1.3373349E+06 | 2.3792 | -1.2901009E+06 | 2.3941 | -1.3612216E+06 |
| 2.5312 | -1.2901179E+06 | 2.5052 | -1.3373350E+06 | 2.5792 | -1.2901007E+06 | 2.5941 | -1.3612216E+06 |
| | | | | | | | |
| | Lumazine keto | | Formaldehyde | | Acetaldehyde | | Formate |
| 1.3736 | -1.3612693E+06 | 1.4423 | -1.0562759E+06 | 1.3584 | -1.0809518E+06 | 1.2919 | -1.1029728E+06 |
| 1.5736 | -1.3612606E+06 | 1.6423 | -1.0562644E+06 | 1.5674 | -1.0809436E+06 | 1.3919 | -1.1029744E+06 |
| 1.7736 | -1.3612466E+06 | 1.8423 | -1.0562504E+06 | 1.7764 | -1.0809290E+06 | 1.4919 | -1.1029750E+06 |
| 1.8736 | -1.3612304E+06 | 2.0423 | -1.0562340E+06 | 1.9854 | -1.0809082E+06 | 1.5919 | -1.1029767E+06 |
| 1.9736 | -1.3612314E+06 | 2.2423 | -1.0562449E+06 | 2.1944 | -1.0809240E+06 | 1.6919 | -1.1029789E+06 |
| 2.1736 | -1.3612450E+06 | 2.4423 | -1.0562462E+06 | 2.4034 | -1.0809258E+06 | 1.8919 | -1.1029710E+06 |
| 2.3736 | -1.3612466E+06 | 2.6435 | -1.0562468E+06 | 2.6124 | -1.0809266E+06 | 1.9919 | -1.1029710E+06 |
| 2.5736 | -1.3612479E+06 | 2.8423 | -1.0562470E+06 | | | 2.3919 | -1.1029856E+06 |
| H (Down conformation) | | H (Up conformation) for deprotonated substrates | | | | | |
| | Formamide | | Purine-$C_8$ | | Purine-$C_2$ | | 6MP-$C_8$ |
| 1.3318 | -1.0910269E+06 | 1.3326 | -1.2428926E+06 | 1.4480 | -1.2428979E+06 | 1.3392 | -1.2676088E+06 |
| 1.6318 | -1.0910141E+06 | 1.5326 | -1.2429274E+06 | 1.5480 | -1.2428928E+06 | 1.5392 | -1.2676022E+06 |
| 1.7318 | -1.0910067E+06 | 1.7326 | -1.2429131E+06 | 1.7480 | -1.2428763E+06 | 1.7392 | -1.2675879E+06 |
| 1.8332 | -1.0909795E+06 | 1.8326 | -1.2428931E+06 | 1.8480 | -1.2428603E+06 | 1.8392 | -1.2675682E+06 |
| 1.9332 | -1.0910045E+06 | 1.9326 | -1.2428926E+06 | 1.9480 | -1.2428610E+06 | 1.9392 | -1.2675682E+06 |

| | | | | | | | | | |
|---|---|---|---|---|---|---|---|---|---|
| 2.0332 | -1.0910073E+06 | | 2.1326 | -1.2428928E+06 | | 2.1480 | -1.2428741E+06 | 2.1392 | -1.2675673E+06 |
| 2.3332 | -1.0910125E+06 | | 2.3326 | -1.2428934E+06 | | 2.3480 | -1.2428757E+06 | 2.3392 | -1.2675686E+06 |
| | | | 2.5326 | -1.2428929E+06 | | 2.5480 | -1.2428761E+06 | 2.5392 | -1.2675681E+06 |
| | Hypoxanthine | | | Xanthine | | | Allopurinol | | Formamide |
| 1.3166 | -1.2901357E+06 | | 1.3140 | -1.3373330E+06 | | 1.3179 | -1.2901261E+06 | 1.3627 | -1.0910257E+06 |
| 1.5166 | -1.2901308E+06 | | 1.5140 | -1.3373673E+06 | | 1.5179 | -1.2901210E+06 | 1.5627 | -1.0910178E+06 |
| 1.7166 | -1.2901167E+06 | | 1.6140 | -1.3373608E+06 | | 1.7179 | -1.2901067E+06 | 1.7626 | -1.0910039E+06 |
| 1.8166 | -1.2901091E+06 | | 1.7140 | -1.3373533E+06 | | 1.8179 | -1.2900991E+06 | 1.8626 | -1.0909972E+06 |
| 1.9166 | -1.2900905E+06 | | 1.8140 | -1.3373330E+06 | | 1.9179 | -1.2900806E+06 | 1.9626 | -1.0909771E+06 |
| 2.0166 | -1.2900924E+06 | | 1.9140 | -1.3373323E+06 | | 2.0179 | -1.2900818E+06 | 2.0626 | -1.0910081E+06 |
| 2.1166 | -1.2901167E+06 | | 2.1140 | -1.3373326E+06 | | 2.1179 | -1.2901105E+06 | 2.1626 | -1.0910101E+06 |
| 2.3166 | -1.2901194E+06 | | 2.3140 | -1.3373320E+06 | | 2.3179 | -1.2901129E+06 | 2.2627 | -1.0910116E+06 |
| 2.5166 | -1.2901198E+06 | | 2.5140 | -1.3373348E+06 | | | | 2.3627 | -1.0910128E+06 |
| Protonated substrates | | | | | | | | | |
| | Xanthine | | | Lumazine enol | | | Lumazine keto | | Formaldehyde |
| 1.3734 | -1.3377567E+06 | | 1.3536 | -1.3616306E+06 | | 1.3568 | -1.3616600E+06 | 1.3967 | -1.0566661E+06 |
| 1.4734 | -1.3377536E+06 | | 1.5536 | -1.3616237E+06 | | 1.4568 | -1.3616577E+06 | 1.4967 | -1.0566618E+06 |
| 1.5734 | -1.3377478E+06 | | 1.6536 | -1.3616104E+06 | | 1.5568 | -1.3616522E+06 | 1.5976 | -1.0566504E+06 |
| 1.6734 | -1.3377405E+06 | | 1.7536 | -1.3616116E+06 | | 1.6568 | -1.3616354E+06 | 1.7967 | -1.0566616E+06 |
| 1.7734 | -1.3377253E+06 | | 1.9536 | -1.3616150E+06 | | 1.7568 | -1.3616354E+06 | 1.9967 | -1.0566655E+06 |
| 1.9734 | -1.3377290E+06 | | 2.1536 | -1.3616222E+06 | | 1.9568 | -1.3616354E+06 | 2.1967 | -1.0566671E+06 |
| 2.1734 | -1.3377318E+06 | | 2.3536 | -1.3616250E+06 | | 2.1568 | -1.3616440E+06 | 2.3967 | -1.0566671E+06 |
| 2.3734 | -1.3377338E+06 | | 2.5536 | -1.3616194E+06 | | 2.3568 | -1.3616453E+06 | | |
| | Acetaldehyde | | | Formate single | | | Formamide | | Formamide |
| 1.3582 | -1.0813591E+06 | | 1.4700 | -1.1034883E+06 | | 1.3439 | -1.0914349E+06 | 1.3690 | -1.0914326E+06 |
| 1.3544 | -1.0813595E+06 | | 1.6700 | -1.1034763E+06 | | 1.5439 | -1.0914279E+06 | 1.4690 | -1.0914298E+06 |
| 1.4544 | -1.0813573E+06 | | 1.7700 | -1.1034690E+06 | | 1.7439 | -1.0914020E+06 | 1.5690 | -1.0914240E+06 |
| 1.5544 | -1.0813519E+06 | | 1.8700 | -1.1034490E+06 | | 1.8439 | -1.0914042E+06 | 1.6690 | -1.0914009E+06 |
| 1.6544 | -1.0813344E+06 | | 1.9700 | -1.1034629E+06 | | 1.9439 | -1.0914066E+06 | 1.7690 | -1.0914018E+06 |
| 1.7544 | -1.0813368E+06 | | 2.5700 | -1.1034670E+06 | | 2.2439 | -1.0914106E+06 | 2.0690 | -1.0914057E+06 |
| 1.8544 | -1.0813389E+06 | | | | | 2.3439 | -1.0914117E+06 | 2.2690 | 1.0914073E+06 |
| 1.9544 | -1.0813408E+06 | | | | | 2.5439 | -1.0914127E+06 | 2.5690 | -1.0914084E+06 |
| 2.2544 | -1.0813448E+06 | | | | | | | | |

Table A. 4. The data for the transition state structure. The calculations were performed for the geometries described in Appendix (VI).

| Substrates | Frequency | Bond distances | | | HOMO | | Bond orders | |
|---|---|---|---|---|---|---|---|---|
| | | $S_{Mo}$-$H_{RH}$ | $C_{CRH}$-$H_{RH}$ | | -1 | 0 | $S_{Mo}$-$H_{RH}$ | $C_{CRH}$-$H_{RH}$ |
| | ($s^{-1}$) | (Å) | (Å) | E (kcal/mol) | (%) | (%) | | |
| Deprotonated substrates | | | | | | | | |
| Purine-$C_8$ | -62.25 | 1.9625 | 1.1980 | -1.242892E+06 | 4.64 | 19.47 | 0.237 | 0.702 |
| Purine-$C_2$ | -239.77 | 1.8480 | 1.2354 | -1.242860E+06 | 9.63 | 22.41 | 0.316 | 0.639 |
| Purine-$C_6$ | -212.88 | 1.8587 | 1.2344 | -1.242875E+06 | 10.91 | 20.75 | 0.491 | 0.409 |
| 6MP-$C_8$ | -53.43 | 1.9747 | 1.1943 | -1.267567E+06 | 4.6 | 18.86 | 0.229 | 0.709 |
| 6MP-$C_2$ | -236.13 | 1.8482 | 1.2357 | -1.267536E+06 | 0.02 | 0 | 0.314 | 0.64 |
| HMP | -431.66 | 1.7799 | 1.2675 | -1.314786E+06 | 4.05 | 21.92 | 0.365 | 0.601 |
| Hypoxanthine | -98.62 | 1.9118 | 1.2097 | -1.290100E+06 | 6.08 | 19.54 | 0.265 | 0.683 |
| Xanthine | -275.80 | 1.8052 | 1.2513 | -1.337333E+06 | 4.68 | 25.41 | 0.347 | 0.618 |
| Allopurinol | -149.09 | 1.8792 | 1.2227 | -1.290100E+06 | 10.86 | 15.16 | 0.288 | 0.661 |
| Lumazine enol | -124.65 | 1.8941 | 1.2195 | -1.361221E+06 | 9.17 | 18.31 | 0.282 | 0.664 |
| Lumazine keto | -169.85 | 1.8736 | 1.2262 | -1.361231E+06 | 8.72 | 20.82 | 0.297 | 0.653 |
| Formaldehyde | -326.39 | 2.0423 | 1.1971 | -1.056234E+06 | 2.22 | 20.59 | 0.215 | 0.725 |
| Acetaldehyde | -340.58 | 1.9854 | 1.2079 | -1.080909E+06 | 2.3 | 23.1 | 0.241 | 0.685 |
| Formate | -523.10 | 1.4919 | 1.6857 | -1.102938E+06 | 1.3 | 43.98 | 0.751 | 0.254 |
| Formamide | -538.88 | 1.8318 | 1.2534 | -1.090980E+06 | 35.21 | 2.19 | 0.33 | 0.617 |
| H(Up conformation) for deprotonated substrates | | | | | | | | |
| Purine-$C_8$ | -89.20 | 1.9326 | 1.2081 | -1.242893E+06 | 0.39 | -0.36 | 0.258 | 0.684 |
| 6MP-$C_8$ | -79.23 | 1.9392 | 1.2063 | -1.267568E+06 | 3.53 | 22.94 | 0.253 | 0.688 |
| Hypoxanthine | -136.96 | 1.9166 | 1.2136 | -1.290092E+06 | 26.72 | 2.73 | 0.259 | 0.68 |
| Xanthine | -247.13 | 1.8140 | 1.2469 | -1.337333E+06 | 5.53 | 24.03 | 0.335 | 0.629 |
| Allopurinol | -156.73 | 1.9179 | 1.2177 | -1.290082E+06 | 28.08 | 3.02 | 0.263 | 0.669 |
| Formamide | -414.57 | 1.9626 | 1.2081 | -1.090981E+06 | 27.62 | 2.4 | 0.245 | 0.689 |
| Protonated substrates | | | | | | | | |
| Xanthine | -909.27 | 1.6734 | 1.3591 | -1.337725E+06 | 45.43 | 4.9 | 0.505 | 0.474 |
| Lumaazine enol | -935.53 | 1.6536 | 1.3641 | -1.361611E+06 | 40.32 | 4.16 | 0.49 | 0.492 |
| Lumazine keto | -936.83 | 1.6568 | 1.3621 | -1.361636E+06 | 42.01 | 4.1 | 0.486 | 0.497 |
| Formaldehyde | -988.61 | 1.5967 | 1.4324 | -1.056650E+06 | 55.85 | 4.46 | 0.561 | 0.447 |
| Acetaldehyde | -1007.54 | 1.6544 | 1.4400 | -1.081334E+06 | 52.83 | 4.26 | 0.536 | 0.45 |
| Formate single | -392.36 | 1.8700 | 1.2352 | -1.103449E+06 | 35.56 | 2.34 | 0.3 | 0.644 |
| Formate double | -1001.40 | 1.6207 | 1.4061 | -1.103866E+06 | 54.33 | 4.54 | 0.529 | 0.455 |
| Formamide U | -880.60 | 1.6690 | 1.3513 | -1.091401E+06 | 50.91 | 4.42 | 0.47 | 0.511 |
| Formamide D | -995.37 | 1.6439 | 1.3824 | -1.091400E+06 | 53.56 | 4.59 | 0.497 | 0.472 |

Table A. 5. The raw data for the Mulliken atomic charges. The calculations were performed for the geometries described in Appendix (VI).

| | S-H (Å) | Mo | $O_{Mo(Apical)}$ | $O_{Mo}$ | $S_{Mo}$ | $S_{dithiolene\ (b)}$ | $S_{dithiolene\ (a)}$ | $C_{CRH}$ | $H_{RH}$ |
|---|---|---|---|---|---|---|---|---|---|
| H(Down conformation) for deprotonated substrates | | | | | | | | | |
| Purine-$C_6$ | 1.3587 | 0.4227 | -0.4993 | -0.4550 | -0.3917 | -0.2207 | -0.2434 | 0.3145 | -0.0089 |
| | 1.5587 | 0.4192 | -0.4962 | -0.4551 | -0.3759 | -0.2170 | -0.2409 | 0.3187 | -0.0390 |
| | 1.7587 | 0.4197 | -0.4924 | -0.4570 | -0.3630 | -0.2100 | -0.2371 | 0.3252 | -0.0774 |
| | 1.8587 | 0.5644 | -0.5138 | -0.5336 | -0.4140 | -0.1829 | -0.1956 | 0.1856 | 0.0472 |
| | 1.9587 | 0.5888 | -0.5120 | -0.5440 | -0.4313 | -0.1753 | -0.1862 | 0.1822 | 0.0568 |
| | 2.1587 | 0.4209 | -0.4947 | -0.4661 | -0.3474 | -0.1832 | -0.2134 | 0.3469 | -0.1764 |
| | 2.3587 | 0.3935 | -0.4769 | -0.4729 | -0.3448 | -0.1733 | -0.2051 | 0.3533 | -0.2106 |
| | 2.5587 | 0.4128 | -0.4844 | -0.4755 | -0.3456 | -0.1640 | -0.1978 | 0.3613 | -0.2486 |
| 6MP- $C_2$ | 1.3482 | 0.4375 | -0.5052 | -0.4574 | -0.4083 | -0.2333 | -0.2628 | 0.3811 | -0.0106 |
| | 1.5482 | 0.4322 | -0.5020 | -0.4565 | -0.3917 | -0.2279 | -0.2553 | 0.3875 | -0.0417 |
| | 1.6482 | 0.4321 | -0.5028 | -0.4575 | -0.3829 | -0.2241 | -0.2509 | 0.3919 | -0.0616 |
| | 1.7482 | 0.4235 | -0.5039 | -0.4605 | -0.3771 | -0.2195 | -0.2460 | 0.3973 | -0.0781 |
| | 1.8482 | 0.5474 | -0.5188 | -0.5282 | -0.4179 | -0.1880 | -0.2052 | 0.2403 | 0.0492 |
| | 1.9482 | 0.5913 | -0.5178 | -0.5430 | -0.4500 | -0.1791 | -0.1921 | 0.2392 | 0.0592 |
| | 2.1482 | 0.6131 | -0.5396 | -0.5522 | -0.6458 | -0.1950 | -0.2400 | 0.1714 | 0.1420 |
| | 2.3482 | 0.6125 | -0.5378 | -0.5536 | -0.6551 | -0.1980 | -0.2446 | 0.1586 | 0.1570 |
| | 2.5482 | 0.6468 | -0.5523 | -0.5874 | -0.6182 | -0.1836 | -0.2774 | 0.1183 | 0.1134 |
| 6MP- $C_8$ | 1.3875 | 0.4005 | -0.5099 | -0.4651 | -0.3993 | -0.2072 | -0.2176 | 0.4494 | -0.0067 |
| | 1.5875 | 0.3958 | -0.5083 | -0.4668 | -0.3856 | -0.2024 | -0.2144 | 0.4543 | -0.0345 |
| | 1.7747 | 0.3688 | -0.5067 | -0.4703 | -0.3673 | -0.1874 | -0.2020 | 0.4624 | -0.0768 |
| | 1.8747 | 0.5528 | -0.5125 | -0.5211 | -0.4242 | -0.1673 | -0.1828 | 0.2993 | 0.0471 |
| | 1.9875 | 0.5889 | -0.5123 | -0.5315 | -0.4400 | -0.1601 | -0.1723 | 0.3009 | 0.0564 |
| | 2.1747 | 0.6173 | -0.5132 | -0.5587 | -0.4490 | -0.1460 | -0.1643 | 0.2888 | 0.0672 |
| | 2.3747 | 0.5732 | -0.4976 | -0.5631 | -0.4621 | -0.1416 | -0.1538 | 0.2851 | 0.0724 |
| | 2.5747 | 0.6251 | -0.5097 | -0.5592 | -0.4726 | -0.1399 | -0.1486 | 0.2799 | 0.0751 |
| HMP | 1.3799 | 0.3916 | -0.4979 | -0.4516 | -0.3927 | -0.2028 | -0.2177 | 0.4526 | -0.0096 |
| | 1.5799 | 0.3882 | -0.4968 | -0.4533 | -0.3788 | -0.1981 | -0.2150 | 0.4573 | -0.0379 |
| | 1.6799 | 0.3853 | -0.4952 | -0.4549 | -0.3713 | -0.1939 | -0.2128 | 0.4611 | -0.0576 |
| | 1.7799 | 0.5416 | -0.5151 | -0.5224 | -0.3815 | -0.1673 | -0.1958 | 0.2937 | 0.0448 |
| | 1.8799 | 0.5804 | -0.5101 | -0.5414 | -0.3986 | -0.1547 | -0.1815 | 0.2912 | 0.0564 |
| | 1.9799 | 0.6493 | -0.5165 | -0.5528 | -0.4039 | -0.1473 | -0.1766 | 0.2926 | 0.0627 |
| | 2.1799 | 0.6052 | -0.5092 | -0.5537 | -0.4376 | -0.1426 | -0.1584 | 0.2905 | 0.0697 |
| | 2.3799 | 0.6136 | -0.5069 | -0.5581 | -0.4472 | -0.1359 | -0.1483 | 0.2874 | 0.0738 |
| | 2.5799 | 0.6502 | -0.5119 | -0.5552 | -0.4554 | -0.1297 | -0.1409 | 0.2853 | 0.0762 |
| Hypoxanthine | 1.3118 | 0.3893 | -0.5134 | -0.4542 | -0.3846 | -0.2109 | -0.2254 | 0.4389 | -0.0029 |
| | 1.5118 | 0.3882 | -0.5128 | -0.4550 | -0.3729 | -0.2077 | -0.2230 | 0.4429 | -0.0272 |
| | 1.7118 | 0.3820 | -0.5103 | -0.4577 | -0.3587 | -0.1994 | -0.2180 | 0.4503 | -0.0633 |
| | 1.8118 | 0.3783 | -0.5082 | -0.4596 | -0.3526 | -0.1926 | -0.2137 | 0.4549 | -0.0875 |
| | 1.9118 | 0.5780 | -0.5148 | -0.5379 | -0.4251 | -0.1714 | -0.1870 | 0.2905 | 0.0556 |
| | 2.1312 | 0.6189 | -0.5227 | -0.5649 | -0.4687 | -0.1561 | -0.1634 | 0.2869 | 0.0705 |
| | 2.3312 | 0.6335 | -0.5411 | -0.5747 | -0.6782 | -0.1695 | -0.2195 | 0.2048 | 0.1603 |
| | 2.5312 | 0.6357 | -0.5399 | -0.5784 | -0.6788 | -0.1667 | -0.2205 | 0.1928 | 0.1705 |

| | | | | | | | | | |
|---|---|---|---|---|---|---|---|---|---|
| Xanthine | 1.3052 | 0.3997 | -0.5160 | -0.4579 | -0.3858 | -0.2051 | -0.2236 | 0.4546 | -0.0053 |
| | 1.5052 | 0.3990 | -0.5153 | -0.4594 | -0.3750 | -0.2019 | -0.2213 | 0.4584 | -0.0292 |
| | 1.7052 | 0.3900 | -0.5120 | -0.4620 | -0.3604 | -0.1930 | -0.2164 | 0.4656 | -0.0652 |
| | 1.8052 | 0.5127 | -0.5087 | -0.5351 | -0.3873 | -0.1709 | -0.1997 | 0.3062 | 0.0461 |
| | 1.9052 | 0.5527 | -0.5078 | -0.5510 | -0.4097 | -0.1617 | -0.1871 | 0.2982 | 0.0580 |
| | 2.1052 | 0.5609 | -0.5009 | -0.5613 | -0.4450 | -0.1513 | -0.1681 | 0.2986 | 0.0672 |
| | 2.3052 | 0.6334 | -0.5118 | -0.5664 | -0.4709 | -0.1475 | -0.1608 | 0.2939 | 0.0715 |
| | 2.5052 | 0.6486 | -0.5097 | -0.5711 | -0.4711 | -0.1434 | -0.1547 | 0.2897 | 0.0749 |
| Allopurinol | 1.3792 | 0.3875 | -0.5114 | -0.4453 | -0.3715 | -0.2055 | -0.2267 | 0.4490 | -0.0123 |
| | 1.5792 | 0.3850 | -0.5108 | -0.4466 | -0.3584 | -0.2011 | -0.2236 | 0.4544 | -0.0395 |
| | 1.7792 | 0.6150 | -0.5112 | -0.5366 | -0.4461 | -0.1612 | -0.1661 | 0.3018 | 0.0574 |
| | 1.8792 | 0.5672 | -0.5117 | -0.5354 | -0.4041 | -0.1661 | -0.1833 | 0.3020 | 0.0500 |
| | 1.9792 | 0.6150 | -0.5112 | -0.5366 | -0.4461 | -0.1612 | -0.1661 | 0.3018 | 0.0574 |
| | 2.1792 | 0.6433 | -0.5185 | -0.5560 | -0.4636 | -0.1524 | -0.1544 | 0.3023 | 0.0670 |
| | 2.3792 | 0.5877 | -0.5004 | -0.5709 | -0.4620 | -0.1418 | -0.1442 | 0.3000 | 0.0726 |
| | 2.5792 | 0.6657 | -0.5174 | -0.5690 | -0.4815 | -0.1431 | -0.1397 | 0.2982 | 0.0752 |
| Lumazine *enol* | 1.3941 | 0.3932 | -0.5128 | -0.4704 | -0.3587 | -0.1999 | -0.2337 | 0.3477 | -0.0166 |
| | 1.5941 | 0.4001 | -0.5180 | -0.4639 | -0.3471 | -0.1989 | -0.2284 | 0.3504 | -0.0446 |
| | 1.7941 | 0.4042 | -0.5166 | -0.4717 | -0.3339 | -0.1871 | -0.2226 | 0.3565 | -0.0893 |
| | 1.8941 | 0.5323 | -0.5086 | -0.5411 | -0.4044 | -0.1618 | -0.1818 | 0.2083 | 0.0438 |
| | 1.9941 | 0.5985 | -0.5123 | -0.5525 | -0.4419 | -0.1535 | -0.1639 | 0.2082 | 0.0501 |
| | 2.1941 | 0.5686 | -0.4943 | -0.5687 | -0.4605 | -0.1470 | -0.1545 | 0.2099 | 0.0594 |
| | 2.3941 | 0.6591 | -0.5156 | -0.5762 | -0.4858 | -0.1445 | -0.1473 | 0.2067 | 0.0651 |
| | 2.5941 | 0.6469 | -0.5064 | -0.5870 | -0.4863 | -0.1392 | -0.1423 | 0.2028 | 0.0692 |
| Lumazine *keto* | 1.3736 | 0.3869 | -0.5090 | -0.4687 | -0.3712 | -0.2038 | -0.2371 | 0.3414 | -0.0103 |
| | 1.5736 | 0.3927 | -0.5089 | -0.4648 | -0.3642 | -0.2069 | -0.2312 | 0.3444 | -0.0377 |
| | 1.7736 | 0.3867 | -0.5176 | -0.4671 | -0.3436 | -0.1920 | -0.2240 | 0.3512 | -0.0816 |
| | 1.8736 | 0.5427 | -0.5088 | -0.5402 | -0.4142 | -0.1677 | -0.1887 | 0.1941 | 0.0438 |
| | 1.9736 | 0.6106 | -0.5104 | -0.5524 | -0.4537 | -0.1614 | -0.1727 | 0.1955 | 0.0526 |
| | 2.1736 | 0.6175 | -0.5308 | -0.5915 | -0.6187 | -0.1745 | -0.2208 | 0.0818 | 0.1413 |
| | 2.3736 | 0.6047 | -0.5317 | -0.5908 | -0.6189 | -0.1697 | -0.2176 | 0.0741 | 0.1507 |
| | 2.5736 | 0.6001 | -0.5301 | -0.5880 | -0.5919 | -0.1608 | -0.2122 | 0.0388 | 0.1436 |
| Formaldehyde | 1.4423 | 0.4041 | -0.5300 | -0.4376 | -0.3896 | -0.2387 | -0.2402 | 0.2670 | -0.0309 |
| | 1.6423 | 0.4063 | -0.5285 | -0.4408 | -0.3772 | -0.2327 | -0.2342 | 0.2717 | -0.0667 |
| | 1.8423 | 0.4089 | -0.5261 | -0.4465 | -0.3679 | -0.2210 | -0.2243 | 0.2792 | -0.1164 |
| | 2.0423 | 0.5483 | -0.5330 | -0.5633 | -0.4993 | -0.2032 | -0.2090 | 0.2495 | 0.0197 |
| | 2.2423 | 0.6304 | -0.5505 | -0.5839 | -0.6318 | -0.1924 | -0.2333 | 0.1314 | 0.1228 |
| | 2.4423 | 0.6282 | -0.5499 | -0.5879 | -0.6362 | -0.1917 | -0.2336 | 0.1216 | 0.1268 |
| | 2.6435 | 0.6230 | -0.5497 | -0.5890 | -0.6326 | -0.1899 | -0.2349 | 0.1092 | 0.1240 |
| | 2.8423 | 0.6206 | -0.5495 | -0.5888 | -0.6248 | -0.1879 | -0.2365 | 0.1028 | 0.1086 |
| Acetaldehyde | 1.3584 | 0.4304 | -0.5393 | -0.4571 | -0.3995 | -0.2351 | -0.2359 | 0.3420 | -0.0138 |
| | 1.5674 | 0.4320 | -0.5379 | -0.4588 | -0.3860 | -0.2307 | -0.2309 | 0.3468 | -0.0470 |
| | 1.7764 | 0.4308 | -0.5351 | -0.4634 | -0.3711 | -0.2201 | -0.2212 | 0.3559 | -0.0977 |
| | 1.9854 | 0.6085 | -0.5430 | -0.5784 | -0.4808 | -0.2012 | -0.2096 | 0.3210 | 0.0107 |
| | 2.1944 | 0.6292 | -0.5504 | -0.5923 | -0.6360 | -0.1860 | -0.2330 | 0.2043 | 0.1281 |
| | 2.4034 | 0.6243 | -0.5500 | -0.5957 | -0.6427 | -0.1858 | -0.2331 | 0.1942 | 0.1382 |
| | 2.6124 | 0.6195 | -0.5498 | -0.5987 | -0.6442 | -0.1858 | -0.2335 | 0.1866 | 0.1422 |
| | 1.3919 | 0.4665 | -0.5887 | -0.5466 | -0.6043 | -0.3208 | -0.3039 | 0.3848 | 0.1170 |

| | | | | | | | | | |
|---|---|---|---|---|---|---|---|---|---|
| Formate | 1.4919 | 0.3766 | -0.5714 | -0.5228 | -0.6912 | -0.3130 | -0.3101 | 0.3936 | 0.1946 |
| | 1.5919 | 0.3451 | -0.5760 | -0.5068 | -0.7693 | -0.3021 | -0.3185 | 0.3991 | 0.2461 |
| | 1.6919 | 0.3233 | -0.5769 | -0.4923 | -0.8132 | -0.2988 | -0.3231 | 0.3987 | 0.2681 |
| | 1.8919 | 0.5572 | -0.5934 | -0.5817 | -0.4435 | -0.2353 | -0.3805 | 0.1717 | -0.0168 |
| | 1.9919 | 0.5572 | -0.5934 | -0.5817 | -0.4435 | -0.2353 | -0.3805 | 0.1717 | -0.0168 |
| | 2.1919 | 0.6467 | -0.5910 | -0.5743 | -0.4974 | -0.2257 | -0.3712 | 0.1492 | -0.0015 |
| | 2.3919 | 0.6705 | -0.5815 | -0.5858 | -0.5150 | -0.2217 | -0.3596 | 0.1369 | 0.0080 |
| Formamide | 1.3318 | 0.4439 | -0.5190 | -0.4777 | -0.4151 | -0.2307 | -0.3073 | 0.3885 | 0.0137 |
| | 1.6318 | 0.4453 | -0.5177 | -0.4736 | -0.3994 | -0.2257 | -0.3027 | 0.3901 | -0.0255 |
| | 1.7318 | 0.4425 | -0.5169 | -0.4719 | -0.3863 | -0.2192 | -0.2979 | 0.3934 | -0.0512 |
| | 1.8332 | 0.5913 | -0.5409 | -0.5773 | -0.4471 | -0.2117 | -0.2283 | 0.3408 | 0.0190 |
| | 1.9332 | 0.6568 | -0.5467 | -0.6416 | -0.5712 | -0.1749 | -0.2291 | 0.2120 | 0.0739 |
| | 2.0332 | 0.6601 | -0.5474 | -0.6392 | -0.5861 | -0.1764 | -0.2283 | 0.2105 | 0.0802 |
| | 2.3332 | 0.6470 | -0.5407 | -0.6433 | -0.5996 | -0.1793 | -0.2330 | 0.2023 | 0.0925 |
| H(Up conformation) for deprotonated substrates | | | | | | | | | |
| Purine-$C_8$ | 1.3326 | 0.5617 | -0.5329 | -0.5276 | -0.4394 | -0.1765 | -0.1786 | 0.3015 | 0.0591 |
| | 1.5326 | 0.4063 | -0.5678 | -0.4688 | -0.3641 | -0.2081 | -0.2161 | 0.4595 | -0.0073 |
| | 1.7326 | 0.4060 | -0.5648 | -0.4671 | -0.3542 | -0.2012 | -0.2109 | 0.4638 | -0.0425 |
| | 1.8326 | 0.5147 | -0.5363 | -0.5108 | -0.4143 | -0.1874 | -0.1942 | 0.3117 | 0.0402 |
| | 1.9326 | 0.5617 | -0.5329 | -0.5276 | -0.4394 | -0.1765 | -0.1786 | 0.3015 | 0.0591 |
| | 2.1326 | 0.6062 | -0.5307 | -0.5446 | -0.4662 | -0.1636 | -0.1608 | 0.2963 | 0.0700 |
| | 2.3326 | 0.6109 | -0.5304 | -0.5577 | -0.4740 | -0.1590 | -0.1556 | 0.2933 | 0.0754 |
| | 2.5326 | 0.5893 | -0.5245 | -0.5668 | -0.4798 | -0.1515 | -0.1447 | 0.2866 | 0.0798 |
| Purine-$C_2$ | 1.4480 | 0.4416 | -0.5046 | -0.4532 | -0.3986 | -0.2304 | -0.2587 | 0.3794 | -0.0253 |
| | 1.5480 | 0.4408 | -0.5046 | -0.4526 | -0.3895 | -0.2277 | -0.2550 | 0.3824 | -0.0422 |
| | 1.7480 | 0.4387 | -0.4859 | -0.4537 | -0.3690 | -0.2174 | -0.2440 | 0.3738 | -0.0848 |
| | 1.8480 | 0.5443 | -0.5240 | -0.5231 | -0.4168 | -0.1886 | -0.2032 | 0.2423 | 0.0494 |
| | 1.9480 | 0.5935 | -0.5175 | -0.5424 | -0.4503 | -0.1804 | -0.1913 | 0.2390 | 0.0594 |
| | 2.1480 | 0.6457 | -0.5575 | -0.5775 | -0.6319 | -0.1925 | -0.2454 | 0.1708 | 0.1456 |
| | 2.3480 | 0.6427 | -0.5575 | -0.5813 | -0.6387 | -0.1930 | -0.2477 | 0.1589 | 0.1623 |
| | 2.5480 | 0.6395 | -0.5583 | -0.5847 | -0.6396 | -0.1930 | -0.2499 | 0.1462 | 0.1761 |
| 6MP-$C_8$ | 1.3392 | 0.4035 | -0.5681 | -0.4720 | -0.3696 | -0.2108 | -0.2190 | 0.4598 | 0.0124 |
| | 1.5392 | 0.4065 | -0.5671 | -0.4708 | -0.3641 | -0.2082 | -0.2165 | 0.4620 | -0.0088 |
| | 1.7392 | 0.4067 | -0.5651 | -0.4696 | -0.3538 | -0.2007 | -0.2112 | 0.4669 | -0.0442 |
| | 1.8392 | 0.5172 | -0.5361 | -0.5129 | -0.4185 | -0.1871 | -0.1944 | 0.3126 | 0.0424 |
| | 2.1392 | 0.6203 | -0.5290 | -0.5527 | -0.4566 | -0.1627 | -0.1656 | 0.2981 | 0.0709 |
| | 2.3392 | 0.6122 | -0.5304 | -0.5580 | -0.4754 | -0.1595 | -0.1579 | 0.2952 | 0.0753 |
| | 2.5392 | 0.6242 | -0.5329 | -0.5609 | -0.4933 | -0.1499 | -0.1390 | 0.2888 | 0.0782 |
| Hypoxanthine | 1.3166 | 0.4074 | -0.5718 | -0.4572 | -0.3735 | -0.2129 | -0.2167 | 0.4431 | 0.0197 |
| | 1.5166 | 0.4127 | -0.5724 | -0.4558 | -0.3699 | -0.2107 | -0.2141 | 0.4448 | 0.0008 |
| | 1.7166 | 0.4178 | -0.5699 | -0.4543 | -0.3517 | -0.2037 | -0.2080 | 0.4463 | -0.0384 |
| | 1.8166 | 0.4146 | -0.5656 | -0.4570 | -0.3430 | -0.1990 | -0.2046 | 0.4531 | -0.0651 |
| | 1.9166 | 0.6172 | -0.5209 | -0.5274 | -0.4253 | -0.1806 | -0.1807 | 0.2819 | 0.0586 |
| | 2.0166 | 0.6016 | -0.5305 | -0.5563 | -0.4469 | -0.1676 | -0.1665 | 0.2688 | 0.0726 |
| | 2.1166 | 0.6668 | -0.5273 | -0.6700 | -0.5762 | -0.1637 | -0.2014 | 0.1641 | 0.1343 |
| | 2.3166 | 0.6654 | -0.5278 | -0.6741 | -0.5816 | -0.1650 | -0.1998 | 0.1509 | 0.1457 |
| | 2.5166 | 0.6358 | -0.6634 | -0.5409 | -0.5864 | -0.1468 | -0.2077 | 0.1444 | 0.1574 |
| Xanthine | 1.3140 | 0.5097 | -0.5171 | -0.5219 | -0.3981 | -0.1784 | -0.1973 | 0.3173 | 0.0317 |

| | | | | | | | | | |
|---|---|---|---|---|---|---|---|---|---|
| | 1.5140 | 0.4081 | -0.5639 | -0.4650 | -0.3628 | -0.2079 | -0.2184 | 0.4695 | -0.0084 |
| | 1.6140 | 0.4066 | -0.5620 | -0.4639 | -0.3588 | -0.2055 | -0.2161 | 0.4714 | -0.0233 |
| | 1.7140 | 0.4111 | -0.5610 | -0.4639 | -0.3487 | -0.2013 | -0.2139 | 0.4727 | -0.0443 |
| | 1.8140 | 0.5097 | -0.5171 | -0.5219 | -0.3981 | -0.1784 | -0.1973 | 0.3173 | 0.0317 |
| | 1.9140 | 0.5261 | -0.5130 | -0.5354 | -0.4160 | -0.1669 | -0.1823 | 0.3134 | 0.0494 |
| | 2.1140 | 0.5511 | -0.5084 | -0.5440 | -0.4527 | -0.1553 | -0.1629 | 0.3151 | 0.0610 |
| | 2.3140 | 0.5884 | -0.5099 | -0.5438 | -0.4815 | -0.1531 | -0.1668 | 0.3136 | 0.0725 |
| | 2.5140 | 0.6403 | -0.5152 | -0.5664 | -0.4744 | -0.1435 | -0.1446 | 0.2896 | 0.0762 |
| Allopurinol | 1.3179 | 0.4048 | -0.5908 | -0.4600 | -0.3649 | -0.2066 | -0.2103 | 0.4430 | 0.0243 |
| | 1.5179 | 0.4114 | -0.5890 | -0.4584 | -0.3655 | -0.2062 | -0.2101 | 0.4451 | 0.0074 |
| | 1.7179 | 0.4153 | -0.5853 | -0.4586 | -0.3428 | -0.1989 | -0.2025 | 0.4474 | -0.0364 |
| | 1.8179 | 0.4192 | -0.5800 | -0.4584 | -0.3433 | -0.1963 | -0.1989 | 0.4516 | -0.0576 |
| | 1.9179 | 0.5995 | -0.5416 | -0.5211 | -0.4105 | -0.1752 | -0.1700 | 0.2768 | 0.0617 |
| | 2.0179 | 0.6086 | -0.5372 | -0.5443 | -0.4354 | -0.1655 | -0.1569 | 0.2662 | 0.0737 |
| | 2.1179 | 0.6311 | -0.5231 | -0.6972 | -0.5751 | -0.1466 | -0.1891 | 0.1618 | 0.1185 |
| | 2.3179 | 0.5885 | -0.6764 | -0.5391 | -0.5957 | -0.1102 | -0.2002 | 0.1556 | 0.1298 |
| | 2.5179 | 0.5793 | -0.6542 | -0.5377 | -0.6099 | -0.1105 | -0.1968 | 0.1422 | 0.1258 |
| Formamide | 1.3627 | 0.4143 | -0.5432 | -0.4781 | -0.3983 | -0.2372 | -0.2387 | 0.3941 | -0.0145 |
| | 1.4627 | 0.4131 | -0.5393 | -0.4784 | -0.3930 | -0.2354 | -0.2366 | 0.3953 | -0.0299 |
| | 1.5627 | 0.4106 | -0.5336 | -0.4790 | -0.3865 | -0.2324 | -0.2337 | 0.3969 | -0.0496 |
| | 1.6627 | 0.4071 | -0.5276 | -0.4807 | -0.3786 | -0.2280 | -0.2295 | 0.3993 | -0.0736 |
| | 1.7626 | 0.4038 | -0.5213 | -0.4838 | -0.3706 | -0.2217 | -0.2239 | 0.4029 | -0.1031 |
| | 1.8626 | 0.4040 | -0.5161 | -0.4874 | -0.3639 | -0.2142 | -0.2182 | 0.4071 | -0.1367 |
| | 1.9626 | 0.5897 | -0.5348 | -0.5744 | -0.4989 | -0.2059 | -0.2070 | 0.3335 | 0.0183 |
| | 2.1626 | 0.6460 | -0.5399 | -0.6399 | -0.5913 | -0.1749 | -0.2374 | 0.2100 | 0.0873 |
| | 2.2627 | 0.6494 | -0.5412 | -0.6424 | -0.5970 | -0.1793 | -0.2330 | 0.2059 | 0.0915 |
| Protonated substrates | | | | | | | | | |
| Xanthine | 1.3734 | 0.3871 | -0.6405 | -0.3872 | -0.2724 | -0.1287 | -0.1850 | 0.5252 | -0.0015 |
| | 1.5734 | 0.3881 | -0.6386 | -0.3861 | -0.2653 | -0.1255 | -0.1841 | 0.5287 | -0.0229 |
| | 1.6734 | 0.3882 | -0.6359 | -0.3857 | -0.2626 | -0.1237 | -0.1832 | 0.5320 | -0.0371 |
| | 1.7734 | 0.5598 | -0.5277 | -0.4944 | -0.3057 | -0.0892 | -0.1192 | 0.3243 | 0.0516 |
| | 1.9734 | 0.5969 | -0.5357 | -0.5012 | -0.3530 | -0.0773 | -0.0831 | 0.3106 | 0.0772 |
| | 2.1734 | 0.6126 | -0.5451 | -0.5048 | -0.3687 | -0.0669 | -0.0631 | 0.3003 | 0.0869 |
| | 2.3734 | 0.6233 | -0.5338 | -0.5177 | -0.3784 | -0.0618 | -0.0547 | 0.2960 | 0.0923 |
| | 2.5734 | 0.6263 | -0.5347 | -0.5168 | -0.3874 | -0.0567 | -0.0440 | 0.2905 | 0.0952 |
| Lumazine *enol* | 1.3536 | 0.3690 | -0.4922 | -0.4386 | -0.2446 | -0.1055 | -0.1673 | 0.3896 | -0.0023 |
| | 1.5536 | 0.3713 | -0.4896 | -0.4379 | -0.2391 | -0.1052 | -0.1648 | 0.3943 | -0.0219 |
| | 1.6536 | 0.5223 | -0.4765 | -0.4984 | -0.2832 | -0.0793 | -0.1322 | 0.2190 | 0.0130 |
| | 1.7536 | 0.5585 | -0.4780 | -0.5161 | -0.3202 | -0.0689 | -0.1130 | 0.2078 | 0.0449 |
| | 1.9536 | 0.5970 | -0.4875 | -0.5370 | -0.3484 | -0.0592 | -0.0971 | 0.2074 | 0.0685 |
| | 2.1536 | 0.6105 | -0.5740 | -0.5298 | -0.3501 | -0.0447 | -0.0482 | 0.1492 | 0.0950 |
| | 2.3536 | 0.6191 | -0.5806 | -0.5299 | -0.3737 | -0.0386 | -0.0351 | 0.1593 | 0.0963 |
| | 2.5536 | 0.6022 | -0.4734 | -0.5455 | -0.3898 | -0.0502 | -0.0751 | 0.2022 | 0.0859 |
| Lumazine *keto* | 1.3568 | 0.3885 | -0.4819 | -0.4394 | -0.2641 | -0.1043 | -0.1651 | 0.4106 | 0.0000 |
| | 1.5568 | 0.3848 | -0.4812 | -0.4363 | -0.2563 | -0.1024 | -0.1637 | 0.4129 | -0.0207 |
| | 1.6568 | 0.5188 | -0.4774 | -0.4912 | -0.2930 | -0.0851 | -0.1371 | 0.2320 | 0.0193 |
| | 1.7568 | 0.5188 | -0.4774 | -0.4912 | -0.2930 | -0.0851 | -0.1371 | 0.2320 | 0.0193 |
| | 1.9568 | 0.5188 | -0.4774 | -0.4912 | -0.2930 | -0.0851 | -0.1371 | 0.2320 | 0.0193 |

| | | | | | | | | | |
|---|---|---|---|---|---|---|---|---|---|
| | 2.1568 | 0.6107 | -0.4841 | -0.5309 | -0.3697 | -0.0557 | -0.0945 | 0.2014 | 0.0771 |
| | 2.3568 | 0.5974 | -0.4712 | -0.5350 | -0.3857 | -0.0529 | -0.0836 | 0.2014 | 0.0821 |
| Formaldehyde | 1.3586 | 0.3577 | -0.5555 | -0.2664 | -0.3014 | -0.1553 | -0.2184 | 0.2996 | -0.0129 |
| | 1.5967 | 0.5062 | -0.4859 | -0.4293 | -0.2804 | -0.1182 | -0.1580 | 0.2283 | -0.0284 |
| | 1.6118 | 0.5363 | -0.4887 | -0.4506 | -0.2874 | -0.1146 | -0.1499 | 0.2224 | -0.0123 |
| | 1.8650 | 0.5661 | -0.4851 | -0.5019 | -0.3533 | -0.0788 | -0.1101 | 0.1852 | 0.0505 |
| | 2.1182 | 0.5780 | -0.4819 | -0.5152 | -0.3851 | -0.0684 | -0.0930 | 0.1868 | 0.0653 |
| | 2.3714 | 0.6280 | -0.4814 | -0.5506 | -0.3746 | -0.0756 | -0.1009 | 0.2154 | 0.0778 |
| | 2.6246 | 0.6225 | -0.4802 | -0.5501 | -0.3842 | -0.0716 | -0.0933 | 0.2090 | 0.0834 |
| Acetaldehyde | 1.3582 | 0.3836 | -0.4921 | -0.3486 | -0.2945 | -0.1373 | -0.2804 | 0.3998 | -0.0205 |
| | 1.3544 | 0.3782 | -0.4954 | -0.3513 | -0.3429 | -0.1491 | -0.2045 | 0.3957 | -0.0013 |
| | 1.4544 | 0.3755 | -0.4951 | -0.3512 | -0.3354 | -0.1476 | -0.2041 | 0.3970 | -0.0121 |
| | 1.5544 | 0.3707 | -0.4945 | -0.3512 | -0.3268 | -0.1450 | -0.2035 | 0.3988 | -0.0254 |
| | 1.6544 | 0.5171 | -0.4891 | -0.4859 | -0.2972 | -0.0944 | -0.1410 | 0.2739 | 0.0156 |
| | 1.7544 | 0.5479 | -0.4883 | -0.5081 | -0.3251 | -0.0845 | -0.1246 | 0.2735 | 0.0342 |
| | 1.8544 | 0.5634 | -0.4874 | -0.5192 | -0.3461 | -0.0777 | -0.1138 | 0.2760 | 0.0444 |
| | 1.9544 | 0.5702 | -0.4862 | -0.5253 | -0.3620 | -0.0722 | -0.1048 | 0.2781 | 0.0516 |
| | 2.6544 | 0.5764 | -0.4748 | -0.5444 | -0.4059 | -0.0558 | -0.0786 | 0.2804 | 0.0699 |
| Formate *single* | 1.4700 | 0.4422 | -0.5101 | -0.4549 | -0.4143 | -0.2352 | -0.2491 | 0.4418 | -0.0142 |
| | 1.6700 | 0.4534 | -0.5183 | -0.4545 | -0.3854 | -0.2265 | -0.2492 | 0.4379 | -0.0618 |
| | 1.7700 | 0.4523 | -0.5171 | -0.4568 | -0.3765 | -0.2207 | -0.2455 | 0.4432 | -0.0885 |
| | 1.8700 | 0.6261 | -0.5344 | -0.5536 | -0.4447 | -0.2027 | -0.2096 | 0.3995 | 0.0015 |
| | 1.9700 | 0.6590 | -0.5500 | -0.5694 | -0.6294 | -0.1942 | -0.2362 | 0.2821 | 0.1274 |
| | 2.5700 | 0.6472 | -0.5520 | -0.5919 | -0.6543 | -0.1946 | -0.2437 | 0.2612 | 0.1859 |
| Formate *double* | 1.3207 | 0.3663 | -0.4725 | -0.3384 | -0.2988 | -0.1354 | -0.2850 | 0.5040 | -0.0047 |
| | 1.4207 | 0.3680 | -0.4729 | -0.3379 | -0.2959 | -0.1350 | -0.2847 | 0.5043 | -0.0112 |
| | 1.5207 | 0.3684 | -0.4723 | -0.3371 | -0.2908 | -0.1341 | -0.2843 | 0.5047 | -0.0221 |
| | 1.6207 | 0.3488 | -0.4761 | -0.3401 | -0.3242 | -0.1418 | -0.1944 | 0.5071 | -0.0284 |
| | 1.7207 | 0.5253 | -0.4773 | -0.4962 | -0.2943 | -0.0812 | -0.1338 | 0.4021 | 0.0324 |
| | 1.8207 | 0.5426 | -0.4757 | -0.5112 | -0.3146 | -0.0729 | -0.1256 | 0.4028 | 0.0454 |
| | 2.0207 | 0.5749 | -0.4755 | -0.5224 | -0.3513 | -0.0662 | -0.1210 | 0.4056 | 0.0607 |
| | 2.5207 | 0.5965 | -0.4673 | -0.5485 | -0.3611 | -0.0488 | -0.1280 | 0.4020 | 0.0801 |
| Formamide | 1.3439 | 0.3946 | -0.6344 | -0.3823 | -0.2824 | -0.1438 | -0.1979 | 0.4712 | 0.0005 |
| | 1.5439 | 0.3970 | -0.6333 | -0.3813 | -0.2756 | -0.1419 | -0.1974 | 0.4738 | -0.0186 |
| | 1.6439 | 0.4859 | -0.5227 | -0.4749 | -0.2705 | -0.1156 | -0.1538 | 0.3478 | 0.0092 |
| | 1.7439 | 0.5452 | -0.5064 | -0.5227 | -0.3034 | -0.0987 | -0.1293 | 0.3244 | 0.0456 |
| | 1.8439 | 0.5728 | -0.5066 | -0.5356 | -0.3273 | -0.0919 | -0.1190 | 0.3253 | 0.0555 |
| | 1.9439 | 0.5722 | -0.4982 | -0.5395 | -0.3529 | -0.0889 | -0.1077 | 0.3243 | 0.0630 |
| | 2.3439 | 0.5997 | -0.5176 | -0.5562 | -0.3641 | -0.0759 | -0.0933 | 0.3304 | 0.0784 |
| | 2.5439 | 0.6160 | -0.5346 | -0.5600 | -0.3689 | -0.0675 | -0.0837 | 0.3313 | 0.0824 |
| Formamide | 1.3690 | 0.3671 | -0.4816 | -0.3834 | -0.3523 | -0.1518 | -0.2215 | 0.4789 | 0.0051 |
| | 1.4690 | 0.3646 | -0.4819 | -0.3832 | -0.3446 | -0.1500 | -0.2214 | 0.4803 | -0.0057 |
| | 1.5690 | 0.3601 | -0.4813 | -0.3829 | -0.3349 | -0.1470 | -0.2204 | 0.4822 | -0.0201 |
| | 1.6690 | 0.4926 | -0.4880 | -0.4682 | -0.3092 | -0.1032 | -0.1409 | 0.3376 | -0.0073 |
| | 1.7690 | 0.5356 | -0.4862 | -0.5003 | -0.3350 | -0.0899 | -0.1210 | 0.3319 | 0.0196 |
| | 2.0690 | 0.5591 | -0.4767 | -0.5227 | -0.3831 | -0.0714 | -0.0906 | 0.3325 | 0.0450 |
| | 2.2690 | 0.5579 | -0.4708 | -0.5299 | -0.3984 | -0.0642 | -0.0779 | 0.3311 | 0.0532 |
| | 2.5690 | 0.5676 | -0.4715 | -0.5382 | -0.4088 | -0.0566 | -0.0666 | 0.3296 | 0.0590 |

Table A. 6. The raw data for the bond order indices. The calculations were performed for the geometries described in Appendix (VI). The bonds were $S_{Mo}$-$H_{RH}$ (S-H), $C_{CRH}$-$H_{RH}$ (C-H), $O_{Mo}$-$C_{CRH}$ (O-C), Mo-$O_{Mo}$ (Mo-O), Mo=$S_{Mo}$ (Mo-S), Mo-$(S_{pterin})_{\beta}$ (Mo-(B), Mo-$(S_{pterin})_{\alpha}$ (Mo-(F), and Mo≡O (Mo-oxo).

| | S-H (Å) | S-H | C-H | O-C | Mo-O | Mo-S | Mo-B | Mo-F | Mo-oxo |
|---|---|---|---|---|---|---|---|---|---|
| H(Down conformation) for deprotonated substrates | | | | | | | | | |
| Purine-$C_6$ | 1.35865 | 1.05 | 0.002 | 1.833 | 0.642 | 1.226 | 1.277 | 1.25 | 2.614 |
| | 1.55865 | 0.969 | 0.003 | 1.828 | 0.646 | 1.3 | 1.269 | 1.236 | 2.611 |
| | 1.75865 | 0.88 | 0.004 | 1.819 | 0.657 | 1.422 | 1.256 | 1.213 | 2.602 |
| | 1.85865 | 0.31 | 0.636 | 1.209 | 1.117 | 1.919 | 1.144 | 1.13 | 2.461 |
| | 1.95865 | 0.224 | 0.716 | 1.115 | 1.194 | 2.021 | 1.127 | 1.117 | 2.44 |
| | 2.15865 | 0.664 | 0.008 | 1.791 | 0.674 | 1.765 | 1.222 | 1.166 | 2.563 |
| | 2.35865 | 0.581 | 0.008 | 1.775 | 0.682 | 1.888 | 1.211 | 1.149 | 2.56 |
| | 2.55865 | 0.51 | 0.008 | 1.763 | 0.689 | 1.982 | 1.203 | 1.138 | 2.544 |
| 6MP-$C_2$ | 1.34815 | 1.053 | 0.002 | 1.784 | 0.673 | 1.213 | 1.291 | 1.233 | 2.595 |
| | 1.54815 | 0.97 | 0.004 | 1.78 | 0.678 | 1.288 | 1.283 | 1.223 | 2.591 |
| | 1.74815 | 0.877 | 0.005 | 1.768 | 0.688 | 1.417 | 1.269 | 1.203 | 2.575 |
| | 1.84815 | 0.314 | 0.64 | 1.177 | 1.127 | 1.909 | 1.141 | 1.127 | 2.458 |
| | 1.94815 | 0.213 | 0.744 | 1.013 | 1.267 | 2.026 | 1.112 | 1.109 | 2.429 |
| | 2.14815 | 0.123 | 0.869 | 0.03 | 2.203 | 1.945 | 1.01 | 1.004 | 2.333 |
| | 2.34815 | 0.077 | 0.887 | 0.03 | 2.199 | 1.972 | 1.006 | 0.999 | 2.334 |
| | 2.54815 | 0.05 | 0.915 | 0.004 | 2.199 | 2.008 | 1.022 | 0.927 | 2.323 |
| 6MP-$C_8$ | 1.387466 | 1.045 | 0.002 | 1.824 | 0.65 | 1.17 | 1.321 | 1.288 | 2.593 |
| | 1.587466 | 0.963 | 0.003 | 1.818 | 0.655 | 1.247 | 1.313 | 1.275 | 2.587 |
| | 1.77466 | 0.87 | 0.005 | 1.804 | 0.665 | 1.382 | 1.302 | 1.257 | 2.572 |
| | 1.87466 | 0.312 | 0.632 | 1.317 | 1.023 | 1.892 | 1.177 | 1.17 | 2.476 |
| | 1.97466 | 0.229 | 0.709 | 1.241 | 1.085 | 1.993 | 1.161 | 1.158 | 2.458 |
| | 2.17466 | 0.124 | 0.809 | 1.088 | 1.197 | 2.144 | 1.126 | 1.135 | 2.425 |
| | 2.37466 | 0.079 | 0.843 | 1.05 | 1.226 | 2.181 | 1.115 | 1.135 | 2.421 |
| | 2.57466 | 0.05 | 0.867 | 1.033 | 1.249 | 2.226 | 1.103 | 1.132 | 2.408 |
| HMP | 1.37991 | 1.043 | 0.002 | 1.85 | 0.637 | 1.169 | 1.326 | 1.292 | 2.602 |
| | 1.57991 | 0.962 | 0.003 | 1.844 | 0.643 | 1.247 | 1.318 | 1.279 | 2.596 |
| | 1.67991 | 0.918 | 0.004 | 1.839 | 0.647 | 1.308 | 1.312 | 1.268 | 2.592 |
| | 1.77991 | 0.365 | 0.601 | 1.331 | 1.002 | 1.868 | 1.186 | 1.167 | 2.477 |
| | 1.87991 | 0.261 | 0.698 | 1.244 | 1.066 | 1.992 | 1.17 | 1.153 | 2.459 |
| | 1.97991 | 0.193 | 0.755 | 1.201 | 1.1 | 2.092 | 1.161 | 1.146 | 2.443 |
| | 2.37991 | 0.075 | 0.848 | 1.123 | 1.17 | 2.205 | 1.135 | 1.141 | 2.418 |
| | 2.57991 | 0.048 | 0.869 | 1.117 | 1.182 | 2.245 | 1.129 | 1.142 | 2.41 |
| Hypoxanthine | 1.3118 | 1.071 | 0.002 | 1.8 | 0.656 | 1.195 | 1.313 | 1.285 | 2.585 |
| | 1.5118 | 0.986 | 0.003 | 1.795 | 0.661 | 1.261 | 1.307 | 1.274 | 2.58 |
| | 1.7118 | 0.899 | 0.004 | 1.785 | 0.67 | 1.375 | 1.294 | 1.255 | 2.571 |
| | 1.8118 | 0.847 | 0.005 | 1.776 | 0.675 | 1.454 | 1.285 | 1.243 | 2.564 |
| | 1.9118 | 0.265 | 0.683 | 1.185 | 1.107 | 1.961 | 1.154 | 1.148 | 2.46 |
| | 2.13118 | 0.144 | 0.798 | 0.977 | 1.282 | 2.094 | 1.115 | 1.134 | 2.416 |
| | 2.33118 | 0.074 | 0.884 | 0.016 | 2.214 | 1.853 | 1.04 | 1.045 | 2.342 |
| | 2.53118 | 0.038 | 0.897 | 0.014 | 2.213 | 1.854 | 1.046 | 1.041 | 2.344 |

| | | | | | | | | | |
|---|---|---|---|---|---|---|---|---|---|
| Xanthine | 1.30524 | 1.075 | 0.002 | 1.838 | 0.638 | 1.178 | 1.323 | 1.293 | 2.586 |
| | 1.50524 | 0.991 | 0.003 | 1.832 | 0.644 | 1.24 | 1.318 | 1.282 | 2.582 |
| | 1.70524 | 0.904 | 0.005 | 1.822 | 0.653 | 1.353 | 1.306 | 1.262 | 2.573 |
| | 1.80524 | 0.347 | 0.618 | 1.303 | 1.01 | 1.868 | 1.186 | 1.155 | 2.48 |
| | 1.90524 | 0.249 | 0.709 | 1.217 | 1.077 | 1.984 | 1.169 | 1.143 | 2.459 |
| | 2.10524 | 0.148 | 0.792 | 1.133 | 1.147 | 2.087 | 1.151 | 1.132 | 2.439 |
| | 2.30524 | 0.09 | 0.838 | 1.095 | 1.186 | 2.157 | 1.14 | 1.124 | 2.423 |
| | 2.50524 | 0.057 | 0.864 | 1.08 | 1.198 | 2.198 | 1.135 | 1.123 | 2.418 |
| Allopurinol | 1.37923 | 1.04 | 0.002 | 1.829 | 0.646 | 1.224 | 1.314 | 1.286 | 2.583 |
| | 1.57923 | 0.959 | 0.004 | 1.823 | 0.652 | 1.302 | 1.306 | 1.273 | 2.577 |
| | 1.77923 | 0.21 | 0.734 | 1.137 | 1.163 | 2.035 | 1.143 | 1.147 | 2.445 |
| | 1.87923 | 0.288 | 0.66 | 1.226 | 1.082 | 1.953 | 1.164 | 1.157 | 2.461 |
| | 1.97923 | 0.21 | 0.734 | 1.137 | 1.163 | 2.035 | 1.143 | 1.147 | 2.445 |
| | 2.17923 | 0.122 | 0.81 | 1.029 | 1.252 | 2.141 | 1.122 | 1.142 | 2.414 |
| | 2.37923 | 0.077 | 0.844 | 0.978 | 1.286 | 2.181 | 1.11 | 1.139 | 2.411 |
| | 2.57923 | 0.049 | 0.867 | 0.963 | 1.309 | 2.218 | 1.1 | 1.137 | 2.398 |
| Lumazine enol | 1.3941 | 1.031 | 0.003 | 1.777 | 0.683 | 1.25 | 1.3 | 1.269 | 2.575 |
| | 1.5941 | 0.948 | 0.006 | 1.774 | 0.691 | 1.334 | 1.287 | 1.259 | 2.563 |
| | 1.7941 | 0.848 | 0.01 | 1.76 | 0.7 | 1.478 | 1.271 | 1.24 | 2.549 |
| | 1.8941 | 0.282 | 0.663 | 1.191 | 1.089 | 1.947 | 1.158 | 1.164 | 2.459 |
| | 1.9941 | 0.204 | 0.738 | 1.101 | 1.161 | 2.037 | 1.141 | 1.155 | 2.441 |
| | 2.1941 | 0.12 | 0.809 | 0.985 | 1.25 | 2.12 | 1.122 | 1.14 | 2.428 |
| | 2.3941 | 0.073 | 0.849 | 0.926 | 1.303 | 2.18 | 1.11 | 1.134 | 2.406 |
| | 2.5941 | 0.047 | 0.87 | 0.895 | 1.321 | 2.207 | 1.104 | 1.132 | 2.405 |
| Lumazine keto | 1.37363 | 1.04 | 0.003 | 1.762 | 0.679 | 1.236 | 1.301 | 1.26 | 2.584 |
| | 1.57363 | 0.957 | 0.004 | 1.758 | 0.687 | 1.313 | 1.288 | 1.25 | 2.578 |
| | 1.77363 | 0.862 | 0.007 | 1.748 | 0.696 | 1.451 | 1.274 | 1.234 | 2.555 |
| | 1.87363 | 0.297 | 0.653 | 1.177 | 1.093 | 1.923 | 1.158 | 1.156 | 2.466 |
| | 1.97363 | 0.205 | 0.744 | 1.046 | 1.202 | 2.029 | 1.133 | 1.142 | 2.443 |
| | 2.17363 | 0.113 | 0.869 | 0.016 | 2.137 | 1.932 | 1.031 | 1.045 | 2.346 |
| | 2.37363 | 0.064 | 0.889 | 0.017 | 2.14 | 1.938 | 1.039 | 1.043 | 2.345 |
| | 2.57363 | 0.035 | 0.909 | 0.005 | 2.149 | 1.896 | 1.047 | 1.048 | 2.346 |
| Formaldehyde | 1.44231 | 0.937 | 0.007 | 1.375 | 0.516 | 0.905 | 0.948 | 0.903 | 1.977 |
| | 1.64231 | 0.887 | 0.01 | 1.363 | 0.523 | 0.966 | 0.945 | 0.893 | 1.971 |
| | 1.84231 | 0.797 | 0.014 | 1.344 | 0.535 | 1.086 | 0.941 | 0.879 | 1.958 |
| | 2.0423 | 0.215 | 0.725 | 0.69 | 1.009 | 1.504 | 0.872 | 0.801 | 1.836 |
| | 2.24231 | 0.061 | 0.885 | 0.057 | 1.614 | 1.522 | 0.821 | 0.765 | 1.766 |
| | 2.44231 | 0.039 | 0.899 | 0.053 | 1.608 | 1.543 | 0.819 | 0.762 | 1.772 |
| | 2.6435 | 0.015 | 0.912 | 0.04 | 1.615 | 1.551 | 0.82 | 0.763 | 1.769 |
| Acetaldehyde | 1.35837 | 0.948 | 0.004 | 1.386 | 0.489 | 0.885 | 0.954 | 0.91 | 1.961 |
| | 1.56737 | 0.913 | 0.005 | 1.377 | 0.493 | 0.926 | 0.953 | 0.902 | 1.957 |
| | 1.77637 | 0.83 | 0.007 | 1.36 | 0.502 | 1.033 | 0.948 | 0.889 | 1.948 |
| | 1.98539 | 0.241 | 0.685 | 0.691 | 0.977 | 1.486 | 0.877 | 0.808 | 1.827 |
| | 2.19439 | 0.066 | 0.873 | 0.019 | 1.612 | 1.52 | 0.825 | 0.765 | 1.77 |
| | 2.61239 | 0.026 | 0.898 | 0.015 | 1.602 | 1.557 | 0.824 | 0.762 | 1.769 |
| Formate | 1.39187 | 0.946 | 0.016 | 1.413 | 0.974 | 1.268 | 1.149 | 1.093 | 2.535 |
| | 1.49187 | 0.793 | 0.029 | 1.499 | 0.898 | 1.394 | 1.13 | 1.12 | 2.537 |
| | 1.59187 | 0.638 | 0.042 | 1.586 | 0.817 | 1.511 | 1.123 | 1.135 | 2.53 |

| | | | | | | | | | |
|---|---|---|---|---|---|---|---|---|---|
| | 1.69187 | 0.514 | 0.05 | 1.646 | 0.76 | 1.598 | 1.113 | 1.151 | 2.527 |
| | 1.89187 | 0.228 | 0.793 | 0.008 | 2.283 | 2.039 | 1.059 | 0.708 | 2.274 |
| | 1.99187 | 0.228 | 0.793 | 0.008 | 2.283 | 2.039 | 1.059 | 0.708 | 2.274 |
| | 2.19187 | 0.107 | 0.874 | 0.003 | 2.287 | 2.134 | 1.064 | 0.715 | 2.275 |
| | 2.39187 | 0.064 | 0.9 | 0.002 | 2.259 | 2.158 | 1.051 | 0.745 | 2.294 |
| Formamide | 1.33184 | 1.055 | 0.001 | 1.691 | 0.746 | 1.227 | 1.273 | 1.201 | 2.582 |
| | 1.63184 | 0.928 | 0.001 | 1.685 | 0.752 | 1.35 | 1.256 | 1.184 | 2.572 |
| | 1.73184 | 0.883 | 0.002 | 1.687 | 0.754 | 1.419 | 1.25 | 1.173 | 2.565 |
| | 1.833184 | 0.33 | 0.617 | 0.938 | 1.316 | 1.91 | 1.098 | 1.105 | 2.433 |
| | 1.933184 | 0.202 | 0.838 | 0.01 | 2.041 | 1.97 | 1.035 | 1.02 | 2.341 |
| | 2.333184 | 0.082 | 0.889 | 0.006 | 2.03 | 2.041 | 1.026 | 1.017 | 2.339 |
| H(Up conformation) for deprotonated substrates | | | | | | | | | |
| Purine-$C_8$ | 1.332581 | 0.258 | 0.684 | 1.238 | 1.072 | 1.942 | 1.168 | 1.151 | 2.439 |
| | 1.532581 | 0.97 | 0.001 | 1.82 | 0.607 | 1.34 | 1.296 | 1.307 | 2.472 |
| | 1.732581 | 0.887 | 0.001 | 1.813 | 0.615 | 1.45 | 1.285 | 1.283 | 2.466 |
| | 1.832581 | 0.385 | 0.552 | 1.373 | 0.963 | 1.798 | 1.195 | 1.173 | 2.465 |
| | 1.932581 | 0.258 | 0.684 | 1.238 | 1.072 | 1.942 | 1.168 | 1.151 | 2.439 |
| | 2.132581 | 0.146 | 0.784 | 1.115 | 1.172 | 2.076 | 1.146 | 1.136 | 2.411 |
| | 2.332581 | 0.09 | 0.831 | 1.043 | 1.23 | 2.143 | 1.132 | 1.127 | 2.393 |
| | 2.532581 | 0.057 | 0.859 | 0.994 | 1.266 | 2.177 | 1.12 | 1.132 | 2.381 |
| Purine-$C_2$ | 1.44804 | 1.011 | 0.003 | 1.786 | 0.678 | 1.247 | 1.288 | 1.231 | 2.592 |
| | 1.54804 | 0.97 | 0.004 | 1.784 | 0.681 | 1.29 | 1.282 | 1.225 | 2.588 |
| | 1.74804 | 0.881 | 0.005 | 1.79 | 0.678 | 1.417 | 1.245 | 1.207 | 2.61 |
| | 1.84804 | 0.316 | 0.639 | 1.179 | 1.128 | 1.906 | 1.142 | 1.127 | 2.454 |
| | 1.94804 | 0.213 | 0.744 | 1.018 | 1.262 | 2.026 | 1.111 | 1.111 | 2.43 |
| | 2.14804 | 0.122 | 0.869 | 0.031 | 2.186 | 1.959 | 1.013 | 1.001 | 2.323 |
| | 2.34804 | 0.075 | 0.887 | 0.03 | 2.182 | 1.987 | 1.013 | 0.994 | 2.321 |
| | 2.54804 | 0.045 | 0.899 | 0.029 | 2.18 | 2.008 | 1.016 | 0.987 | 2.32 |
| 6MP-$C_8$ | 1.33915 | 1.049 | 0.001 | 1.82 | 0.605 | 1.277 | 1.303 | 1.318 | 2.476 |
| | 1.53915 | 0.968 | 0.001 | 1.816 | 0.61 | 1.343 | 1.295 | 1.305 | 2.473 |
| | 1.73915 | 0.884 | 0.002 | 1.808 | 0.618 | 1.456 | 1.284 | 1.281 | 2.465 |
| | 1.83915 | 0.373 | 0.566 | 1.362 | 0.97 | 1.807 | 1.192 | 1.171 | 2.464 |
| | 1.93915 | 0.254 | 0.688 | 1.237 | 1.071 | 1.943 | 1.167 | 1.151 | 2.44 |
| | 2.13915 | 0.141 | 0.789 | 1.114 | 1.168 | 2.092 | 1.148 | 1.136 | 2.412 |
| | 2.33915 | 0.088 | 0.833 | 1.043 | 1.231 | 2.142 | 1.132 | 1.125 | 2.393 |
| | 2.53915 | 0.056 | 0.861 | 0.998 | 1.27 | 2.177 | 1.123 | 1.13 | 2.377 |
| Hypoxanthine | 1.31662 | 1.059 | 0.001 | 1.785 | 0.624 | 1.271 | 1.296 | 1.317 | 2.46 |
| | 1.51662 | 0.977 | 0.001 | 1.781 | 0.627 | 1.333 | 1.289 | 1.306 | 2.456 |
| | 1.71662 | 0.896 | 0.003 | 1.778 | 0.638 | 1.441 | 1.278 | 1.28 | 2.45 |
| | 1.81662 | 0.848 | 0.005 | 1.768 | 0.651 | 1.518 | 1.266 | 1.263 | 2.45 |
| | 1.91662 | 0.26 | 0.68 | 1.156 | 1.142 | 1.987 | 1.152 | 1.144 | 2.436 |
| | 2.01662 | 0.178 | 0.767 | 0.957 | 1.305 | 2.071 | 1.126 | 1.127 | 2.395 |
| | 2.11662 | 0.134 | 0.87 | 0.007 | 1.931 | 2.02 | 1.037 | 1.06 | 2.353 |
| | 2.31662 | 0.085 | 0.889 | 0.007 | 1.904 | 2.057 | 1.035 | 1.061 | 2.352 |
| | 2.51662 | 0.054 | 0.901 | 0.001 | 2.268 | 2.051 | 1.07 | 1.029 | 2.011 |
| Xanthine | 1.31397 | 0.384 | 0.567 | 1.385 | 0.958 | 1.81 | 1.195 | 1.172 | 2.483 |
| | 1.51397 | 0.978 | 0.001 | 1.826 | 0.601 | 1.332 | 1.298 | 1.309 | 2.481 |
| | 1.61397 | 0.939 | 0.001 | 1.824 | 0.605 | 1.376 | 1.291 | 1.301 | 2.483 |

| | | | | | | | | | |
|---|---|---|---|---|---|---|---|---|---|
| | 1.71397 | 0.895 | 0.002 | 1.821 | 0.611 | 1.44 | 1.286 | 1.283 | 2.476 |
| | 1.81397 | 0.384 | 0.567 | 1.385 | 0.958 | 1.81 | 1.195 | 1.172 | 2.483 |
| | 1.91397 | 0.271 | 0.679 | 1.282 | 1.039 | 1.938 | 1.174 | 1.156 | 2.459 |
| | 2.11397 | 0.162 | 0.772 | 1.194 | 1.113 | 2.056 | 1.154 | 1.143 | 2.438 |
| | 2.31397 | 0.101 | 0.817 | 1.157 | 1.136 | 2.102 | 1.14 | 1.144 | 2.429 |
| | 2.51397 | 0.057 | 0.864 | 1.078 | 1.205 | 2.193 | 1.127 | 1.136 | 2.407 |
| Allopurinol | 1.3179 | 1.057 | 0.001 | 1.781 | 0.616 | 1.284 | 1.312 | 1.329 | 2.41 |
| | 1.5179 | 0.975 | 0.001 | 1.776 | 0.62 | 1.344 | 1.304 | 1.317 | 2.409 |
| | 1.7179 | 0.896 | 0.004 | 1.771 | 0.638 | 1.452 | 1.29 | 1.287 | 2.408 |
| | 1.8179 | 0.848 | 0.005 | 1.765 | 0.645 | 1.522 | 1.28 | 1.273 | 2.408 |
| | 1.9179 | 0.263 | 0.669 | 1.173 | 1.121 | 1.983 | 1.169 | 1.157 | 2.394 |
| | 2.0179 | 0.181 | 0.756 | 1.015 | 1.251 | 2.076 | 1.144 | 1.142 | 2.372 |
| | 2.1179 | 0.126 | 0.877 | 0.012 | 1.862 | 2.031 | 1.06 | 1.075 | 2.359 |
| | 2.3179 | 0.079 | 0.896 | 0.001 | 2.293 | 1.98 | 1.106 | 1.028 | 2.019 |
| | 2.5179 | 0.047 | 0.908 | 0 | 2.291 | 1.906 | 1.105 | 1.044 | 2.09 |
| Formamide | 1.36268 | 1.045 | 0.006 | 1.69 | 0.732 | 1.233 | 1.25 | 1.257 | 2.551 |
| | 1.46268 | 1.002 | 0.007 | 1.688 | 0.736 | 1.264 | 1.246 | 1.25 | 2.554 |
| | 1.66268 | 0.914 | 0.008 | 1.679 | 0.747 | 1.364 | 1.232 | 1.228 | 2.559 |
| | 1.76264 | 0.86 | 0.008 | 1.67 | 0.755 | 1.442 | 1.221 | 1.215 | 2.558 |
| | 1.86264 | 0.798 | 0.007 | 1.661 | 0.764 | 1.534 | 1.21 | 1.201 | 2.553 |
| | 1.96264 | 0.245 | 0.689 | 0.837 | 1.412 | 1.959 | 1.098 | 1.089 | 2.412 |
| | 2.16264 | 0.12 | 0.873 | 0.007 | 2.042 | 2.013 | 1.041 | 1.004 | 2.341 |
| | 2.36268 | 0.076 | 0.891 | 0.006 | 2.026 | 2.047 | 1.021 | 1.021 | 2.338 |
| Protonated substrates | | | | | | | | | |
| Xanthine | 1.3734 | 1.03 | 0.001 | 2.011 | 0.44 | 1.359 | 1.467 | 1.422 | 2.216 |
| | 1.5734 | 0.954 | 0.001 | 2.007 | 0.446 | 1.423 | 1.456 | 1.406 | 2.219 |
| | 1.6734 | 0.916 | 0.001 | 2.004 | 0.451 | 1.47 | 1.448 | 1.393 | 2.222 |
| | 1.7734 | 0.31 | 0.668 | 1.416 | 0.912 | 2.001 | 1.285 | 1.234 | 2.4 |
| | 1.9734 | 0.17 | 0.784 | 1.318 | 0.991 | 2.177 | 1.271 | 1.219 | 2.359 |
| | 2.1734 | 0.098 | 0.836 | 1.292 | 1.015 | 2.27 | 1.272 | 1.21 | 2.328 |
| | 2.3734 | 0.058 | 0.865 | 1.282 | 1.019 | 2.321 | 1.269 | 1.202 | 2.324 |
| | 2.5734 | 0.035 | 0.882 | 1.281 | 1.024 | 2.346 | 1.268 | 1.202 | 2.313 |
| Lumazine enol | 1.35362 | 1.042 | 0.002 | 1.804 | 0.731 | 1.287 | 1.315 | 1.309 | 2.557 |
| | 1.55362 | 0.965 | 0.005 | 1.807 | 0.73 | 1.345 | 1.304 | 1.308 | 2.555 |
| | 1.65362 | 0.485 | 0.499 | 1.456 | 0.923 | 1.802 | 1.262 | 1.267 | 2.487 |
| | 1.75362 | 0.329 | 0.656 | 1.346 | 0.975 | 1.981 | 1.244 | 1.251 | 2.465 |
| | 1.95362 | 0.178 | 0.782 | 1.264 | 1.004 | 2.172 | 1.234 | 1.228 | 2.436 |
| | 2.15362 | 0.095 | 0.835 | 1.214 | 1.06 | 2.287 | 1.29 | 1.228 | 2.222 |
| | 2.35362 | 0.056 | 0.861 | 1.204 | 1.072 | 2.323 | 1.289 | 1.223 | 2.204 |
| | 2.55362 | 0.04 | 0.872 | 1.254 | 1.003 | 2.33 | 1.22 | 1.227 | 2.428 |
| Lumazine keto | 1.35681 | 1.041 | 0.002 | 1.812 | 0.695 | 1.275 | 1.306 | 1.292 | 2.582 |
| | 1.45681 | 1.002 | 0.003 | 1.813 | 0.695 | 1.302 | 1.301 | 1.289 | 2.581 |
| | 1.55681 | 0.965 | 0.004 | 1.814 | 0.694 | 1.335 | 1.295 | 1.287 | 2.578 |
| | 1.65681 | 0.462 | 0.531 | 1.425 | 0.919 | 1.821 | 1.255 | 1.267 | 2.493 |
| | 1.75681 | 0.462 | 0.531 | 1.425 | 0.919 | 1.821 | 1.255 | 1.267 | 2.493 |
| | 1.95681 | 0.462 | 0.531 | 1.425 | 0.919 | 1.821 | 1.255 | 1.267 | 2.493 |
| | 2.15681 | 0.106 | 0.83 | 1.248 | 1.007 | 2.25 | 1.223 | 1.225 | 2.436 |
| | 2.35681 | 0.065 | 0.856 | 1.246 | 1.006 | 2.292 | 1.221 | 1.224 | 2.439 |

| | | | | | | | | | |
|---|---|---|---|---|---|---|---|---|---|
| Formaldehyde | 1.39673 | 0.947 | 0.001 | 1.82 | 0.284 | 0.983 | 1.076 | 1.016 | 1.884 |
| | 1.49673 | 0.919 | 0.013 | 1.781 | 0.318 | 0.983 | 1.062 | 1.003 | 1.939 |
| | 1.59763 | 0.508 | 0.449 | 1.34 | 0.573 | 1.309 | 1.032 | 0.939 | 1.922 |
| | 1.79673 | 0.224 | 0.745 | 1.108 | 0.713 | 1.601 | 1.018 | 0.956 | 1.866 |
| | 1.99673 | 0.134 | 0.833 | 1.057 | 0.743 | 1.689 | 1.014 | 0.955 | 1.854 |
| | 2.19673 | 0.093 | 0.876 | 1.029 | 0.721 | 1.777 | 1.011 | 0.904 | 1.846 |
| Acetaldehyde | 1.35438 | 0.947 | 0.004 | 1.668 | 0.347 | 0.773 | 1.073 | 1.023 | 1.987 |
| | 1.45438 | 0.935 | 0.005 | 1.667 | 0.348 | 0.785 | 1.073 | 1.022 | 1.986 |
| | 1.55438 | 0.935 | 0.005 | 1.665 | 0.35 | 0.807 | 1.073 | 1.019 | 1.983 |
| | 1.65438 | 0.367 | 0.594 | 1.169 | 0.655 | 1.466 | 1.029 | 0.961 | 1.886 |
| | 1.75438 | 0.257 | 0.707 | 1.092 | 0.698 | 1.578 | 1.021 | 0.954 | 1.869 |
| | 1.85438 | 0.193 | 0.771 | 1.053 | 0.721 | 1.643 | 1.018 | 0.952 | 1.859 |
| | 1.95438 | 0.149 | 0.813 | 1.03 | 0.736 | 1.687 | 1.016 | 0.953 | 1.851 |
| | 2.25438 | 0.078 | 0.878 | 0.998 | 0.757 | 1.753 | 1.014 | 0.957 | 1.842 |
| | 2.65438 | 0.039 | 0.91 | 0.982 | 0.75 | 1.784 | 1.015 | 0.951 | 1.846 |
| Formate single | 1.47002 | 0.999 | 0.001 | 1.803 | 0.662 | 1.256 | 1.266 | 1.241 | 2.604 |
| | 1.67002 | 0.913 | 0.004 | 1.791 | 0.694 | 1.373 | 1.271 | 1.218 | 2.568 |
| | 1.77002 | 0.861 | 0.005 | 1.782 | 0.7 | 1.453 | 1.26 | 1.204 | 2.561 |
| | 1.87002 | 0.3 | 0.645 | 1.037 | 1.274 | 1.949 | 1.108 | 1.104 | 2.434 |
| | 1.97002 | 0.189 | 0.841 | 0.038 | 2.191 | 1.901 | 1.014 | 1.018 | 2.333 |
| | 2.57002 | 0.04 | 0.899 | 0.032 | 2.168 | 1.999 | 1.013 | 1.002 | 2.327 |
| Formate double | 1.32069 | 1.046 | 0.001 | 2.078 | 0.499 | 1.3 | 1.37 | 1.19 | 2.623 |
| | 1.42069 | 1.018 | 0.001 | 2.078 | 0.499 | 1.318 | 1.367 | 1.187 | 2.622 |
| | 1.52069 | 0.981 | 0.001 | 2.077 | 0.501 | 1.351 | 1.363 | 1.183 | 2.62 |
| | 1.62069 | 0.953 | 0.002 | 2.067 | 0.51 | 1.142 | 1.396 | 1.354 | 2.618 |
| | 1.72069 | 0.324 | 0.671 | 1.399 | 0.966 | 2.031 | 1.227 | 1.234 | 2.474 |
| | 1.82069 | 0.242 | 0.736 | 1.35 | 0.995 | 2.132 | 1.217 | 1.223 | 2.46 |
| | 2.02069 | 0.141 | 0.808 | 1.306 | 1.026 | 2.251 | 1.205 | 1.201 | 2.444 |
| | 2.52069 | 0.04 | 0.878 | 1.281 | 1.039 | 2.363 | 1.206 | 1.162 | 2.437 |
| Formamide | 1.34393 | 1.034 | 0.001 | 1.992 | 0.483 | 1.35 | 1.441 | 1.412 | 2.219 |
| | 1.54393 | 0.966 | 0.001 | 1.989 | 0.488 | 1.406 | 1.432 | 1.398 | 2.222 |
| | 1.64393 | 0.496 | 0.474 | 1.503 | 0.871 | 1.794 | 1.291 | 1.246 | 2.437 |
| | 1.74393 | 0.312 | 0.67 | 1.326 | 0.997 | 2.024 | 1.257 | 1.212 | 2.429 |
| | 1.84393 | 0.233 | 0.734 | 1.281 | 1.03 | 2.119 | 1.249 | 1.2 | 2.415 |
| | 1.94393 | 0.168 | 0.781 | 1.253 | 1.052 | 2.189 | 1.245 | 1.193 | 2.406 |
| | 2.04393 | 0.128 | 0.809 | 1.237 | 1.058 | 2.24 | 1.244 | 1.185 | 2.397 |
| | 2.34393 | 0.058 | 0.858 | 1.218 | 1.076 | 2.326 | 1.244 | 1.173 | 2.356 |
| | 2.54393 | 0.035 | 0.875 | 1.213 | 1.079 | 2.355 | 1.246 | 1.171 | 2.33 |
| Formamide | 1.36902 | 1.049 | 0.001 | 1.984 | 0.529 | 1.068 | 1.4 | 1.346 | 2.622 |
| | 1.46902 | 1.01 | 0.001 | 1.984 | 0.529 | 1.098 | 1.397 | 1.342 | 2.619 |
| | 1.56902 | 0.973 | 0.001 | 1.983 | 0.531 | 1.139 | 1.393 | 1.335 | 2.617 |
| | 1.66902 | 0.469 | 0.512 | 1.516 | 0.887 | 1.794 | 1.266 | 1.26 | 2.499 |
| | 1.76902 | 0.321 | 0.658 | 1.393 | 0.97 | 1.975 | 1.242 | 1.24 | 2.47 |
| | 2.06902 | 0.144 | 0.798 | 1.302 | 1.038 | 2.176 | 1.218 | 1.228 | 2.446 |
| | 2.56902 | 0.042 | 0.871 | 1.271 | 1.057 | 2.268 | 1.211 | 1.224 | 2.439 |

Appendix VIII: The electronic structure data for the charge transfer complexes

Table A.7. The intensity of the MLCT transition was probed by determining the energy differences between Mo($d_{xy}$) LUMO and violapterin HOMO. The electronic transitions as partial charge transfer for the Mo charge transfer (CT) was characterized using the contribution of individual atomic orbitals to the molecular orbital. The Mo CT character was probed using the excitation from $HOMO_{-x}$ to $LUMO_{+y}$ using equation (4.2.1).

| Structures | HOMO | → | LUMO | MLCT | Oscillator strengths (*f*) (from TDDFT) | Extinction coefficients ($M^{-1}cm^{-1}$) | |
|---|---|---|---|---|---|---|---|
| | | | | | | Static | Dynamic |
| | | | | | | | |
| $E_{RED}$-Violapterin (Experimental) | | | | | | 4762.32 | 4978.75 |
| | | | | | | | |
| a | 0, -1 | | 1, 2 | -25.71556927 | 0.0089 | 464.7568121 | 455.9940157 |
| | -2, -3, -4 | | 0, 1, 2 | -3.711064409 | 0.0145 | 757.1880646 | 742.9115986 |
| | -2, -3, -4, -5 | | 1, 2, 4 | -22.53111833 | 0.0148 | 772.8540246 | 758.2821834 |
| | | | | | | | |
| b | 0 | | 1 | 21.4505611 | 0.03 | 1566.595996 | 1537.05848 |
| | 0 | | 2 | 24.62594684 | 0.029 | 1514.376129 | 1485.823197 |
| | -3, -4, -5 | | 0, 1 | 2.492572984 | 0.0125 | 652.7483316 | 640.4410333 |
| | | | | | | | |
| c | 0 | | 0, 1, 2 | 8.189294691 | 0.0912 | 4762.451827 | 4672.657779 |
| | 0 | | 0, 2, 3 | -0.927207561 | 0.0944 | 4929.5554 | 4836.610684 |
| | 0, -1 | | 0, 1, 2 | 14.32590576 | 0.1049 | 5477.863999 | 5374.581152 |
| | 0, -1, -2 | | 0, 4, 8 | 0.820992018 | 0.0332 | 1733.699569 | 1701.011384 |
| | 0, -1, -3 | | 0, 1, 2, 5, 6, 8, 9 | -2.2411849 | 0.0502 | 2621.4373 | 2572.01119 |
| | | | | | | | |
| d | 0 | | 0, 1 | 31.30363926 | 0.1767 | 9227.250415 | 9053.274447 |
| | 0 | | 0, 1 | 34.8260782 | 0.1158 | 6047.060544 | 5933.045733 |
| | -4, -5 | | 0 | 2.186629136 | 0.0384 | 2005.242875 | 1967.434854 |
| | | | | | | | |
| e | 0, -1 | | 0, 1, 2 | -3.570733965 | 0.0334 | 1744.143542 | 1711.258441 |
| | 0, -1, -2 | | 0, 1, 2, 3, 4 | -26.54548161 | 0.07 | 3655.390657 | 3586.469787 |
| | | | | | | | |
| f | 0, -1 | | 0 | -9.25028663 | 0.1048 | 5472.642012 | 5369.457623 |
| | 0, -1,- 2, -3 | | 0 | -9.384241967 | 0.1222 | 6381.267689 | 6260.951542 |
| | 0, -1, -2, -3, -5, -8, -9, -12 | | 0, 1, 2 | -16.05982909 | 0.0279 | 1456.934276 | 1429.464386 |
| | 0, -1, -3, -9, | | 0, 1, 2, | -17.60424597 | 0.0441 | 2302.896114 | 2259.475966 |

| | | | | | | | |
|---|---|---|---|---|---|---|---|
| | -10, -12 | | 3 | | | | |
| | | | | | | | |
| h | 0 | | 0, 2 | 33.99206218 | 0.0412 | 2151.458501 | 2110.893646 |
| | 0, -1 | | 0, 1, 2, 5 | 3.819822602 | 0.0243 | 1268.942757 | 1245.017369 |
| | | | | | | | |
| i | -1, -2, -3, -4 | | 0 | -19.0663278 | 0.0655 | 3420.401257 | 3355.911015 |
| | 0, -2, -3, -4 | | 0, 2, 3 | -17.03330241 | 0.0288 | 1503.932156 | 1475.576141 |
| | 0, -2, -4 | | 0, 2, 3 | -7.864154393 | 0.0639 | 3336.849471 | 3273.934562 |
| | | | | | | | |
| j | 0 | | 0, 1, 2 | 8.189294691 | 0.0912 | 4762.451827 | 4672.657779 |
| | 0 | | 0, 2, 3 | -0.927207561 | 0.0944 | 4929.5554 | 4836.610684 |
| | 0, -1 | | 0, 1, 2 | 14.32590576 | 0.1049 | 5477.863999 | 5374.581152 |
| | -1, -2 | | 0 | -2.382514428 | 0.0464 | 2423.001807 | 2377.317116 |
| | | | | | | | |
| | 0, -1, -2 | | 0, 4, 8 | 0.714710007 | 0.0332 | 1733.699569 | 1701.011384 |
| | 0, -1, -3 | | 0, 1, 2, 5, 5, 8, 9, 10 | -2.24918722 | 0.0502 | 2621.4373 | 2572.01119 |

References


1. Hille, R., (1996). The mononuclear molybdenum enzymes. *Chem. Rev*., **96**, 2757 - 2816.
2. Berry, C. E., and Hare, J. M., (2004). Xanthine oxidoreductase and cardiovascular disease: Molecular mechanisms and pathophysiological implications. *J. Physiol*., **555**, 589 - 606.
3. Garattini, E., Menedel, R., Romao, M. J., Wright, R., and Terao, M., (2003). Mammalian molybdo–flavoenzymes, an expanding family of proteins: Structure, genetics, regulation, function and pathophysiology. *Biochem. J*., **372**, 15 - 32.
4. Schwarz, G. (2005). Molybdenum cofactor biosynthesis and deficiency. *Cell. Mol. Life Sci*,. **62**, 2792 - 2810.
5. Enroth, C., Eger, B. T., Okamoto, T., Nishino, T., Nishino, T., and Pai, E. F., (2000). Crystal structures of bovine milk xanthine dehydrogenase and xanthine oxidase: Structure-based mechanism of conversion. *Proc. Nat. Acad. Sci.*, **97**, 10723 - 10728.
6. Truglio, J. J., Theis, K., Leimkühler, S., Rappa, R., Rajagopalan, K. V., and Kisker, C., (2002). Crystal Structures of the active and alloxanthine-inhibited forms of Xanthine Dehydrogenase from *Rhodobacter capsulatus*. *Structure*, **10**, 115 - 125.
7. Dobbek, H., Gremer, L., Meyer, O., and Huber, R., (1999). Crystal structure and mechanism of CO dehydrogenase, a molybdo iron-sulfur flavoprotein containing *S*-selanylcysteine. *Proc. Nat. Acad. Sci.*, **96**, 8884 - 8889.
8. Dobbek, H., Gremer, L., Kiefersauer, R., Huber, R., and Meyer, O., (2002). Catalysis at a dinuclear [CuSMo(==O)OH] cluster in a CO dehydrogenase resolved at 1.1-Å resolution. *Proc. Nat. Acad. Sci.,* **99**, 15971 - 15976.
9. Hänzelmann, P., Dobbek, H., Gremer, L., Huber, R., and Meyer, O., (2000). The effect of intracellular molybdenum in *Hydrogenophaga pseudoflava* on the crystallographic structure of the seleno-molybdo-iron-sulfur flavoenzyme carbon monoxide dehydrogenase. *J. Mol. Biol.,* **301** (5), 1221 - 1235.

10. Okamoto, K., Matsumoto, K., Hille, R., Eger, B. T., Pai, E. F., and Nishino, T., (2004). The crystal structure of xanthine oxidoreductase during catalysis: Implications for reaction mechanism and enzyme inhibition. *Proc. Nat. Acad. Sci.*, **101**, 7931 - 7936.
11. Resch, M., Dobbek, H., and Meyer, O., (2005). Structural and functional reconstruction in situ of the [$CuSMoO_2$] active site of carbon monoxide dehydrogenase from the carbon monoxide oxidizing eubacterium *Oligotropha carboxidovorans. J. Biol. Inorg. Chem.*, **10** (5), 518 - 528.
12. Bray, R. C., and Meriwether, L. S., (1966). Electron spin resonance of xanthine oxidase substituted with Molybdenum-95. *Nature.*, **212**, 467-469.
13. Romao, M. J., Knablein, J., Huber, R., and Moura, J. J. G., (1997). Structure and function of molybdopterin containing enzymes. *Prog. Biophys. Mol. Biol.,* **68** (2/3), 121 - 144.
14. Romao, M. J., Archer, M., Moura, I., Moura, J. J. G., LeGall, J., Engh, R., Schneider, M., Hof, P., and Huber, R., (1995). Crystal structure of the xanthine oxidase - related aldehyde oxido-reductase from *D. gigas*. *Science* (Washington, D. C.), **270** (5239), 1170 - 6.
15. Kruger, B., and Meyer, O., (1986). The pterin (bactopterin) of carbon monoxide dehydrogenase from *Pseudomonas carboxydoflava*. *Eur. J. Biochem.*, **157**(1), 121 - 128.
16. Meyer, O., and Schlegel, H. G., (1983). Biology of aerobic carbon monoxide-oxidizing bacteria. *Annu. Rev. Microbiol.* **37**, 277 - 310.
17. Rajagopalan, K.V., and Johnson, J. L., (1992). The Pterin Molybdenum Cofactors. *J. Biol. Chem.*, **267** (15), 10199 - 10202.
18. Hille, R., (2006). Structure and function of Xanthine Oxidoreductase. *Eur. J. Inorg. Chem.*, **2006** (10), 1913 - 1926.
19. IUPAC-IUBMB - Joint Commission on Biochemical Nomenclature (JCBN) Nomenclature Committee of the International Union of Biochemistry and Molecular Biology (NC-IUBMB). *Enzyme Nomenclature 1992* [Academic Press, San Diego, CA, U. S. A.

20. Sigel, A., and Sigel H., (2002). Molybdenum and tungsten. Their roles in biological processes. New York: Marcel Dekker.
21. Martz, E., (2002). Protein Explorer: Easy Yet Powerful Macromolecular Visualization, *Trends in Biochem. Sci.*, **27** (February): 107 - 109. http://proteinexplorer.org).
22. Kisker, C., Schindelin, H., Pacheco, A., Wehbi, W. A., Garrett, R. M., Rajagopalan, K. V., Enemark, J. H., and Rees, D. C., (1997). Molecular basis of sulfite oxidase deficiency from the structure of sulfite oxidase. *Cell*, **91** (7), 973 - 983.
23. Schneider, F., Lowe, J., Huber, R., Schindelin, H., Kisker, C., Knablein, J.,(1996) Crystal structure of dimethyl sulfoxide reductase from Rhodobacter capsulatus at 1.88 A resolution. *J. Mol. Biol.,* **263**, 53 - 69.
24. Coughlan, M., (1980). Aldehyde oxidase, xanthine oxidase, and xanthine dehydrogenase: Hydroxylases containing molybdenum, iron sulfur, and flavin in molybdenum and molybdenum containing enzymes. Coughlan, M., ed., pages 119 - 186.
25. Ball, E. G., (1939). Xanthine Oxidase: Purification and properties. *J. Biol. Chem*., **128**, 51 - 67.
26. Dixon, M., and Kodama, K., (1926). On the further purification of xanthine oxidase. *Biochem. J.* **20** (5), 1104 - 1110.
27. Dixon, M., and Thurlow, S., (1924). Studies on xanthine oxidase. *Biochem. J.* **18**, 976 - 988.
28. Kielley, R. K., (1995). Purification of liver xanthine oxidase. *J. Biol. Chem*., **216**, 405 - 412.
29. Cabre, F., and Canela, E. I., (1987). Purification properties and functional groups of bovine liver xanthine oxidase. *Biochem. Trans*., **15**, 511 - 512.
30. Ratnam, K., Brody, M. S., and Hille, R. (1996). Purification of xanthine dehydrogenase and sulfite oxidase from chicken liver. *Prep. Biochem. and biotech.*, **26** (2), 143 - 154.

31. Leimkühler, S., Stockert, A. L., Igarashi, K., Nishino, T., and Hille R., (2004). The Role of Active Site Glutamate Residues in Catalysis of *Rhodobacter capsulatus* Xanthine Dehydrogenase. *J. Biol. Chem*., **279**, 40437 - 40444.
32. Leimkühler, S., Hodson, R., George, G. N., and Rajagopalan, K. V., (2003). Recombinant *Rhodobacter capsulatus* Xanthine Dehydrogenase, a Useful Model System for the Characterization of Protein Variants Leading to Xanthinuria I in Humans. *J. Biol. Chem*., **278**, 20802 - 20811.
33. Palmer, G., (1962). The purification and properties of aldehyde oxidase. *Biochim. et Biophys. Acta*, **56**, 444 - 59.
34. Maia, L., and Mira L., (2002). Xanthine oxidase and aldehyde oxidase: a simple procedure for the simultaneous purification from rat liver. *Arch. Biochem. and Biophys.*, **400** (1), 48 - 53.
35. Li-Calzi, M., Raviolo, C., Ghibaudi, E., De Gioia, L., Salmona, M., Cazzaniga, G., Kurosaki, M., Terao, M., and Garattini, E., (1995). Purification, cDNA cloning, and tissue distribution of bovine liver aldehyde oxidase. *J. Biol. Chem*., **270**, 31037 - 31045.
36. Cabre, F., and Canela, E. I., (1987). Purification and properties of bovine liver aldehyde oxidase, *Biochem. Trans.*, **15**, 882 - 883.
37. Nishino, T., (1994). The conversion of xanthine dehydrogenase to xanthine oxidase and the role of the enzyme in reperfusion injury. *J. Biochem*, **116**, 1 - 6.
38. Nishino, T., Okamoto, K., Kawaguchi, Y., Hori, H., Matsumura, T., Eger, B. T., Pai, E. F., and Nishino, T., (2005). Mechanism of the conversion of Xanthine Dehydrogenase to Xanthine Oxidase: Identification of the two cysteine disulfide bonds and crystal structure of a non-convertible rat liver xanthine dehydrogenase mutant. *J. Biol. Chem*., **280**, 24888 - 24894.
39. Yamaguchi, Y., Matsumura, T., Ichida, K., Okamoto, K., and Nishino, T., (2007). Human Xanthine Oxidase changes its substrate specificity to Aldehyde Oxidase type upon mutation of amino acid residues in the active site: Roles of active site residues in binding and activation of purine substrate. *J. Biochem*., **141**, 513 - 524.
40. Beedham C., (1985). Molybdenum hydroxylases as drug-metabolizing enzymes. *Drug Metab. Rev*., **16** (1-2), 119 - 56.

41. Hille, R., (1992). Xanthine oxidase, xanthine dehydrogenase, and aldehyde oxidase. *Chem. Biochem. Flavoenzymes.* **3**, 21 - 68.
42. Rebelo, J. M., Dias, J. M., Huber, R., Moura, J. J. G., and Romao, M. J., (2001). Structure refinement of the aldehyde oxidoreductase from *Desulfovibrio gigas* (MOP) at 1.28 Å. *J. Biol. Inorg. Chem.*, **6**, 791 - 800.
43. Harrison, R., (2002). Structure and function of xanthine oxidoreductase: Where are we now? *Free Radical Biol. Med.*, **33**, 774 - 797.
44. Ventom, A. M., Deistung, J., and Bray, R. C., (1988). The isolation of demolybdo xanthine oxidase from bovine milk. *Biochem. J.*, **255** (3), 949 - 56.
45. Wahl, R C., and Rajagopalan, K.V., (1982). Evidence for the inorganic nature of the cyanolyzable sulfur of molybdenum hydroxylases. *J. Biol. Chem.*, **257** (3), 1354 - 9.
46. Massey, V., Brumby, P. E., Komai, H., and Palmer, G., (1969). Studies on Milk Xanthine Oxidase: Some spectral and kinetic properties. *J. Biol. Chem.***, 244**, 1682 - 1691.
47. Komai, H., Massey, V., and Palmer, G., (1969). The preparation and properties of deflavo xanthine oxidase. *J. Biol. Chem.*, **244** (7), 1692 - 1700.
48. Gnida, M., Ferner, R., Gremer, L., Meyer, O., and Meyer-Klaucke, W., (2003). A Novel Binuclear [ CuSMo ] Cluster at the Active Site of Carbon Monoxide Dehydrogenase: Characterization by X-ray Absorption Spectroscopy. *Biochemistry* , **42** (1), 222 - 230.
49. Gremer, L., Kellner, S., Dobbek, H., Huber, R., and Meyer, O., (2000). Binding of Flavin Adenine Dinucleotide to molybdenum-containing Carbon Monoxide Dehydrogenase from *Oligotropha carboxidovorans* structural and functional analysis of a carbon monoxide dehydrogenase species in which the native flavoprotein has been replaced by its recombinant counterpart produced in *escherichia coli* . *J. Biol. Chem.*, **275** (3), 1864 - 1872.
50. Pauff, J. M., Cao, H., and Hille, R., (2009). Substrate orientation and catalysis at the Molybdenum site in Xanthine Oxidase: Crystal structures pictures in complex with xanthine and lumazine. *J. Biol. Chem.*, **284** (13), 8760 – 8767.

51. Pauff, J. M., Zhang, J., Bell, C. E., and Hille, R., (2008). Substrate orientation in Xanthine Oxidase: Crystal structure of enzyme in reaction with 2-Hydroxy-6-methylpurine. *J. Biol. Chem.*, **283** (8), 4818 - 4824.
52. Dietzel, U., Kuper, J., Doebbler, J. A., Schulte, A., Truglio, J. J., Leimkühler, S., and Kisker, C., (2009). Mechanism of substrate and inhibitor binding of *Rhodobacter capsulatus* Xanthine Dehydrogenase. *J. Biol. Chem.*, **284** (13), 8768 - 8776.
53. Pauff, J. M., Hemann, C. F., Jünemann, N., Leimkühler, S., and Hille, R., (2007). The Role of Arginine 310 in catalysis and substrate specificity in Xanthine Dehydrogenase from *Rhodobacter capsulatus. J. Biol. Chem.,* **282** (17), 12785 - 12790.
54. Siegbahn, P. E. M., and Shestakov, A. F., (2005). Quantum chemical modeling of CO oxidation by the active site of molybdenum CO dehydrogenase. *J. Comput. Chem.,* **26** (9), 888 - 898.
55. Olson J. S., Ballou, D. P., Palmer, G., and Massey, V., (1974) The mechanism of action of xanthine oxidase. *J. Biol. Chem.,* **249** (14), 4363 - 82.
56. Howes, B, D., Bray, R. C., Richards, R. L., Turner, N. A., Bennett, B., and Lowe, D. J., (1996). Evidence favoring molybdenum-carbon bond formation in xanthine oxidase action: 17Q- and 13C-ENDOR and kinetic studies. *Biochemistry*, **35** (5), 1432 - 1443.
57. Hille, R., (2005). Molybdenum-containing hydroxylases. *Arch. of Biochem. and Biophys.,* **433** (1), 107 - 116.
58. Davis, M. D., Olson, J. S., and Palmer, G., (1984). The reaction of xanthine oxidase with lumazine. Characterization of the reductive half-reaction. *J. Biol. Chem.*, **259** (6), 3526 - 3533.
59. Xia, M., Dempski, R., and Hille, R., (1999). The reductive half-reaction of xanthine oxidase. Reaction with aldehyde substrates and identification of the catalytically labile oxygen *J. Biol. Chem.*, **274** (6), 3323-3330.
60. Cleland, W. W., (1963). The kinetics of enzyme-catalyzed reactions with two or more substrates or products: I. Nomenclature and rate equations. *Biochim. et Biophys. Acta,*, **67**, 104 - 137.

61. Cleland, W. W., (1973). Derivation of Rate Equations for Multisite Ping-Pong Mechanisms with Ping-Pong Reactions at One or More Sites. *J. Biol. Chem.*, **248**, 8353 - 8355.
62. Hille, R., and Massey, V., (1982). The oxidative half-reaction of xanthine oxidase. Developments in Biochemistry, **21** (Flavins Flavoproteins), 786-791.
63. Olson, J. S., Ballou, D. P., Palmer, G., and Massey, V., (1974). The Reaction of xanthine oxidase with molecular oxygen. *J. Biol. Chem.*, **249** (14), 4350 - 4362.
64. Hille, R., and Nishino, T., (1995). Flavoprotein structure and mechanism. 4. Xanthine oxidase and xanthine dehydrogenase. *FASEB J.*, **9**, 995 - 1003.
65. Hänzelmann, P., and Meyer, O., (1998). Effect of molybdate and tungstate on the biosynthesis of CO dehydrogenase and the molybdopterin cytosine-dinucleotide-type of molybdenum cofactor in *Hydrogenophaga pseudoflava. Eur. J. Biochem*. **255**, 755 - 765.
66. Voityuk, A. A., Albert, K., Romao, M. J., Huber, R., and Roesch, N., (1998). Substrate oxidation in the active site of Xanthine Oxidase and related enzymes. A model density functional study. *Inorg. Chem*., **37** (2), 176 - 180.
67. Greenwood, R. J., Wilson, G. L., Pilbrow, J. R., and Wedd, A. G., (1993). Molybdenum(V) sites in xanthine oxidase and relevant analog complexes: comparison of oxygen-17 hyperfine coupling. *J. Am. Chem. Soc*., **115** (13), 5385 - 5392.
68. Doonan, C.J., Stockert, A., Hille, R., and George, G. N., (2005). Nature of the catalytically labile oxygen at the active site of Xanthine Oxidase. *J. Am. Chem. Soc*., **127** (12), 4518 - 4522.
69. Amano, T., Ochi, N., Sato, H., and Sakaki, S., (2007). Oxidation reaction by Xanthine Oxidase. Theoretical study of reaction mechanism. *J. Am. Chem. Soc*., **129**, 8131 - 8138.
70. Meyer, O., Gremer, L., Ferner, R., Ferner, M., Dobbek, H., Gnida, M., and Meyer-Klaucke, W., and Huber, R., (2000). The role of Se , Mo and Fe in the structure and function of carbon monoxide dehydrogenase. *Biological chemistry*, **381** (9-10), 865 - 876.

71. Hofmann, M., Kassube, J. K., and Graf, T., (2005). The mechanism of Mo-/Cu-dependent CO dehydrogenase. *J. Biol. Inorg. Chem.,* **10** (5), 490 - 495.
72. Doonan, C. J., Rubie, N. D., Peariso, K., Harris, H. H., Knottenbelt, S. Z., George, G. N., Young, C. Y., and Kirk, M. L., (2008). Electronic structure description of the cis-MoOS unit in models for molybdenum hydroxylases. *J. Am. Chem. Soc.*, **130**, 55 - 65.
73. Bray, R. C., Bennett, B., Burke, J. F., Chovnick, A., Doyle, W. A., Howes, B. D., Lowe, D. J., Richards, R. L., and Turner, N. A., (1996). Recent studies on xanthine oxidase and related enzymes. *Biochem. Soc. Trans.*, **24** (1), 99 - 105.
74. Bray, R. C., Malmstrom, B. G., Vanngard, T., (1959). Chemistry of xanthine oxidase.V. Electron-spin resonance of xanthine oxidase solutions. *Biochem. J.*, **73,** 193 - 197.
75. Beedham, C., (1987). Molybdenum hydroxylases: Biological distribution and substrate-inhibitor specificity. *Prog. Med. Chem.,* **24**, 85 - 127.
76. McWhirter, R. B., and Hille, R., (1991). The reductive half-reaction of xanthine oxidase. Identification of spectral intermediates in the hydroxylation of 2-hydroxy-6-methylpurine. *J. Biol. Chem.*, **266**, 23724 - 23731.
77. Hofstee, B. H. J., (1955). On the mechanism of inhibition of xanthine oxidase by the substrate xanthine. *J. Biol. Chem.*, **216**, 235 - 244.
78. Beedham, C., (1998). Oxidation of carbon via molybdenum hydroxylases. *Biomedical and Health Research.* **25,** 39 - 52.
79. Hodges, G. R., Young, M. J., Paul, T., and Ingold, K. U., (2000). How should xanthine oxidase-generated superoxide yields be measured? *Free Radical Biology & Medicine*, **29** (5), 434 - 441.
80. Kim, J. H., and Hille, H., (1993). Reductive half-reaction of xanthine oxidase with xanthine. Observation of a spectral intermediate attributable to the molybdenum center in the reaction of enzyme with xanthine. *J. Biol. Chem.*, **268**, 44 - 51.
81. Hille, R., George, G. N., Eidsness, M. K., and Cramer, S. P., (1989). EXAFS analysis of xanthine oxidase complexes with alloxanthine, violapterin, and 6-pteridylaldehyde. *Inorg. Chem.*, **28** (21), 4018 - 4022.

82. Xiang, Q., and Edmondson, D., (1996). Purification and characterization of a prokaryotic xanthine dehydrogenase from Comamonas acidovorans. *Biochemistry,* **35** (17), 5441 - 5450.
83. Hille, R., and Massey, V., (1981). Tight binding inhibitors of xanthine oxidase. *Pharmacology & Therapeutics*, **14** (2), 249 - 263.
84. Kim, J. H., Ryan, M. G., Knaut, H., and Hille, R., (1996). The reductive half-reaction of xanthine oxidase. The involvement of prototropic equilibria in the course of the catalytic sequence. *J. Biol. Chem.,* **271** (12), 6771 - 80.
85. Hemann, C., Ilich, P., Stockert, A. L., Choi, E., and Hille, R., (2005). Resonance Raman Studies of Xanthine Oxidase: the Reduced Enzyme-Product Complex with Violapterin. *J. Phys. Chem. B,* **109**, 3023 - 3031.
86. Pick, F. M., McGartoll, M. A. and Bray, R. C., (1971). Reaction of formaldehyde and of methanol with xanthine oxidase. *Eur. J. Biochem.,* **18** (1), 65 - 72.
87. Aversa, M. L., and Meany, J. E., (1996). The inhibition of xanthine oxidase by acetaldehyde in aqueous solution. *Physiol. Chem. and Phys. and Med. NMR,* **28** (3), 153 - 162.
88. Morpeth, F. F., (1983). Studies on the specificity toward aldehyde substrates and steady-state kinetics of xanthine oxidase. *Biochim. et Biophys. Acta (Protein Structure and Molecular Enzymology)*, **744** (3), 328 - 334.
89. Krenitsky, T. A., Spector, T., and Hall, W. W., (1986). Xanthine oxidase from human liver: purification and characterization. *Arch. Biochem. and Biophys*., **247**(1), 108 - 119.
90. Krenitsky, T. A., Neil, S. M., Elion, G. B., and Hitchings, G. H., (1972). A Comparison of the specificities of xanthine oxidase and aldehyde oxidase. *Arch. Biochem. and Biophys*., **150** (2), 585 - 599.
91. Coughlan, M. P., and Rajagopalan, K. V., (1980). The Kinetic Mechanism of Xanthine Dehydrogenase and Related Enzymes. *Eur. J. Biochem.,* **105**, 81 - 84.
92. Sanders, S. A., Eisenthal, R., and Harrison, R., (1997). NADH oxidase activity of human xanthine oxidoreductase--generation of superoxide anion. *Eur. J. Biochem.*, **245**, 541 - 548.

93. Hille, R., and Massey, V., (1981). Studies on the oxidative half-reaction of xanthine oxidase. *J. Biol. Chem.*, **256**, 9090 - 9095.
94. Harris, C. M., and Massey, V., (1997). The oxidative half-reaction of xanthine dehydrogenase with NAD; reaction kinetics and steady-state mechanism. *J. Biol. Chem*., **272**, 28335 - 28341.
95. Porras, A. G., Olson, J. S., and Palmer, G., (1981). The reaction of reduced xanthine oxidase with oxygen. Kinetics of peroxide and superoxide formation. *J. Biol. Chem.*, **256**, 9096 - 9103.
96. Fred, L., Gough, D. A., Schmid-Schonbein, G. W. (1998). Role of xanthine oxidase in hydrogen peroxide production. *Free Radical Biology & Medicine*, **25** (6), 720 - 727.
97. Lineweaver, H., and Burk, D., (1934). The determination of enzyme dissociation constants. *J. Am. Chem. Soc*., **56**, 658 - 666.
98. Nishino, T., Nishino, T., Schopfer, L. M., and Massey, V., (1989). The reactivity of chicken liver xa nthine dehydrogenase with molecular oxygen. *J. Biol. Chem.*, **264**, 2518 - 2527.
99. McCord, J. M., and Fridovich, I., (1968). The Reduction of Cytochrome c by Milk Xanthine Oxidase. *J. Biol. Chem*., **243**, 5753 - 5760.
100. Bayse, C. A., (2009). Density-functional theory models of xanthine oxidoreductase activity: comparison of substrate tautomerization and protonation. *Dalton Trans.*, 2306–2314
101. Hille, R., (1993). The reaction mechanism of xanthine oxidase. ACS Symposium Series, 535 (Molybdenum Enzymes, Cofactors, and Model Systems), 22 - 37.
102. Gurtoo, H. L., and Johns, D. G., (1971). On the interaction of the electron acceptor 2,6-dichlorophenolindophenol with bovine milk xanthine oxidase. *J. Biol. Chem.*, **246** (2), 286 - 293.
103. Mengyan, Y., Yunyun, Z., Qingzhi, L., and Yuhuan, D., (1997). A simple method for measuring the kinetics of the formation of oxygen radicals. *Biotechnology Techniques*, **11** (11), 825 - 827.

104. Mest, S. J., Kosted, P. J., Van Kuijk, F. J. G. M., (1992). 2, 6-Dichlorophenolindophenol is a competitive inhibitor for xanthine oxidase and is therefore not usable as an electron acceptor in the fluorometric assay. *Free Radical Biology & Medicine*, **12** (3), 189 - 192.

105. Rajagopalan, K. V., and Handler, P., (1964). Hepatic Aldehyde Oxidase. III. The substrate-binding site. *J. Biol. Chem.*, **239**, 2027 - 2035.

106. Massey, V., and Edmondson, D., (1970). On the Mechanism of Inactivation of Xanthine Oxidase by Cyanide. *J. Biol. Chem.*, **245**, 6595 - 6598.

107. Muraoka, S., Enomoto, H., Sugiyama, M., and Yamasaki, H., (1967). Mechanism of the reduction of cytochrome c by xanthine oxidase. *Biochim. et Biophys. Acta. (Bioenergetics),***143** (2), 408 - 415.

108. Towne, V., Will, M., Oswald, B., and Zhao, Q., (2004). Complexities in horseradish peroxidase-catalyzed oxidation of dihydroxyphenoxazine derivatives: appropriate ranges for pH values and hydrogen peroxide concentrations in quantitative analysis. *Anal. Biochem.,* **334** (2), 290 - 296.

109. Kitson, T. M., (1999). A colourful journey through the chemistry of resorufin-enzyme interactions. *Chemistry in New Zealand*, **63**, 7 - 12.

110. Ishiyama, M., Furusawa, H., Shiga, M., Ohseto, F., and Sasamoto, K., (1999). A resorufin derivative as a fluorogenic indicator for cell viability. *Anal. Sci*., **15** (10), 1025 - 1028.

111. Slebocka-Tilk, H., Neverov, A. A., and Brown, R. S., (2003). Proton inventory study of the base-catalyzed hydrolysis of formamide. Consideration of the nucleophilic and general base mechanisms. *J. Am. Chem. Soc.*, **125** (7), 1851 - 1858.

112. Ilich, P., and Hille, R., (1999). Mechanism of formamide hydroxylation catalyzed by a molybdenum-dithiolene complex: A model for xanthine oxidase reactivity. *J. Phys. Chem. B*, **103** (25), 5406 - 5412.

113. Ilich, P., and Hille, R., (2002). Oxo, Sulfido, and Tellurido Mo-enedithiolate models for xanthine oxidase: Understanding the basis of enzyme reactivity. *J. Am. Chem. Soc.,* **124** (24), 6796 - 6797.

114. Zhang, X., and Wu, Y., (2005). A theoretical study on the mechanism of the reductive half-reaction of xanthine oxidase. *Inorg. Chem.*, **44** (5), 1466-1471.

115. Habtegabre, A. B., Knottenbelt, S., Guo, H., and Kirk, M. L., (2009). On the mechanism of substrate oxidation by xanthine oxidase: An electronic structure description of formal hydride transfer. *In Preparation*.

116. Morpeth, F. F., George, G. N., and Bray, R. C., (1984). Formamide as a substrate of xanthine oxidase. *Biochem. J.*, **220** (1), 235 - 242.

117. Beedham, C., Critchley, D. J. P., and Rance, D. J., (1995). Substrate Specificity of Human Liver Aldehyde Oxidase toward Substituted Quinazolines and Phthalazines: A Comparison with Hepatic Enzyme from Guinea Pig, Rabbit, and Baboon. *Arch. Biochem. and Biophys.* **319** (2), 481 - 490.

118. Morpeth, F. F., and Bray, R. C., (1984). Inhibition of xanthine oxidase by various aldehydes. *Biochemistry*, **23** (6), 1332 - 1338.

119. Voet, D., and Voet, J. G., Biochemistry, 2nd edition. John Wiley and Sons, Inc., 1995. New York. Pp. 331 - 410.

120. Menten, M. L., (1912). The relation of potassium salts and other substances to local anaesthesia of nerves. *Am. J. Phys.*, **31**, 85 - 93.

121. Briggs, G. E., and Haldane, J. B. S., (1925). A note on the kinetics of enzyme action. *Biochem. J.*, **19**, 338 - 339.

122. Atkins, P. W., (1994). *Physical chemistry* (5th ed.). New York: W.H. Freeman and CO. [Pages (a) 595 - 597 and 622 and (b) 864 - 942]

123. Eadie, G. S., (1942). The inhibition of cholinesterase by physostigmine and prostigmine. *J. Biol. Chem.*, **146** (1), 85 - 93.

124. Bunting, J. W., Laderoute, K. R., and Norris, D. J., (1980). The pH dependence of xanthine oxidase catalysis in basic solution. *Can. J. Biochem.*, **58** (5), 394 - 398.

125. Self, W. T., and Stadtman, T. C., (2000). Selenium-dependent metabolism of purines: A selenium-dependent purine hydroxylase and xanthine dehydrogenase were purified from Clostridium purinolyticum and characterized. *Proc. Nat. Acad. Sci.*, **97 (13)**, 7208–7213.

126. Parschat, K., Canne, C., Hüttermann, J., Kappl, R., and Fetzner, S., (2001). Xanthine dehydrogenase from Pseudomonas putida 86: specificity, oxidation-reduction potentials of its redox-active centers, and first EPR characterization. *Biochimica et Biophysica Acta,* **1544,** 151-165.

127. Fhaolain, I, N., Hynes, M. J., and Coughlan, M. P. (1978). Stopped-Flow Spectrophotometric Studies on the Reaction of Turkey Liver Xanthine Dehydrogenase with Reducing Substrates. *Biochem. J.*, **171**, 83 - 88.

128. Swann, J. C., and Bray, R. C., (1972). Multiple Phases in the Reduction of Xanthine Oxidase by Substrates. *Eur. J. Biochem*. **26**, 407 – 415.

129. Harris, C. M., and Massey, V., (1997). The Reaction of Reduced Xanthine Dehydrogenase with Molecular Oxygen. Reaction kinetics and measurement of superoxide radical. *J. Biol. Chem*., **272** (13), 8370–8379.

130. Davis, M. D., Olson, J. S., and Palmer, G., (1982). Charge transfer complexes between pteridine substrates and the active center molybdenum of xanthine oxidase. *J. Biol. Chem.,* **257,** 14730 - 14737.

131. Rantam, K., and Hille, R., (1993). Paradoxical stabilization of the neutral flavin semiquinone of xanthine dehydrogenase at high pH. *Biochem. and Biophys. Res. Comm.,* **194** (3), 1097 - 1102.

132. Saito, T., and Nishino, T., (1989). Differences in redox and kinetic properties between NAD-dependent and O2-dependent types of rat liver xanthine dehydrogenase. *J. Biol. Chem.,* **264**, 10015 - 10022.

133. Ryan, M. G., Ratnam, K., and Hille, R., (1995). The Molybdenum centers of Xanthine Oxidase and Xanthine Dehydrogenase. *J. Biol. Chem.,* **270,** 19209 - 19212.

134. Kirk, M. L., Knottenbelt, S. Z., Habtegabre, A., (2009) *Comput. Inorg. Bioinorg. Chem.* (accepted for publication)

135. Meyer, O., and Schlegel, H. G., (1979). Oxidation of carbon monoxide in cell extracts of Pseudomonas carboxydovorans. *J. Bacteriology.*, **137**, 811 - 817.

136. Choi, E., Stockert, A. L., Leimkühler, S., and Hille, R., (2004). Studies on the mechanism of action of xanthine oxidase. *J. Inorg. Biochem.,* **98** (5), 841 - 848.

137. Gorelsky, S. I., (2009). AOMix: Program for molecular orbital analysis; University of Ottawa, http://www.sg-chem.net/

138. Foresman, J. B., and Frisch, A., (1993). Exploring Chemistry with electronic structure methods, 2nd edition, Gaussian, Inc. Pittsburgh, PA.[Pages (a) 118, (b) 46, (c) 62, (d) 171, (e) 119 and 149, (f) 295, (g) 53 and 98, (h) 66, (i) 101, 133, and 134, (j) 42, and (k) 13].

139. Solomon, E. I., and Hanson, M. A., (2006). Bioinorganic Spectroscopy in inorganic electronic structure and spectroscopy. Volume II: Application and case studies. Solomon, E. I., and Lever, A. B. P., ed., pages 1 - 131. John Wiley and Sons, Inc.

140. Lever, A. B. P., and Dodsworth, E. S., (2006). Electochemistry, charge transfer spectroscopy, and electronic structure in inorganic electronic structure and spectroscopy. Volume II: Application and case studies. Solomon, E. I., and Lever, A. B. P., ed., Pages 227 – 281. John Wiley and Sons, Inc.